Application of biophysical methods to assess the role of platelet cytoskeletal proteins in platelet biomechanics

I n a u g u r a l d i s s e r t a t i o n

zur

Erlangung des akademischen Grades eines

Doktors der Naturwissenschaften (Dr. rer. nat.)

der

Mathematisch-Naturwissenschaftlichen Fakultät

der

Universität Greifswald

vorgelegt von

Laura Rumprecht geb. Sachs

Greifswald, März 2022

Dekan: Prof. Dr. Gerald Kerth

1. Gutachter: Prof. Dr. Oliver Otto

2. Gutachter: Prof. Dr. Andreas Greinacher

3. Gutachter: Prof. (apl) Dr. Peter Bugert

4. Gutachter: Prof. PhD. Alice Assinger

Tag der Promotion: 17. August 2022

Contents

1. Zusammenfassung

Die biomechanischen (Elastizitätsmodul, Adhäsionskraft, Verformbarkeit) Eigenschaften von Thrombozyten hängen vom Zytoskelett ab und haben einen unbestrittenen Einfluss auf physiologische und pathologische Prozesse wie Hämostase und Thrombose. Die Veränderungen dieser biomechanischen Eigenschaften können als markierungsfreie diagnostische Marker bei beginnenden oder fortschreitenden Erkrankungen wie der *MYH9*-vererbten Erkrankung verwendet werden. Daher war der Fokus meiner Doktorarbeit, die Beziehung zwischen den Veränderungen in den Proteinen des Thrombozyten-Zytoskeletts und den daraus resultierenden biomechanischen Eigenschaften mit biophysikalischen Methoden zu untersuchen.

Im ersten Kapitel meiner Doktorarbeit habe ich mich auf die biophysikalischen Methoden konzentriert, die am häufigsten zur Bewertung und Quantifizierung der biomechanischen Eigenschaften von Thrombozyten verwendet werden. In meinem Übersichtsartikel gebe ich einen detaillierten Einblick in die zugrunde liegenden Prinzipien, den Aufbau der Instrumente und diskutiere relevante Beispiele. Darüber hinaus fasse ich die Grenzen dieser biophysikalischen Methoden zusammen und weise auf aktuelle Verbesserungen hin. Die Übersicht umfasst die folgenden Techniken: Mikropipettenaspiration, Rasterkraftmikroskopie (AFM), Raster-Ionenleitfähigkeitsmikroskopie (SICM), Zugkraftmikroskopie auf Hydrogelsubstraten, Mikrosäulen und verformbare 3D-Substrate sowie Echtzeit-Verformbarkeitszytometrie (RT-DC). Dieser Übersichtsartikel richtet sich an klinisch-wissenschaftliche Forscher, die daran interessiert sind, die Rolle der Thrombozytenbiomechanik in der Hämostase- und Thromboseforschung mit Hilfe dieser einzellbasierten biophysikalischen Methoden zu erforschen.

Im zweiten Kapitel meiner Doktorarbeit stelle ich meine Forschungsarbeit über den Einfluss von üblicherweise verwendeten *Ex-vivo*-Antikoagulanzien auf die intrinsischen biomechanischen Eigenschaften und funktionellen Parametern (z.B. Aktivierungsprofile) menschlicher Thrombozyten vor. Um dies umfassend zu beurteilen, wurden Thrombozyten verwendet, die in verschiedenen *Ex-vivo*-Antikoagulanzien wie ACD-A, Na-Citrat, K_2-EDTA, Li-Heparin und r-Hirudin gewonnen

wurden und ihre biomechanischen Eigenschaften wurden durch Echtzeit-Fluoreszenz- und Verformbarkeitszytometrie (RT-FDC) bestimmt. Mit Hilfe der Durchflusszytometrie und konfokale Laser-Scanning-Fluoreszenzmikroskopie wurden die Eigenschaften der Thrombozytenfunktion ermittelt. Es wurde festgestellt, dass K_2-EDTA und Li-Heparin die biomechanischen Eigenschaften von Thrombozyten beeinflussen, indem die Aktinpolymerisation von nicht stimulierten menschlichen Thrombozyten erhöht wird. Diese erhöhte Aktinpolymerisation führt zu einer geringeren Verformung der Thrombozyten. Es wird empfohlen, für die Untersuchung des Zytoskeletts menschlicher Thrombozyten ein *Ex-vivo*-Antikoagulans wie ACD-A, Na-Citrat oder r-Hirudin zu wählen und es nach Möglichkeit nicht auszutauschen, da die Vergleichbarkeit der Ergebnisse nicht gewährleistet ist. Darüber hinaus demonstriere ich die Bedeutung der Wahl der richtigen *Ex-vivo*-Antikoagulanzien mit Hilfe der RT-FDC, indem ich zeige, dass Thrombozyten von einem gesunden Spender und einem *MYH9*-Patienten mit der Punktmutation E1841K sich in ihrer Verformung unterscheiden. Diese Forschungsarbeit ist die erste umfassende Untersuchung auf der Ebene einzelner Thrombozyten, die die Bedeutung der präanalytischen Standardisierung bei der Vorbereitung von Thrombozytenproben für biomechanische Studien belegt.

Das dritte Kapitel meiner Doktorarbeit befasst sich mit den biomechanischen Analysen von Thrombozyten und Thromben von der *MYH9*-vererbten Erkrankung. Dafür wurden drei *Myh9*-Mauslinien mit einer Punktmutation im *Myh9*-Gen an den Positionen 702, 1424 oder 1841 sowie zwei *MYH9*-Patienten (*MYH9* p.D1424N, *MYH9* p.E1841K) untersucht. Die *MYH9*-vererbte Erkrankung äußert sich in einer Makrothrombozytopenie mit mäßiger Blutungsneigung. Sie wird durch Mutationen im *MYH9*-Gen verursacht, die zu einer Veränderung der schweren Ketten des nicht muskulären Myosins Typ IIA (NMMHC IIA) und damit zu einer Störung im Zytoskelett der Thrombozyten führen. Durch Western-Blot Analyse, Durchflusszytometrie, *in-vitro* Aggregometrie und Transmissionselektronenmikroskopie wurde gezeigt, dass *Myh9*-Punktmutanten-Mäuse im Vergleich zur Kontrollgruppe eine vergleichbare Primärfunktion haben. Die heterozygoten Punktmutationen im *Myh9*-Gen führten zu einer geringeren Verformung der Thrombozyten (RT-FDC), zu einer verminderten Thrombozytenadhäsion auf Kollagen (Kraft-Spektroskopie einzelner Thrombozyten - SPFS) und verminderten Thrombozyten-Thrombozyten-Interaktionskräften (SPFS).

Die verminderte Thrombozytenkraft (Micropost Arrays) führt zu weicheren Thromben (kolloidale Probenspektroskopie), zu einer beeinträchtigten Retraktion des Blutgerinnsels und somit zu einer verlängerten Blutungszeit. Die Mutationen R702C, D1424N und E1841K haben eine ähnliche Wirkung auf die biomechanischen Funktionen der Thrombozyten, wobei die Mutation E1841K eine geringere Auswirkung auf die Thrombusbildung und -steifigkeit hatte. *MYH9*-Patienten haben ein erhöhtes Blutungsrisiko und das Antifibrinolytikum Tranexamsäure (TXA) ist eine Möglichkeit, Blutungskomplikationen bei diesen Patienten zu kontrollieren. Es wurde gezeigt, dass die TXA Behandlung die Blutungszeit in den drei *Myh9*-Mausmodellen signifikant reduziert und somit bestätigt, dass der verstärkte Blutungsphänotyp aufgrund der verminderten Thrombozytenkräfte in *Myh9*-Mutantenmäusen durch die Zugabe von TXA kompensiert werden kann.

Mit den in meiner Doktorarbeit vorgestellten biophysikalischen Methoden und Forschungsergebnissen wird deutlich, dass es essentiell wichtig ist, die veränderte Reaktion des Zytoskeletts der Thrombozyten durch Zytoskelettmutationen, biochemische, physikalische Stimuli oder durch pharmakologische Aspekte zu untersuchen. Damit wird uns eine Möglichkeit gegeben, die zugrunde liegenden Mechanismen besser zu verstehen und somit zu einer besseren klinischen Behandlung beizutragen.

2. Summary

The biomechanical (Young's modulus, adhesion force, deformability) properties of platelets depend on the cytoskeleton and have an undisputed influence on physiological and pathological processes such as hemostasis and thrombosis. The alterations of these biomechanical properties can be used as label-free diagnostic markers in initiation or progressive diseases such as *MYH9*-inherited disease. Therefore, the focus of my thesis was to investigate the relationship between the changes in platelet cytoskeleton proteins and the resulting biomechanical properties using biophysical methods.

In the first chapter of my thesis I focused on my review of the biophysical methods that are most commonly used to assess and quantify the biomechanical properties of platelets. In this review, I provide an in-depth insight into the governing principles and instrumentation setup and discuss relevant examples applied to platelet mechanics. In addition, my review also summarizes the limitations of these biophysical methods and highlight latest improvements. The review covers the following techniques: micropipette aspiration, atomic force microscopy (AFM), scanning ion conductance microscopy (SICM), tensile force microscopy on hydrogel substrates, microcolumns, and deformable 3D substrates, and real-time deformability cytometry (RT-DC). This review is directed toward clinician scientists who are interested in exploring applications of single-cell based biophysical approaches in unraveling the role of platelet biomechanics in hemostasis and thrombosis research.

In the second chapter of my thesis, I present my research paper on the influence of commonly used *ex vivo* anticoagulants on the intrinsic biomechanical properties and functional parameters (e.g. activation profils) of human platelets. To comprehensively assess this, platelets obtained in different *ex vivo* anticoagulants such as ACD-A, Na-Citrate, K_2-EDTA, Li-Heparin, and r-Hirudin were used, and their biomechanical properties were determined by real-time fluorescence and deformability cytometry (RT-FDC). Flow cytometry, and confocal laser scanning fluorescence microscopy were used to determine platelet function properties. K_2-EDTA and Li-Heparin were found to affect platelet biomechanics by increasing actin polymerization of non-stimulated human platelets. This increased actin polymerization results in decreased platelet

deformation. It is recommended that an *ex vivo* anticoagulant such as ACD-A, Na-Citrate, or r-Hirudin be chosen for the study of the cytoskeleton of human platelets and, if possible, that it not be exchanged, because comparability of results is not assured. Furthermore, I demonstrate the significance of choosing correct *ex vivo* anticoagulants in RT-FDC by showing that platelets from a healthy donor and a *MYH9* patient with the E1841K point mutation differ in their deformation. This paper is the first comprehensive investigation at the single platelet level to establish the relevance of preanalytical standardization in platelet sample preparation for biomechanical studies.

The third chapter of my thesis is focused on the biomechanical analyses of platelets and thrombi from *MYH9*-related disease. Here I studied three *Myh9* mouse lines with a point mutation in the *Myh9* gene at positions 702, 1424, or 1841. Furthermore, two *MYH9* patients (*MYH9* p.D1424N, *MYH9* p.E1841K) were examined. *MYH9*-related disease (*MYH9*-RD) presents with macrothrombocytopenia with a moderate bleeding tendency. It is caused by mutations in the *MYH9* gene that lead to alteration of non-muscle myosin heavy chains type IIA (NMMHC IIA), resulting in disruption of the platelet cytoskeleton. Western blot analysis, flow cytometry, *in vitro* aggregometry, and transmission electron microscopy demonstrated that *Myh9* point mutant mice have comparable primary function compared to the control group. The heterozygous point mutations in the *Myh9* gene resulted in decreased platelet deformation (RT-FDC), decreased platelet adhesion to collagen (single platelet force spectroscopy-SPFS), and decreased platelet-platelet interaction forces (SPFS). Decreased platelet force (Micropost Arrays) results in softer thrombi (colloidal probe Spectroscopy), impaired clot retraction, and thus prolonged bleeding time. The R702C, D1424N, and E1841K mutations have a similar effect on platelet biomechanical functions, although the E1841K mutation had less impact on thrombus formation and stiffness. *MYH9*-RD patients have an increased risk of bleeding, and the antifibrinolytic drug tranexamic acid (TXA) is one way to control bleeding complications in these patients. It was shown that TXA treatment significantly reduced bleeding time in the three *Myh9* mouse models, confirming that the enhanced bleeding phenotype due to decreased platelet forces in *Myh9* mutant mice can be compensated by the addition of TXA.

With the biophysical methods and research results presented in my thesis, it is clear that it is essential to study the altered response of the platelet cytoskeleton by cytoskeletal mutations, biochemical, physical stimuli, or by pharmacological aspects.

This will provide us with an opportunity to better understand the underlying mechanisms and thus contribute to better clinical treatment.

3. Introduction

The initiation or presence of diseases is usually accompanied not only by biological and functional changes, but also by alterations in the biomechanical properties of cells (Lee, Lim, 2007), such as in cancer, malaria, and sickle cell anemia. Current laboratory-based diagnostic techniques rely on assessing molecular markers using biochemical assays and immunological approaches to underpin pathological changes in cells and tissues. Within this context, little explored are the biomechanical fingerprints of cells in the pathophysiology of diseases. Biomechanical changes in cells can serve as promising label-free biomarkers to detect the initiation and progression of the disease or to better understand the underlying mechanism (Di Carlo, 2012). These biomechanical (Young's modulus, adhesion force, deformability) properties depend, for example, on the cytoskeleton, an interconnected network of filamentous polymers and regulatory proteins. Platelets are an optimal biological system to study the cytoskeleton and analyze the biophysical processes associated with biomechanical force generation, because platelets have a high actin content (Pollard, Goldman, 2017). In the first section of this chapter, I provide a brief overview of platelet function and review the components and functions of the platelet cytoskeleton. While an overview of the different techniques for biomechanical evaluation of platelets is given in the second part, I focus on cytoskeletal alterations in inherited platelet disorders in the third part.

3.1. Platelets

Platelets are small, anucleated cell fragments (1-3 µm in diameter) formed from megakaryocytes in the bone marrow (Machlus, Italiano, 2013). In humans, platelets in peripheral blood range from 150000 to 450000/µl (Daly, 2011). The lifetime of a platelet is approximately 10 days (Harker et al., 2000). Platelets are devoid of a nucleus but possess mitochondria, open canalicular system (OCS), a dense tubular system, and three different secretory granules: α-granules, dense granules, and lysosomes. The dense granules contain mainly non-protein compounds that support platelet aggregation. The lysosomes store proteolytic enzymes. The α-granules contain more

than 300 different proteins involved in functions such as coagulation, platelet adhesion, inflammation, wound healing, and angiogenesis. Platelets ensure the integrity of the vascular system, and are an intergral part of hemostasis (Harrison, Martin Cramer, 1993, Thomas, 2019). As soon as platelets encounter a damaged vessel wall and the exposed components of the subendothelial extracellular matrix, they are rapidly activated and adhere to both the vessel wall, and other platelets. The components of the secretory granules are released, and locally produced thrombin enhances platelet activation by cleaving fibrinogen to fibrin, and supports thrombus formation. Fibrinolytic processes eventually dissolve the formed thrombus by releasing plasminogen activators (tissue plasminogen activator, tPA and urokinase plasminogen activator, uPA) from the endothelial cells, and these serine proteases activate plasminogen to plasmin. Plasmin cleaves the fibrin of the blood clot. When there is increased clotting, and excessive thrombus formation and/or a reduction in fibrinolytic processes, thrombosis occurs, and leads to occlusion of the blood vessel (Montague et al., 2020, Packham, 1994). From a biological perspective, the role of platelets in hemostasis, and thrombosis is well described, but the biomechanical aspects are poorly understood.

3.2. Cytoskeleton of platelets

The biomechanical (Young's modulus, adhesion force, deformability) properties of platelets are determined, for example, by the cytoskeleton. The cytoskeleton of platelets supports the maintenance of discoid shape, and cell integrity in the presence of shear, and other forces in blood circulation. Another function is the rapid shape change, and associated reorganization of the cytoskeleton in response to external stimuli at sites of vascular injury (Falet, 2002). Thus platelet cytoskeleton plays an essential role in platelet adhesion, and activation, as well as spreading, and generation of contractile forces (Figure 1).

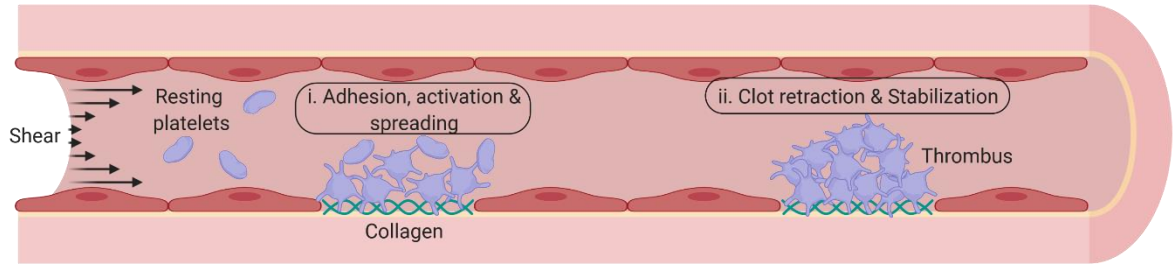

Figure 1: Schematic illustration of thrombus formation.
Resting platelets circulate in the blood flow, and when a vessel injury is detected by exposed extracellular matrix proteins (von Willebrand factor, collagen), the platelets adhere. The GPIb-IX-V complex, and GPVI receptor on platelets regulate the adhesion, downstream signalling, and activation process. Platelets are activated, release P-selectin, and secrete secondary mediators (ADP, thromboxane). Activation of the αIIbβ3 receptor occurs, leading to a conformational change from the αIIbβ3 receptor through the binding of fibrinogen to the activated αIIbβ3 integrin. A cascade of intracellular signaling events leads to irreversible stable adhesion, spreading, clot retraction, irreversible aggregation, and cytoskeleton reorganization of platelets and subsequent thrombus formation. Schematic was created with BioRender.com.

The cytoskeleton of platelets consists of spectrin, tubulin, and actin, as well as several proteins that regulate the cytoskeleton (Bender, Palankar, 2021) (Figure 2A). Spectrin is linked to the plasma membrane, and the actin filaments via filamin, and thus supports the maintenance of the platelet shape. Actin is the most abundant protein in platelets, accounting for 15 - 20% of the total cellular protein by mass. In resting platelets, about 40% of the total actin is composed of dynamic filaments (F-actin). F-actin are polymers of the globular actin (G-actin) which polymerize in a head-to-tail manner (Bearer et al., 2002, Thomas, 2019). Actin is bound via filamin to the glycoproteins GP Iα (receptor for collagen), GP Ib (receptor for thrombin and von Willebrand factor (vWF)), and GP IX in the membrane (Hartwig, DeSisto, 1991) (Figure 2B). Microtubules are dynamic, polarized structures, and form 8 to 12 microtubule coils, called the marginal band, in resting platelets. Under this condition, the marginal band is the main factor for the maintenance of platelet size, and shape (Bender, Palankar, 2021).

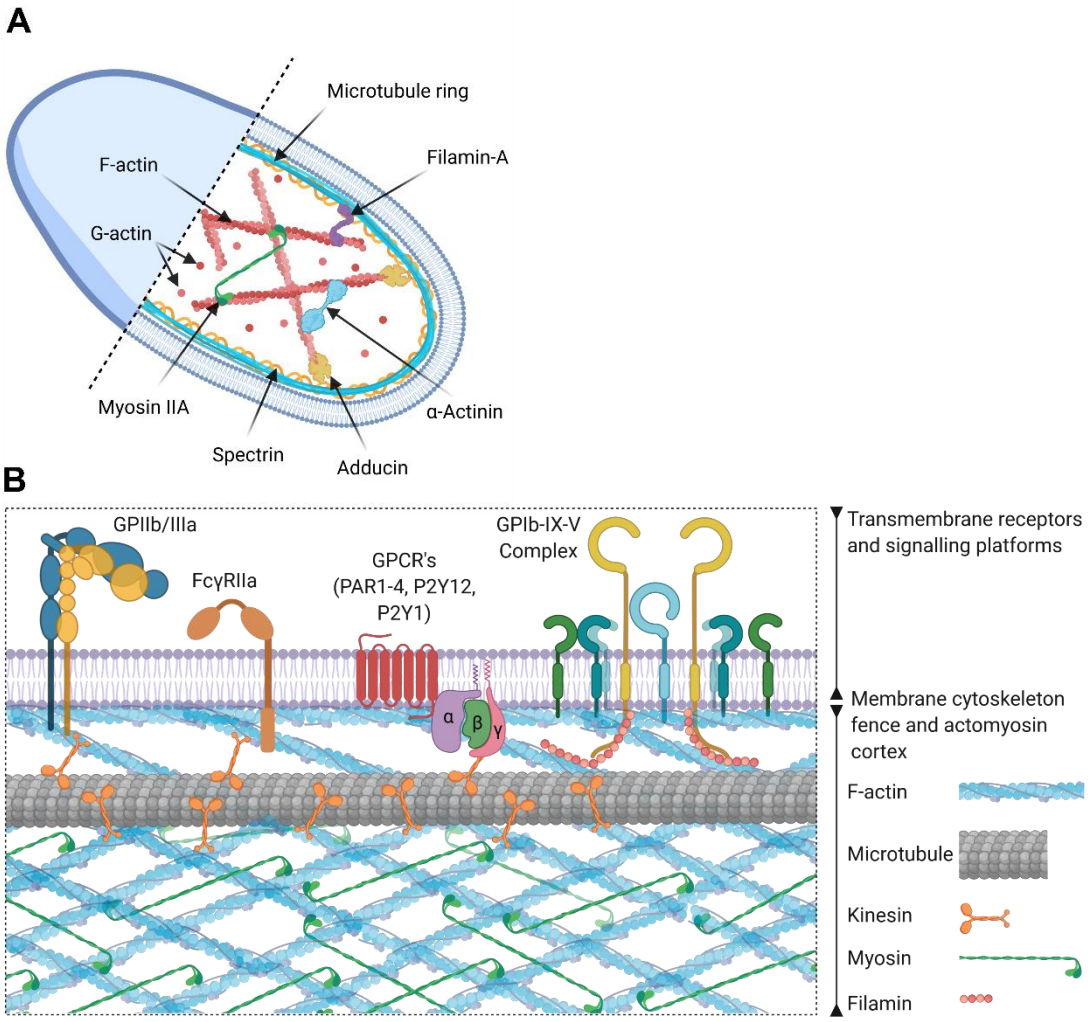

Figure 2: Platelet cytoskeleton. (A) Schematic illustration of the cytoskeleton of resting platelets. **(B)** Schematic representation of the cytoskeletal framework in platelets shows the major structural components and the structural connection between the cytoskeleton components and the receptors. (A) from (Bender, Palankar, 2021) and (B) adapted from (Zaninetti et al., 2020).

Several receptor-ligand interactions mediate platelet adhesion, and thrombus formation. In the damaged vessel, binding between GP Ib-IX-V complex, and immobilized vWF on subendothelial collagen occurs. This interaction allows binding of the receptor GPVI to the collagen, initiating platelet activation. This leads to the activation of platelet integrins αIIbβ3 (GP IIb/IIIa, fibrinogen receptor). In particular, GP IIb/IIIa changes the conformation of its extracellular β3-domain, thereby increasing affinity for fibrinogen, fibronectin, and vWF (Fox, 2001, Thomas, 2019, Zaninetti et al., 2020). As a result, stronger adhesion of platelets to extracellular ligands via integrins is achieved. During these processes, the marginal band is compressed, and depolymerized due to altered motor protein activities (dynein/kinesin). It contributes to

granule secretion, and mechanical resistance to shear forces, and charge distribution around the platelet (Thomas, 2019).

Polymerization of actin filaments (about 80%) drives the spreading process. Upon initial contact with the surface or activation by soluble platelet agonists, the shape of the platelet changes from a disk to a sphere. Filopodia (finger-like extensions) form from the platelet, extending from the cell periphery. The platelet then begins to flatten, and forms thin leaves of broad lamellipodia with the initiation of OCS extrusion. During this time, the platelet centralizes organelles, and granules. The centralized granules fuse with the OCS, allowing secretion of their contents, a process promoted by actin polymerization. To prevent further blood loss, restore blood flow past potentially occluding thrombi, and promote wound healing, thrombus contraction occurs. Contractile forces are generated by the cyclic interaction of myosin with actin. The major form of myosin is non-muscle myosin IIA (myosin II). Interaction with actin filaments generates protrusive, and contractile forces important for cell shape and their mechanical properties. Myosin is rapidly activated, and associated with the actin cytoskeleton upon platelet activation.

Activation and contractility of myosin II are required for the maintenance/integrity of platelet spreading, aggregate stability and retraction of blood clots (Thomas, 2019).

3.3. Techniques for biomechanical assessment of platelets

Changes in biomechanical properties can be used as label-free diagnostic markers for a pathophysiological state of platelets. For example, forces generated during adhesion and spreading and contraction of single platelets in health and disease can be evaluated and quantified. These biomechanical properties of platelets can be studied using biophysical methods (Table 1). In my review, I address which biophysical methods are used to study platelets, the limitations of these methods and their improvements (Article 1., concluded in Section 4.1). Typical methods are micropipette aspiration, atomic force microscopy (AFM), scanning ion conductance microscopy (SICM), traction force microscopy on hydrogel substrates, micropillars, and deformable 3D substrates, and real-time deformability cytometry (RT-DC) or real-time fluorescence and deformability cytometry (RT-FDC). The difference between RT-DC and RT-FDC is that RT-FDC includes a fluorescence module. The fluorescence

module is equipped with excitation lasers of 488 nm, 561 nm, and 640 nm, and emission is detected at the following wavelengths: 500-550 nm, 570-616 nm, 663-737 nm on avalanche photodiodes (Rosendahl et al., 2018). In a typical RT-FDC measurement, 1000 cells per second are measured and plotted in a scatter plot of deformation versus area. Since larger cells are subjected to higher stresses in the constriction, deformation is not a direct measure of cell mechanical properties. This means that when comparing two cells with similar stiffness but different area, the larger cell will deform more. Thus, an analytical model (Mietke et al., 2015) and numerical simulations (Mokbel et al., 2017) allow isoelasticity lines to be established for finding cells of different area with corresponding stiffness and to determine the elastic modulus for each cell. Due to the area of the platelets of 5 μm^2 on average, the deformability/elastic modulus of the platelets could not be determined. In my manuscripts I was able to show differences in deformation and area, but only in the case of equal area was the difference in deformation interpreted as changes in biomechanical properties.

Table 1: Comparison of biophysical methods for the evaluation of biomechanical properties of platelets and thrombi. Adapted from (Sachs et al., 2020).

Biophysical method	Biomechanical properties	Restrictions	Throughput
Micropipette aspiration	Viscosity and elasticity	Nonadherent In suspension adherent	Low 1-5 platelets/hour
AFM	Viscosity, elasticity and adhesion forces	Adherent	Low 1-5 platelets/hour
Colloidal probe spectroscopy	Viscosity and elasticity	Adherent	Medium 10-15 thrombi/hour
SICM	Viscosity and elasticity	Adherent	Low 1-10 platelets/hour
Traction force microscopy on hydrogel substrates	Adhesion contraction	Adherent	Medium to high
Micropillars and deformable 3D substrates	Adhesion contraction	Adherent	Medium
RT-DC/RT-FDC	Elasticity	Nonadherent In suspension	Very high 100-1000 platelets/second
Thromboelastometry	Viscoelasticity	Clot	4 whole blood sampels/hour

Our laboratory has introduced a modified version of AFM called colloidal probe spectroscopy in platelet research (Figure 3A). Although colloidal probe spectroscopy is similar to AFM in its basic operation, a micrometer-sized sphere is immobilized at the end of the cantilever instead of a sharp tip. In a typical experiment, the tip of the colloidal probe (i.e., the microsphere) is gently pressed against a single thrombus by applying a force on the order of a few nano-Newtons perpendicular to the horizontal plane of the thrombus. This induces a deflection of the cantilever that is representative of the resistance force of the thrombus (Zaninetti et al., 2020). To generate thrombi, recalcified whole blood is perfused in a collagen-coated flow chamber for 5 minutes at a shear rate of 100 µl/min. This approach allows systematic characterization of the biomechanical properties of thrombi formed on a wide range of adhesive matrices under different shear stress conditions that mimic vascular flow dynamics, microenvironment, and local architecture.

Another method we use is thromboelastometry. Thromboelastometry (Figure 3B) is a viscoelastometric method for testing hemostasis in whole blood and measures interactions of clotting factors, inhibitors, and cellular components during the clotting phases and subsequent lysis. Whole blood is placed in a cuvette, and a cylindrical pin is immersed. The pin oscillates left and right by a spring and moves freely at the beginning of the measurement. When the blood begins to clot, the clot increasingly restricts the oscillation of the pin as the clot strength increases. These kinetics are recorded mechanically and displayed graphically. After retraction of the clot, lysis occurs, and the motion transmission of the cup is reduced (Crochemore et al., 2017).

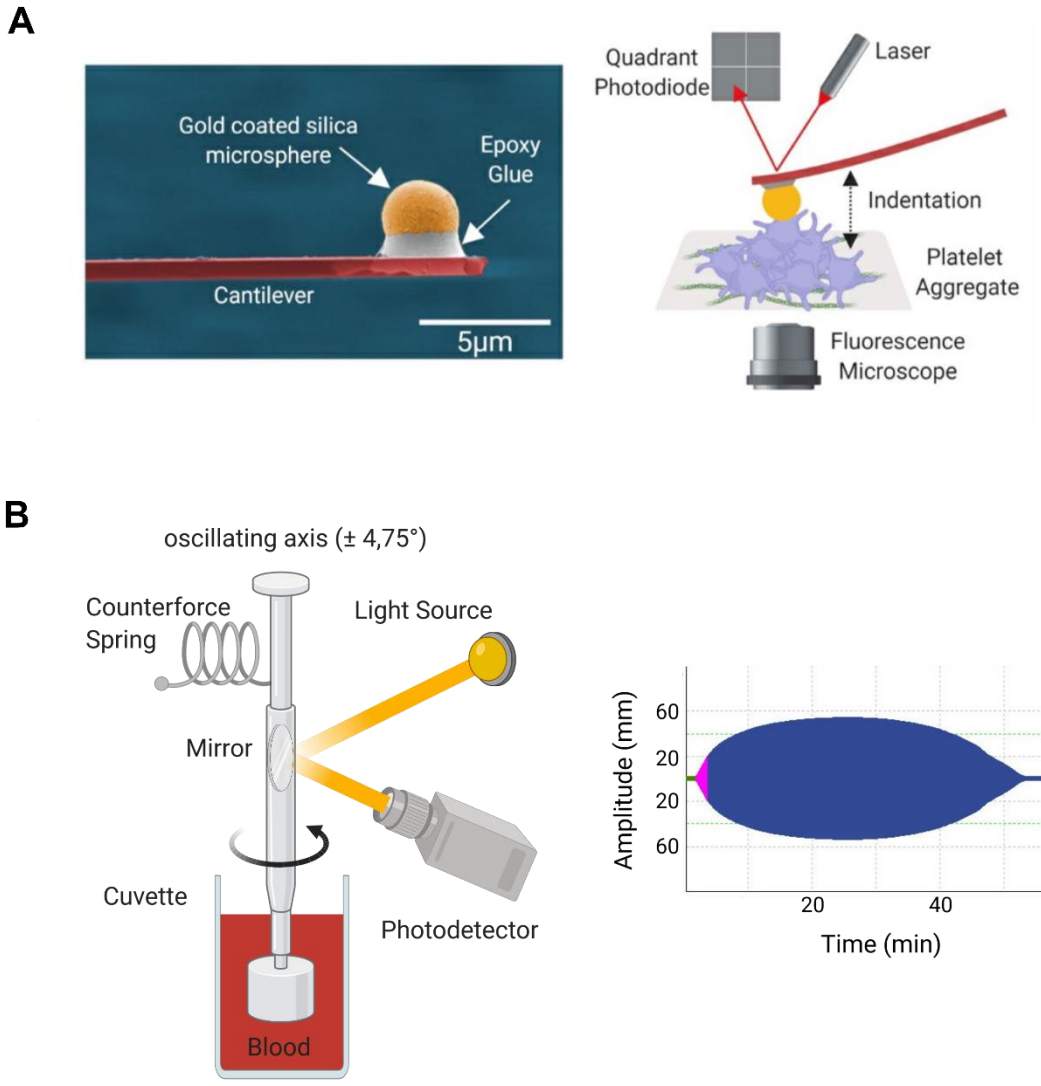

Figure 3: Colloidal probe spectroscopy and thromboelastometry. Measurement principle of colloidal probe spectroscopy with setup of the cantilever (A) and measurement principle of thromboelastometry with a representative curve of a healthy donor (B). Some schematics were created with BioRender.com.

With attention to preanalytical variability in blood sample preparation, biophysical methods are not well standardized (Guck, 2019). To establish standardization in sample preparation of platelets for biomechanical studies, we used *ex vivo* anticoagulants in blood collection using RT-FDC. Typically used *ex vivo* anticoagulants are ACD-A, Na-Citrate, K_2-EDTA, Li-Heparin, and r-Hirudin. ACD-A, Na-Citrate, and K_2-EDTA chelate free calcium, thereby reducing the activity of components of the coagulation pathway. Li-Heparin activates antithrombin, which in turn inhibits proteases essential for coagulation, including thrombin and factor (F)Xa. r-Hirudin is a

highly specific thrombin inhibitor that binds to active thrombin and irreversibly inactivates it. It binds exclusively to thrombin and has no effect on the coagulation cascade, the complement cascade, or blood cells (Krueger et al., 2002) (Article 2., concluded in Section 4.2).

Biophysical methods are essential to explain the causes of cytoskeleton alterations, such as inherited platelet disorders, and thus to contribute to improved clinical treatment. Our study examined single platelets and thrombi from three *Myh9* mouse lines and two *MYH9* patients to demonstrate that platelet force generation mediated by non-muscle myosin IIA is critical for adequate coagulation response and hemostatic function (Manuscript 3., concluded in Section 4.3).

3.4. Cytoskeleton alterations in inherited platelet disorders

Several inherited platelet disorders are caused by mutations in key cytoskeleton-regulating proteins, such as Wiskott-Aldrich syndrome, filamin A defect, or myosin heavy chain 9 (*MYH9*)-associated disease (Drachman, 2004, Nurden, Nurden, 2011). Defects in the cytoskeleton usually cause thrombocytopenia. Wiskott-Aldrich syndrome is an X-linked inherited disorder characterized by small platelets, immunodeficiency, eczema, and increased risk of autoimmune diseases and cancer. It is caused by a mutation in the WAS gene and results in impaired F-actin polymerization (Althaus et al., 2019).

MYH9-related disease (*MYH9*-RD) is a rare inherited platelet disorder. It is caused by alterations in the *MYH9* gene. Heterozygous mutations in this gene lead to the four distinct syndromes: May-Hegglin anomaly, Epstein syndrome, Fechtner syndrome, and Sebastian platelet syndrome. All four syndromes have clinically in common: macrothrombocytopenia with a moderate bleeding tendency (Althaus et al., 2019, Palma-Barqueros et al., 2021). The *MYH9* gene encodes the non-muscle myosin heavy chain IIA (NMMHC-IIA), an actin-binding protein with contractile properties.

Non-muscle myosin class II belongs to the myosin superfamily (Hodge, Cope, 2000). In humans, there are three isozymes of non-muscle myosin II: NMM-IIA, NMM-IIB, and NMM-IIC. Platelets express only NMM-IIA (Maupin et al., 1994). NMM-IIA is composed of two non-muscle myosin heavy chains (NMMHC; MW 220 kDa) and four light chains (MLC; MW 16.5 kDa). It has an N-terminal head, a neck, and a C-terminal tail (Marigo

et al., 2004, Simons et al., 1991, Toothaker et al., 1991). The N-terminal head interacts with actin and exposes the ATP-binding side. The neck is an important binding site for the MLCs. The MLC is responsible for triggering the contractile response of actomyosin. Phosphorylation of MLC activates myosin and allows it to interact with actin filaments (Fox, Phillips, 1982, Kumar et al., 1989, Suzuki et al., 1999). The C-terminal tail domain is important for filament assembly and cargo binding (Berg et al., 2001).

Depending on the position of the mutations, the risk for other symptoms such as kidney failure, hearing loss, and cataract increases (Althaus, Greinacher, 2009). Patients with a mutation at amino acid position 702, located in the motor domain of non-muscle myosin IIA, are at higher risk for increased bleeding. Mutations in the rod domain (amino acid positions 1424 and 1841) cause a milder phenotype (Althaus, Greinacher, 2009, Palma-Barqueros et al., 2021).

In clinics, there are several approaches to treat bleeding complications in *MYH9*-RD patients (Pecci, Balduini, 2021).Thrombopoietin receptor agonists are an option for short-term treatment by increasing platelet counts (Zaninetti et al., 2019). Desmopressin is a synthetic derivative of vasopressin. As a selective agonist at arginine vasopressin receptor-2, it exhibits an antidiuretic but not a vasoconstrictor effect. Desmopressin acts primarily via an increase in Von Willebrand factor and clotting factor VIII and can be administered to adults before surgery in combination with Tranexamic acid (TXA). In addition, TXA is also used alone to treat excessive bleeding during menstruation or for local application after dental procedures (Althaus et al., 2011, Althaus, Greinacher, 2010). TXA inhibits the activation of plasminogen to plasmin and thus fibrinolysis (Dunn, Goa, 1999).

4. Results and Discussion

This thesis aims to investigate the relationship between the changes in platelet cytoskeleton proteins and the resulting biomechanical properties using biophysical methods, such as RT-FDC and AFM. In the following chapter, I will present the main results from the review and the two research articles aimed at this goal. In the review, we present biophysical methods that can be applied to study platelets. In the first research article, we introduce standardization in sample preparation of blood cells, especially for platelets used in biomechanical studies to ensure comparability of experiments. In the second research manuscript, we focus on investigating the biomechanical mechanisms involved in clot formation and stabilization for three *Myh9* mouse lines and two *MYH9* patients to understand further platelet force generation mediated by non-muscle myosin IIA. The review was published in Research and Practice in Thrombosis and Haemostasis (RPTH), the first research article was published in Communications Biology, and the second research manuscript was accepted at Science Advances.

4.1. Article 1: Quantifying single-platelet biomechanics: An outsider's guide to biophysical methods and recent advances

Commonly used *in vitro* and *ex vivo* assays include platelet aggregometry, impedance aggregometry, rheological techniques, flow cytometry, and real-time thrombus formation in parallel plate flow chambers (Cardigan et al., 2005). These assays have greatly improved our understanding of hemostasis and thrombosis from a biochemical and cell biological perspective. Still, they do not provide insight into the underlying biomechanical properties and the biophysical forces generated during hemostasis or thrombosis. Biomechanical properties can be determined by biophysical methods.

In **micropipette aspiration**, a part of the membrane of a single platelet is aspirated into a borosilicate glass micropipette, and negative pressure is applied stepwise. The changed length of the aspirated platelet membrane is recorded using video microscopy (González-Bermúdez et al., 2019, Kee, Robinson, 2013). Micropipette aspiration has been used in studies to evaluate the biomechanical alterations induced by platelet

agonists (thrombin, ADP) and platelet aggregation inhibitors such as acetylsalicylic acid (Burris et al., 1986, Burris et al., 1987). However, micropipette aspiration is rarely used because only low throughput can be measured, and high technical requirements are necessary. Recent developments use a microfluidic device in which micropipettes are arranged in parallel and thus would facilitate the study of platelets (Mak, Erickson, 2013, Myrand-Lapierre et al., 2015).

Atomic force microscopy (AFM) enables three-dimensional imaging of samples at the nanometer scale and investigates intermolecular/intercellular forces in the sub-pico Newton range (Gross et al., 2018). The main component of the atomic force microscope is a thin, flexible silicon nitride cantilever 100-200 µm long with a pyramid-shaped probe tip at one end that is passed over the sample in the *x*, *y*, and *z* axes (scanning mode). The cantilever deflection is registered on a quadrant photodiode by a reflected laser and provides a quantitative signal for the applied force. Alternatively, the cantilever can be pressed onto the sample, and the forces required to deflect it are measured, or an adhesive tip can be used to pull on the sample. Theoretical models such as Hertz, Sneddon, Derjaguin-Müller-Toporov and Johnson-Kendall-Roberts models are used to evaluate mechanical properties of biological systems (Krieg et al., 2019). However, the use of AFM to study platelets is a time-consuming technique with low throughput and requires immobilization of platelets (Nguyen et al., 2016). Despite these limitations, important insights into platelet biomechanics have been obtained with AFM. For example, elastic moduli for single platelets and areas of higher (e.g., platelet margins) and lower (e.g., granulomers) stiffness in platelet adhesion were determined (Radmacher et al., 1996).

Scanning ion conductivity microscopy (SICM) is a label-free, non-contact, non-invasive, and high-resolution topography imaging technique and offers a resolution from several micrometers to a few nanometers (Happel et al., 2012, Schäffer, 2013, Shevchuk et al., 2006). SICM analyzes the sample by detecting ion current interference induced by the properties of the sample in response to the application of hydrostatic pressure and is emerging as the method of choice for high-speed morphometric and biomechanical characterization of single platelets (Hansma et al., 1989, Happel et al., 2012). Thus, one study showed that the mean elastic modulus of single platelets increased during spreading. Furthermore, the elastic modulus of platelets decreased significantly in the presence of thrombin (Rheinlaender et al., 2015). The application of

the SICM does not allow fast and large area scanning of living biological samples. Technical improvements in the design of the SICM now allow a scanning area of 20 × 20 μm^2 within 10 seconds (Zhukov et al., 2012).

Traction force microscopy (TFM) are methods for precise measurement and quantification of cellular traction forces or contractile forces (Roca-Cusachs et al., 2017). The principle is based on quantitative optical microscopy to measure substrate displacements, which are then converted into forces (Ribeiro et al., 2016, Schwarz, Soiné, 2015). TFM on hydrogel substrates and bending of elastomeric micropillar arrays are most commonly used to measure generated tensile forces.

TFM on hydrogel substrates is a versatile and interference-free approach to measure cellular forces from single cells to tissue planes. It measures exerted tensile forces from spatial images of substrate stress by tracking the displacement of reference markers (fluorescent tracer beads) (Plotnikov et al., 2014). TFM is a relatively simple method with high sensitivity but has low measurement throughput. In addition, artifacts associated with variations in the mechanical properties of the hydrogel may occur. To address these drawbacks, a chip-based platelet contraction cytometer with high throughput was developed (Myers et al., 2017). This method has fibrinogen-passivated microdot pairs on a hydrogel substrate with different stiffness to evaluate the nanomechanics of hundreds of single platelets under physiologically relevant conditions. In one study, the contractile forces of platelets from patients with Wiskott-Aldrich syndrome and *MYH9*-disorder (non-muscle myosin IIa mutations) were determined using a platelet contraction cytometer. These data show that up to 30% of these platelets have almost no contractile forces on stiffer substrates, whereas this was the case in only 6% of healthy controls (Myers et al., 2017).

The deformable micropillar (micropost) arrays are compliant vertical elastomeric cylindrical cantilevers made of polydimethylsiloxane with defined dimensions (diameter and height) and stiffness (linear elastic) (Gupta et al., 2015). The ligand-functionalized tips of the microcolumns serve as adhesive surfaces (Sniadecki et al., 2014). After cell adhesion, the displacements of the single microcolumns in an array are tracked using video microscopy, and the force exerted on the cantilever is calculated using beam theory (Tan et al., 2003). For example, Liang et al. quantified the contractile forces generated by platelets in a microthrombus and demonstrated quantitatively for the first time that each platelet functions as an active contractile force-generating unit in the

microthrombus (Liang et al., 2010). Fabricating deformable micropillar arrays is a labor-intensive and time-consuming process, limiting the rapid prototyping required to optimize substrate deformation and increase measurement sensitivity. In addition, by replica molding process is not possible to fabricate complex geometries to measure cellular tensile forces on 3D substrates. Therefore, a laboratory has introduced a maskless technique based on direct laser writing with 2-photon polymerization (2PP) in 3D photosensitive resists to 3D print high-resolution deformable micro- and nanostructures (Klein et al., 2010).

Real-time deformability cytometry (RT-DC) is a microfluidic technique that allows to record and evaluate the morphology and mechanics of up to 1000 cells/second in a narrow channel (with a cross-section of 15-40 µm). The cells are deformed by hydrodynamic shear, and normal stresses without channel contact and the resulting deformation and its magnitude are quantified in real-time, without prior labeling of the cells (Otto et al., 2015b). Thus, it is possible to identify comprehensive biomechanical signatures of single cell types in blood in a short time (Otto et al., 2015a). The deformed cells inside the narrow channel are illuminated with a high-power LED and recorded with a high-speed complementary metal-oxide-semiconductor (CMOS) camera. The analysis software ShapeIn2 (Zellmechanik Dresden) analyzes several parameters like cell size and deformation. For example, in the scatter plot the deformation versus the cell size (cross-sectional area) or porosity, circularity and images from every single platelet can be displayed. Each event in the scatter plot represents a measured cell and can be selected through evaluation software ShapeOut (Zellmechanik Dresden) to get additional information like the cell image and calculated contours (Mietke et al., 2015). Because of these abilities, RT-DC is a promising method with potential relevance to various areas of the life sciences (Urbanska et al., 2018).

These biophysical methods have enhanced our understanding of the biomechanical principles that influence hemostasis and thrombus formation. However, to maximize the potential of many of these biophysical methods to answer outstanding questions in platelet biology requires extensive collaboration among interdisciplinary teams.

4.2. Article 2: *Ex vivo* anticoagulants affect human blood platelet biomechanics with implications for high-throughput functional mechanophenotyping.

Deciphering the cytoskeleton-dependent intrinsic biomechanical properties of platelets using biophysical methods is highly desirable to enhance our understanding of platelets in physiological and pathological processes and to improve diagnostic perspectives (Lam et al., 2011, Zhang et al., 2018). However, biophysical methods are not well standardized with respect to preanalytical variability in sample preparation of peripheral blood cells, including platelets (Guck, 2019). Thus, we used the *ex vivo* anticoagulants ACD-A, Na-Citrate, K_2-EDTA, Li-Heparin, and r-Hirudin to investigate the influence of *ex vivo* anticoagulants on the intrinsic biomechanical properties of human platelets from healthy donors (*n* = 6) and an *MYH9* patient with the point mutation E1841K using RT-FDC.

Our study showed that unstimulated platelets anticoagulated with Li-Heparin had higher F-actin content, lower deformation, smaller platelets, and higher PAC-1 expression (change in integrin αIIbβ3 receptor) compared with platelets in ACD-A, Na-Citrate, and r-Hirudin. The disc-shaped morphology and a subcortical marginal band microtubule were comparable in unstimulated platelets in Li-Heparin with platelets in ACD-A, Na-Citrate, and r-Hirudin. Activation of platelets with the agonist TRAP-6 in ACD-A, Na-Citrate, Li-Heparin, and r-Hirudin resulted in a significant decrease in platelet deformation, a decrease in platelet size, an increased F-actin content, a reduction in the edge-to-edge coiling of the microtubule ring, an increase in CD62P surface expression, and PAC1-FITC binding. However, the apparent discrepancies between Li-Heparin and ACD-A, Na-Citrate and r-Hirudin indicate that Li-Heparin is inducing artifacts in the biomechanical properties of platelets. One explanation would be the strong negative charge of heparin and its binding to αIIbβ3, which triggers αIIbβ3-mediated outside-in signaling, initiating cytoskeleton reorganization. (Gao et al., 2011, Sobel et al., 2001).

Unstimulated platelets collected in K_2-EDTA had the highest F-actin content, a coiled microtubule ring, showed the lowest deformation, and were the smallest compared with the other anticoagulants. Platelets stimulated with TRAP-6 in K_2-EDTA showed only minor changes in deformation, platelet size, F-actin content, CD62P expression, and

PAC-1 binding. Our observations are consistent with previous studies demonstrating K_2-EDTA induced ultrastructural changes in the surface-bound channel system (constriction and dilation of the OCS) and irreversible dissociation of αIIbβ3 complexes. (Gachet et al., 1993, Golański et al., 1996, Ma, Wong, 2007, White, 2000). It is possible that the high level of F-actin in non-stimulated and TRAP-6 stimulated platelets and the associated platelet deformation could be explained by the irreversible dissociation of the αIIbβ3 complex and the associated reorganization of the cytoskeleton.

To support these findings and to establish the direct link between platelet deformation and F-actin content, we used latrunculin B (LatB), an inhibitor of actin polymerization. Our results showed that LatB increased platelet deformation in unstimulated and TRAP-6 stimulated platelets in all *ex vivo* anticoagulants compared with the respective vehicle control. In particular, the significant increase in deformation of stimulated platelets in K_2-EDTA indicated that the increased F-actin content of platelets in K_2-EDTA is responsible for the increased deformation when actin polymerization is blocked by LatB, leading to destabilization of the actin cytoskeleton. Unstimulated and TRAP-6 stimulated platelets had reduced CD62P expression with LatB, with the exception of K_2-EDTA, for which no change occurred, as expected. Resting platelets showed a decrease in PAC-1 binding after LatB treatment with ACD-A, Li-Heparin, and r-Hirudin, suggesting a reorganization of the cytoskeleton. A reduction of PAC-1 binding after TRAP-6 activation is observed only with Li-Heparin, confirming our hypothesis that Li-Heparin induces cytoskeleton reorganization by binding to αIIbβ3, resulting in greater platelet deformation.

The practical relevance of our findings is evident when *MYH9* p.E1841K platelets are examined in ACD-A compared with K_2-EDTA. In ACD-A, unstimulated and TRAP-6 stimulated *MYH9* p.E1841K platelets deformed less and were larger compared with platelets from healthy controls. In K_2-EDTA, unstimulated and stimulated platelets from healthy donors and *MYH9* patients showed significantly reduced deformation compared with their counterparts in ACD-A. CD62P surface expression and PAC-1 binding were comparable in unstimulated and stimulated platelets from the *MYH9* p.E1841K patient and the healthy donor. The F-actin content is higher in non-stimulated platelets from *MYH9* p.E1841K patients in ACD-A than the platelets from the control donor. In K_2-EDTA, the F-actin content is higher for the healthy donor and the *MYH9* patient compared with their counterparts in ACD-A. Activation with TRAP-6

leads to an increase in F-actin content in ACD-A for the *MYH9* patient and healthy donor, and in K_2-EDTA it remains unchanged for both donors.

In conclusion, we find that K_2-EDTA and Li-Heparin affect platelet biomechanics by decreasing deformation and increasing actin polymerization of non-stimulated human platelets. It is recommended that an *ex vivo* anticoagulant such as ACD-A, Na-Citrate, or r-Hirudin be chosen for the study of the cytoskeleton of human platelets and, if possible, that it not be interchanged, as comparability of results is not guaranteed otherwise. With RT-FDC, we have a promising method to study the platelet skeleton in platelet-rich plasma (PRP), which according to our study, provides very solid and rapid results.

4.3. Manuscript 3: Reduced platelet forces underlie impaired hemostasis in mouse models of *MYH9*-related disease.

Patients with *MYH9*-related disease most commonly have a point mutation in the *MYH9* gene at positions 702, 1424, or 1841 (Balduini et al., 2011). For this study, three different mouse lines were generated with the knock-in mutations Arg702Cys (R702C), Asp1424Asn (D1424N), and Glu1841Lys (E1841K) (Zhang et al., 2012). These heterozygous point mutant mice recapitulated the major features of human patients, such as macrothrombocytopenia, moderately prolonged bleeding times, decreased ability to retract clots, and nonhematologous defects (Zhang et al., 2012). From a biological point of view, the role of platelets in preventing blood loss is well described, but the mechanobiological aspects are poorly understood. Therefore, we analyzed the three point mutant *Myh9* mouse models and two *MYH9*-RD patients with point mutations 1424 and 1841 (Baumann et al., 2022).

We demonstrated by Western blot analysis the presence of myosin IIA protein in control and heterozygous mutant mice (*Myh9* R702C/+, *Myh9* D1424N/+, *Myh9* E1841K/+). *Myh9* mutant mice exhibited a significant reduction in platelet count and increased platelet size. We analyzed platelet activation of *Myh9* R702C, D1424N, and E1841K mutant mice, which was comparable overall to controls when platelets of similar size were compared. The kinetics and extent of platelet aggregation did not differ between mutants and controls. Transmission electron microscopic (TEM) analysis of mutant platelets revealed a heterogeneous population of platelet size but

otherwise comparable ultrastructure. Thus, it can be concluded that *Myh9* point mutant mice have comparable primary function compared with the control group.

The mutant platelets exhibited increased F-actin content, likely due to the increased platelet size. The spreading experiments on a fibrinogen-coated surface showed comparable spreading kinetics of the *Myh9* mutant R702C/+ platelets. Slightly faster spreading was shown for *Myh9* D1424N/+ and *Myh9* E1841K/+ mutant platelets, probably due to the size of the *Myh9* mutant platelets and thus earlier adhesion to the activating surface. The mutant platelets were able to reorganize the cytoskeleton and form filopodia and lamellipodia. A capillary-based immunoassay was used to detect phosphorylation of myosin light chain 2 (MLC2) in resting and thrombin-activated platelets. Expression of MLC2 and myosin phosphatase 1 (MYPT1) was comparable in control and mutant samples. However, phosphorylation of MLC2 after activation with thrombin was greatly reduced in *Myh9* mutant platelets compared with control platelets. These data suggest that heterozygous mutations in the motor domain (R702C) and the rod domain (D1424N, E1841K) may affect the contractile properties of mutant platelets.

Biomechanical analysis showed that *Myh9* mutant platelets exhibited significantly reduced deformation (RT-FDC), which could be explained by the increased F-actin content. *Myh9* mutant platelets have lower adhesion forces on collagen (single platelet force spectroscopy - SPFS), lower interaction forces between platelets (SPFS), and generate lower traction forces on fibrinogen (micropost arrays). Spread mutant platelets on fibrinogen (R702C/+. D1424N/+) have lower elastic modulus (= softer platelets, SICM), which would be due to altered platelet actomyosin network. *Myh9* platelets E1841K/+ showed a comparable elastic modulus to control platelets. *Ex vivo* assay of thrombus formation on collagen showed that platelets from *Myh9* mutant mice (D1424N/+, R702C/+) formed fewer and smaller thrombi. Platelets from *Myh9* mutant mice E1841K/+ had fewer and smaller thrombi only under thrombocytopenic conditions. Colloidal probe spectroscopy showed that thrombi formed by platelets from *Myh9* mutant mice had a reduced elastic modulus (= softer thrombi). We showed that *in vitro* clot retraction of samples from *Myh9* mutant mice was impaired in both unmatched and matched platelets, suggesting a less central role of platelet count.

To verify our biomechanical results from the analyses of the mutant mice, we analyzed the deformation and force generation of platelets from two patients with the

corresponding mutations (*MYH9* p.D1424N, *MYH9* p.E1841K). Biomechanical analyses showed that platelets from the patients were stiffer and larger (RT-FDC). Thrombus formation on collagen under shear, showed significantly fewer and smaller thrombi and decreased kinetics of thrombus formation over time. Colloidal probe spectroscopy showed that thrombi from the *MYH9* p.D1424N patient were significantly softer and moderately but not significantly softer from the *MYH9* p.E1841K patient. These results indicate that the overall biomechanical properties of human and mouse platelets with point mutations in non-muscle myosin IIA are comparable, with the exception of thrombus stiffness in the *MYH9* p.E1841K sample, which showed a tendency toward softer thrombi only.

MYH9-RD patients have an increased risk of bleeding, which we also determined in the *Myh9* mutant mice with bleeding time (Zhang et al., 2012). The antifibrinolytic drug TXA is one way to control bleeding complications in these patients (Althaus et al., 2011, Althaus, Greinacher, 2009). Thus, our results show that TXA treatment significantly reduced bleeding time in the three *Myh9* mutant mouse models. Thus, it can be said that the enhanced bleeding phenotype due to decreased platelet forces in *Myh9* mutant mice can be compensated by the addition of TXA.

The improved clot stability of the mutant mouse samples prompted us to investigate the effect of TXA on clot formation and stability in patient samples. Whereas the onset of lysis (LOT) measured by thromboelastometry occurred earlier in the human patient sample with the addition of rtPA, the defect was reversed by the addition of TXA. Similarly, *ex vivo* thrombus stability of *MYH9*-RD patient platelets was improved under shear in the presence of TXA. We measured the stiffness of thrombi by colloidal probe spectroscopy and found that TXA significantly increased the stiffness of thrombi from the *MYH9* p.D1424N sample. However, the improvement in thrombus stiffness by TXA was achieved to a lesser extent for the patient sample with the E1841K mutation. Overall, this indicates that TXA can also stabilize clots and thrombi from *MYH9*-RD patients.

In conclusion, we find that heterozygous point mutations in the *Myh9* gene lead to decreased platelet adhesion and decreased platelet-platelet interaction forces in mice and *MYH9*-RD patients. The decreased platelet force results in impaired clot retraction and prolonged bleeding time. The R702C, D1424N, and E1841K mutations have a similar effect on platelet biomechanical function, although the E1841K mutation had a

reduced effect on thrombus formation and stiffness. Inhibition of fibrinolysis with TXA can improve hemostatic function in *Myh9* mutant mice.

5. Outlook

With the biophysical methods and research results presented in this thesis, it is clear that it is essential to study the altered response of the platelet cytoskeleton by cytoskeletal mutations, biochemical, physical stimuli, or by pharmacological aspects (Finkenstaedt-Quinn et al., 2015, George et al., 2018, Hartwig, 2013, Qiu et al., 2015). Thus, the influence of drugs on platelet biomechanics is rarely discussed. Several drugs, such as aspirin, clopidogrel, and prasugrel, modulate platelet activation and have been developed to prevent thrombotic diseases and complications (Collins, Hollidge, 2003, Rao et al., 2006). In contrast to the mechanisms of action, which are well studied, little is known about the role of platelet morphological changes and cytoskeleton (Shin et al., 2016). In the following chapter, I will present my preliminary data on the influence of *ex vivo* aspirin on the biomechanics of single platelets and thrombi.

Aspirin is not only an analgesic, anti-inflammatory, and antipyretic drug but also a potent antiplatelet agent. It acts by irreversibly blocking cyclooxygenase-1 or -2 (acetylation of a serine residue), thereby inhibiting the conversion of arachidonic acid to prostaglandin H2. It exerts its antiplatelet effect primarily by inhibiting thromboxane A2 synthesis, which is irreversible for the life of treated platelets. It is used to reduce the risk of myocardial infarction in stable or unstable angina by inhibiting platelet aggregation and thus having a cardioprotective effect (Barry S. Coller, 2013). However, it is increasingly suspected that the antiplatelet effect of aspirin is not only due to the blockade of prostaglandins but that aspirin may also have impact on the platelet cytoskeleton (Malinin et al., 2003). Therefore, it seemed reasonable to us to investigate the impact of 5.5 µM and 55 µM aspirin (reflecting plasma levels of therapeutic doses (Benedek et al., 1995, Thiessen, 1983, Thorir et al., 1987)) on biomechanical parameters, such as deformation of single platelets, stiffness of single thrombi, and property in clot formation. To this end, we performed a comprehensive analysis of biomechanical platelet function using RT-FDC, colloidal probe spectroscopy, thromboelastometry. For this purpose, *ex vivo* aspirin was incubated in ACD-A whole blood for 10 min, and PRP was prepared by centrifugation for RT-FDC measurements.

First, we used RT-FDC to investigate whether aspirin affects the cytoskeleton-dependent hydrodynamic deformation of single platelets. Unstimulated platelets exposed to aspirin *ex vivo* in whole blood showed significantly reduced median deformation of 0.068 ± 0.015 (mean ± SD) at 5.5 µM aspirin and 0.059 ± 0.013 at 55 µM aspirin in contrast to a higher deformation of 0.097 ± 0.015 (*n* = 6 donors) in control platelets (Figure 4A).

To determine whether aspirin-induced reduced deformation of single platelets influences thrombus mechanics, we performed colloidal probe spectroscopy. The data showed a significant decrease in Young's modulus of 2.55 ± 0.91 kPa (mean ± SD, 5.5 µM aspirin) and 2.43 ± 0.72 kPa (55 µM aspirin) compared to the control sample of 2.99 ± 0.91 kPa (*n* = 8 donors). This means that aspirin thrombi formed under shear flow are softer than control thrombi (Figure 4B).

To support the results of colloidal probe spectroscopy, we analyzed control whole blood and whole blood incubated with 55 µM aspirin in thromboelastometry (Figure 4C). The aspirin thrombi had a lower elastic shear modulus (G: 7570 ± 846 dyn/cm^2, mean ± SD) and thrombodynamic potential index (TPI: 45.8 ± 16.6) than control thrombi (G: 8051 ± 778 dyn/cm^2; TPI: 56 ± 20). This means that the density of the blood clot (TPI) (Kairov et al., 2018) and platelet-fibrin interactions (G) decrease in aspirin thrombi. The decrease in platelet-fibrin interactions results in a decrease in clot strength and clot firmness (G) (Chandler, 1995, Hochleitner et al., 2017, Sharma et al., 1997).

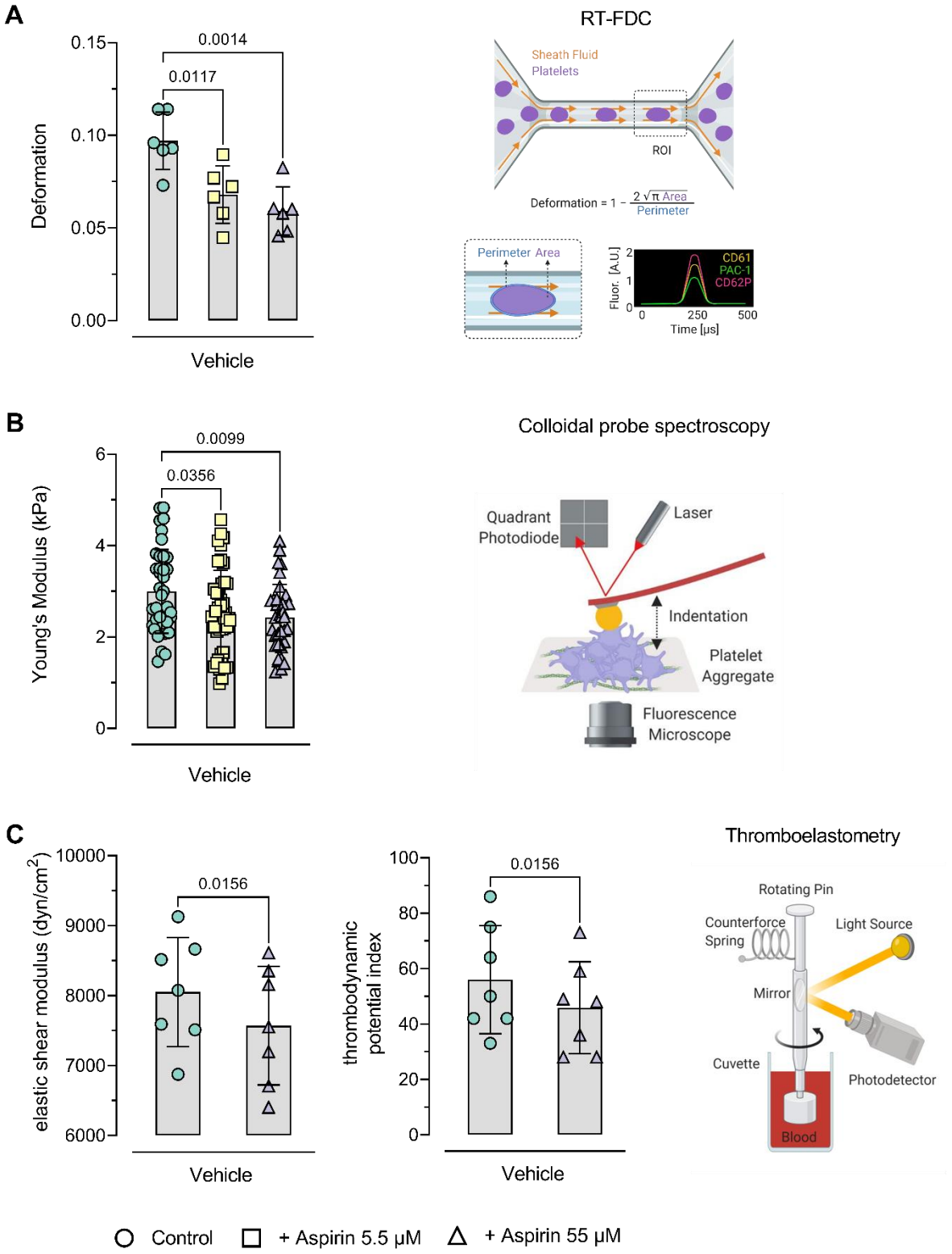

Figure 4: Effect of *ex vivo* aspirin (5.5 µM, 55 µM) on single platelets and thrombi. Each data point of **(A)** RT-FDC measurement shows the median deformation of at least 2500 platelets from one donor and bar plots show mean ± standard deviation of median deformation of vehicle platelets without/with aspirin treatment (5.5 µM or 55 µM aspirin; n = 6 donors). RT-FDC measurements were carried out in a microchannel of 15 x 15 µm cross section and of 300 µm length at a flow rate of 0.006 µl/s. Each data point of **(B)** colloidal probe spectroscopy

shows the median Young´s modulus of one control or aspirin thrombi (5.5 µM or 55 µM aspirin) and bar plots show mean ± standard deviation of median Young´s modulus (n = 8 donors). Each data point of **(C)** thromboelastometry shows the elastic shear modulus and thrombodynamic potential index of one donor and bar plots show mean ± standard deviation of elastic shear modulus and thrombodynamic potential index from control whole blood and aspirin treated whole blood (55 µM, n = 7 donors). Statistical analysis for RT-FDC and colloidal probe spectroscopy is performed using ordinary one-way ANOVA with Sidak multiple comparison test, statistical analysis for thromboelastometry was performed using Wilcoxon matched-pairs signed rank test. P values < 0.05 were considered statistically significant. Schematics were created with BioRender.com.

In conclusion, we found that *ex vivo* aspirin significantly affects the platelet cytoskeleton. Our data showed that single aspirin treated platelets deform less, but thrombi formed under shear flow on a collagen-coated slide are softer. Aspirin-influenced thrombi have a lower clot density and show a decrease in clot strength/clot firmness. These preliminary research results may provide a new perspective on the current mechanism of action of aspirin and decipher the interplay between mechanism of action, drug action, and mechanics. Thus, platelet biomechanics could play an important role in disease onset, progression, and treatment, providing a new diagnostic approach for disease diagnosis and clinical treatment. Potentially, deriving the mechanical properties of thrombi from the mechanics of single platelets could allow earlier diagnosis of stroke, heart attack, or thrombosis.

6. References

Althaus, K.; Greinacher, A. MYH9-related platelet disorders. *Seminars in thrombosis and hemostasis* **2009,** *35* (2), 189–203. DOI: 10.1055/s-0029-1220327.

Althaus, K.; Greinacher, A. MYH-9 Related Platelet Disorders: Strategies for Management and Diagnosis. *Transfusion medicine and hemotherapy : offizielles Organ der Deutschen Gesellschaft fur Transfusionsmedizin und Immunhamatologie* **2010,** *37* (5), 260–267. DOI: 10.1159/000320335.

Althaus, K.; Najm, J.; Greinacher, A. MYH9 related platelet disorders - often unknown and misdiagnosed. *Klinische Padiatrie* **2011,** *223* (3), 120–125. DOI: 10.1055/s-0031-1275664.

Althaus, K.; Wagner, M.; Bakchoul, T. Diagnose der Thrombozytenfunktionsstörungen – eine Herausforderung im Labor. *Transfusionsmedizin* **2019,** *9* (02), 96–108. DOI: 10.1055/a-0626-6467.

Balduini, C. L.; Pecci, A.; Savoia, A. Recent advances in the understanding and management of MYH9-related inherited thrombocytopenias. *British journal of haematology* **2011,** *154* (2), 161–174. DOI: 10.1111/j.1365-2141.2011.08716.x.

Barry S. Coller. A Brief History of Ideas About Platelets in Health and Disease. *Platelets* **2013**, xix–xliv. DOI: 10.1016/B978-0-12-387837-3.00069-9.

Baumann, J.; Sachs, L.; Otto, O.; Schoen, I.; Nestler, P.; Zaninetti, C.; Kenny, M.; Kranz, R.; Eysmondt, H. von; Rodriguez, J.; Schäffer, T. E.; Nagy, Z.; Greinacher, A.; Palankar, R.; Bender, M. *Reduced platelet forces underlie impaired hemostasis in mouse models of MYH9-related disease*, 2022.

Bearer, E. L.; Prakash, J. M.; Li, Z. Actin Dynamics in Platelets. *International Review of Cytology* **2002,** *217*, 137–182.

Bender, M.; Palankar, R. Platelet Shape Changes during Thrombus Formation: Role of Actin-Based Protrusions. *Hamostaseologie* **2021,** *41* (1), 14–21. DOI: 10.1055/a-1325-0993.

Benedek, I. H.; Joshi, A. S.; Pieniaszek, H. J.; King, S. Y.; Kornhauser, D. M. Variability in the pharmacokinetics and pharmacodynamics of low dose aspirin in healthy male volunteers. *Journal of clinical pharmacology* **1995,** *35* (12), 1181–1186. DOI: 10.1002/j.1552-4604.1995.tb04044.x.

Berg, J. S.; Powell, B. C.; Cheney, R. E. A millennial myosin census. *Molecular biology of the cell* **2001,** *12* (4), 780–794. DOI: 10.1091/mbc.12.4.780.

Burris, S. M.; Smith, C. M.; Rao, G. H.; White, J. G. Aspirin treatment reduces platelet resistance to deformation. *Arteriosclerosis (Dallas, Tex.)* **1987,** *7* (4), 385–388. DOI: 10.1161/01.atv.7.4.385.

Burris, S. M.; Smith, C. M.; Tukey, D. T.; Clawson, C. C.; White, J. G. Micropipette aspiration of human platelets after exposure to aggregating agents. *Arteriosclerosis (Dallas, Tex.)* **1986,** *6* (3), 321–325. DOI: 10.1161/01.atv.6.3.321.

Cardigan, R.; Turner, C.; Harrison, P. Current methods of assessing platelet function: relevance to transfusion medicine. *Vox sanguinis* **2005,** *88* (3), 153–163. DOI: 10.1111/j.1423-0410.2005.00618.x.

Chandler, W. L. The thromboelastography and the thromboelastograph technique. *Seminars in thrombosis and hemostasis* **1995,** *21 Suppl 4*, 1–6.

Collins, B.; Hollidge, C. Antithrombotic drug market. *Nature reviews. Drug discovery* **2003,** *2* (1), 11–12. DOI: 10.1038/nrd966.

Crochemore, T.; Piza, F. M. d. T.; Rodrigues, R. D. R.; Guerra, J. C. d. C.; Ferraz, L. J. R.; Corrêa, T. D. A new era of thromboelastometry. *Einstein (Sao Paulo, Brazil)* **2017,** *15* (3), 380–385. DOI: 10.1590/S1679-45082017MD3130.

Daly, M. E. Determinants of platelet count in humans. *Haematologica* **2011,** *96* (1), 10–13. DOI: 10.3324/haematol.2010.035287.

Di Carlo, D. A mechanical biomarker of cell state in medicine. *Journal of laboratory automation* **2012,** *17* (1), 32–42. DOI: 10.1177/2211068211431630.

Drachman, J. G. Inherited thrombocytopenia: when a low platelet count does not mean ITP. *Blood* **2004,** *103* (2), 390–398. DOI: 10.1182/blood-2003-05-1742.

Dunn, C. J.; Goa, K. L. Tranexamic acid: a review of its use in surgery and other indications. *Drugs* **1999,** *57* (6), 1005–1032. DOI: 10.2165/00003495-199957060-00017.

Falet, H. Anatomy of the Platelet Cytoskeleton. In *Platelets in thrombotic and non-thrombotic disorders*: *Pathophysiology, pharmacology and therapeutics*; Gresele, P., Kleiman, N. S., Lopez, J. A., Page, C. P., Eds.; Nambridge University Press: Nambridge, U.K, New York, 2002; pp 139–156. DOI: 10.1007/978-3-319-47462-5_11.

Finkenstaedt-Quinn, S. A.; Ge, S.; Haynes, C. L. Cytoskeleton dynamics in drug-treated platelets. *Analytical and bioanalytical chemistry* **2015,** *407* (10), 2803–2809. DOI: 10.1007/s00216-015-8523-7.

Fox, J. Cytoskeletal Proteins and Platelet Signaling. *Thromb Haemost* **2001,** *86* (07), 198–213. DOI: 10.1055/s-0037-1616218.

Fox, J. E.; Phillips, D. R. Role of phosphorylation in mediating the association of myosin with the cytoskeletal structures of human platelets. *The Journal of biological chemistry* **1982,** *257* (8), 4120–4126.

Gachet, C.; Hanau, D.; Spehner, D.; Brisson, C.; Garaud, J. C.; Schmitt, D. A.; Ohlmann, P.; Cazenave, J. P. Alpha IIb beta 3 integrin dissociation induced by EDTA results in morphological changes of the platelet surface-connected canalicular system with differential location of the two separate subunits. *The Journal of cell biology* **1993,** *120* (4), 1021–1030. DOI: 10.1083/jcb.120.4.1021.

Gao, C.; Boylan, B.; Fang, J.; Wilcox, D. A.; Newman, D. K.; Newman, P. J. Heparin promotes platelet responsiveness by potentiating αIIbβ3-mediated outside-in signaling. *Blood* **2011,** *117* (18), 4946–4952. DOI: 10.1182/blood-2010-09-307751.

George, M. J.; Bynum, J.; Nair, P.; Cap, A. P.; Wade, C. E.; Cox, C. S.; Gill, B. S. Platelet biomechanics, platelet bioenergetics, and applications to clinical practice and translational research. *Platelets* **2018,** *29* (5), 431–439. DOI: 10.1080/09537104.2018.1453062.

Golański, J.; Pietrucha, T.; Baj, Z.; Greger, J.; Watala, C. MOLECULAR INSIGHTS INTO THE ANTICOAGULANT-INDUCED SPONTANEOUS ACTIVATION OF PLATELETS IN WHOLE BLOOD - VARIOUS ANTICOAGULANTS ARE NOT EQUAL. *Thrombosis Research* **1996,** *83* (3), 199–216. DOI: 10.1016/0049-3848(96)00129-6.

González-Bermúdez, B.; Guinea, G. V.; Plaza, G. R. Advances in Micropipette Aspiration: Applications in Cell Biomechanics, Models, and Extended Studies. *Biophysical Journal* **2019,** *116* (4), 587–594. DOI: 10.1016/j.bpj.2019.01.004.

Gross, L.; Schuler, B.; Pavliček, N.; Fatayer, S.; Majzik, Z.; Moll, N.; Peña, D.; Meyer, G. Atomic Force Microscopy for Molecular Structure Elucidation. *Angewandte Chemie (International ed. in English)* **2018,** *57* (15), 3888–3908. DOI: 10.1002/anie.201703509.

Guck, J. Some thoughts on the future of cell mechanics. *Biophysical reviews* **2019,** *11* (5), 667–670. DOI: 10.1007/s12551-019-00597-0.

Gupta, M.; Kocgozlu, L.; Sarangi, B. R.; Margadant, F.; Ashraf, M.; Ladoux, B. Micropillar substrates: a tool for studying cell mechanobiology. *Methods in cell biology* **2015,** *125*, 289–308. DOI: 10.1016/bs.mcb.2014.10.009.

Hansma, P. K.; Drake, B.; Marti, O.; Gould, S. A.; Prater, C. B. The scanning ion-conductance microscope. *Science (New York, N.Y.)* **1989,** *243* (4891), 641–643. DOI: 10.1126/science.2464851.

Happel, P.; Thatenhorst, D.; Dietzel, I. D. Scanning ion conductance microscopy for studying biological samples. *Sensors (Basel, Switzerland)* **2012,** *12* (11), 14983–15008. DOI: 10.3390/s121114983.

Harker, L. A.; Roskos, L. K.; Marzec, U. M.; Carter, R. A.; Cherry, J. K.; Sundell, B.; Cheung, E. N.; Terry, D.; Sheridan, W. Effects of megakaryocyte growth and development factor on platelet production, platelet life span, and platelet function in healthy human volunteers. *Blood* **2000,** *95* (8), 2514–2522. DOI: 10.1182/blood.V95.8.2514.

Harrison, P.; Martin Cramer, E. Platelet α-granules. *Blood reviews* **1993,** *7* (1), 52–62. DOI: 10.1016/0268-960X(93)90024-X.

Hartwig, J. H. The Platelet Cytoskeleton. In *Platelets,* 3rd ed.; Michelson, A. D., Ed.; Elsevier Science & Technology: San Diego, 2013; pp 145–168. DOI: 10.1016/B978-0-12-387837-3.00008-0.

Hartwig, J. H.; DeSisto, M. The cytoskeleton of the resting human blood platelet: structure of the membrane skeleton and its attachment to actin filaments. *The Journal of cell biology* **1991,** *112* (3), 407–425. DOI: 10.1083/jcb.112.3.407.

Hochleitner, G.; Sutor, K.; Levett, C.; Leyser, H.; Schlimp, C. J.; Solomon, C. Revisiting Hartert's 1962 Calculation of the Physical Constants of Thrombelastography. *Clin Appl Thromb Hemost* **2017,** *23* (3), 201–210. DOI: 10.1177/1076029615606531.

Hodge, T.; Cope, M. J. A myosin family tree. *Journal of cell science* **2000,** *113 Pt 19*, 3353–3354.

Kairov, G. T.; Solovev, M. A.; Kotlovskaya, L. Y.; Udut, V. V. Features of Pharmacodynamics of the Anticoagulant Dabigatran in Secondary Thrombophilia. *Clin Appl Thromb Hemost* **2018,** *24* (9_suppl), 323S-331S. DOI: 10.1177/1076029618814344.

Kee, Y.-S.; Robinson, D. N. Micropipette aspiration for studying cellular mechanosensory responses and mechanics. *Methods in molecular biology (Clifton, N.J.)* **2013,** *983*, 367–382. DOI: 10.1007/978-1-62703-302-2_20.

Klein, F.; Striebel, T.; Fischer, J.; Jiang, Z.; Franz, C. M.; Freymann, G. von; Wegener, M.; Bastmeyer, M. Elastic fully three-dimensional microstructure scaffolds for cell force measurements. *Advanced materials (Deerfield Beach, Fla.)* **2010,** *22* (8), 868–871. DOI: 10.1002/adma.200902515.

Krieg, M.; Fläschner, G.; Alsteens, D.; Gaub, B. M.; Roos, W. H.; Wuite, G. J. L.; Gaub, H. E.; Gerber, C.; Dufrêne, Y. F.; Müller, D. J. Atomic force microscopy-based mechanobiology. *Nat Rev Phys* **2019,** *1* (1), 41–57. DOI: 10.1038/s42254-018-0001-7.

Krueger, L. A.; Barnard, M. R.; Frelinger, A. L.; Furman, M. I.; Michelson, A. D. Immunophenotypic analysis of platelets. *Current protocols in cytometry* **2002,** *Chapter 6*, Unit 6.10. DOI: 10.1002/0471142956.cy0610s19.

Kumar, C. C.; Mohan, S. R.; Zavodny, P. J.; Narula, S. K.; Leibowitz, P. J. Characterization and differential expression of human vascular smooth muscle myosin light chain 2 isoform in nonmuscle cells. *Biochemistry* **1989,** *28* (9), 4027–4035. DOI: 10.1021/bi00435a059.

Lam, W. A.; Chaudhuri, O.; Crow, A.; Webster, K. D.; Li, T.-D.; Kita, A.; Huang, J.; Fletcher, D. A. Mechanics and contraction dynamics of single platelets and implications for clot stiffening. *Nature materials* **2011,** *10* (1), 61–66. DOI: 10.1038/nmat2903.

Lee, G. Y. H.; Lim, C. T. Biomechanics approaches to studying human diseases. *Trends in biotechnology* **2007,** *25* (3), 111–118. DOI: 10.1016/j.tibtech.2007.01.005.

Liang, X. M.; Han, S. J.; Reems, J.-A.; Gao, D.; Sniadecki, N. J. Platelet retraction force measurements using flexible post force sensors. *Lab on a chip* **2010,** *10* (8), 991–998. DOI: 10.1039/b918719g.

Ma, Y.; Wong, K. Reassociation and translocation of glycoprotein IIB-IIIA in EDTA-treated human platelets. *Platelets* **2007,** *18* (6), 451–459. DOI: 10.1080/09537100701194889.

Machlus, K. R.; Italiano, J. E. The incredible journey: From megakaryocyte development to platelet formation. *The Journal of cell biology* **2013,** *201* (6), 785–796. DOI: 10.1083/jcb.201304054.

Mak, M.; Erickson, D. A serial micropipette microfluidic device with applications to cancer cell repeated deformation studies. *Integrative biology : quantitative biosciences from nano to macro* **2013,** *5* (11), 1374–1384. DOI: 10.1039/c3ib40128f.

Malinin, A. I.; Atar, D.; Callahan, K. P.; McKenzie, M. E.; Serebruany, V. L. Effect of a single dose aspirin on platelets in humans with multiple risk factors for coronary artery disease. *European Journal of Pharmacology* **2003,** *462* (1-3), 139–143. DOI: 10.1016/S0014-2999(02)02956-4.

Marigo, V.; Nigro, A.; Pecci, A.; Montanaro, D.; Di Stazio, M.; Balduini, C. L.; Savoia, A. Correlation between the clinical phenotype of MYH9-related disease and tissue distribution of class II nonmuscle myosin heavy chains. *Genomics* **2004,** *83* (6), 1125–1133. DOI: 10.1016/j.ygeno.2003.12.012.

Maupin, P.; Phillips, C. L.; Adelstein, R. S.; Pollard, T. D. Differential localization of myosin-II isozymes in human cultured cells and blood cells. *Journal of cell science* **1994,** *107 (Pt 11)*, 3077–3090.

Mietke, A.; Otto, O.; Girardo, S.; Rosendahl, P.; Taubenberger, A.; Golfier, S.; Ulbricht, E.; Aland, S.; Guck, J.; Fischer-Friedrich, E. Extracting Cell Stiffness from Real-Time Deformability Cytometry: Theory and Experiment. *Biophysical Journal* **2015,** *109* (10), 2023–2036. DOI: 10.1016/j.bpj.2015.09.006.

Mokbel, M.; Mokbel, D.; Mietke, A.; Träber, N.; Girardo, S.; Otto, O.; Guck, J.; Aland, S. Numerical Simulation of Real-Time Deformability Cytometry To Extract Cell Mechanical Properties. *ACS Biomater. Sci. Eng.* **2017,** *3* (11), 2962–2973. DOI: 10.1021/acsbiomaterials.6b00558.

Montague, S. J.; Lim, Y. J.; Lee, W. M.; Gardiner, E. E. Imaging Platelet Processes and Function-Current and Emerging Approaches for Imaging in vitro and in vivo. *Frontiers in immunology* **2020,** *11*, 78. DOI: 10.3389/fimmu.2020.00078.

Myers, D. R.; Qiu, Y.; Fay, M. E.; Tennenbaum, M.; Chester, D.; Cuadrado, J.; Sakurai, Y.; Baek, J.; Tran, R.; Ciciliano, J. C.; Ahn, B.; Mannino, R. G.; Bunting, S. T.; Bennett, C.; Briones, M.; Fernandez-Nieves, A.; Smith, M. L.; Brown, A. C.; Sulchek, T.; Lam, W. A. Single-platelet nanomechanics measured by high-

throughput cytometry. *Nature materials* **2017,** *16* (2), 230–235. DOI: 10.1038/nmat4772.

Myrand-Lapierre, M.-E.; Deng, X.; Ang, R. R.; Matthews, K.; Santoso, A. T.; Ma, H. Multiplexed fluidic plunger mechanism for the measurement of red blood cell deformability. *Lab on a chip* **2015,** *15* (1), 159–167. DOI: 10.1039/c4lc01100g.

Nguyen, T.-H.; Palankar, R.; Bui, V.-C.; Medvedev, N.; Greinacher, A.; Delcea, M. Rupture Forces among Human Blood Platelets at different Degrees of Activation. *Scientific reports* **2016,** *6*, 25402. DOI: 10.1038/srep25402.

Nurden, A.; Nurden, P. Advances in our understanding of the molecular basis of disorders of platelet function. *Journal of thrombosis and haemostasis : JTH* **2011,** *9 Suppl 1*, 76–91. DOI: 10.1111/j.1538-7836.2011.04274.x.

Otto, O.; Rosendahl, P.; Golfier, S.; Mietke, A.; Herbig, M.; Jacobi, A.; Topfner, N.; Herold, C.; Klaue, D.; Girardo, S.; Winzi, M.; Fischer-Friedrich, E.; Guck, J. Real-time deformability cytometry as a label-free indicator of cell function. *Conference proceedings : … Annual International Conference of the IEEE Engineering in Medicine and Biology Society. IEEE Engineering in Medicine and Biology Society. Annual Conference* **2015a,** *2015*, 1861–1864. DOI: 10.1109/EMBC.2015.7318744.

Otto, O.; Rosendahl, P.; Mietke, A.; Golfier, S.; Herold, C.; Klaue, D.; Girardo, S.; Pagliara, S.; Ekpenyong, A.; Jacobi, A.; Wobus, M.; Töpfner, N.; Keyser, U. F.; Mansfeld, J.; Fischer-Friedrich, E.; Guck, J. Real-time deformability cytometry: on-the-fly cell mechanical phenotyping. *Nature methods* **2015b,** *12* (3), 199-202, 4 p following 202. DOI: 10.1038/nmeth.3281.

Packham, M. A. Role of platelets in thrombosis and hemostasis. *Canadian journal of physiology and pharmacology* [Online] **1994,** *72* (3), 278–284. https:// pubmed.ncbi.nlm.nih.gov/8069774/.

Palma-Barqueros, V.; Revilla, N.; Sánchez, A.; Zamora Cánovas, A.; Rodriguez-Alén, A.; Marín-Quílez, A.; González-Porras, J. R.; Vicente, V.; Lozano, M. L.; Bastida, J. M.; Rivera, J. Inherited Platelet Disorders: An Updated Overview. *International journal of molecular sciences* **2021,** *22* (9). DOI: 10.3390/ijms22094521.

Pecci, A.; Balduini, C. L. Inherited thrombocytopenias: an updated guide for clinicians. *Blood reviews* **2021,** *48*, 100784. DOI: 10.1016/j.blre.2020.100784.

Plotnikov, S. V.; Sabass, B.; Schwarz, U. S.; Waterman, C. M. High-resolution traction force microscopy. *Methods in cell biology* **2014,** *123*, 367–394. DOI: 10.1016/B978-0-12-420138-5.00020-3.

Qiu, Y.; Ciciliano, J.; Myers, D. R.; Tran, R.; Lam, W. A. Platelets and physics: How platelets "feel" and respond to their mechanical microenvironment. *Blood reviews* **2015,** *29* (6), 377–386. DOI: 10.1016/j.blre.2015.05.002.

Radmacher, M.; Fritz, M.; Kacher, C. M.; Cleveland, J. P.; Hansma, P. K. Measuring the viscoelastic properties of human platelets with the atomic force microscope. *Biophysical Journal* **1996,** *70* (1), 556–567. DOI: 10.1016/S0006-3495(96)79602-9.

Rao, A. K.; Vaidyula, V. R.; Bagga, S.; Jalagadugula, G.; Gaughan, J.; Wilhite, D. B.; Comerota, A. J. Effect of antiplatelet agents clopidogrel, aspirin, and cilostazol on circulating tissue factor procoagulant activity in patients with peripheral arterial disease. *Thromb Haemost* **2006,** *96* (6), 738–743.

Rheinlaender, J.; Vogel, S.; Seifert, J.; Schächtele, M.; Borst, O.; Lang, F.; Gawaz, M.; Schäffer, T. E. Imaging the elastic modulus of human platelets during thrombin-induced activation using scanning ion conductance microscopy. *Thromb Haemost* **2015,** *113* (2), 305–311. DOI: 10.1160/TH14-05-0414.

Ribeiro, A. J. S.; Denisin, A. K.; Wilson, R. E.; Pruitt, B. L. For whom the cells pull: Hydrogel and micropost devices for measuring traction forces. *Methods (San Diego, Calif.)* **2016,** *94*, 51–64. DOI: 10.1016/j.ymeth.2015.08.005.

Roca-Cusachs, P.; Conte, V.; Trepat, X. Quantifying forces in cell biology. *Nature cell biology* **2017,** *19* (7), 742–751. DOI: 10.1038/ncb3564.

Rosendahl, P.; Plak, K.; Jacobi, A.; Kraeter, M.; Toepfner, N.; Otto, O.; Herold, C.; Winzi, M.; Herbig, M.; Ge, Y.; Girardo, S.; Wagner, K.; Baum, B.; Guck, J. Real-time fluorescence and deformability cytometry. *Nature methods* **2018,** *15* (5), 355–358. DOI: 10.1038/nmeth.4639.

Sachs, L.; Denker, C.; Greinacher, A.; Palankar, R. Quantifying single-platelet biomechanics: An outsider's guide to biophysical methods and recent advances. *Research and practice in thrombosis and haemostasis* **2020,** *4* (3), 386–401. DOI: 10.1002/rth2.12313.

Sachs, L.; Wesche, J.; Lenkeit, L.; Greinacher, A.; Bender, M.; Otto, O.; Palankar, R. Ex vivo anticoagulants affect human blood platelet biomechanics with implications

for high-throughput functional mechanophenotyping. *Communications biology* **2022,** *5* (1), 86. DOI: 10.1038/s42003-021-02982-6.

Schäffer, T. E. Nanomechanics of molecules and living cells with scanning ion conductance microscopy. *Analytical chemistry* **2013,** *85* (15), 6988–6994. DOI: 10.1021/ac400686k.

Schwarz, U. S.; Soiné, J. R. D. Traction force microscopy on soft elastic substrates: A guide to recent computational advances. *Biochimica et biophysica acta* **2015,** *1853* (11 Pt B), 3095–3104. DOI: 10.1016/j.bbamcr.2015.05.028.

Sharma, S. K.; Philip, J.; Wiley, J. Thromboelastographic changes in healthy parturients and postpartum women. *Anesthesia and analgesia* **1997,** *85* (1), 94–98. DOI: 10.1097/00000539-199707000-00017.

Shevchuk, A. I.; Frolenkov, G. I.; Sánchez, D.; James, P. S.; Freedman, N.; Lab, M. J.; Jones, R.; Klenerman, D.; Korchev, Y. E. Imaging proteins in membranes of living cells by high-resolution scanning ion conductance microscopy. *Angewandte Chemie (International ed. in English)* **2006,** *45* (14), 2212–2216. DOI: 10.1002/anie.200503915.

Shin, E.-K.; Park, H.; Noh, J.-Y.; Lim, K.-M.; Chung, J.-H. Platelet Shape Changes and Cytoskeleton Dynamics as Novel Therapeutic Targets for Anti-Thrombotic Drugs. *Biomolecules & Therapeutics* **2016,** *25* (3), 223–230. DOI: 10.4062/biomolther.2016.138.

Simons, M.; Wang, M.; McBride, O. W.; Kawamoto, S.; Yamakawa, K.; Gdula, D.; Adelstein, R. S.; Weir, L. Human nonmuscle myosin heavy chains are encoded by two genes located on different chromosomes. *Circulation research* **1991,** *69* (2), 530–539. DOI: 10.1161/01.res.69.2.530.

Sniadecki, N. J.; Han, S. J.; Ting, L. H.; Feghhi, S. Micropatterning on micropost arrays. *Methods in cell biology* **2014,** *121*, 61–73. DOI: 10.1016/B978-0-12-800281-0.00005-1.

Sobel, M.; Fish, W. R.; Toma, N.; Luo, S.; Bird, K.; Mori, K.; Kusumoto, S.; Blystone, S. D.; Suda, Y. Heparin modulates integrin function in human platelets. *Journal of vascular surgery* **2001,** *33* (3), 587–594. DOI: 10.1067/mva.2001.112696.

Suzuki, Y.; Yamamoto, M.; Wada, H.; Ito, M.; Nakano, T.; Sasaki, Y.; Narumiya, S.; Shiku, H.; Nishikawa, M. Agonist-induced regulation of myosin phosphatase

activity in human platelets through activation of Rho-kinase. *Blood* **1999,** *93* (10), 3408–3417.

Tan, J. L.; Tien, J.; Pirone, D. M.; Gray, D. S.; Bhadriraju, K.; Chen, C. S. Cells lying on a bed of microneedles: an approach to isolate mechanical force. *Proceedings of the National Academy of Sciences of the United States of America* [Online] **2003,** *100* (4), 1484–1489. https://pubmed.ncbi.nlm.nih.gov/12552122/.

The Cytoskeleton; Pollard, T. D., Goldman, R. D., Eds.; Cold Spring Harbor Laboratory Press: Cold Spring Harbor, New York, 2017.

Thiessen, J. J. Aspirin: Plasma concentration and effects. *Thrombosis Research* **1983,** *29*, 105–111. DOI: 10.1016/0049-3848(83)90365-1.

Thomas, S. G. The Structure of Resting and Activated Platelets. In *Platelets,* Fourth edition; Michelson, A. D., Cattaneo, M., Frelinger, A. L., Newman, P. J., Eds.; Elsevier/Academic Press: London, 2019; pp 47–77. DOI: 10.1016/B978-0-12-813456-6.00003-5.

Thorir, D.; Bjornsson, M. D.; Berger, H. ASPIRIN ACETYLATES FIBRINOGEN AND ENHANCES FIBRINOLYSIS IN VIVO. FIBRINOLYTIC EFFECT IS INDEPENDENT OF CHANGES IN PLASMINOGEN ACTIVATOR LEVELS. In *XIth International Congress on Thrombosis and Haemostasis*; Schattauer GmbH, 1987. DOI: 10.1055/s-0038-1642938.

Toothaker, L. E.; Gonzalez, D. A.; Tung, N.; Lemons, R. S.; Le Beau, M. M.; Arnaout, M. A.; Clayton, L. K.; Tenen, D. G. Cellular myosin heavy chain in human leukocytes: isolation of 5' cDNA clones, characterization of the protein, chromosomal localization, and upregulation during myeloid differentiation. *Blood* **1991,** *78* (7), 1826–1833.

Urbanska, M.; Rosendahl, P.; Kräter, M.; Guck, J. High-throughput single-cell mechanical phenotyping with real-time deformability cytometry. *Methods in cell biology* **2018,** *147*, 175–198. DOI: 10.1016/bs.mcb.2018.06.009.

White, J. G. EDTA-induced changes in platelet structure and function: clot retraction. *Platelets* **2000,** *11* (1), 49–55. DOI: 10.1080/09537100075805.

Zaninetti, C.; Barozzi, S.; Bozzi, V.; Gresele, P.; Balduini, C. L.; Pecci, A. Eltrombopag in preparation for surgery in patients with severe MYH9-related thrombocytopenia. *American journal of hematology* **2019,** *94* (8), E199-E201. DOI: 10.1002/ajh.25500.

Zaninetti, C.; Sachs, L.; Palankar, R. Role of Platelet Cytoskeleton in Platelet Biomechanics: Current and Emerging Methodologies and Their Potential Relevance for the Investigation of Inherited Platelet Disorders. *Hamostaseologie* **2020,** *40* (3), 337–347. DOI: 10.1055/a-1175-6783.

Zhang, Y.; Conti, M. A.; Malide, D.; Dong, F.; Wang, A.; Shmist, Y. A.; Liu, C.; Zerfas, P.; Daniels, M. P.; Chan, C.-C.; Kozin, E.; Kachar, B.; Kelley, M. J.; Kopp, J. B.; Adelstein, R. S. Mouse models of MYH9-related disease: mutations in nonmuscle myosin II-A. *Blood* **2012,** *119* (1), 238–250. DOI: 10.1182/blood-2011-06-358853.

Zhang, Y.; Qiu, Y.; Blanchard, A. T.; Chang, Y.; Brockman, J. M.; Ma, V. P.-Y.; Lam, W. A.; Salaita, K. Platelet integrins exhibit anisotropic mechanosensing and harness piconewton forces to mediate platelet aggregation. *Proceedings of the National Academy of Sciences of the United States of America* **2018,** *115* (2), 325–330. DOI: 10.1073/pnas.1710828115.

Zhukov, A.; Richards, O.; Ostanin, V.; Korchev, Y.; Klenerman, D. A hybrid scanning mode for fast scanning ion conductance microscopy (SICM) imaging. *Ultramicroscopy* **2012,** *121* (11), 1–7. DOI: 10.1016/j.ultramic.2012.06.015.

7. Abbreviations

ACD-A	acid citrate dextrose solution A
ADP	Adenosine diphosphate
AFM	atomic force microscope
CLSM	confocal laser scanning microscope
CMOS	complementary metal-oxide-semiconductor
DMSO	dimethyl sulfoxide
F-Actin	filamentous actin
G	elastic shear modulus
G-Actin	globular actin
g-Mean	geometric mean of fluorescence
GP	Glycoprotein
K_2EDTA	dipotassium ethylenediaminetetraacetic acid
LatB	latrunculin B
LED	light-emitting diode
LOT	lysis on-set time
Li-Heparin	Lithium-Heparin
MLC2	myosin light chain 2
MYH9	Myosin Heavy Chain 9
MYH9–RD	Myosin Heavy Chain 9-related disease
MYPT1	myosin phosphatase 1
Na-Citrate	3.8% buffered trisodium citrate
NMMHC-IIA	non-muscle myosin heavy chain IIa
OCS	open canalicular system
PRP	platelet-rich plasma
r-Hirudin	recombinant hirudin
RT-DC	real-time deformability cytometry
RT-FDC	real-time fluorescence and deformability cytometry
SICM	scanning ion conductance microscopy
SPFS	single platelet force spectroscopy
TEM	Transmission electron microscopic

TFM	traction force microscopy
TPI	thrombodynamic potential index
TRAP-6	thrombin receptor-activating peptide-6
TXA	tranexamic acid
vwF	von Willebrand factor
2PP	2 photons polymerization

8. Author contributions

Article 1: **Sachs, L.**; Denker, C.; Greinacher, A.; Palankar, R. Quantifying single-platelet biomechanics: An outsider's guide to biophysical methods and recent advances. *Research and practice in thrombosis and haemostasis* 2020, 4 (3), 386–401. DOI: 10.1002/rth2.12313.

RP and LS performed literature review, composition of the primary manuscript, preparation of figures, and editing. AG and CD contributed to the primary text and participated in revision of the manuscript. RP, LS, and CD performed the experiments, analyzed the results, and prepared the RT-DC, micropost, and micropillar data presented in the review. RP and CD acquired the funding. All authors contributed to revision of the final version of the manuscript.

Article 2: **Sachs, L.**; Wesche, J.; Lenkeit, L.; Greinacher, A.; Bender, M.; Otto, O.; Palankar, R. *Ex vivo* anticoagulants affect human blood platelet biomechanics with implications for high-throughput functional mechanophenotyping. *Communications biology* 2022, 5 (1), 86. DOI: 10.1038/s42003-021-02982-6.

LS, AG, MB, OO, and RP designed the study. LS performed all RT-FDC experiments. JW and LL performed flow cytometry. LS and RP performed CLSM experiments. LS analyzed RT-FDC and flow cytometry data and RP analyzed CLSM data. LS prepared RT-FDC and flow cytometry figures and RP prepared CLSM figures. LS wrote the manuscript. AG provided access to *MYH9* patient platelets. AG, MB, OO and RP contributed to writing the manuscript. All authors contributed to the critical revision of the manuscript. MB, OO and RP obtained funding.

Manuscript 3: Baumann, J., **Sachs, L.**, Oliver, O., Schoen, I., Nestler, P., Zaninetti, C., Kenny, M., Kranz, R., von Eysmondt, H., Rodriguez, J., Schäffer, T. E., Nagy, Z., Greinacher, A., Palankar, P., Bender, M. Reduced platelet forces underlie impaired hemostasis in mouse models of *MYH9*-related disease. Accepted at *Science Advances* (2022).

Experiment performance, data analysis and figure preparation:

Blood parameters of mice: JB (Fig. 1A-B, Suppl. Tabl. 1, Suppl. Fig. 2A-B)

Blood parameters of humans: LS (Suppl. Tabl. 3)

Immunoblotting: JB (Suppl. Fig. 1A)

Immunoblotting with ProteinSimple Jess: JB, ZN (Fig. 2D, Suppl. Fig. 1B-C, 7A-B)

Transmission electron microscopy: JB, MB (Fig. 1F, 2C, Suppl. Fig. 4C, 6C)

Flow cytometry: JB (Fig. 1C-E, 2A, Suppl. Fig. 2C-D, 3, 6A)

Aggregometry: JB (Suppl. Tabl. 2, Suppl. Fig. 4A-B)

Platelet Spreading: JB (Fig. 2B, Suppl. Fig. 6B)

Immunostaining of Platelets: JB (Suppl. Fig. 6D)

Clot retraction: JB (Fig. 3C-D, 6A-B, Suppl. Fig. 10, 13, 14)

Bleeding time: JB (Fig. 6C, Suppl. Fig. 15)

Platelet adhesion under shear flow (mice): JB (Fig. 4A, Suppl. Fig. 11A)

Platelet adhesion under shear flow (human): RP (Fig. 5B, 7B-C, Suppl. Fig. 12B, 17 A-B)

RT-FDC: LS (Fig. 1G, 5A, Suppl. Fig. 5, 12A)

Single Platelet Force Spectroscopy: RP (Fig. 4B-C, Suppl. Fig. 11B-C)

Colloidal Probe Spectroscopy: LS (Fig. 4D, 5C, 7D, Suppl. Fig. 11D, 12C, 17C)

Micropost assays: JB, TS, MK (Fig. 3A, Suppl. Fig. 8)

SICM: JB, HE, JR, TES (Fig. 3B, Suppl. Fig 9)

Thromboelastography: CZ (Fig. 7A, Suppl. Fig. 16)

JB, LS, RP and MB wrote the manuscript. OO, AG, TES, RP and MB supervised the research. OO, IS, TES, RP and MB obtained funding. All authors have critically revised and approved the final version of the manuscript.

Greifswald, 25. March 2022

Prof. Dr. Oliver Otto Laura Sachs

9. Publications

9.1. Article 1: Quantifying single-platelet biomechanics: An outsider’s guide to biophysical methods and recent advances

Sachs, L.; Denker, C.; Greinacher, A.; Palankar, R. Quantifying single-platelet biomechanics: An outsider's guide to biophysical methods and recent advances. *Research and practice in thrombosis and haemostasis* 2020, 4 (3), 386–401.
DOI: 10.1002/rth2.12313.

Published: 17 February 2020

Received: 21 August 2019 | Revised: 10 December 2019 | Accepted: 7 January 2020

DOI: 10.1002/rth2.12313

REVIEW ARTICLE

rpth research & practice in thrombosis & haemostasis

Quantifying single-platelet biomechanics: An outsider's guide to biophysical methods and recent advances

Laura Sachs Dipl-Pharm[1] | Christian Denker PhD[2] | Andreas Greinacher MD[1] | Raghavendra Palankar PhD[1]

[1]Institute of Immunology and Transfusion Medicine, University Medicine Greifswald, Greifswald, Germany

[2]Department of Physics, University of Greifswald, Greifswald, Germany

Correspondence
Raghavendra Palankar, Institute of Immunology and Transfusion Medicine, University Medicine Greifswald, Greifswald, Germany.
Email: palankarr@uni-greifswald.de

Funding information
LS is funded by the Deutsche Forschungsgemeinschaft (DFG, German Research foundation) Project Number 374031971 – TRR 240, Project A06 granted to RP and Forschungsverbund für Molekulare Medizin, Universitätsmedizin Greifswald (Research Network Molecular Medicine of University of Medicine Greifswald) FOVB-2017-07 to CD and RP.

Handling Editor: Yotis Senis.

Abstract

Platelets are the key cellular components of blood primarily contributing to formation of stable hemostatic plugs at the site of vascular injury, thus preventing excessive blood loss. On the other hand, excessive platelet activation can contribute to thrombosis. Platelets respond to many stimuli that can be of biochemical, cellular, or physical origin. This drives platelet activation kinetics and plays a vital role in physiological and pathological situations. Currently used bulk assays are inadequate for comprehensive biomechanical assessment of single platelets. Individual platelets interact and respond differentially while modulating their biomechanical behavior depending on dynamic changes that occur in surrounding microenvironments. Quantitative description of such a phenomenon at single-platelet regime and up to nanometer resolution requires methodological approaches that can manipulate individual platelets at submicron scales. This review focusses on principles, specific examples, and limitations of several relevant biophysical methods applied to single-platelet analysis such as micropipette aspiration, atomic force microscopy, scanning ion conductance microscopy and traction force microscopy. Additionally, we are introducing a promising single-cell approach, real-time deformability cytometry, as an emerging biophysical method for high-throughput biomechanical characterization of single platelets. This review serves as an introductory guide for clinician scientists and beginners interested in exploring one or more of the above-mentioned biophysical methods to address outstanding questions in single-platelet biomechanics.

KEYWORDS

biophysics, cytoskeleton, force microscopy, mechanobiology, platelets, single-cell analysis

Essentials

- Platelets form hemostatic plugs and under pathological conditions contribute to thrombosis.
- Platelets sense and mechanotransduce physicochemical cues and generate biomechanical forces.
- Biophysical tools can quantify single-platelet biomechanics during hemostasis and thrombosis.
- Platelet biomechanical properties may serve as useful biomarkers of platelet dysfunction.

1 | INTRODUCTION

Platelets are discoidal, anucleate, multifunctional cellular fragments (1-3 μm in diameter) generated from bone marrow megakaryocytes and are released into the blood circulation.[1] Circulating platelets are essential for hemostasis. They "survey" the integrity of the vascular system. Upon vascular injury, platelets adhere to the exposed extracellular matrix (ECM) and form a hemostatic plug to seal the wound. However, platelets may also contribute to thrombosis, in case of pathological clot formation. Platelets function as complex biological units that sense and mechanotransduce physicochemical cues and stimuli from their surrounding environment (ie, outside-in signaling via ligand receptor–mediated interactions) and actively respond through mechanotransduction events (ie, inside-out signaling triggering platelet adhesion, activation, spreading and contraction).[2] Platelet activation at interfaces is associated with spreading and involves the formation of lamellipodial and filopodial protrusions. These processes result in generation of biomechanical contractile forces through interactions between platelet cytoskeletal components (eg, actin, myosin, tubulin, and several other proteins), which regulate, from the internal side of platelets, distribution of surface receptors (eg, glycoprotein Ib-V-IX complex, integrin $\alpha 2\beta 1$ and $\alpha IIb\beta 3$) that recognize the ligands (eg, von Willebrand factor), exposed ECM (eg, collagen), and activated platelets.[3] Apart from their protective function, platelets contribute to pathophysiological conditions and onset of diseases as they interact with cells of the vasculature, a wide variety of cells from the adaptive and innate immune system, and pathogens of viral and bacterial origins.[4] These dynamic interactions occur at length scales from nanometers to several microns and at time scales of milliseconds up to minutes mediated by specific receptors. Little is known about the longer-term functions of platelets, that are incorporated into a thrombus. Currently, in platelet research a wide array of methods are practiced routinely to decipher such interactions and their outcomes for research as well as for diagnostic purposes in clinical practice. Frequently used in vitro and ex vivo assays are platelet aggregometry in platelet-rich plasma or in whole blood by impedance aggregometry and rheological techniques (require relatively large sample volumes); flow cytometry (requires small sample volumes but is often restricted to end-point readout); and real-time thrombus formation in parallel plate flow chambers (which allows insights into clot formation).[5] Although these approaches have significantly improved our understanding of hemostasis and thrombosis from a biochemical and cell biological perspective, much less is known about underlying biomechanical properties and biophysical forces generated, which govern protective functions such as hemostasis and pathophysiological origins of thrombosis. Within this context, several of these methods are not sufficiently informative to assess directly biomechanical properties of single platelets and how these in turn influence platelet function and how they drive the complex spatiotemporal dynamics during hemostasis and thrombosis.

1.1 | Why should we investigate biomechanical properties of single platelets using single-cell biophysical techniques, and what does this add to our current knowledge of platelets in both hemostasis and thrombosis?

Given the extent of cell-to-cell variations, rare subpopulations, and intrinsic fluctuations within biological systems, bulk population-level experiments often conceal and average out vital causal relationships underlying the biological phenomena.[6] Single-cell biophysical techniques and their sensitivity have enabled quantification and unveiling of previously unknown relationships and fundamental paradigms in platelet biology and their underlying biomechanical principles with a resolution up to single-molecule level.[7–10] However, many of these single-cell techniques are still limited in their ability to scale to measure a suitably large number of individual cells and independent samples.[11] In this review, we focus on biophysical methods suitable to assess and quantify biomechanical characteristics such as elastic modulus, stiffness (or deformability), forces generated during adhesion, and spreading and contraction of single platelets in health and disease states. We also provide some insights into limitations and highlight improvements of the methods described herein. Most of the methods described in this review rely on application of external mechanical forces such as stretch, compression, and shear (Figure 1) to quantify biomechanical properties of single platelets. This review is specifically directed toward clinician scientists and beginners who are interested in exploring applications of single-cell–based biophysical approaches in unraveling the role of platelet biomechanics in hemostasis and thrombosis research.

2 | TECHNIQUES FOR MEASURING THE BIOMECHANICAL PROPERTIES OF SINGLE PLATELETS

2.1 | Micropipette aspiration

Micropipette aspiration has been indispensable for membrane biophysicists interested in quantifying phase behavior, elasticity, and rupture tension of lipid bilayers.[12–14] When applied to single cells, micropipette aspiration allows for measuring the biomechanical properties of single cells by observing cellular deformation upon application of defined suction pressure.[15] It is one of the earliest biophysical tools used in single-platelet manipulation and quantification of platelet biomechanics.[16] Micropipette aspiration (Figure 2A), as the name suggests, relies on suction of part of the single-platelet membrane into a borosilicate glass micropipette (inner diameter of 0.5-1.5 μm) connected to a micromanipulator by applying negative pressure in a stepwise manner. The subsequent change in the length of the platelet membrane aspirated into the micropipette over time is tracked by video microscopy (Figure 2B).[15,17] The data obtained from this type of experiment is then used to characterize material

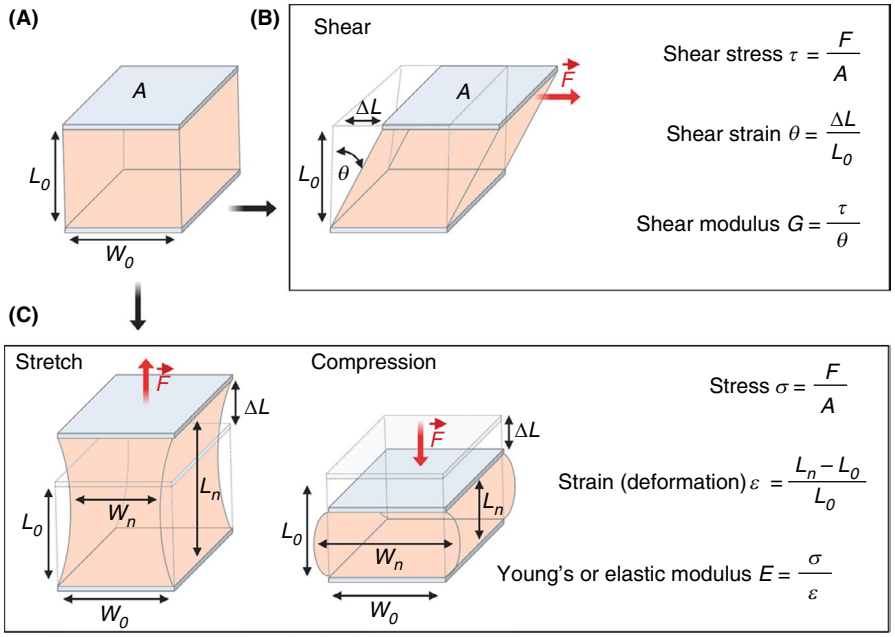

FIGURE 1 Simplified schematics and glossary of terms used for defining mechanical properties of a deformable biological viscoelastic material (A) with a defined area *A*, initial length *L0* and width *W0* under applied shear force $\vec{F}$ undergoing sample elongation ΔL along the direction of the shear (B). The same deformable viscoelastic material can be either stretched (ie, material undergoes elongation) (C) or compressed (ie, material undergoes deformation) under the application of external force $\vec{F}$ perpendicular to the surface area A, resulting in changes in length *Ln* and width *Wn*, thereby allowing determination of several mechanical parameters including the Young's modulus *E*. (Figure 1 was adapted and modified from Wu et al.[11])

Stress (σ) - force per unit area. (SI unit: Newtons, N/m^2)

Stress - quantifies extent of deformation in a material after application of mechanical stress. (unitless parameter)

Elongational strain or Deformation (ε) - fractional change in length of a material under strain.

Shear Stress (τ) - force acting parallel to the materials axis per unit area. (SI unit: Pascal, Pa)

Shear Stress (γ) - quantifies extent of deformation in a material after application of shear stess. (SI unit: radian, rad)

Shear Modulus (*G*) - extent of a materials resistance to deformation under shear stress. (SI unit: Pascal, Pa)

Elasticity - the property of a material to undergo deformation under force (stress) and return to its original shape upon removal of the force. For an elastic material, the relationship between force and deformation is linear.

Young's or elastic modulus (*E*) - describes a materials resistance to deformation under extention or compression. (SI unit: Pascal, Pa)

Viscoelasticity - property of a material that exhibits both viscous and elastic charateristics under external stress or shear.

Stiffness - resistance of a material to deform under applied external force.

Biomechanics (or Mechanobiology) - an interdisciplinary field that applies principles of physics to quantitatively assess biological systems from single molecules up to organismic level. At cellular-level, biomechanics refers to dynamic mechanotransduction events that support fundamental cellular functions such as adhesion, spreading, migration, differentiation, etc. by generating and transducing mechanical forces in reponce to physicochemical stimuli.

Mechanotransduction (or Mechanosignaling) - refers to a biological process where signaling pathway(s) is triggered by mechanical force such as shear or strech/compression acting via structural or confirmational changes at molecular levels.

properties of a deforming cell using the Law of Laplace, which gives the relationship between the surface tension and pressure within a fluid drop that has a membrane with surface tension in it (Figure 2C). Depending on the instrument setup, suction pressures from 0.1 pN/μm^2 up to 101 325 N/m^2 (ie, atmospheric) can be applied and membrane tension forces between 10 pN up to 10^4 nN can be measured with a membrane edge detection accuracy of ±25 nm.[18] Using micropipette aspiration viscoelastic and biomechanical changes

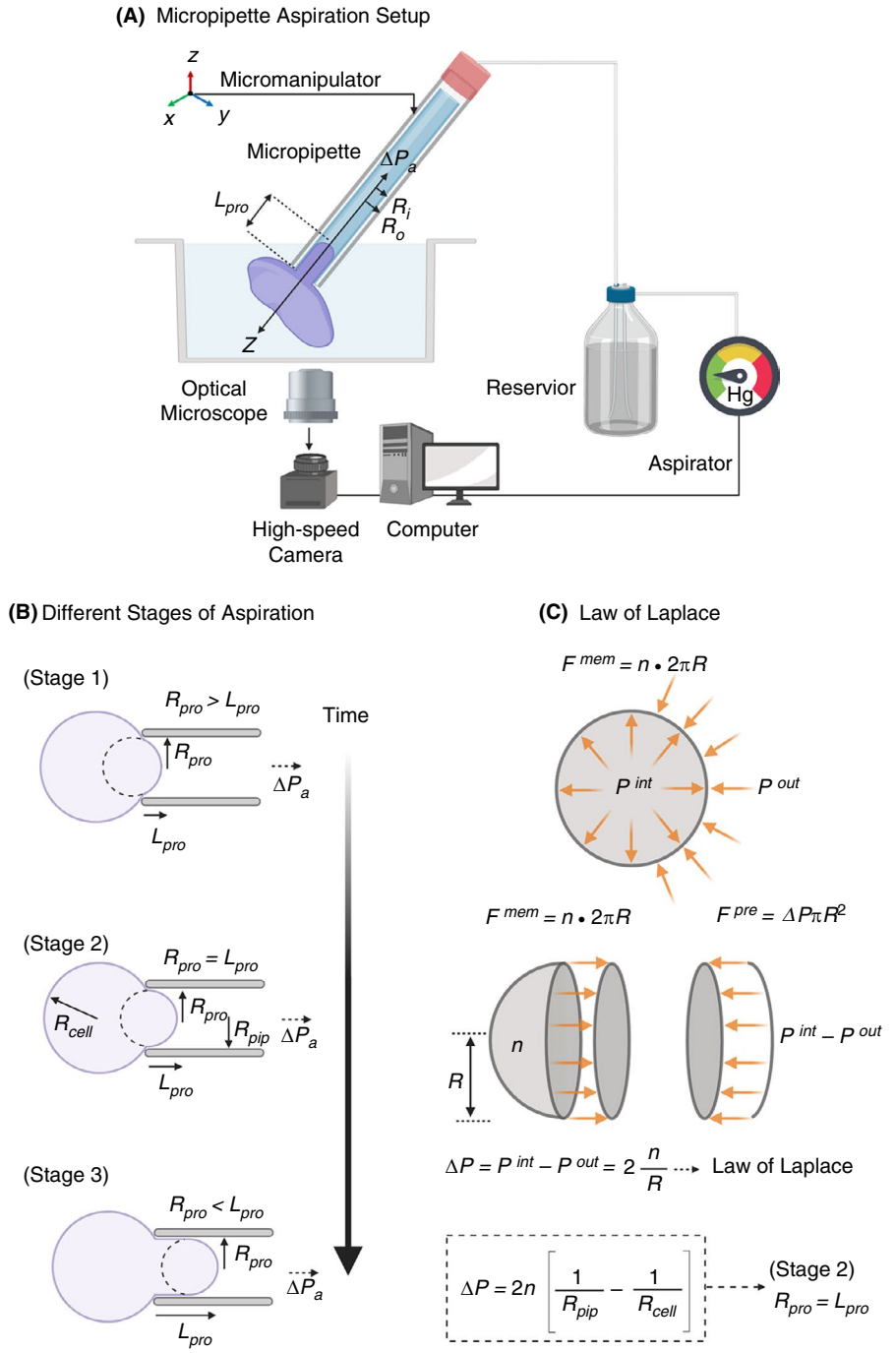

FIGURE 2 A, Schematic diagram of micropipette aspiration setup of a single resting platelet. The micropipette movement immersed in platelet suspension is controlled by a precision micromanipulator, ΔPa is the aspiration pressure applied parallel to the *z*-axis through the aspirator, *R*i and *R*o-inner and outer radius of the micropipette respectively and L_{pro} is the length of the protrusion of platelet body into the micropipette. Change in L_{pro} is recorded continuously with a high-speed camera. B, Micropipette aspiration is a dynamic procedure with three distinct stages: In Stage I (initial), radius of protrusion $R_{pro} > L_{pro}$, the length of protrusion. During Stage II (critical) $R_{pro} = L_{pro}$ and in Stage III (final) $R_{pro} < L_{pro}$. In Stage II when $L_{pro}/R_{pro} = 1$, the Law of Laplace can be applied to determine the surface tension n (SI units pN/μm). C, Simplified schematics of the Law of Laplace, which provides a relationship between the radius *R* of a membrane of a spherical cell subjected to the pressure difference $\Delta P = P^{int} - P^{out}$, where P^{int} and P^{out} are the pressures inside and outside the cell, respectively. The membrane force $F^{mem} = n\,2\pi R$ is the result of the surface tension n acting on the cell membrane along the circumference $C = 2PR$ as shown in the free body diagram of a spherical cell cut in half. It is in equilibrium with the forces F^{pre} resulting from the pressure difference ΔP acting on the cell area $A = PR^2$. Combining these two we arrive at the Law of Laplace, which gives the relationship between cell wall and its curvature $1/R$ in terms with the surface tension n. Applying this to the critical Stage II during micropipette aspiration where $R_{pro} = L_{pro}$ for radius of protrusion and that of cell we can effectively determination the surface tension n of the cell. (Figure modified from Gonzalez-Bermudez et al.[15])

in single platelets induced by soluble antithrombotic drugs (eg, acetylsalicylic acid), platelet agonists (eg, ADP, thrombin, and the calcium ionophore A23187) and influence of cytoskeleton destabilizing drugs (eg, vincristine, colchicine, taxol, and cytochalasin D) on platelet cytoskeleton have been comprehensively assessed.[16,19,20] Micropipette aspiration measurements show the Young's modulus of resting platelets is about $1.7 \pm 0.63 \times 10^3$ dyn cm^{-2} with a viscous modulus of $1.0 \pm 0.5 \times 10^4$ dyn s cm^{-2}.[21] In addition, the mechanistic effect of low-temperature–induced (platelets cooled to 4°C and rewarmed to 37°C) platelet deformation was shown to be directly dependent on microtubule integrity.[22] Furthermore, the capacity of platelets from patients with Bernard–Soulier syndrome, gray platelet syndrome, and MYH9 disorders to undergo membrane deformation based on their size have been characterized by micropipette aspiration.[23] In particular, these measurements revealed that platelets from Bernard–Soulier syndrome required application of lower suction pressure thresholds during aspiration, showed longer membrane protrusions within the micropipette, and were highly deformable in comparison to normal platelets. Apart from single platelets, recently, micropipette aspiration has been also used to investigate the megakaryocyte cytoskeletal biomechanics and its influence on pro-platelet formation.[24]

Even though there are several elegant examples of the use of micropipette aspiration to elucidate fundamental biophysical properties of platelets, this method is seldom used for single-platelet analysis. This is mainly due to its low throughput, and it is technically highly demanding. Recent developments in miniaturization and automation to biomechanically characterize a few hundred cells in a single experiment by using parallel arrays of serial micropipettes assembled into a microfluidic device may potentially be able to also facilitate investigation of platelets.[25,26] Additionally, such devices would have the advantage over rapid exchange of soluble agonists/antagonists around the cells within millisecond time scales, thus facilitating measurement of kinetics of biomechanical changes in real time.

2.2 | Atomic force microscopy

The technique of atomic force microscopy (AFM), also known as scanning force microscopy, provides the capability to simultaneously visualize and quantify mechanical properties of both organic and inorganic materials in 3 dimensions on a nanometer (nm) scale at ambient atmospheric conditions, and in solution, including (biological) buffers, beyond the light diffraction limit.[27] AFM can achieve a lateral resolution up to 1 nm, or below with a subatomic vertical resolution limit of <0.1 nm while simultaneously allowing direct visualization of dynamic molecular events at millisecond time scales.[28,29] One of the most important features of AFM is its ability to manipulate single molecules and cells, thus facilitating measurement of intermolecular forces generated by biological systems down to sub-picoNewton (pN) regimes. These powerful features have made AFM the tool of choice for biologists, chemists, and physicists alike. The typical AFM setup combines a sensitive octapoled piezoelectric transducer for *x*-*y* scanning, and the third dimension, *z*, correlates to height movement in the piezo linked to an optical lever detection system. Scanning is performed with a thin flexible silicon nitride (Si_3N_4) cantilever, 100-200 μm in length, with an integrated pyramidal probe tip 4 to 8 μm tall with a radius of curvature of 5 to 10 nm at tip apex (Figure 3A). The cantilever is moved over the sample (*x*- and *y*-axis) and deflected (*z*-axis) according to the height of the sample (ie, scanning mode). The cantilever deflection (*d*) is registered onto a quadrant photo diode from reflected laser and provides a quantitative signal for the applied force (*F*). This information can be now used to calculate *F* based on Hooke's law: $F = -k\,d$, where *k* is the calibrated spring constant of the cantilever. Alternatively, the cantilever can be pressed on the sample (ie, tapping mode), and the forces needed to deflect it are measured (Figure 3B, 3, and 3), or it can be used to pull on the sample using an adhesive tip. Determination of the spring constant *k* of the AFM cantilever is the most critical step of setting up an AFM experiment. This can be measured by applying classical cantilever-beam theory (or Euler–Bernoulli beam theory) to determine the spring constant of the cantilever under investigation with cantilever tips shaped as a sphere, cone, or a pyramid and taking into account the geometric constrains of the cantilever (Figure 3A). Furthermore, after data acquisition, it is also necessary to apply suitable theoretical models such as Hertz, Sneddon, Derjaguin–Müller–Toporov, and Johnson–Kendall–Roberts (JKR) models to extract mechanical properties of biological systems.[30]

Since its development in the early 1990's, AFM has accelerated our understanding of biophysical properties governing hemostasis at the molecular and cellular levels.[31–40] With respect to surface characterization of platelets using AFM in scanning mode, Fritz et al[41,42] were first to report on detailed topography maps of human platelets upon adhesion and spreading on glass substrates. Subsequent tapping-mode AFM tip-based indentation imaging studies revealed the elastic modulus of adherent human platelets to be in the range of 1 to 50 kPa.[43] It was found that platelet granulomere was the softest part of platelets (1.5-4 kPa), and areas surrounding the granulomere were heterogeneous in their stiffness (10-40 kPa), while platelet edges were the stiffest (up to 53 kPa). Since the subcortical architecture of actin cytoskeleton influences elastic modulus of cells, the observed increased stiffness at platelet edges is a result of shorter, densely packed, and homogeneous distribution actin filaments.[43] These observations were recently confirmed by Sorrentino et al,[44] who investigated the mechanical stiffness of thrombin-activated single platelets spreading on fibrinogen surface by force-volume mapping by acquiring force-distance curves in *x*-*y* plane (Figure 3B-D) revealing Young's modulus of platelet granulomere to be 32 kPa, and the peripheral regions showed higher stiffness of ~224 kPa.

Using bulk methods, it has been shown previously that elasticity of platelet-rich clots is 10-fold greater (~600 Pa) than the elasticity of a clot devoid of platelets (~70 Pa). This is mainly due to high

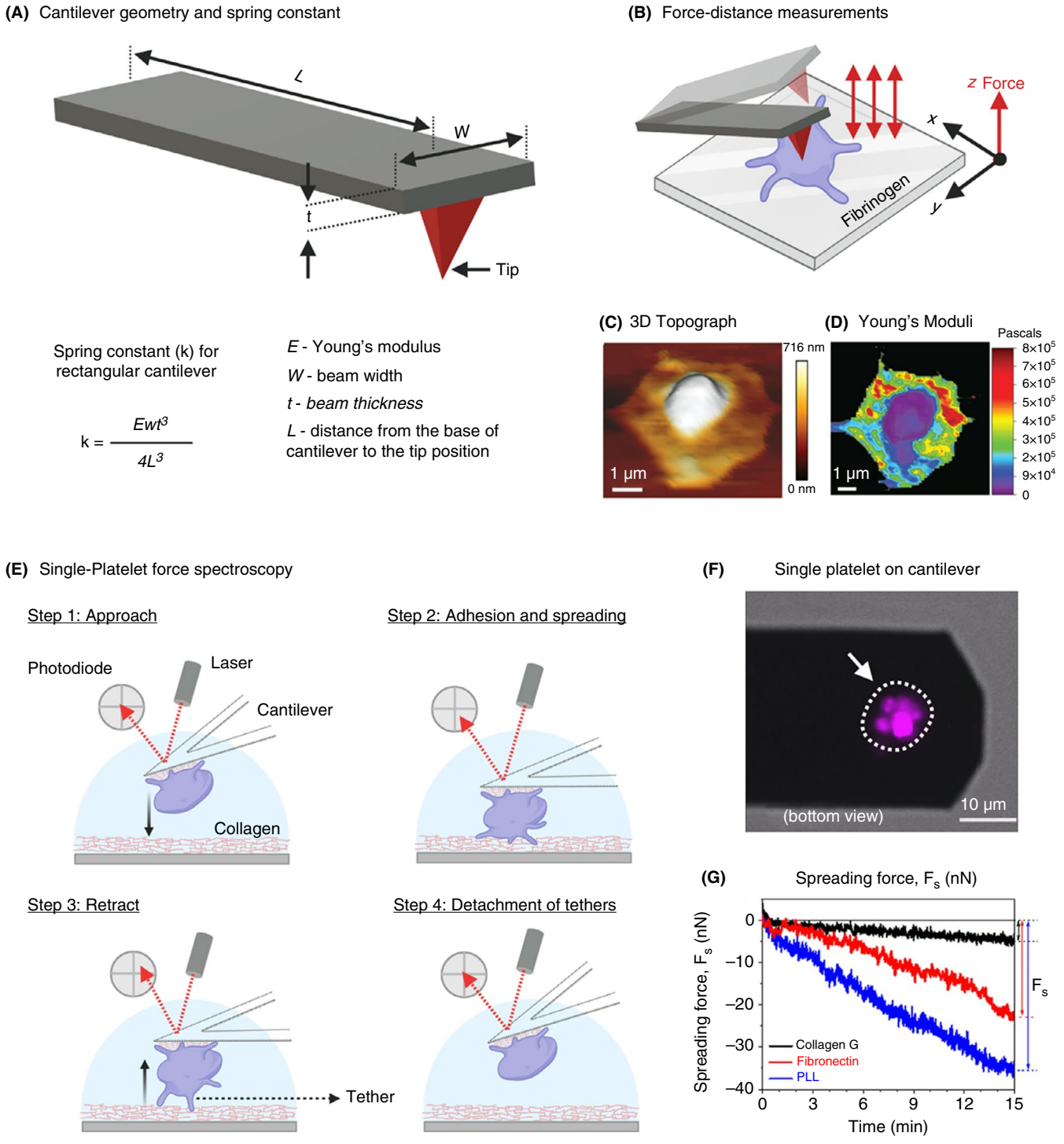

FIGURE 3 A, Schematic representation of a typical rectangular cantilever with a pyramidal sharp tip used for AFM and the equation for determination of cantilever spring constant k based on beam theory; C, 3D topography (height) and D, Young's modulus E of a single platelet spreading on fibrinogen passivated surface obtained by force-volume imaging by acquiring force-distance curves in *x-y* plane. (B, C, and D adapted and modified from Sorrentino et al.[44]) E, Schematic diagram of single platelet force spectroscopy using flat cantilever to assess biomechanical forces generated during single platelet adhesion at the tip of the cantilever. Single platelet firmly adhering on the lower side of a collagen-coated tipless cantilever (fplatelet labeled with plasma membrane dye DiI and imaged with confocal florescence microscopy) lowered along the *z*-axis (Step 1) and allowed to approach and contact briefly with collagen coated substrate (Step 2) to facilitate adhesion. Next, the cantilever is then retracted along *z*-axis in (Step 3) to allow the platelet to detach from the adhesive substrate (Step 4). These steps are repeated several hundreds of times in *x*-, *y*-, and *z*-axis to scan a defined area to obtain precise quantification of single platelet adhesion and spreading forces (g) on different substrates. (E, F, and G are adapted and modified from Nguyen et al.[46])

contractile forces generated by platelet actomyosin machinery on the fibrin network. To investigate these processes at single-platelet level, Lam et al[9,45] and Chaudhuri et al[9,45]used a custom-designed AFM setup that simultaneously allowed single-platelet manipulation and fluorescence imaging from the sides. A single platelet was suspended between a flat AFM cantilever passivated with fibrinogen and a fibrinogen-coated planar surface. The subsequent adhesion and spreading of the platelet between both fibrinogen surfaces generates adhesive and contractile forces that induce cantilever bending, which was the readout for quantifying the generated forces. This approach for the first time revealed that single platelets undergo instantaneous contact activation on fibrinogen while generating average maximum contractile and adhesive forces of 29 nN and 70 nN, respectively. These forces peaked at 2 to 3 minutes after contact with fibrinogen and were sustained beyond 15 minutes.[9] Furthermore, when platelets were held under an isometric clamp, they exerted higher force (2-fold increase) and became stiffer and more adhesive. This implies that platelets are able to modulate their contractile forces depending of the mechanical properties of the microenvironment. Recently, Nguyen et al,[46] using a similar approach investigated adhesive and rupture forces generated by single platelets (Figure 3E-G) and between 2 single platelets adhered to ECM proteins. Single-platelet interaction assays showed that human platelets produce an adhesion force of 23 ± 5 nN and ≥35 ± 4 nN on fibronectin and collagen type 1, respectively. However, when 2 individual platelets were brought into contact, the platelet-platelet interaction forces were found to be much lower, 1.50 ± 0.05 nN, when platelets adhered on collagen and 2.01 ± 0.05 nN when they adhered on fibronectin. These observations suggest that single platelets generate differential adhesion forces on different ECM substrates, which may depend on platelet activation states.

One of the most complex sets of multiple biomolecular direct and indirect interactions occurs when platelets engage with Gram-negative and Gram-positive bacteria.[47,48] These interactions often lead to platelet activation and in part contribute to the pathophysiology of infective endocarditis and disseminated intravascular coagulopathy. So far, little is known about how these interactions come into play and how this affects platelet activation from a biophysical perspective. Using AFM imaging, Xu and Siedlecki[49] showed that platelet adhesion to *Staphylococcus epidermidis* is mainly promoted by fibrinogen and fibronectin, which induces platelet activation, resulting in bacteria/platelet aggregates. These observations may further explain recently observed platelet-bacteria interactions leading to bacterial capture and their killing. Biomechanical properties of platelets are important, as bacterial killing by platelets is dependent on the integrity of the platelet acto-myosin complex.[50,51] Additionally, bacterial secret products such as pore-forming toxins: α-hemolysin (from *Staphylococcus aureus*) and streptolysin O (from *Streptococcus pyogenes*), which are known to permeabilize platelet membranes.[52] AFM made it possible to obtain detailed dynamic maps and kinetics of elasticity changes in the presence of streptolysin O on the platelet plasma membrane.[53] Streptolysin O induced a gradual increase in platelet elasticity starting from the granulomere, then spreading to the periphery. Upon stabilization of the F-actin cytoskeleton by phalloidin, streptolysin O–treated platelets undergo a marked decrease in their stiffness. These intriguing observations highlight the role of major cytoskeletal proteins to stabilize plasma membrane elasticity in platelets.

Although AFM has emerged as an excellent tool for precise measurements of single-platelet biomechanics, there are still many limitations mainly related to tip scan speed (temporal resolution for profiling rapid changes in platelet shape) and scan area, thereby restricting the throughput to a few adherent platelets. Additionally, single-platelet force spectroscopy experiments require immobilization of platelets to measure forces, either on the cantilever or on the solid phase. This immobilization procedure may cause undesirable platelet preactivation, may affect adhesion kinetics, and potentially introduce additional artifacts including operator bias. However, such artifacts can be minimized by carefully selecting immobilizing substrates depending on the scientific objectives.[46] Recently, automation and parallelization combined with positioning of cells on prepatterned adhesive substrates have achieved higher-throughput measurements of cell mechanics using AFM.[54,55] However, these advanced setups are not widely available yet.

2.3 | Scanning ion-conductance microscopy

Scanning ion-conductance microscopy (SICM) is a label-free, non-force contact, noninvasive, and high-resolution topography imaging technique suitable for biophysical characterization of biological samples from several micrometers down to molecular resolution of few nanometers.[56–58] The resolution limit in SICM is mainly determined by the nanopipette inner radius, which is typically in the range of 8 nm up to 2 µm.[56,59,60] In addition, SICM is also capable of monitoring surface charge and ion flux across membranes during topography imaging of biological samples.[61,62] The working principle of SICM is based on precise measurement of ionic current that flows between a quasi-reference counter electrode (QRCE) inside a borosilicate glass nanopipette and a second QRCE immersed in an electrolyte solution connected to a feedback control system that maintains the pipette-sample distance along a vertical axis (z) during the lateral scanning process (Figure 4A).[63] Topography imaging is then performed by immersing the nanopipette in the bath, where the ion current is limited initially by the resistance of the pipette. As the pipette gradually approaches the surface (eg, platelet membrane), the ion current (I_L) reduces. This reduction in ion current is used for distance feedback control and high-resolution noncontact topographical imaging. In order to map the local biomechanical properties such as elasticity, SICM uses application of hydrostatic pressure (0.1-150 kPa) through the nanopipette aperture at the surface of a cell membrane (Figure 4B). The deformation of membrane triggers the distance feedback control, adjusting the nanopipette position, thereby keeping the reduction in ion current at a constant value. Since the pipette position z (Figure 4A and 4) is a function of applied hydrostatic pressure

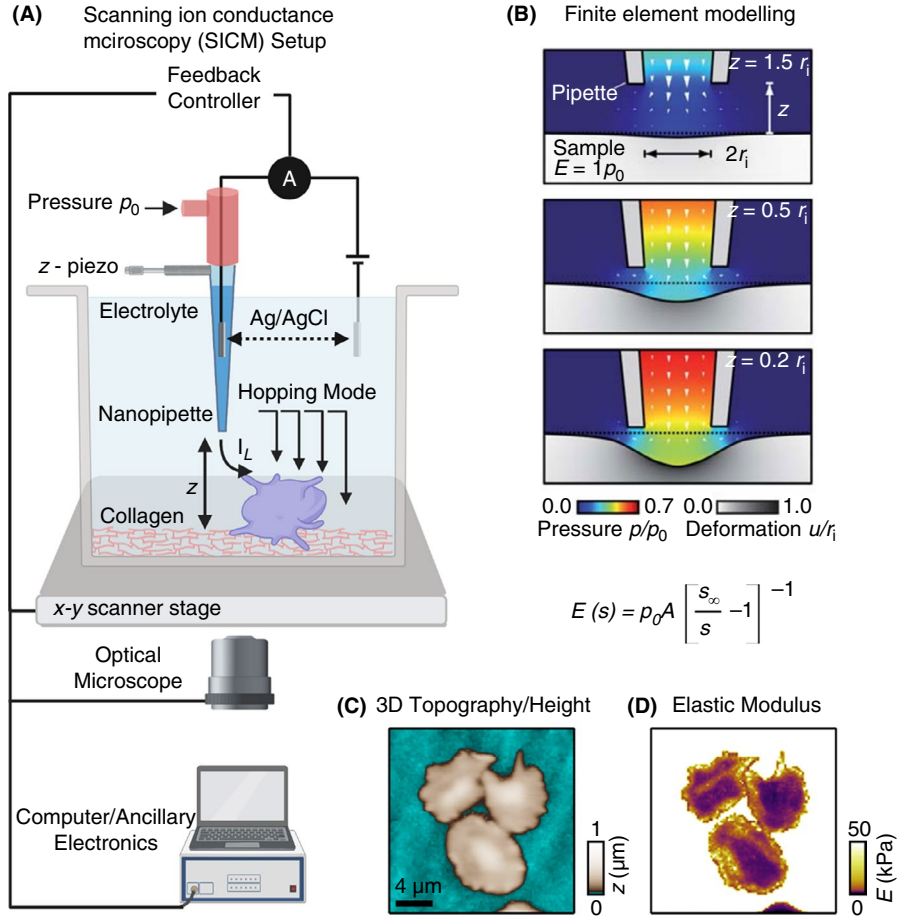

FIGURE 4 A, Schematics of scanning ion conductance microscopy (SICM) used for high-resolution topography imaging and biomechanical characterization of adherent platelets. The SICM setup consists of a pressure-controlled borosilicate glass nanopipette with a Ag/AgCl electrode and a second electrode connects the electrolyte-filled culture dish with the nanopipette. The culture dish is mounted on a sample scanner that drive in *x* and *y*-axis (for lateral movement) and *z*-piezo motors (for vertical scanning). An applied voltage between 2 electrodes induces an ionic leakage current IL through the electrolyte-filled nanopipette, which depends on the distance d between pipette and sample. A controller records this ion current and drives the *xy*- and *z*-piezo. For cell biological applications the SICM can be easily integrated with an optical microscope. B, Theoretical modeling using in silico finite element mechanics (FEM) simulation and calculations showing resulting deformation of an elastic sample as a function of the vertical SICM nanopipette position upon application of fluid flow induced by the pressure p0 applied to the upper pipette end.; C, Representative SICM 3D topography and Young's modulus mapping of spreading platelets. (Figure adapted and modified from Rheinlaender and Schaffer[65] and Rheinlaender et al.[66])

and corresponding response of the mechanical properties of the cell beneath the pipette, one can noninvasively locally indent the cell membrane.[64,65] This facilitates simultaneous noncontact true topography imaging and biomechanical characterization of platelets (Figure 4C and 4).[66] Recently, SICM has attracted considerable attention among platelet biologists and is fast emerging as the method of choice for high-speed morphometric and biomechanical characterization of single platelets.[67] Using SICM, Rheinlaender et al[66] elegantly demonstrated simultaneous imaging of morphodynamics at submicrometer resolution and showed that the mean elastic modulus of single platelets during spreading increased 5-fold from 3 to 15 kPa within 20 minutes. In addition, in the presence of thrombin, the elastic modulus of platelets decreased significantly from 12.4 kPa (resting platelet) to 7.5 kPa (thrombin activation) with a mean softening time of 7.1 minutes. Surprisingly, in platelets treated with cytochalasin D, mean elastic modulus decreased from 11.1 kPa to 6.5 kPa with a mean softening time of 2.7 minutes. These findings revealed platelet activation by thrombin and cytoskeleton depolymerization by cytochalasin D result in differential spatial distributions of the stiffening and softening regions on platelets, respectively. Subsequent SICM investigations of contribution of motor proteins such as dynein in the presence of inhibitors ciliobrevin D and erythro-9-(2-hydroxy-3-nonyl)-adenine revealed decreased contact-induced platelet spreading activity in thrombin-treated platelets, whereas blebbistatin (myosin II inhibitor), Y-27632 (ROCK inhibitor), nocodazole (microtubule polymerization inhibitor), and aurintricarboxylic acid-ATA (kinesin ATPase inhibitor) showed no significant effects.[68] Recently, in a clinically relevant study, SICM was found to be a useful label-free morphometric biophysical tool for obtaining fast 3-dimensional (3D) topographic images to unravel a critical role of platelet-derived high-mobility group box 1 (HMGB1) in

trauma and hemorrhagic shock, linking inflammation and microvascular thrombosis.[69] Platelet-derived HMGB1 was instrumental on acceleration of adhesion speed and increased spreading area of platelets on collagen and von Willebrand factor (VWF). Similarly, 3D topographic measurements using SICM have shown that platelets deficient in anaphylatoxin receptor C3aR exhibit a reduced spreading area on fibrinogen after thrombin stimulation compared to their normal platelets.[70] These observations indicate a role of complement activation fragment C3a and C3aR for platelet function during thrombus formation.

Even though SICM has attracted a broader attention of biologists, most SICM instrument setups do not allow fast and large-area scanning of live biological samples. For those interested in simultaneous mapping of platelet topography and elastic properties, the time factor is of key importance, since platelet morphodynamics occur within seconds in response to agonists. Recent technical improvements in SICM instrument design have specifically addressed these challenges and facilitate imaging of a 20 × 20 μm^2 scan area within 10 seconds.[71] It is foreseen that adaptation of these technical improvements will generate a broader appeal of SICM and pave the way for new discoveries in platelet biology.

3 | TRACTION FORCE MEASUREMENTS

Platelets exert traction (or contractile) forces. These are generated by the actomyosin-motor protein complex in activated platelets upon specific receptor-ligand interactions on exposed subendothelial ECM during blood clot and thrombus formation.[72,73] Broadly categorized under traction force microscopy (TFM), several methods are currently available to precisely measure and quantify cellular traction forces at a single or multicellular level in 2D and 3D.[74] In principle, these techniques rely on quantitative light microscopy to measure substrate displacements, which are then converted into forces. However, substrate preparation methods, implementation, modeling and data analysis of TFM varies between different approaches.[75,76] To measure traction forces produced by platelets, displacement tracking by TFM on hydrogel substrates and bending of elastomeric micropillar arrays are most commonly used.

3.1 | TFM on hydrogel substrates

TFM on hydrogel substrates is a versatile and perturbation-free approach to access cellular forces from single cells up to tissue levels. In its simplest implementation, TFM on hydrogel substrates measures cell-exerted traction forces from the spatial images of substrate stress by tracking the displacement of fiducial markers such as fluorescent tracer beads embedded in a continuum soft elastic substrate that undergoes linear deformations (Figure 5A and 5).[77] Traction forces are then computed by applying appropriate assumptions/constraints, taking into account substrate stiffness and its deformation in response to traction force and boundary conditions such as cell geometry. The resolution of measured force relies on substrate stiffness, density of tracer beads, image acquisition parameters, and the mathematical algorithm applied for data assessment.[76,78,79]

Blood clots are mainly composed of platelets, red blood cells, and a dense network of fibrin fibers. During hemostasis, the terminal stage of blood clot maturation by platelet-driven clot retraction and fibrin matrix remodeling is one of the physiologically most relevant mechanisms where integrin αIIbβ3-mediated fibrin interactions and contractile force generation by the actomyosin complex acting through talin comes into play.[80] Primarily, this allows for reestablishing nonobstructed blood flow and normal hemodynamics past otherwise obstructive thrombi within a blood vessel.[81] Although the biochemical nature of this process is well understood, the mechanobiological principles have remained elusive. Using TFM, Schwarz Henriques et al[82] showed for the first time temporal evolution of contractile forces in thrombin-activated platelets spreading on fibrinogen functionalized polyacrylamide gel with a physiologically relevant elastic modulus of 4 kPa. They observed, upon reaching steady state after 25 minutes, that single platelets were able to exert a traction field (ie, displacement field of gel surface) as large as ≈3.3 × 10^3 Pa with total forces in the range of ≈34 nN. Using polyacrylamide gels with a tunable elastic modulus, Qiu et al[83] observed that fibrinogen functionalized stiffer gels (elastic modulus of 5.0 kPa and 50 kPa) promoted platelet adhesion, spreading, and activation, while on soft gels (0.5 kPa) platelet function was abrogated and was dependent on Rac1 and actomyosin activity. Subsequent TFM experiments on substrates of higher elastic modulus (from 19 kPa up to 83 kPa) revealed that traction forces generated by fully activated platelets were independent of the matrix stiffness.[84] Although platelets generated isotropic contractile traction forces, at the steady state, assessment of force localization showed that these were largest at the periphery of platelets, while the traction force was focused near the platelet granulomere. From a broader perspective, single-platelet TFM experiments have provided meaningful biophysical insight into how isotropic contractile traction and subsequent mechanotransduction events driven by the actomyosin complex may play an important role in engagement of platelet $\alpha_{IIb}\beta_3$ on fibrin during clot retraction in hemostasis.[80] Recently, quantitative fluorescence microscopy provided mechanistic insights into how transmission of contractile forces generated by single platelets occurs via filopodial extensions, which bend and shorten fibrin fibers, thereby causing clot volume shrinkage and alterations at the macro level.[85] Additionally, single-platelet contractile force measurements also explain the role of mechanotransduction in innate immune responses of platelets such as those involving FcγRIIA-mediated recognition, sequestration, and killing of immunoglobulin G opsonized bacteria under the platelet granulomere.[51]

TFM has gained wide popularity due to its high sensitivity and relative simplicity. However, traditional TFM suffers from

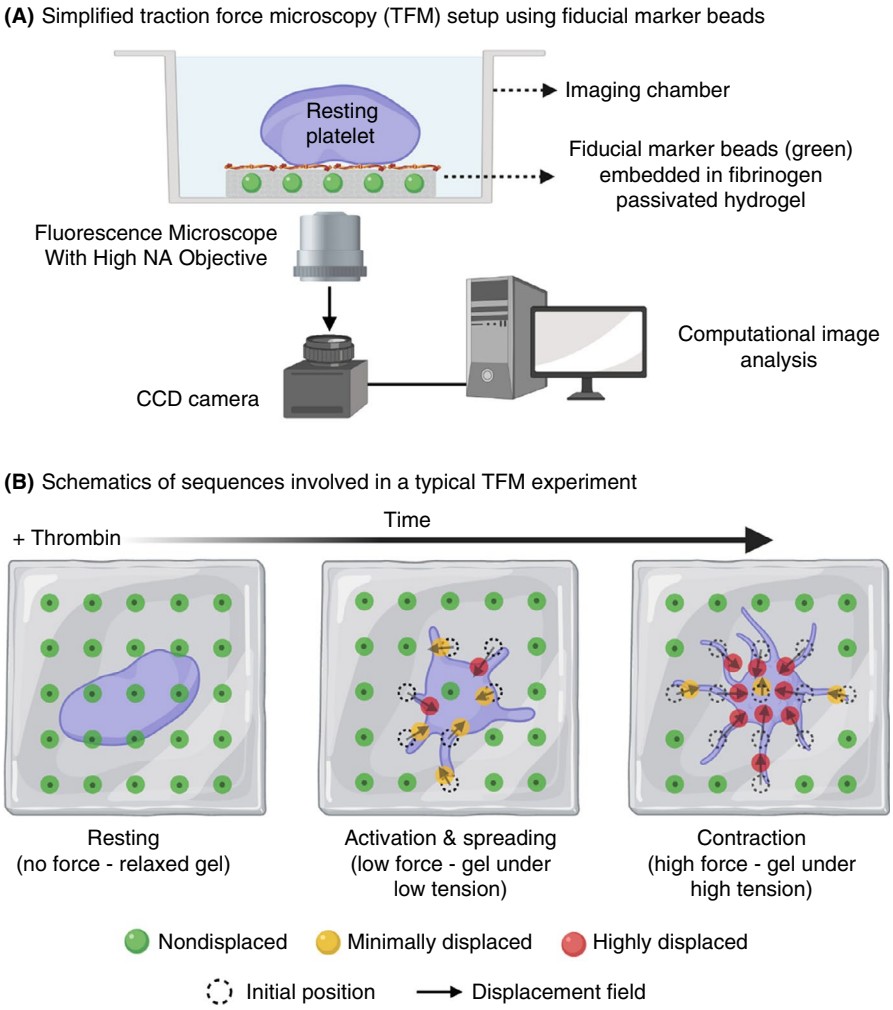

FIGURE 5 A, Schematic diagram showing set-up of a traction force microscopy experiment using fibrinogen passivated hydrogel of known stiffness embedded with of fiducial marker microbeads; B, Resting platelets are seeded low densities on the fibrinogen passivated hydrogel surface. Upon thrombin stimulation, activated platelets adhere, spread, and ultimately contract resulting in generation of "traction forces" over the entire process. These forces exert mechanical tension on the hydrogel that leads to displacement of embedded microbeads. These displacements can be precisely imaged and tracked overtime with a fluorescence microscope. Post-image acquisition, image-processing algorithms are used to compute displacement fields that provide spatial and temporal dynamics of platelet generated traction forces

low measurement throughput and artifacts related to variations in hydrogel mechanical properties. To address these drawbacks, a chip-based high-throughput platelet contraction cytometer was developed recently.[86] The chip-based contraction cytometer uses microfabrication technology to fabricate a large array of fibrinogen passivated microdot pairs on a hydrogel substrate with varied stiffness to assess the nanomechanics of hundreds of individual platelets under physiologically relevant conditions. The readout of contractile force output is based on measurement of lateral displacement of 2 adjacent fibrinogen microdots by a single activated platelet. Using a platelet contraction cytometer, Myers et al[86] revealed that platelet-generated contractile force during clot formation requires both biochemical (eg, thrombin) and mechanical (eg, substrate stiffness) inputs and the mechanosensitive contraction is highly dependent on the Rho/ROCK pathway. Furthermore, assessment of platelet contractile forces from patients with Wiskott-Aldrich syndrome and MYH9 disorder (nonmuscle myosin IIa mutations) on a platelet contraction cytometer showed that up to 30% of these platelets from patients with cytoskeleton-related platelet disorders exhibit the near-zero contractile forces on stiffer substrates, while this was limited to only 6% in healthy controls. These findings are significant, as they point toward the critical role of platelet cytoskeletal machinery at a single-platelet level in achieving a mechanically stable hemostatic plug.

3.2 | Deformable elastomeric micropillar and microbeam arrays

As an alternative to the continuum substrates used in TFM, deformable micropillar (also called as micropost) arrays are uniformly spaced, compliant, vertical elastomeric cylindrical cantilevers made of polydimethylsiloxane (PDMS) of defined dimensions (diameter and height) and stiffness (linearly elastic).[87] In contrast to TFM, the ligand functionalized tips of the micropillars serve as adhesive surfaces.[88] Upon cell adhesion, the displacements of each micropillar in an array is tracked by video microscopy, and the applied force on the cantilever can be calculated from force-displacement relationship for pure bending of an elastic cylindrical beam using beam theory (Figure 6A and 6).[89] Micropillar arrays have been used in a wide variety of contexts, not only to measure cell-generated forces (as low as 1 nN), but also to analyze the relationship between substrate rigidity and single-cell responses as well as at the tissue level, thus making it a highly versatile biophysical tool.[90,91] Liang et al[92]

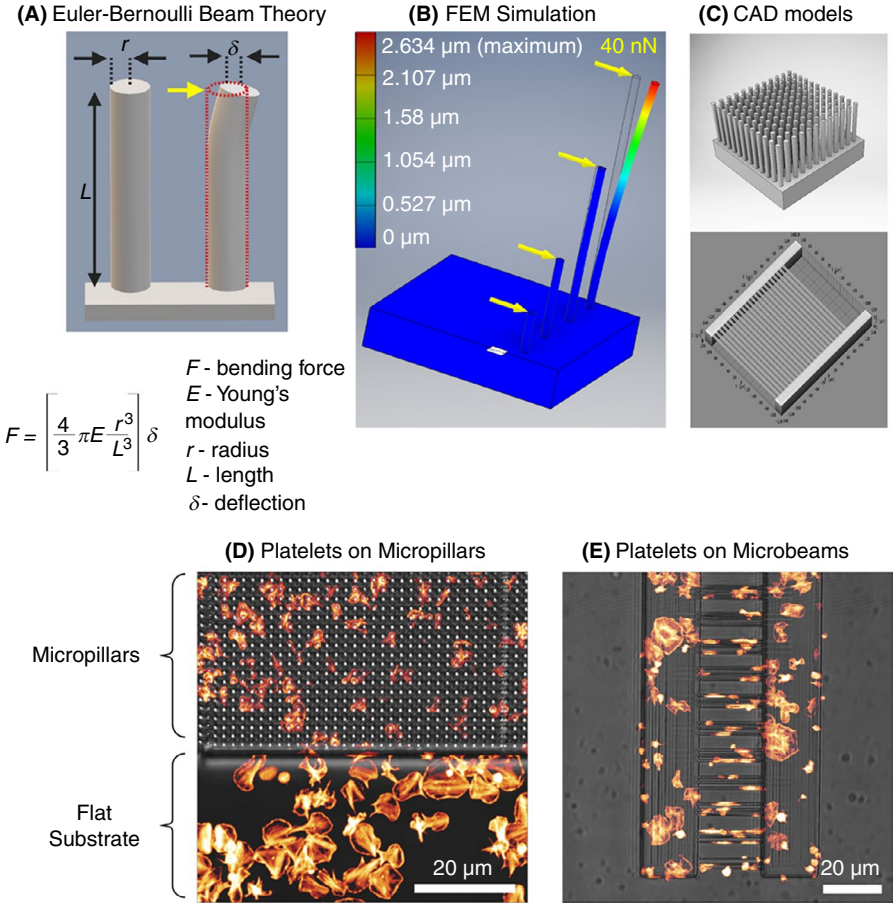

FIGURE 6 A, Schematics showing Euler-Bernouli beam theory as applied to calculation of lateral force (yellow arrow) acting on the free end of a micropillar attached to a solid base leading to its deflection of the vertical micropillar. B, In silico finite element mechanics (SEM) simulation of bending of micropillars upon application of a lateral force of 40 nN acting on the free end of the micropillar causing a maximum defection of 2.62 μm. C, Models of computer-assisted design (CAD) used for fabrication of deformable elastomeric micropillar (D) and microbeam array microstructures using 2-photon polymerization (2PP) and 3D printing functionalized with fibrinogen showing comparative differences in platelet spreading and cytoskeletal organization on different substrate geometries

adapted micropillar arrays spaced at 9 μm apart and passivated with fibrinogen to quantify contractile forces produced by platelets in a microthrombus. The average contractile force produced by a single platelet in microthrombi on micropillars was found to be 2.1 ± 0.1 nN that was dependent on thrombin concentration, while the contractile force increased steadily overtime as the microthrombus grew. These results demonstrated quantitatively for the first time that each platelet acts as an active contractile force–producing unit in the microthrombus and subsequent recruitment of platelets leads to incremental augmentation of total contractile force. Follow-up investigations by Feghhi et al[93] using fibronectin passivated micropillars revealed that the generation of contractile forces by platelets in microthrombi is regulated by nonmuscle myosin IIA ATPase activity through Rho kinase (ROCK) and myosin light-chain kinase. Additionally, elastomeric micropillars coated with VWF have been found to be useful in assessing the role of integrin αIIbβ3 and GPIb-IX-V complex in mechanotransduction of forces through cytoskeleton at the single-platelet level.[94] Currently, deformable micropillar arrays are fabricated using a photolithographic technique followed by replica molding using PDMS. However, this labor-intensive and time-consuming process limits rapid prototyping necessary for optimizing substrate deformation to increase measurement sensitivity. In addition, fabrication of complex geometries to measure cellular traction forces on 3D substrates is impossible to achieve via replica molding. To address these issues our laboratory has adopted a maskless technique based on direct laser writing using 2-photon polymerization (2PP) in 3D of photosensitive resists to print high-resolution deformable micro- and nanostructures in 3D.[95] Using 2PP we have 3D printed deformable micropillars as wells as suspended horizontal microbeams that can be functionalized with platelet adhesive ligand of choice (Figure 6D and 6).[96] Quantification of micropillar and microbeam deformation upon platelet adhesion showed single platelets generate a mean traction force of 46.3 nN on micropillars of aspect ratio of 1:10 (diameter 700 nm and height 7 μm) and 31.9 nN on microbeams (diameter 400 nm, length 25 μm) functionalized with fibrinogen. We assume these differences in measured forces arise as a result of differential platelet adhesion and spreading that is unique to substrate geometry and depends on ligand-functionalized surface area (Figure 5C and 5). We are currently further investigating these observations to better understand whether platelets sense and modulate traction forces in response to changes in topography and the chemical nature of their microenvironment.

4 | REAL-TIME DEFORMIBILITY CYTOMETRY

Real-time deformability cytometry is a rapidly emerging mechanophenotyping approach that combines the technique of flow

cytometry with measuring cell stiffness using microfluidic technology. As discussed in previous sections, currently available biophysical techniques for biomechanical characterization of platelets are labor intensive, suffer from measurement throughput, and most importantly cannot be performed in complex fluids such as whole blood. These limitations have restricted the adoption of such techniques to investigate platelet biology and function testing for diagnostic purposes in clinical and translational scenarios. Real-time deformability cytometry (RT-DC) has shown to be capable of probing single-cell deformation at >1000 cells per second in real time in whole blood thereby providing comprehensive biomechanical signatures of individual cell types in blood in a short period of time.[97,98] RT-DC uses application of hydrodynamic shear stress to induce cell deformation as the cells pass through a narrow microfluidic channel (15-30 µm in cross section). During this passage, the sample is illuminated with a high-power light-emitting diode (LED) as a light source and imaged concurrently with a high-speed camera synchronized with the LED at millisecond intervals and cell contour images are computationally analyzed on the fly, providing rapid insights into cellular physiological states based on their stiffness contributed by cytoskeletal components (Figure 7A-C). This approach facilitates extraction of additional quantitative parameters such as cell size and morphology, thus typifying cells and simultaneously characterizing cell deformability at single-cell resolution without prior separation, enrichment, and labeling procedures.[99] Due to these capabilities, RT-DC is a promising method with potential relevance to several fields of life sciences.[100] To demonstrate the potential of RT-DC as a high-throughput biophysical method for mechanophenotyping platelets, as a proof of principle we exposed human platelets to agonists and cytoskeleton destabilizing chemical agents for 10 minutes and subsequently performed RT-DC measurements on live platelets (Figure 7D, unpublished results). Thrombin receptor activator for peptide 6 (TRAP-6) treated platelets deformed

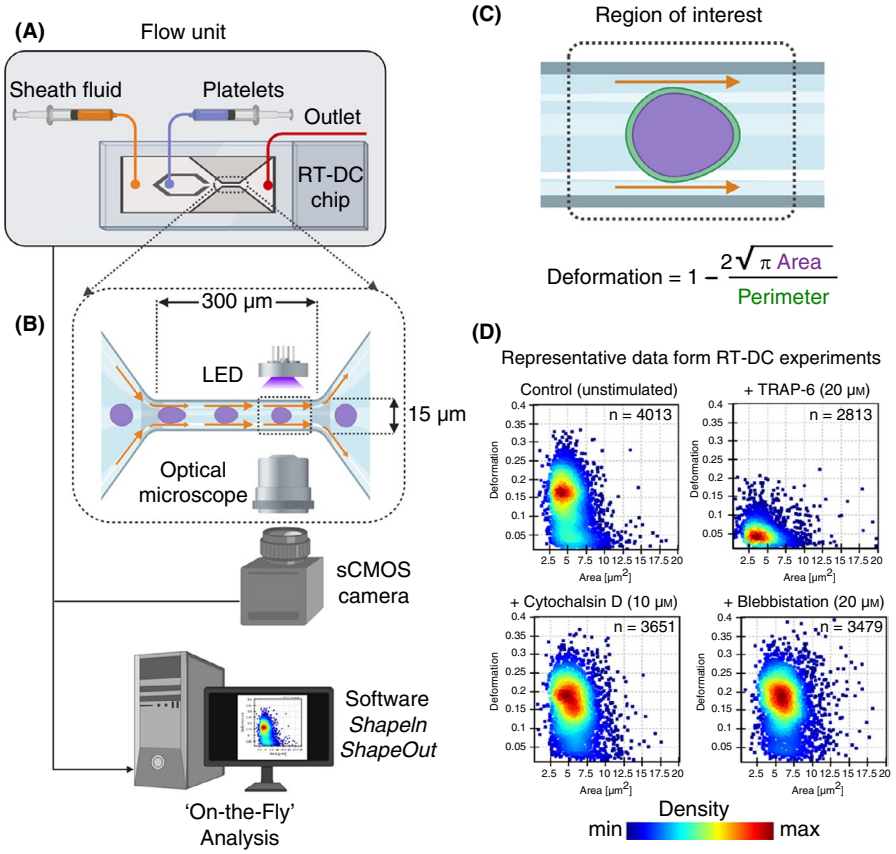

FIGURE 7 The real-time deformability cytometry (RT-DC) microfluidic chip connected to a flow unit (A) consist of dedicated inlets for sheath fluid and for cells/platelets, which combine into to a channel with narrow constriction zone (B) where cell/platelets undergo deformation as a result of hydrodynamic compression brought about by sheath fluid. A high-powered light-emitting diode (LED) is used to illuminate the samples. Images are recorded by a scientific complementary metal–oxide–semiconductor (sCMOS) camera working at high frame rates (≈2000 images/s) that is synchronized with the frequency of illumination time. This combined together with microfluidic flow, RT-DC allows for mechanoprofiling of >100 unique cells/platelets per second in a contact- and label-free manner. Platelet deformation (C) is determined on the fly in real time by computational image processing algorithm that taking into account the area and perimeter of the deformed platelet as it passes through the region of interest. Results of a typical RT-DC measurements involving washed platelets (D) show that unstimulated deform more (ie, softer), while those treated with agonist (TRAP-6) deform less (ie, stiffer; upper panels). Platelets preincubated with cytochalasin D and blebbistatin lead to increased deformation (ie, softer; lower panels). Data show density maps of deformation against area (µm^2) from n ≥ 2500 individual platelets from a single experiment

TABLE 1 Comparison of currently available biophysical tools suitable for biomechanical assessment of platelets

Biophysical method	Biomechanical properties	Restrictions	Throughput	Technical know-how	Commercial vendors
Micropipette aspiration	Elastic and viscoelastic	Nonadherent/In suspension and adherent	Low 1-5 platelets/h	Highly skilled	NA
Atomic force microscopy	Elastic, viscoelastic, and adhesion forces	Adherent	Low 1-5 platelets/h	Highly skilled	Yes
Scanning ion conductance microscopy	Elastic and viscoelastic	Adherent	Low 1-10 platelets/h	Highly skilled	Yes
Traction force microscopy on hydrogel substrates	Adhesion and contraction	Adherent	Medium to high	Skilled	NA
Micropillars and deformable 3D substrates	Adhesion and contraction	Adherent	Medium	Skilled	Yes
Real-time deformability cytometry	Deformability	Nonadherent/In suspension	Very high 100-1000 platelets/sec	Skilled	Yes

less, that is, platelets became stiffer (median deformation, 0.0475, n = 2813 single platelets), whereas cytochalasin D and blebbistatin showed increased deformation, that is, platelets became softer (0.166, n = 3651; and 0.176, n = 3479, respectively), in comparison to resting platelets (0.139, n = 4013). Our preliminary results are encouraging since they hint at the role of the platelet cytoskeleton contributing to intrinsic biomechanical deformation characteristics of platelets depending on their physiological state. We are currently evaluating the suitability of RT-DC to understand the relationship between platelet activation status and corresponding biomechanical characteristics as a novel approach for platelet function testing, quality control of platelets during storage, and diagnostics of inherited platelet diseases related to the cytoskeleton.

5 | CONCLUSIONS

Current knowledge of fundamental biochemical and cell biological processes governing thrombosis and hemostasis have been steadily advanced as result of continued development and implementation methods, which vary widely in their readouts, sensitivities, and spatiotemporal resolution on a macroscale. Building on this, using cutting-edge biophysical methods to manipulate single platelets, one can gain novel insights into biomechanical principles influencing hemostasis and thrombus formation at subnanoscale regimes. Adaptation of the appropriate biophysical platform will mainly depend on the primary research question and on availability and suitability of one or more of the methods described here (Table 1).

Due to the highly interdisciplinary nature of these investigations, clinicians and basic scientists are encouraged to collaborate extensively to maximize the potential of many of such biophysical methods to address outstanding questions in platelet biology.

ACKNOWLEDGMENTS

The authors thank Prof. Dr Markus Münzenburg, Interface and Surface Physics, and Dr Oliver Otto, Biomechanics, Center for Innovation Competence at University of Greifswald, Germany, for providing access instrumentation and facilities. The authors also thank Prof. Dr Ohad Medalia, Department of Biochemistry, University of Zurich, Switzerland, and Prof. Dr Tilman E. Schäffer, Institute of Applied Physics, University of Tübingen, Germany, for providing high-resolution, representataive AFM and SICM images of biomechanical charaterization of single platelets, respectively.

RELATIONSHIP DISCLOSURE

The authors report nothing to disclose.

AUTHOR CONTRIBUTIONS

RP and LS performed literature review, composition of the primary manuscript, preparation of figures, and editing. AG and CD contributed to the primary text and participated in revision of the manuscript. RP, LS, and CD performed the experiments, analyzed the results, and prepared the RT-DC, micropost, and micropillar data presented in the review. RP and CD acquired the funding. All authors contributed to revision of the final version of the manuscript.

ORCID

Raghavendra Palankar https://orcid.org/0000-0002-8957-1103

TWITTER

Raghavendra Palankar @palankarr

REFERENCES

1. Machlus KR, Italiano Jr JE. The incredible journey: from megakaryocyte development to platelet formation. J Cell Biol. 2013;201:785–96.

2. Qiu Y, Ciciliano J, Myers DR, Tran R, Lam WA. Platelets and physics: how platelets "feel" and respond to their mechanical microenvironment. Blood Rev. 2015;29:377–86.
3. Hansen CE, Qiu Y, McCarty OJT, Lam WA. Platelet mechanotransduction. Annu Rev Biomed Eng. 2018;20:253–75.
4. Yeaman MR. Platelets: at the nexus of antimicrobial defence. Nat Rev Microbiol. 2014;12:426–37.
5. Cardigan R, Turner C, Harrison P. Current methods of assessing platelet function: relevance to transfusion medicine. Vox Sang. 2005;88:153–63.
6. Taheri-Araghi S, Brown SD, Sauls JT, McIntosh DB, Jun S. Single-cell physiology. Annu Rev Biophys. 2015;44:123–42.
7. Ju L, Chen Y, Xue L, Du X, Zhu C. Cooperative unfolding of distinctive mechanoreceptor domains transduces force into signals. Elife. 2016;5:e15447.
8. Butera D, Passam F, Ju L, Cook KM, Woon H, Aponte-Santamaria C, et al. Autoregulation of von Willebrand factor function by a disulfide bond switch. Sci Adv. 2018;4:eaaq1477.
9. Lam WA, Chaudhuri O, Crow A, Webster KD, Li TD, Kita A, et al. Mechanics and contraction dynamics of single platelets and implications for clot stiffening. Nat Mater. 2011;10:61–6.
10. Chen Y, Ju LA, Zhou F, Liao J, Xue L, Su QP, et al. An integrin αIIbβ3 intermediate affinity state mediates biomechanical platelet aggregation. Nat Mater. 2019;18:760–9.
11. Wu P-H, Aroush DR-B, Asnacios A, Chen W-C, Dokukin ME, Doss BL, et al. A comparison of methods to assess cell mechanical properties. Nat Methods. 2018;15:491–8.
12. Evans E, Needham D. Physical properties of surfactant bilayer membranes: thermal transitions, elasticity, rigidity, cohesion and colloidal interactions. J Phys Chem. 1987;91:4219–28.
13. Dimova R. Recent developments in the field of bending rigidity measurements on membranes. Adv Colloid Interface Sci. 2014;208:225–34.
14. Longo ML, Ly HV. Micropipet aspiration for measuring elastic properties of lipid bilayers. Methods Mol Biol. 2007;400:421–37.
15. Gonzalez-Bermudez B, Guinea GV, Plaza GR. Advances in micropipette aspiration: applications in cell biomechanics, models, and extended studies. Biophys J. 2019;116:587–94.
16. White JG, Burris SM, Tukey D, Smith C 2nd, Clawson CC. Micropipette aspiration of human platelets: influence of microtubules and actin filaments on deformability. Blood. 1984;64:210–4.
17. Kee YS, Robinson DN. Micropipette aspiration for studying cellular mechanosensory responses and mechanics. Methods Mol Biol. 2013;983:367–82.
18. Hochmuth RM. Micropipette aspiration of living cells. J Biomech. 2000;33:15–22.
19. Burris SM, Smith 2nd CM, Tukey DT, Clawson CC, White JG. Micropipette aspiration of human platelets after exposure to aggregating agents. Arteriosclerosis. 1986;6:321–5.
20. Burris SM, Smith CM 2nd, Rao GH, White JG. Aspirin treatment reduces platelet resistance to deformation. Arteriosclerosis. 1987;7:385–8.
21. Haga JH, Beaudoin AJ, White JG, Strony J. Quantification of the passive mechanical properties of the resting platelet. Ann Biomed Eng. 1998;26:268–77.
22. Burris SM, Smith CM 2nd, Tukey D, Clawson CC, White JG. Micropipette aspiration of human platelets: influence of rewarming on deformability of chilled cells. J Lab Clin Med. 1986;107:238–43.
23. White JG, Burris SM, Hasegawa D, Johnson M. Micropipette aspiration of human blood platelets: a defect in Bernard-Soulier's syndrome. Blood. 1984;63:1249–52.
24. Chen Y, Aardema J, Kale S, Whichard ZL, Awomolo A, Blanchard E, et al. Loss of the F-BAR protein CIP4 reduces platelet production by impairing membrane-cytoskeleton remodeling. Blood. 2013;122:1695–706.
25. Mak M, Erickson D. A serial micropipette microfluidic device with applications to cancer cell repeated deformation studies. Integr Biol (Camb). 2013;5:1374–84.
26. Myrand-Lapierre ME, Deng X, Ang RR, Matthews K, Santoso AT, Ma H. Multiplexed fluidic plunger mechanism for the measurement of red blood cell deformability. Lab Chip. 2015;15:159–67.
27. Patel AN, Kranz C. (Multi)functional atomic force microscopy imaging. Annu Rev Anal Chem (Palo Alto Calif). 2018;11:329–50.
28. Gross L, Schuler B, Pavlicek N, Fatayer S, Majzik Z, Moll N, et al. Atomic force microscopy for molecular structure elucidation. Angew Chem Int Ed Engl. 2018;57:3888–908.
29. Ando T. Directly watching biomolecules in action by high-speed atomic force microscopy. Biophys Rev. 2017;9:421–9.
30. Krieg M, Fläschner G, Alsteens D, Gaub BM, Roos WH, Wuite GJL, et al. Atomic force microscopy-based mechanobiology. Nat Rev Phys. 2019;1(1):41–57.
31. Hussain MA, Siedlecki CA. The platelet integrin alpha(IIb) beta(3) imaged by atomic force microscopy on model surfaces. Micron. 2004;35:565–73.
32. Carvalho FA, Connell S, Miltenberger-Miltenyi G, Pereira SV, Tavares A, Ariens RA, et al. Atomic force microscopy-based molecular recognition of a fibrinogen receptor on human erythrocytes. ACS Nano. 2010;4:4609–20.
33. Tobimatsu H, Nishibuchi Y, Sudo R, Goto S, Tanishita K. Adhesive forces between A1 domain of von Willebrand factor and N-terminus domain of glycoprotein ibalpha measured by atomic force microscopy. J Atheroscler Thromb. 2015;22:1091–9.
34. Soman P, Rice Z, Siedlecki CA. Measuring the time-dependent functional activity of adsorbed fibrinogen by atomic force microscopy. Langmuir. 2008;24:8801–6.
35. Aponte-Santamaria C, Huck V, Posch S, Bronowska AK, Grassle S, Brehm MA, et al. Force-sensitive autoinhibition of the von Willebrand factor is mediated by interdomain interactions. Biophys J. 2015;108:2312–21.
36. Posch S, Obser T, Konig G, Schneppenheim R, Tampe R, Hinterdorfer P. Interaction of von Willebrand factor domains with collagen investigated by single molecule force spectroscopy. J Chem Phys. 2018;148:123310.
37. Kang I, Raghavachari M, Hofmann CM, Marchant RE. Surface-dependent expression in the platelet GPIb binding domain within human von Willebrand factor studied by atomic force microscopy. Thromb Res. 2007;119:731–40.
38. Marchant RE, Lea AS, Andrade JD, Bockenstedt P. Interactions of von Willebrand factor on mica studied by atomic force microscopy. J Colloid Interface Sci. 1992;148:261–72.
39. Zhmurov A, Protopopova AD, Litvinov RI, Zhukov P, Weisel JW, Barsegov V. Atomic structural models of fibrin oligomers. Structure. 2018;26(6):857–868.e4.
40. Brown AE, Litvinov RI, Discher DE, Weisel JW. Forced unfolding of coiled-coils in fibrinogen by single-molecule AFM. Biophys J. 2007;92:L39–41.
41. Fritz M, Radmacher M, Gaub HE. In vitro activation of human platelets triggered and probed by atomic force microscopy. Exp Cell Res. 1993;205:187–90.
42. Fritz M, Radmacher M, Gaub HE. Granula motion and membrane spreading during activation of human platelets imaged by atomic force microscopy. Biophys J. 1994;66:1328–34.
43. Radmacher M, Fritz M, Kacher CM, Cleveland JP, Hansma PK. Measuring the viscoelastic properties of human platelets with the atomic force microscope. Biophys J. 1996;70:556–67.
44. Sorrentino S, Studt JD, Horev MB, Medalia O, Sapra KT. Toward correlating structure and mechanics of platelets. Cell Adh Migr. 2016;10:568–75.

45. Chaudhuri O, Parekh SH, Lam WA, Fletcher DA. Combined atomic force microscopy and side-view optical imaging for mechanical studies of cells. Nat Methods. 2009;6:383–7.
46. Nguyen TH, Palankar R, Bui VC, Medvedev N, Greinacher A, Delcea M. Rupture forces among human blood platelets at different degrees of activation. Sci Rep. 2016;6:25402.
47. Hamzeh-Cognasse H, Damien P, Chabert A, Pozzetto B, Cognasse F, Garraud O. Platelets and infections - complex interactions with bacteria. Front Immunol. 2015;6:82.
48. Fitzgerald JR, Foster TJ, Cox D. The interaction of bacterial pathogens with platelets. Nat Rev Microbiol. 2006;4:445–57.
49. Xu L-C, Siedlecki CA. Effects of plasma proteins on staphylococcus epidermidis RP62A adhesion and interaction with platelets on polyurethane biomaterial surfaces. J Biomater Nanobiotechnol. 2012;03:487–98.
50. Gaertner F, Ahmad Z, Rosenberger G, Fan S, Nicolai L, Busch B, et al. Migrating platelets are mechano-scavengers that collect and bundle bacteria. Cell. 2017;171(6):1368–1382.e23.
51. Palankar R, Kohler TP, Krauel K, Wesche J, Hammerschmidt S, Greinacher A. Platelets kill bacteria by bridging innate and adaptive immunity via platelet factor 4 and FcgammaRIIA. J Thromb Haemost. 2018;16:1187–97.
52. Flaumenhaft R. Platelet Permeabilization. In: Gibbins JM, Mahaut-Smith MP, editors. Platelets and Megakaryocytes: Volume 2: Perspectives and Techniques. Totowa, NJ: Humana Press, 2004; 365–78.
53. Walch M, Ziegler U, Groscurth P. Effect of streptolysin O on the microelasticity of human platelets analyzed by atomic force microscopy. Ultramicroscopy. 2000;82:259–67.
54. Favre M, Polesel-Maris J, Overstolz T, Niedermann P, Dasen S, Gruener G, et al. Parallel AFM imaging and force spectroscopy using two-dimensional probe arrays for applications in cell biology. J Mol Recognit. 2011;24:446–52.
55. Wang Z, Liu L, Wang Y, Xi N, Dong Z, Li M, et al. A fully automated system for measuring cellular mechanical properties. J Lab Autom. 2012;17:443–8.
56. Schaffer TE. Nanomechanics of molecules and living cells with scanning ion conductance microscopy. Anal Chem. 2013;85:6988–94.
57. Happel P, Thatenhorst D, Dietzel ID. Scanning ion conductance microscopy for studying biological samples. Sensors (Basel). 2012;12:14983–5008.
58. Shevchuk AI, Frolenkov GI, Sanchez D, James PS, Freedman N, Lab MJ, et al. Imaging proteins in membranes of living cells by high-resolution scanning ion conductance microscopy. Angew Chem Int Ed Engl. 2006;45:2212–6.
59. Rheinlaender J, Schaffer TE. Lateral resolution and image formation in scanning ion conductance microscopy. Anal Chem. 2015;87:7117–24.
60. Korchev YE, Milovanovic M, Bashford CL, Bennett DC, Sviderskaya EV, Vodyanoy I, et al. Specialized scanning ion-conductance microscope for imaging of living cells. J Microsc. 1997;188:17–23.
61. Page A, Perry D, Young P, Mitchell D, Frenguelli BG, Unwin PR. Fast nanoscale surface charge mapping with pulsed-potential scanning ion conductance microscopy. Anal Chem. 2016;88:10854–9.
62. Chen CC, Zhou Y, Morris CA, Hou J, Baker LA. Scanning ion conductance microscopy measurement of paracellular channel conductance in tight junctions. Anal Chem. 2013;85:3621–8.
63. Hansma PK, Drake B, Marti O, Gould SA, Prater CB. The scanning ion-conductance microscope. Science. 1989;243:641–3.
64. Sánchez D, Johnson N, Li C, Novak P, Rheinlaender J, Zhang Y, et al. Noncontact measurement of the local mechanical properties of living cells using pressure applied via a pipette. Biophys J. 2008;95:3017–27.
65. Rheinlaender J, Schäffer TE. Mapping the mechanical stiffness of live cells with the scanning ion conductance microscope. Soft Matter. 2013;9:3230–6.
66. Rheinlaender J, Vogel S, Seifert J, Schachtele M, Borst O, Lang F, et al. Imaging the elastic modulus of human platelets during thrombin-induced activation using scanning ion conductance microscopy. Thromb Haemost. 2015;113:305–11.
67. Kraus MJ, Seifert J, Strasser EF, Gawaz M, Schaffer TE, Rheinlaender J. Comparative morphology analysis of live blood platelets using scanning ion conductance and robotic dark-field microscopy. Platelets. 2016;27:541–6.
68. Seifert J, Rheinlaender J, Lang F, Gawaz M, Schaffer TE. Thrombin-induced cytoskeleton dynamics in spread human platelets observed with fast scanning ion conductance microscopy. Sci Rep. 2017;7:4810.
69. Vogel S, Bodenstein R, Chen Q, Feil S, Feil R, Rheinlaender J, et al. Platelet-derived HMGB1 is a critical mediator of thrombosis. J Clin Invest. 2015;125:4638–54.
70. Sauter RJ, Sauter M, Reis ES, Emschermann FN, Nording H, Ebenhoch S, et al. A functional relevance of the anaphylatoxin receptor C3aR for platelet function and arterial thrombus formation marks an intersection point between innate immunity and thrombosis. Circulation. 2018;138(16):1720–35.
71. Zhukov A, Richards O, Ostanin V, Korchev Y, Klenerman D. A hybrid scanning mode for fast scanning ion conductance microscopy (SICM) imaging. Ultramicroscopy. 2012;121:1–7.
72. Carr ME Jr, Zekert SL. Measurement of platelet-mediated force development during plasma clot formation. Am J Med Sci. 1991;302:13–8.
73. Carr Jr ME. Development of platelet contractile force as a research and clinical measure of platelet function. Cell Biochem Biophys. 2003;38:55–78.
74. Roca-Cusachs P, Conte V, Trepat X. Quantifying forces in cell biology. Nat Cell Biol. 2017;19:742–51.
75. Ribeiro AJ, Denisin AK, Wilson RE, Pruitt BL. For whom the cells pull: Hydrogel and micropost devices for measuring traction forces. Methods. 2016;94:51–64.
76. Schwarz US, Soine JR. Traction force microscopy on soft elastic substrates: a guide to recent computational advances. Biochim Biophys Acta. 2015;1853:3095–104.
77. Plotnikov SV, Sabass B, Schwarz US, Waterman CM. High-resolution traction force microscopy. Methods Cell Biol. 2014;123:367–94.
78. Zundel M, Ehret AE, Mazza E. Factors influencing the determination of cell traction forces. PLoS ONE. 2017;12:e0172927.
79. Style RW, Boltyanskiy R, German GK, Hyland C, MacMinn CW, Mertz AF, et al. Traction force microscopy in physics and biology. Soft Matter. 2014;10:4047–55.
80. Osdoit S, Rosa JP. Fibrin clot retraction by human platelets correlates with alpha(IIb)beta(3) integrin-dependent protein tyrosine dephosphorylation. J Biol Chem. 2001;276:6703–10.
81. Muthard RW, Diamond SL. Blood clots are rapidly assembled hemodynamic sensors: flow arrest triggers intraluminal thrombus contraction. Arterioscler Thromb Vasc Biol. 2012;32:2938–45.
82. Schwarz Henriques S, Sandmann R, Strate A, Koster S. Force field evolution during human blood platelet activation. J Cell Sci. 2012;125:3914–20.
83. Qiu Y, Brown AC, Myers DR, Sakurai Y, Mannino RG, Tran R, et al. Platelet mechanosensing of substrate stiffness during clot formation mediates adhesion, spreading, and activation. Proc Natl Acad Sci U S A. 2014;111:14430–5.
84. Hanke J, Probst D, Zemel A, Schwarz US, Koster S. Dynamics of force generation by spreading platelets. Soft Matter. 2018;14: 6571–81.

85. Kim OV, Litvinov RI, Alber MS, Weisel JW. Quantitative structural mechanobiology of platelet-driven blood clot contraction. Nat Commun. 2017;8:1274.
86. Myers DR, Qiu Y, Fay ME, Tennenbaum M, Chester D, Cuadrado J, et al. Single-platelet nanomechanics measured by high-throughput cytometry. Nat Mater. 2017;16:230–5.
87. Gupta M, Kocgozlu L, Sarangi BR, Margadant F, Ashraf M, Ladoux B. Micropillar substrates: a tool for studying cell mechanobiology. Methods Cell Biol. 2015;125:289–308.
88. Sniadecki NJ, Han SJ, Ting LH, Feghhi S. Micropatterning on micropost arrays. Methods Cell Biol. 2014;121:61–73.
89. Tan JL, Tien J, Pirone DM, Gray DS, Bhadriraju K, Chen CS. Cells lying on a bed of microneedles: an approach to isolate mechanical force. Proc Natl Acad Sci U S A. 2003;100:1484–9.
90. Han SJ, Bielawski KS, Ting LH, Rodriguez ML, Sniadecki NJ. Decoupling substrate stiffness, spread area, and micropost density: a close spatial relationship between traction forces and focal adhesions. Biophys J. 2012;103:640–8.
91. Song J, Shawky JH, Kim Y, Hazar M, LeDuc PR, Sitti M, et al. Controlled surface topography regulates collective 3D migration by epithelial-mesenchymal composite embryonic tissues. Biomaterials. 2015;58:1–9.
92. Liang XM, Han SJ, Reems JA, Gao D, Sniadecki NJ. Platelet retraction force measurements using flexible post force sensors. Lab Chip. 2010;10:991–8.
93. Feghhi S, Tooley WW, Sniadecki NJ. Nonmuscle myosin IIA regulates platelet contractile forces through rho kinase and myosin light-chain kinase. J Biomech Eng. 2016;138:1045061–4.
94. Feghhi S, Munday AD, Tooley WW, Rajsekar S, Fura AM, Kulman JD, et al. Glycoprotein Ib-IX-V complex transmits cytoskeletal forces that enhance platelet adhesion. Biophys J. 2016;111:601–8.
95. Klein F, Striebel T, Fischer J, Jiang Z, Franz CM, von Freymann G, et al. Elastic fully three-dimensional microstructure scaffolds for cell force measurements. Adv Mater. 2010;22:868–71.
96. Palankar R, Denker C, Varma M, Münzenberg M, Greinacher A. Deformable nano and microstructures for quantifying platelet contractile forces and platelet cytoskeletal mechanics. Hamostaseologie. 2018;38:A2–A91.
97. Otto O, Rosendahl P, Mietke A, Golfier S, Herold C, Klaue D, et al. Real-time deformability cytometry: on-the-fly cell mechanical phenotyping. Nat Methods. 2015;12:199–202, 4 p following.
98. Otto O, Rosendahl P, Golfier S, Mietke A, Herbig M, Jacobi A, et al. Real-time deformability cytometry as a label-free indicator of cell function. Conf Proc IEEE Eng Med Biol Soc. 2015;2015:1861–4.
99. Mietke A, Otto O, Girardo S, Rosendahl P, Taubenberger A, Golfier S, et al. Extracting cell stiffness from real-time deformability cytometry: theory and experiment. Biophys J. 2015;109:2023–36.
100. Urbanska M, Rosendahl P, Krater M, Guck J. High-throughput single-cell mechanical phenotyping with real-time deformability cytometry. Methods Cell Biol. 2018;147:175–98.

How to cite this article: Sachs L, Denker C, Greinacher A, Palankar R. Quantifying single-platelet biomechanics: An outsider's guide to biophysical methods and recent advances. *Res Pract Thromb Haemost*. 2020;4:386–401. https://doi.org/10.1002/rth2.12313

9.2. Article 2: *Ex vivo* anticoagulants affect human blood platelet biomechanics with implications for high-throughput functional mechanophenotyping.

Sachs, L.; Wesche, J.; Lenkeit, L.; Greinacher, A.; Bender, M.; Otto, O.; Palankar, R. *Ex vivo* anticoagulants affect human blood platelet biomechanics with implications for high-throughput functional mechanophenotyping. *Communications biology* 2022, 5 (1), 86. DOI: 10.1038/s42003-021-02982-6.

Published: 21 January 2022

Supplementary Information are available at https://www.nature.com/articles/s42003-021-02982-6#Sec19

communications biology

ARTICLE

https://doi.org/10.1038/s42003-021-02982-6 OPEN

Ex vivo anticoagulants affect human blood platelet biomechanics with implications for high-throughput functional mechanophenotyping

Laura Sachs[1], Jan Wesche[1], Lea Lenkeit[1], Andreas Greinacher[1], Markus Bender[2], Oliver Otto[3,4]✉ & Raghavendra Palankar[1]✉

Inherited platelet disorders affecting the human platelet cytoskeleton result in increased bleeding risk. However, deciphering their impact on cytoskeleton-dependent intrinsic biomechanics of platelets remains challenging and represents an unmet need from a diagnostic and prognostic perspective. It is currently unclear whether ex vivo anticoagulants used during collection of peripheral blood impact the mechanophenotype of cellular components of blood. Using unbiased, high-throughput functional mechanophenotyping of single human platelets by real-time deformability cytometry, we found that ex vivo anticoagulants are a critical pre-analytical variable that differentially influences platelet deformation, their size, and functional response to agonists by altering the cytoskeleton. We applied our findings to characterize the functional mechanophenotype of platelets from a patient with Myosin Heavy Chain 9 (*MYH9*) related macrothrombocytopenia. Our data suggest that platelets from *MYH9* p.E1841K mutation in humans affecting platelet non-muscle myosin heavy chain IIa (NMMHC-IIA) are biomechanically less deformable in comparison to platelets from healthy individuals.

[1] Institute for Immunology and Transfusion Medicine, University Medicine Greifswald, Fleischmannstr.8, 17475 Greifswald, Germany. [2] Institute of Experimental Biomedicine - Chair I, University Hospital and Rudolf Virchow Center, Würzburg, Germany. [3] Zentrum für Innovationskompetenz – Humorale Immunreaktionen bei Kardiovaskulären Erkrankungen, Universität Greifswald, Fleischmannstr. 42, 17489 Greifswald, Germany. [4] Deutsches Zentrum für Herz-Kreislauf-Forschung e.V., Standort Greifswald, Universitätsmedizin Greifswald, Fleischmannstr. 42, 17489 Greifswald, Germany. ✉email: oliver.otto@uni-greifswald.de; raghavendra.palankar@med.uni-greifswald.de

Blood platelets are anucleate, discoidal multifunctional cellular fragments (1–3 µm in diameter) generated by bone marrow megakaryocytes and released into blood circulation[1]. On exposed extracellular matrix at the sites of the vascular breach, rapid recruitment of platelets is essential for forming a primary hemostatic plug. However, under pathological procoagulatory conditions, platelets contribute to intravascular thrombosis, a leading cause of cardiovascular complications and morbidities[2–4]. Platelets function as complex biological sensor and actuator units that respond to a broad spectrum of physicochemical stimuli via ligand-receptor-mediated interactions (i.e., outside-in signaling) and mechanotransduction events (i.e., both outside-in and inside-out signaling)[5–7]. This complex interplay results in the coordinated regulation of signaling kinetics, including cytoskeletal remodeling that initiates platelet adhesion, activation, spreading, and platelet contraction[8].

It has been well established that cytoskeleton-dependent biomechanics governs diverse aspects of platelet function during hemostasis and thrombosis[9,10]. Beyond this, the significance of platelet cytoskeletal integrity and its functional role in platelet-mediated innate immune responses such as mechano-scavenging, host defense during platelet-bacteria interactions, and vascular surveillance is emerging[11–13]. Recent studies have also demonstrated changes in platelet biomechanical properties, and subsequent defective mechanotransduction may serve as a biophysical marker for assessing bleeding risk in individuals with inherited platelet cytoskeletal defects[14]. Thus, deciphering cytoskeleton-dependent intrinsic biomechanical properties of platelets is highly desirable for broadening our understanding of the functional role of platelets in physiological and pathological processes and from translationally relevant diagnostic and prognostic perspectives[6,10].

Currently, a wide array of biophysical methods is available for the investigation of platelet biomechanics. They include micropipette aspiration[15–17], atomic force microscopy[18–20], scanning ion conductance microscopy[21,22], traction force microscopy[23,24], including flexible micropost arrays[25–27]. Although these methods have proven valuable in advancing our insights into platelet biomechanics, these are technically demanding, labor-intensive, and mostly limited to analysis of adherent platelets[28]. Besides, these methods also lack throughput, which results in implicit bias during single platelet measurements resulting from undersampling of innate heterogeneity found in donor platelet populations[29–31].

The recently introduced on-chip, high-throughput real-time fluorescence and deformability cytometry (RT-FDC) has rapidly emerged as a biophysical method to address these challenges[32,33]. RT-FDC enables continuous on-the-fly mechanophenotyping of single cells at real-time analysis rates exceeding 1000 cells/s combined with the capability of achieving molecular specificity through the application of fluorescent probes, which further opens up exciting possibilities[34–37].

However, on-chip deformability cytometry and other biophysical methods have not been well standardized regarding preanalytical variability in sample preparation of cells from peripheral blood, including platelets[38]. Specifically, it is unclear whether different ex vivo anticoagulants commonly used during blood sampling influence blood platelet biomechanics. Using high-throughput functional mechanophenotyping of single platelets in RT-FDC, here we demonstrate that ex vivo anticoagulants differentially impact intrinsic biomechanical properties (i.e., deformation and size) of human platelets. Besides this, we establish a link between platelet functional mechanophenotype, particularly their deformation and associated activation profiles as well as functional response in resting platelets and after activation with platelet agonist, respectively, in different ex vivo anticoagulants. We explain these findings by showing that ex vivo anticoagulants and platelet activation alter the content and subcellular organization of major platelet cytoskeletal components such as actin cytoskeleton and marginal band tubulin ring. Furthermore, in a potentially diagnostically relevant development, using *MYH9* related macrothrombocytopenia as a model for an inherited human platelet cytoskeletal disorder, affecting platelet nonmuscle myosin heavy chain IIa (NMMHC-IIA), we demonstrate that the choice of ex vivo anticoagulant may strongly impact the outcomes of mechanophenotyping.

Results

Ex vivo anticoagulants affect human platelet deformation and size. We first evaluated the effects of ex vivo anticoagulants on platelet deformation, and their corresponding size in live non-stimulated (i.e., resting) platelets in PRP by RT-FDC prepared from blood collected in ACD-A, Na-Citrate, K_2-EDTA, Li-Heparin, and r-Hirudin (Fig. 1a). Non-stimulated platelets showed deformation of 0.127 ± 0.033 (mean ± SD, $n = 6$ donors) in ACD-A, 0.111 ± 0.025 in Na-Citrate, and 0.1 ± 0.023 in r-Hirudin, which was higher in comparison to the lower deformation of platelets at 0.071 ± 0.016 observed in Li-Heparin and 0.037 ± 0.01 in K_2-EDTA. (Fig. 1b and Supplementary Fig. 4 for statistical distribution plots of individual donors). Assessment of corresponding platelet size in different ex vivo anticoagulants from non-stimulated platelets revealed differences in platelet size measuring at 5.035 ± 0.49 µm^2 (mean ± SD, $n = 6$ donors) in ACD-A in comparison to K_2-EDTA and Li-Heparin where platelets were smaller in size measuring at 4.158 ± 0.241 and 4.337 ± 0.344 µm^2, respectively (Fig. 1c and Supplementary Fig. 5 for statistical distribution plots of individual donors).

Next, to test whether agonist-induced platelet activation leads to measurable changes in platelet deformation and their corresponding size depending on the type of ex vivo anticoagulant, TRAP-6 was used. Platelet activation by TRAP-6 resulted in a noticeable decrease in platelet deformation and a concomitant reduction in platelet size in all ex vivo anticoagulants except for K_2-EDTA (Fig. 1d–f). Assessment of fold change in platelet deformation before and after TRAP-6 stimulation showed a decrease in platelet deformation by a factor of 2.76 ± 0.64 (mean ± SD, $n = 6$ donors) in ACD-A, 2.58 ± 0.49 in Na-Citrate, 1.72 ± 0.47 Li-Heparin, and 2.27 ± 0.45 in r-Hirudin (Fig. 1g). On the contrary, in K_2-EDTA, TRAP-6 stimulation resulted in a minimal fold change in platelet deformation by a factor of 1.14 ±0.33 (Fig. 1g). Similarly, platelet size decreased upon TRAP-6 stimulation by a factor of 1.28 ± 0.13 (mean ± SD, $n = 6$ donors) in ACD-A, 1.14 ± 0.14 in Na-Citrate and 1.18 ± 0.16 in r-Hirudin, while it remained unchanged at 0.98 ± 0.08 in K_2-EDTA and 1.04 ± 0.04 in Heparin (Fig. 1h). Furthermore, the changes in platelet shape observed in the RT-FDC differed between the ex vivo anticoagulants in non-stimulated and TRAP-6 stimulated platelets (Supplementary Fig. 6 representative bright-field images of single platelets in measurement channel overlaid with contour).

Platelet deformation in response to platelet activation. In non-stimulated platelets, basal CD62P surface expression was not altered between all ex vivo anticoagulants even though platelets in K_2-EDTA exhibited decreased deformation relative to other ex vivo anticoagulants (Fig. 2a–c). Upon activation of platelets by TRAP-6, a decrease in platelet deformation with a concomitant increase in CD62P surface expression and CD62P % positive platelets was observed in all ex vivo anticoagulants except in K_2-EDTA (Fig. 2d–f). Assessment of fold change in CD62P expression levels showed an increase by a factor of 18.19 ± 8.88 (mean ± SD, $n = 6$ donors) in ACD-A, 21.48 ± 8.54 in Na-Citrate, 9.82 ± 7.78 in Li-Heparin, and

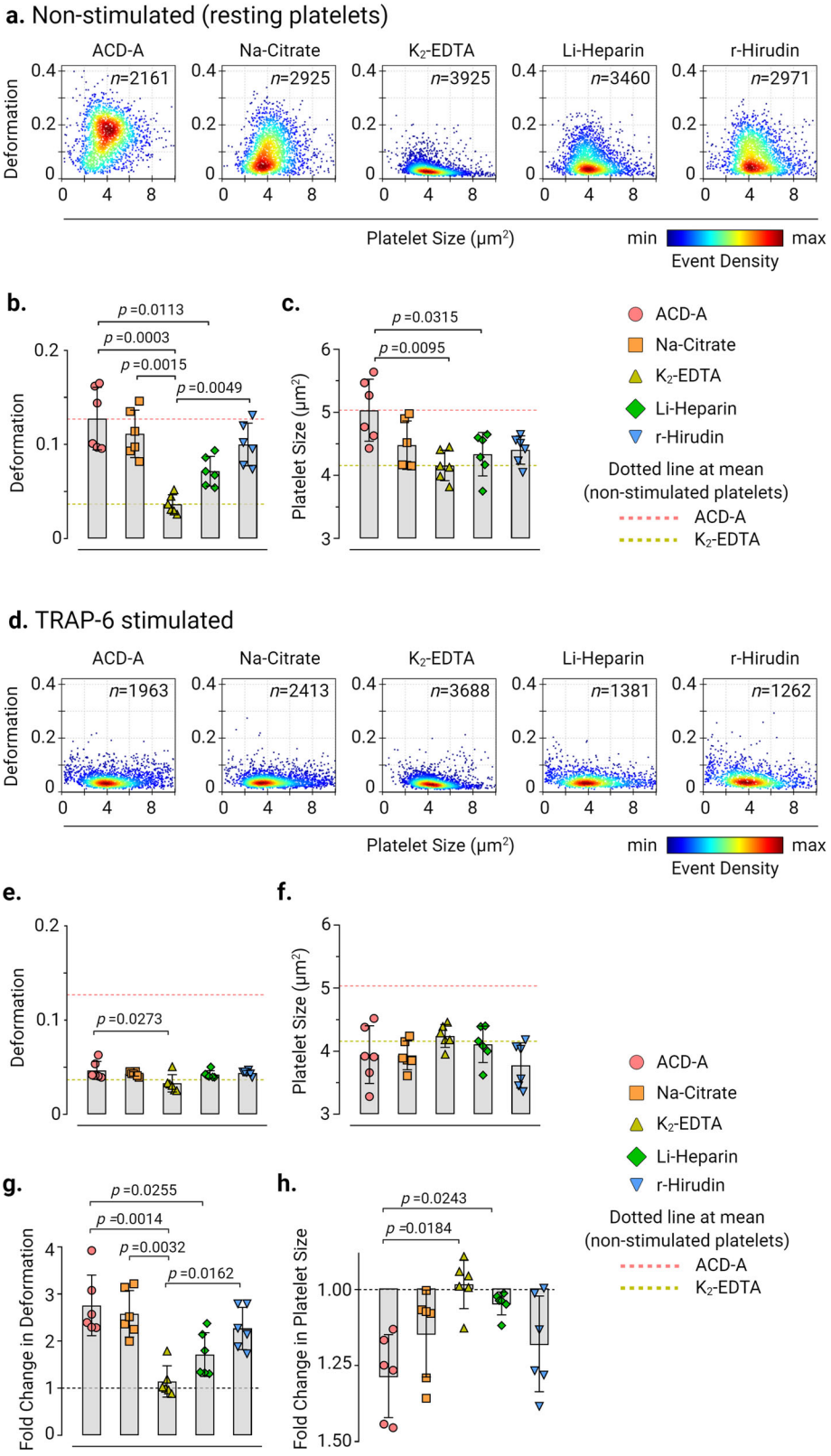

Fig. 1 Ex vivo anticoagulants influence the deformation and size of human platelets. Representative KDE scatter plots of deformation and size of live single platelets in PRP prepared from whole blood collected in different ex vivo anticoagulants from **a** non-stimulated (i.e., resting) platelets and **d** after stimulation with TRAP-6 (n = number of single platelets from the same donor measured for each condition). Color coding of event density in scatter plots indicates a linear density scale from min (blue) to max (dark red). Summary data points show the median values of individual donors, and bar plots show mean ± SD of platelet deformation and size from non-stimulated (**b**) and (**c**) and TRAP-6 stimulated platelets (**e**) and (**f**), respectively ($n = 6$ donors). Fold change in platelet deformation and size upon stimulation with TRAP-6 are shown in (**g**) and (**h**), respectively, where dotted control baseline = 1 ($n = 6$ donors). Statistical analysis: mixed-effects model (restricted maximum likelihood, REML) followed by Tukey's multiple comparisons tests, with single pooled variance and $p < 0.05$ was considered significant.

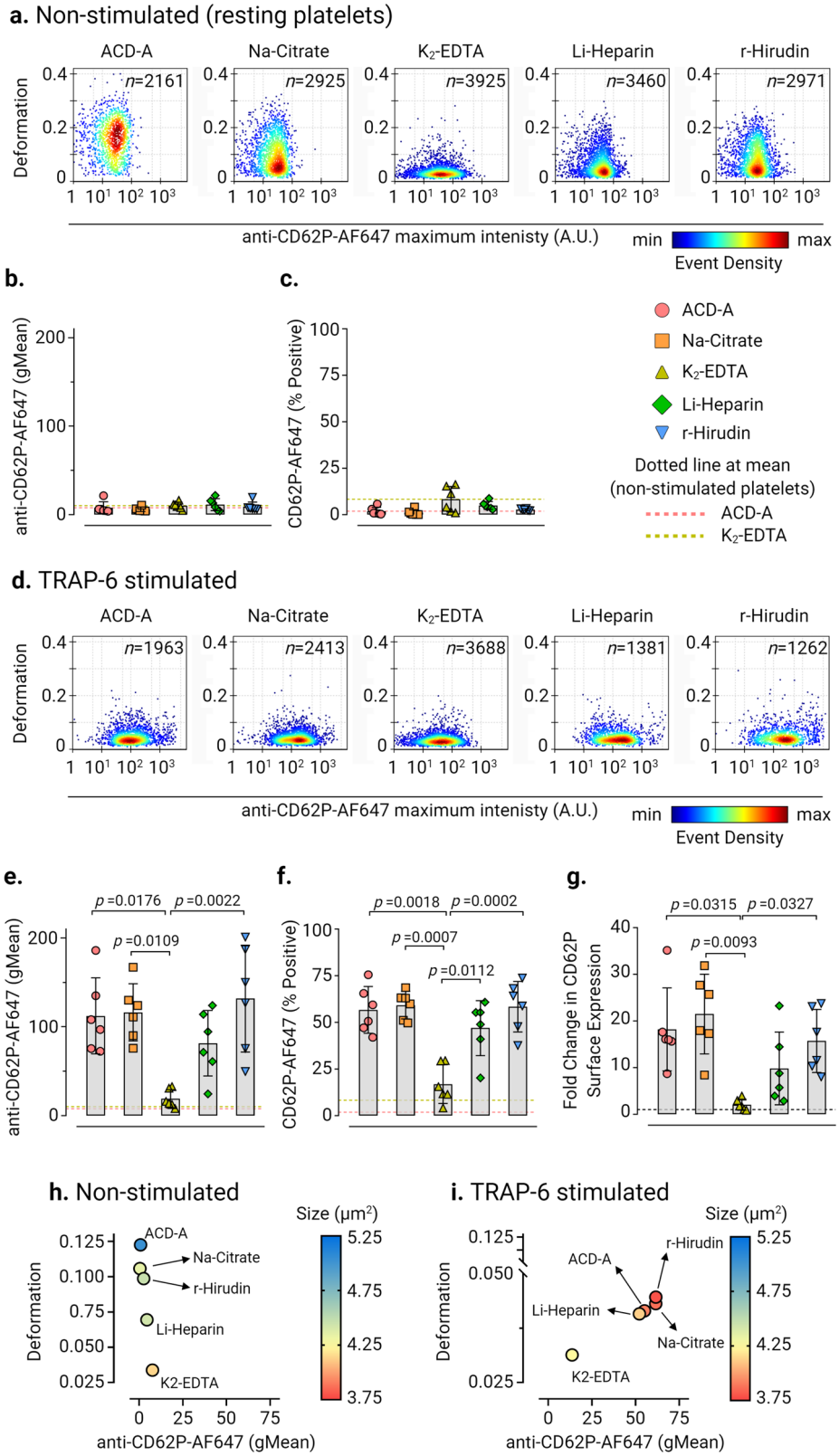

15.72 ± 6.76 in r-Hirudin in comparison to a fold change of 2.03 ± 1.16 in K_2-EDTA (Fig. 2g). Multivariate analysis of continuous variables from RT-FDC data from non-stimulated and TRAP-6 stimulated platelets (Fig. 2h, i) further confirmed platelet deformation, size, and CD62P expression is strongly affected in K_2-EDTA.

Next, we assessed conformational changes in platelet integrin $\alpha_{IIb}\beta_3$ as a marker for platelet activation by PAC-1 antibody binding (Fig. 3). Baseline activation levels of integrin $\alpha_{IIb}\beta_3$ in non-stimulated platelets (Fig. 3a–c) were highest in Li-Heparin (PAC-1-FITC gMean of 82.48 ± 12.16 and PAC-1-FITC % positive platelets at 36.02 ± 9.3%, mean ± SD, $n = 6$ donors). In contrast, K_2-EDTA showed the lowest basal activation of integrin $\alpha_{IIb}\beta_3$ of all ex vivo anticoagulants. In TRAP-6 stimulated platelets, PAC-1-FITC binding and PAC-1-FITC % positive

Fig. 2 Platelet deformation and the corresponding CD62P surface expression upon activation in different ex vivo anticoagulants. Representative KDE scatter plots of platelet deformation and CD62P expression on single platelets expression (plotted on log10 scale of maximum intensity in arbitrary units (A.U.) of anti-CD62P-AlexaFluor647 antibody) in PRP different ex vivo anticoagulants in **a** non-stimulated (i.e., resting) platelets and **d** upon TRAP-6 stimulation (n = number of single platelets from the same donor measured for each condition). Color coding of event density in scatter plots indicates a linear density scale from min (blue) to max (dark red). Summary graphs show of median values of individual donors, while bar graphs show mean ± SD of geometric mean fluorescence intensity (gMean) of CD62P expressing platelets (**b**) and (**e**) and percent positive platelets (**c**) and (**f**) above the cut-off of 5000 events or 10 min in non-stimulated and TRAP-6 stimulated platelets, respectively (n = 6 donors). Fold change in CD62P surface expression on platelets upon stimulation with TRAP-6 are shown in (**g**) where dotted control baseline = 1 (n = 6 donors). Multivariate analysis plots of continuous variables from RT-FDC, (**h**) and (**i**) of non-stimulated and TRAP-6 stimulated platelets, respectively, displaying the relationships between platelet deformation, size, and related CD62P surface expression levels in different ex vivo anticoagulants. (Data represents median values of individual variables from n = 6 donors). Statistical analysis: mixed-effects model (restricted maximum likelihood, REML) followed by Tukey's multiple comparisons tests, with single pooled variance and $p < 0.05$ was considered significant.

platelets increased significantly ($p < 0.0001$) in all ex vivo anticoagulants in comparison to K_2-EDTA (Fig. 3d–f). Furthermore, fold change in PAC-1 binding to platelets after TRAP-6 stimulation increased by a factor of 2.86 ± 0.82 (mean ± SD, n = 6 donors) in ACD-A, 3.39 ± 0.9 in Na-Citrate, 2.64 ± 0.7 in Li-Heparin, and 3.55 ± 0.98 in r-Hirudin in comparison to non-stimulated platelets, but did not increase in K_2-EDTA (Fig. 3g). Also, multivariate analysis of continuous variables from RT-FDC data from non-stimulated and TRAP-6 stimulated platelets (Fig. 3h, i) revealed together with platelet deformation, size, and PAC-1 binding is strongly affected in K_2-EDTA. Our results concerning the reduced binding of PAC-1 antibody to platelet integrin αIIbβ3 are consistent with previous observations in potent chelators of divalent cations such as EDTA[39].

Decreased platelet deformation is an indicator of alterations in platelet cytoskeletal organizations and F-actin content. Fluorescence CLSM imaging and subsequent line profile analysis of non-stimulated platelets in ACD-A, Na-Citrate, Li-Heparin, and r-Hirudin showed discoidal morphology, a uniform intracellular distribution of F-actin (Phalloidin, green), and a well-defined subcortical marginal band microtubule ring (α-tubulin, edge-to-edge fluorescence intensity signal in magenta) (Fig. 4a and Supplementary Fig. 8). In contrast, platelets in K_2-EDTA platelets lost their discoidal shape and were comparatively smaller. Besides, we observed a significant increase ($p < 0.001$) in subcortical localization of F-actin (Fig. 4b and Supplementary Fig. 8) and coiling of microtubule ring indicated by white arrowhead in grayscale subfigures in Fig. 4a and edge-to-edge fluorescence line profile intensity in Fig. 4c and Supplementary Fig. 8 for K_2-EDTA. Upon TRAP-6 stimulation, platelets showed substantial morphological changes compared to their non-stimulated counterparts (Fig. 4d). Line profile analysis of fluorescence intensities further revealed a significantly increased F-actin localization ($p < 0.001$) at subcortical regions and a decrease in edge-to-edge coiling of microtubule ring in all ex vivo anticoagulants except for K_2-EDTA (Fig. 4e, f and Supplementary Fig. 8).

Next, we analyzed the total F-actin content in non-stimulated and TRAP-6 stimulated platelets in different ex vivo anticoagulants by flow cytometry (Fig. 5a, b and Supplementary Fig. 7). We observed a significantly higher F-actin content in non-stimulated platelets in K_2-EDTA (Phalloidin AF647 fluorescence gMean: 162.2 ± 30.47, mean ± CD from $n = 6$ donors) in comparison to non-stimulated platelets measuring at 110.7 ± 32.11, $p = 0.036$, in ACD-A, 107 ± 23.86, $p = 0.0285$ in Na-Citrate and 94.24 ± 28.91, $p = 0.0023$ in r-Hirudin (Fig. 5a). The basal F-actin content of platelets in Li-Heparin was found to be relatively higher (Phalloidin AF647 fluorescence gMean: 146.5 ± 9, mean ± CD from $n = 6$ donors) than in ACD-A and Na-Citrate, statistically significant differences ($p = 0.024$) were apparent between Li-Heparin and r-Hirudin in non-stimulated platelets (Fig. 5a). TRAP-6 stimulation resulted in the increase of total F-actin in platelets by a factor of 2.18 ± 0.28 in ACD-A, 2.13 ± 0.38 in Na-Citrate, and 2.1 ± 0.27 in r-Hirudin. In contrast, only a minor change in total F-actin content by a factor of 1.49 ± 0.26 in Li-Heparin and 0.96 ±0.14 in K_2-EDTA was observed (Fig. 5b, c and Supplementary Fig. 7).

Next, a multivariate analysis of continuous variables was performed to verify whether the changes in actin polymerization status, i.e., total F-actin content measured by flow cytometry, reflect the observed differences in platelet deformation and their corresponding size by RT-FDC in different ex vivo anticoagulants. As shown, non-stimulated (i.e., resting) platelets (Fig. 5d) were found to deform more with low basal F-actin content in ACD-A, Na-Citrate r-Hirudin than those in Li-Heparin. Furthermore, platelets in K_2-EDTA deformed least with higher basal F-actin content and smallest in size. Under TRAP-6 stimulation, except in K_2-EDTA, platelets in all ex vivo anticoagulants showed decreased deformation, a smaller size, and increased total F-actin content (Fig. 5e).

Actin disassembly by LatB increases platelet deformation. Next, we used latrunculin B (LatB) an actin polymerization inhibitor, to gain mechanistic insights into whether impairing actin polymerization influences biomechanical deformation and functional response of platelets in different ex vivo anticoagulants (Fig. 6a–d and Supplementary Fig. 9). In non-stimulated platelets, LatB significantly increased ($p < 0.001$) platelet deformation in all ex vivo anticoagulants compared to their respective vehicle control. Similarly, in contrast to the vehicle control (6e) in the presence of LatB, TRAP-6 stimulated platelets deformed more (Fig. 6g). Furthermore, only in ACD-A, LatB induced increase in platelet deformation was higher in resting platelets in all donors (Fig. 6f) compared to all ex vivo anticoagulants. In addition, in the presence of LatB basal CD62P surface expression and PAC-1 binding were unaltered in all ex vivo anticoagulants (Supplementary Fig. 9a, c). Although after TRAP-6 stimulation, LatB treated platelets in all donors showed a markedly increased deformation, however, only in K_2-EDTA platelets deformation was significant ($p = 0.0066$) compared to other ex vivo anticoagulants (Fig. 6h). Furthermore, TRAP-6 induced functional response of LatB treated platelets showed reduced CD62P surface expression in all ex vivo anticoagulants compared to respective vehicle controls but remained unchanged in K_2-EDTA (Supplementary Fig. 9b).

ACD-A, but not K_2-EDTA, allows mechanophenotyping of *MYH9* related disease mutations in human platelets. By RT-FDC, we next analyzed platelets from an individual with *MYH9* p.E1841K mutation in the rod region of NMMHC-IIA, an essential platelet cytoskeletal protein[40]. In ACD-A, *MYH9* p.E1841K platelets

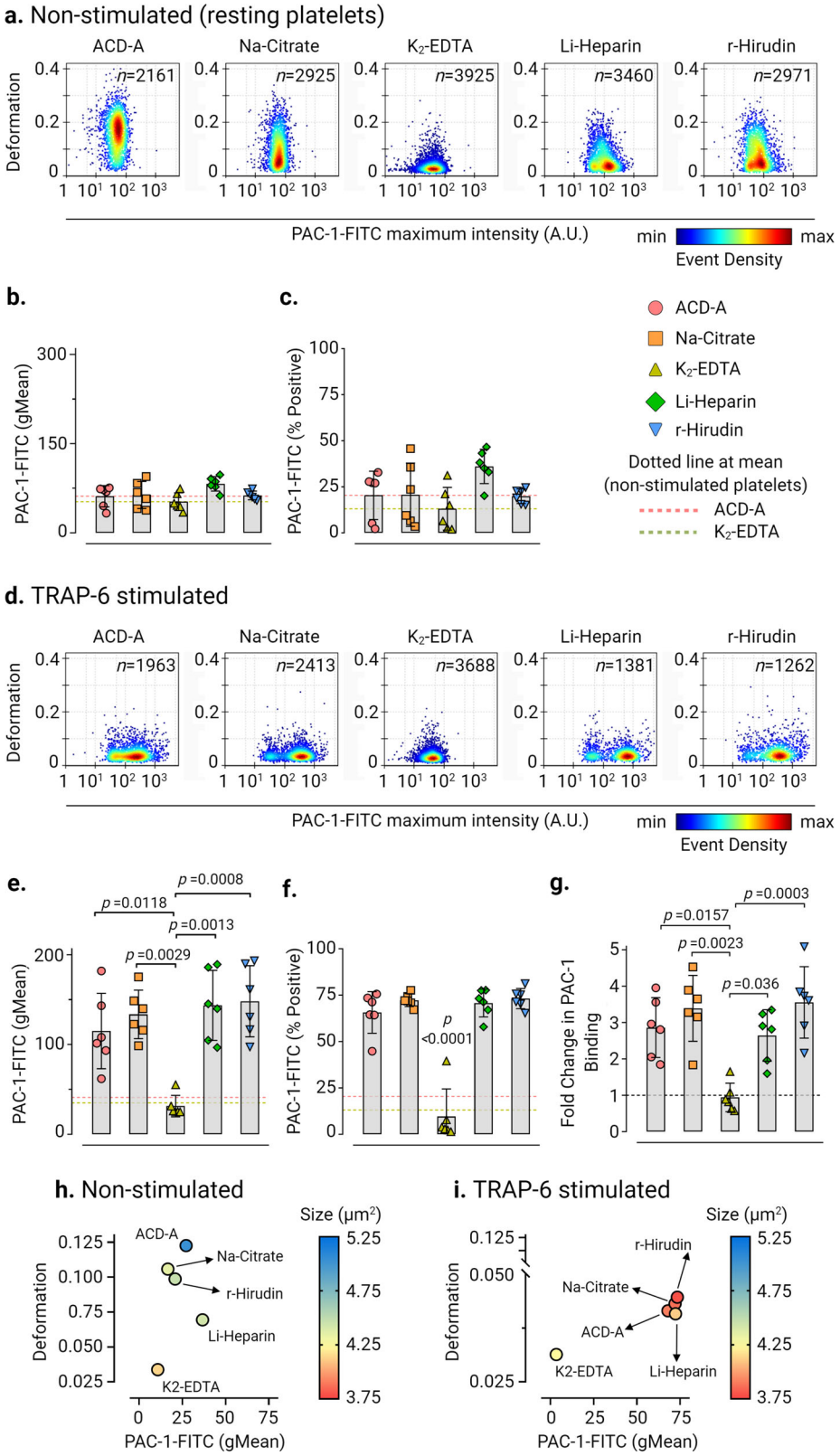

in comparison to platelets from healthy controls deform less (0.068, median $n = 955$ single platelets vs. 0.122, median $n = 2326$ single platelets) and are larger (5.77 μm², median $n = 955$ single platelets vs. 4.05 μm², median $n = 2326$ single platelets) (Fig. 7a and Supplementary Fig. 10a) under non-stimulated (i.e., resting) conditions. With TRAP-6 stimulation, platelets from the individual with *MYH9* p.E1841K in ACD-A deform further less (0.036, median $n = 1112$ single platelets), but intriguingly their size increased (6.585 μm², median $n = 1112$ single platelets). In contrast, the platelets from the healthy individual showed decreased deformation (0.0455, median $n = 720$ single platelets) and size (2.595 μm²) (Fig. 7b and Supplementary Fig. 10b). On the other hand, in K_2-EDTA, non-stimulated healthy control platelets showed ≈ 3-fold decreased deformation (0.036, median $n = 1960$ single platelets) and while *MYH9* p.E1841K

Fig. 3 Platelet deformation and activation-induced exposure of the conformational epitope of the integrin αIIbβ3 is strongly influenced by ex vivo anticoagulants. Representative KDE scatter plots of platelet deformation and their corresponding activation status as a readout for binding of integrin αIIbβ3 specific ligand-mimetic PAC-1 antibody (plotted on log10 scale of maximum intensity in arbitrary units (AU) of PAC-1-FITC antibody) on single platelets in different ex vivo anticoagulants in (**a**) non-stimulated (i.e., resting) platelets and upon stimulation TRAP-6 (**d**) from a single donor (n= number of single platelets from the same donor measured for each condition). Color coding of event density in scatter plots indicates a linear density scale from min (blue) to max (dark red). Summary graphs show of median values of individual donors, while bar graphs show mean ± SD of geometric mean fluorescence intensity (gMean) of PAC-1-FITC antibody bound to platelets (**b**) and (**e**) and PAC-1-FITC antibody percent positive platelets (**c**) and (**f**) above the cut-off of 5000 events or 10 min in non-stimulated and TRAP-6 stimulated platelets, respectively ($n = 6$ donors). Fold change in PAC-1 Binding on platelets upon stimulation with TRAP-6 from six donors are shown in (**g**) where dotted control baseline = 1 ($n = 6$ donors). Multivariate analysis plots of continuous variables from RT-FDC, (**h**) and (**i**) of non-stimulated and TRAP-6 stimulated platelets, respectively, displaying the relationships between platelet deformability, size, and PAC-1 antibody biding to integrin αIIbβ3 in different ex vivo anticoagulants. (Data represents median values of individual variables from $n = 6$ donors). Statistical analysis: mixed-effects model (restricted maximum likelihood, REML) followed by Tukey's multiple comparisons tests, with single pooled variance and $p < 0.05$ was considered significant.

platelets showed a ≥ 3-fold decreased deformation (0.0195, median $n = 2406$ single platelets) in comparison to their counterparts in ACD-A (Fig. 7c, e and Supplementary Fig. 11a).

Besides, in K_2-EDTA, platelets from the healthy individual became smaller (3.27 μm^2, median $n = 1960$ single platelets). In contrast, platelets from the *MYH9* p.E1841K individual were slightly increased in their size (7.515 μm^2, median $n = 2406$ single platelets) compared to non-stimulated platelets in ACD-A. Furthermore, TRAP-6 stimulation of platelets in K_2-EDTA only resulted in minor changes in platelet deformation and size compared to their non-stimulated counterparts (Fig. 7d and Supplementary Fig. 11b). Although differences in platelet deformation and size were apparent between the platelets from *MYH9* p.E1841K patient and healthy control in ACD-A; their CD62P surface expression levels and PAC-1 binding in response to TRAP-6 were comparable (Supplementary Fig. 12 and Fig. 13).

Consistent with our observations reported above, in K_2-EDTA platelets from both *MYH9* p.E1841K patient and healthy control failed to respond to TRAP-6 (Supplementary Figs. 12 and 13). Furthermore, in ACD-A, assessment of F-actin content revealed a higher basal total F-actin content in non-stimulated platelets from *MYH9* p.E1841K patient at 192.86 (Phalloidin AF647 gMean) compared to the healthy control at 154.96, which upon TRAP-6 stimulation increased to 250.16 and 286.36, (Supplementary Fig. 14a). On the other hand, in K_2-EDTA, the basal total F-actin content in non-stimulated platelets from *MYH9* p.E1841K patient was found to be at 250.42 (Phalloidin AF647 gMean) and for healthy control at 206.6, that remained unchanged upon TRAP-6 stimulation (Supplementary Fig. 14b).

Discussion

Clinically relevant translational applications for the diagnosis of disease states by morpho-rheological and biomechanical characterization of a variety of cells by RT-DC are fast emerging. These include biomechanical differentiation for diagnosis of hereditary spherocytosis and malaria infections in peripheral blood cells[41] and in biophysical fingerprinting of primary human skeletal stem cells from bone marrow[42]. In addition, the feasibility of RT-DC in routine quality control of platelet concentrates and transplantable hematopoietic stem cells in blood banks is currently being tested[43]. More recently Kubankova et al. using RT-DC performed biomechanical fingerprinting of erythrocytes, lymphocytes, monocytes, neutrophils, and eosinophils in clinical induced by severe acute respiratory syndrome corona virus2 (COVID-19 disease)[44]. The study results showed highly deformable lymphocytes and neutrophils, increased size of monocytes, lymphocytes, and neutrophils, and the appearance of smaller and less deformable erythrocytes.

The present study shows that K_2-EDTA and Li-Heparin should not be used as ex vivo anticoagulants for studies on human platelet biomechanical properties. Platelets collected in ACD-A, Na-Citrate, or r-Hirudin may be used for biomechanical studies. Still, due to minor differences in the effects on platelets, results cannot be directly compared between platelets anticoagulated with these different anticoagulants. Platelets anticoagulated with Li-Heparin show some differences in their biomechanical characteristics compared to platelets in ACD-A, Na-Citrate, or r-Hirudin. Heparinized platelets show a two-fold higher F-actin content, decreased deformation, and higher PAC-1 expression. The most crucial difference between Li-Heparin and r-Hirudin compared to the other anticoagulants is that Li-Heparin and r-Hirudin do not chelate calcium. However, the apparent discrepancies between Li-Heparin and r-Hirudin indicate that Li-Heparin is inducing artifacts in the biomechanical properties of platelets. One explanation is the strong negative charge of heparin and its binding to αIIbβ3, which triggers αIIbβ3-mediated outside-in signals and thus initiates cytoskeletal reorganization[45,46]. Platelets collected in K_2-EDTA have the highest F-actin content under resting conditions in comparison to the other anticoagulants and show the lowest deformation. Our observations are in agreement with previous studies, which have demonstrated K_2-EDTA induced ultrastructural changes of the surface-bound canal system (narrowing and dilatation of the OCS) and an irreversible dissociation of the αIIbβ3 complexes[47–50]. It is possible that the high content of F-actin in non-stimulated and TRAP-6 stimulated platelets and the associated platelet deformation could be explained by the irreversible dissociation of the αIIbβ3 complex and the associated cytoskeletal reorganization.

To support these findings, we employed LatB, an inhibitor of actin polymerization, to provide biomechanical insights into whether impairing actin polymerization influences the biomechanical deformation and functional response of platelets in different ex vivo anticoagulants, thus providing a direct link between platelet deformability and F-actin content. Our results show that LatB increased platelet deformability in unstimulated platelets in all ex vivo anticoagulants compared with the respective vehicle control. Similarly, TRAP-6-stimulated platelets were more deformable in the presence of LatB than in the vehicle control. We also investigated the effect of actin depolymerization by LatB on the surface expression of CD62P and integrin activation by PAC-1 binding. CD62P surface expression after TRAP-6 stimulation was reduced by LatB treatment in the anticoagulants ACD-A, Li-Heparin, and r-Hirudin. In K_2-EDTA, no change in CD62P expression occurred after TRAP-6 stimulation in the vehicle control and LatB, confirming our data that CD62P expression is impaired after TRAP-6 activation in K_2-EDTA. Our results are consistent with the data of Woronowicz et al. showing that LatA (an isomer of latrunculin that binds gelsolin) inhibits alpha-granule secretion by disrupting the actin cytoskeleton[51]. We also observed a marked reduction in PAC-1 binding after LatB treatment of resting platelets with the anticoagulants

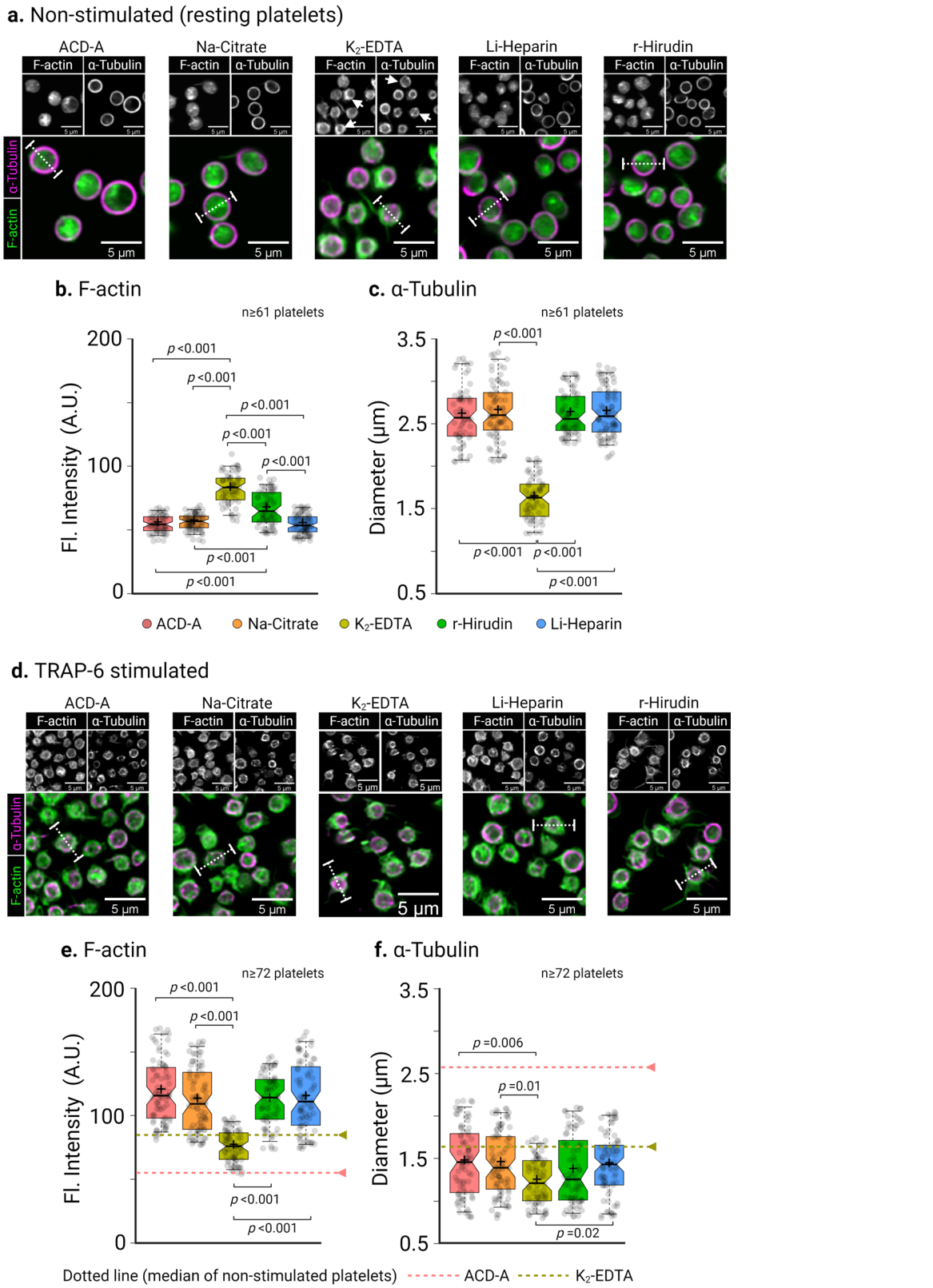

Fig. 4 Cytoskeletal organization in resting and TRAP-6 stimulated human platelets are altered in different ex vivo anticoagulants. Representative confocal laser scanning fluorescence microscopic images of F-actin (green) distribution and marginal band α-tubulin (magenta) organization of human platelets in different ex vivo anticoagulants in (**a**) non-stimulated (resting platelets) and (**d**) 10 min after TRAP-6 stimulation. Line profile fluorescence intensity distribution analysis of F-actin and edge-to-edge distance of α-tubulin (**b**) and (**c**) in non-stimulated platelets and after TRAP-6 stimulation (**e**) and (**f**). Dotted horizontal lines in (**e**) and (**f**) correspond to the median fluorescence intensity and diameter of respective parameters from non-stimulated platelets. Notch in the box plot and the plus sign depicts median and mean, respectively, and the interquartile ranges. Staggered dots in gray show the distribution of data points. Statistical assessment by Kruskal-Wallis-Test followed by Dunn's multiple comparisons test $p < 0.05$ was considered significant.

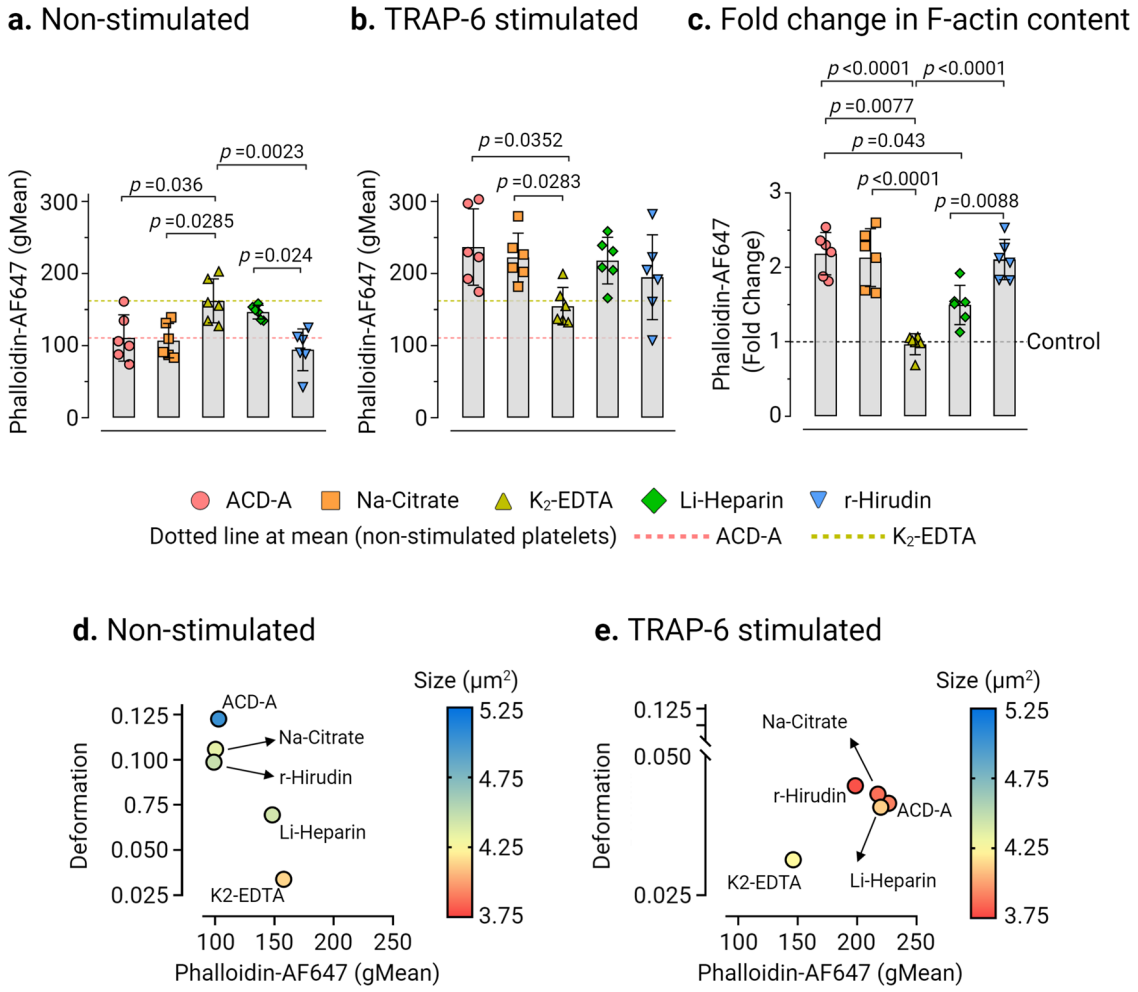

Fig. 5 The change of F-actin content in platelets is an indicator of platelet deformation. Comparison of platelet F-actin (Phalloidin AF647 fluorescence, gMean) measured by flow cytometry in **a** non-stimulated and **b** TRAP-6 stimulated platelets in different ex vivo anticoagulants. Fold change in phalloidin binding (**c**) after stimulation with TRAP-6, where control baseline = 1 and plots show mean ± SD from $n = 6$ donors. Multivariate analysis plots of continuous variables from RT-FDC and flow cytometry, (**d**) and (**e**) of non-stimulated and TRAP-6 stimulated platelets, respectively, displaying the relationships between platelet deformation, size, and the F-actin content in different ex vivo anticoagulants, shown as a measure of phalloidin binding. (Data represents median values of individual variables from $n = 6$ donors). Statistical assessment was performed by applying the mixed-effects model (restricted maximum likelihood, REML) followed by Tukey's multiple comparisons test, with single pooled variance and $p < 0.05$ was considered significant.

ACD-A, Li-Heparin, and r-Hirudin. Interestingly, an apparent decrease in PAC-1 binding is observed after TRAP-6 activation only with Li-heparin, confirming our hypothesis that Li-heparin induces cytoskeletal reorganization by binding to αIIbβ3, making platelets deform more.The difference in deformation of activated platelets between vehicle control and LatB in K_2-EDTA indicates that the increased F-actin content in resting platelets in K_2-EDTA is responsible for the increased deformation when actin polymerization is blocked by LatB, resulting in destabilization of the actin cytoskeleton.

The practical relevance of our findings is exemplified by the results obtained with *MYH9* p.E1841K platelets in ACD-A compared to K_2-EDTA. The non-stimulated platelets in ACD-A deform more than those in K_2-EDTA, even after TRAP-6 induced activation. We conclude that the anticoagulants K_2-EDTA and Li-Heparin are not suitable for the study of the human platelet cytoskeleton, while ACD-A, Na-Citrate, or r-Hirudin can be used. Concerning our reasoning behind choosing ACD-A over Na-Citrate as an ex vivo anticoagulant as a comparator to K_2-EDTA for the analysis of platelets from a patient with *MYH9* mutation in RT-FDC, there are several lines of experimental evidence which indicate ACD-A is superior to Na-Citrate in terms of maintaining platelet physiology. In practice, blood collection systems anticoagulated with Na-Citrate are primarily used for studies of plasmatic coagulation and aggregation studies. Intriguingly, Na-Citrate may induce the formation of micro-aggregates, thus leading to a decrease in platelet count over time[52,53]. On the contrary, ACD-A is a more physiological anticoagulant capable of maintaining platelet physiology and signal transduction mechanisms with minimal impact on platelet responsiveness to agonists[54]. These results may facilitate a comparison between different laboratories using shear-based deformability cytometry such as RT-FDC to address fundamental questions of platelet physiology and its relationship with biomechanical phenotype and may help to avoid artifacts when these new technologies are applied to investigate patients with platelet disorders.

Conclusions

In summary, we can conclude that K_2-EDTA and Li-Heparin influence the biomechanics of platelets by decreasing the deformation and increasing actin polymerization of non-stimulated human platelets. It is recommended for the examination of the human platelet cytoskeleton to select an ex vivo anticoagulant

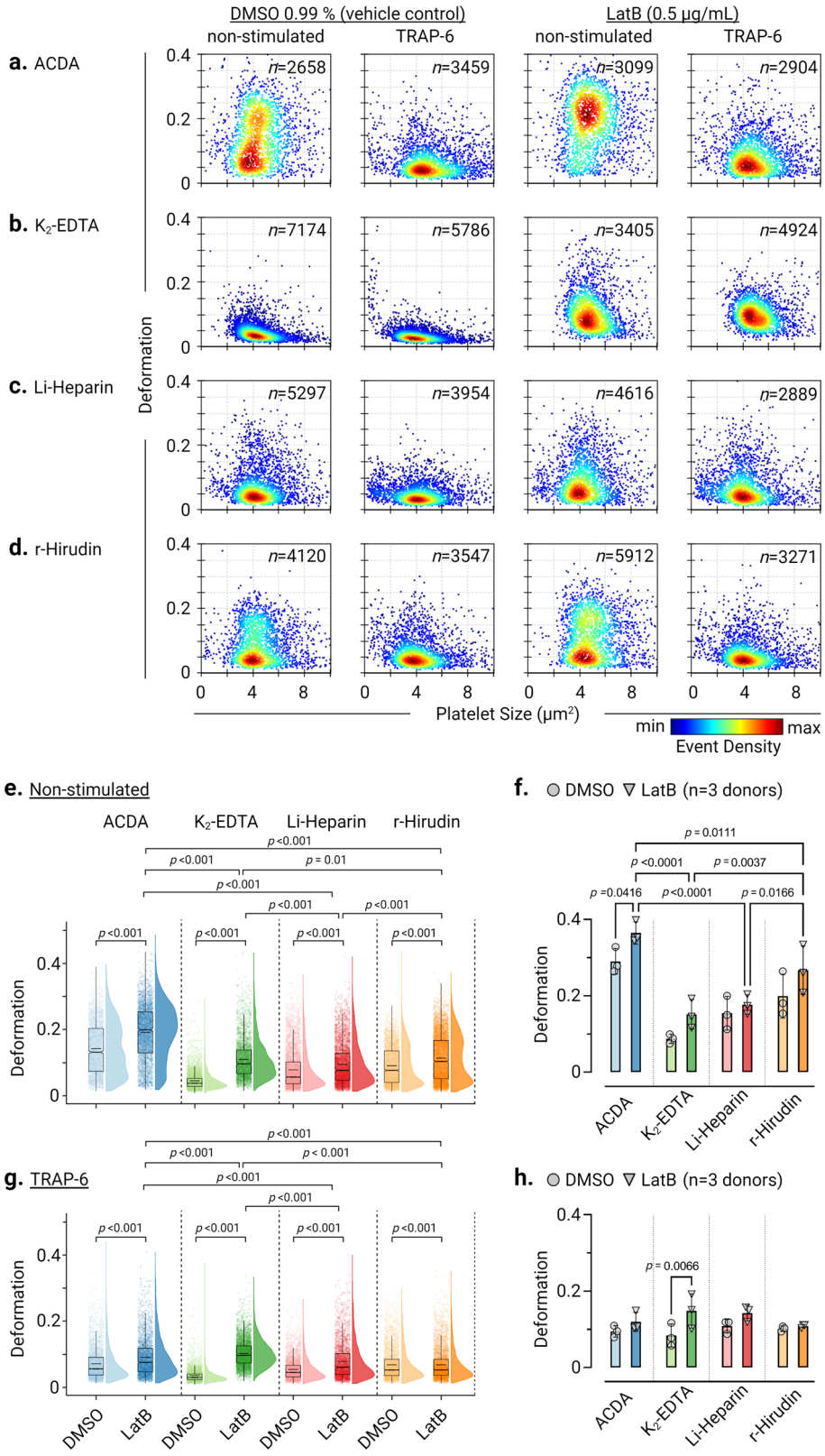

Fig. 6 Inhibition of actin polymerization by LatB strongly affects platelet deformation. KDE scatter plots showing the impact of LatB on single platelet deformation and size on non-stimulated (resting) platelets and after TRAP-6 stimulation compared to the vehicle control (DMSO 0.99 %) in **a** ACD-A, **b** K_2-EDTA, **c** Li-Heparin and in **d** r-Hirudin (n= number of single platelets). Statistical distribution plots for platelet deformation from non-stimulated platelets (**e**) and (**f**) after TRAP-6 stimulation (**g**) and (**h**). Notch in the box plot and the horizontal line depicts median and mean, respectively, and the interquartile ranges. The full distribution of the data for each parameter is depicted by half-violin plots and staggered dots. (Individual data points in (**f**) and (**h**) show median values of platelet deformation from $n = 3$ donors). Statistical assessment by Kruskal-Wallis-Test followed by Dunn's multiple comparisons test and repeated measures one-way ANOVA followed by Tukey's multiple comparisons test. $p < 0.05$ was considered significant.

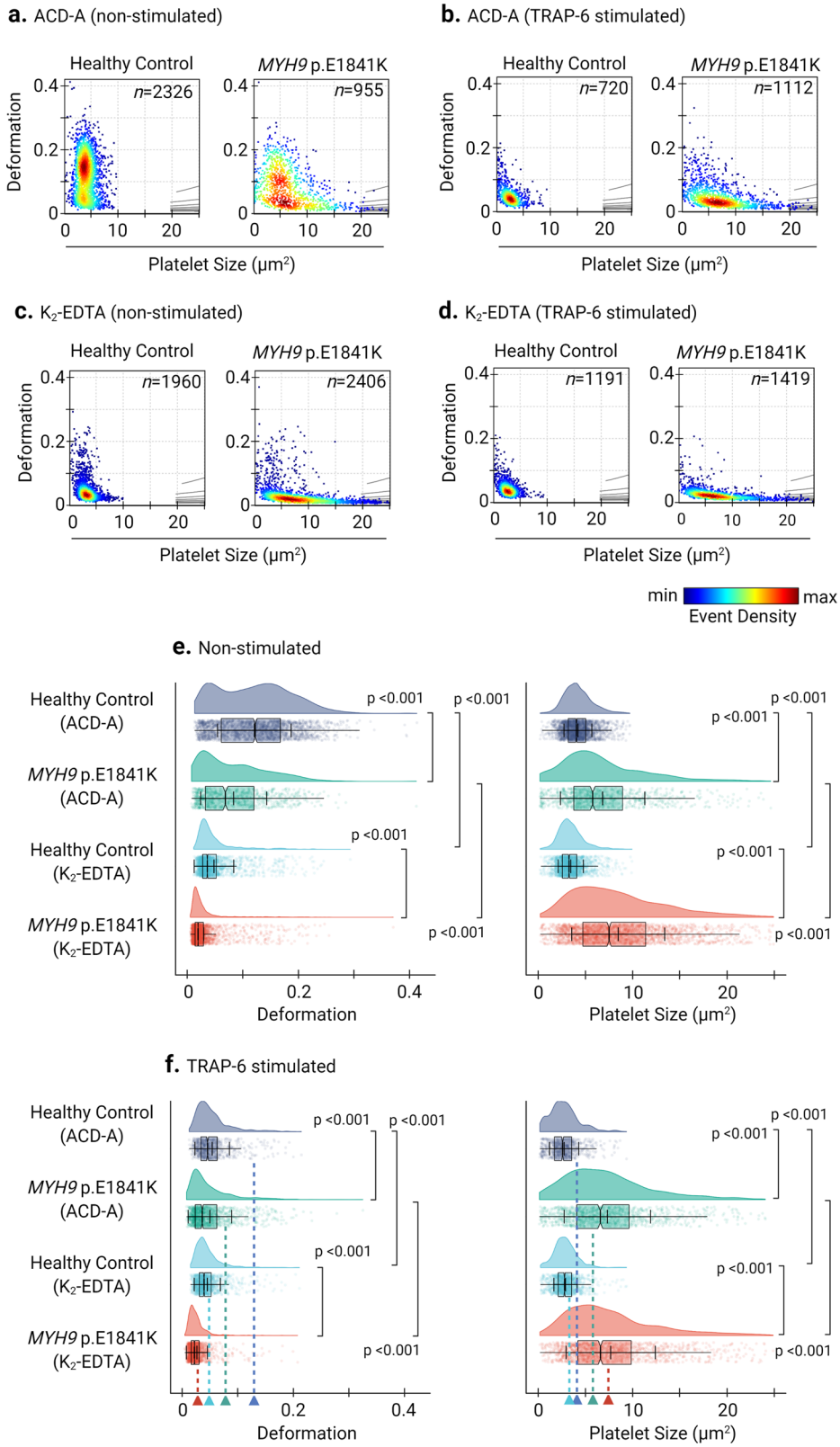

Fig. 7 Deformability and size of platelets from a healthy individual and from a patient carrying *MYH9* p.E1841K mutation. KDE scatter plots from RT-FDC measurements performed on the same day of displaying the distribution of single platelet deformability and their corresponding size between single platelets from a healthy individual (control) and from a patient carrying the mutation *MYH9* p.E1841K for non-muscle myosin heavy chain IIa, in ex vivo anticoagulant (**a**) ACD-A and (**c**) in K_2-EDTA before and after stimulation with platelet agonist TRAP-6, (**b**) and (**d**), respectively (n = number of single platelets). Statistical distribution plots for platelet deformation and size for (**e**) non-stimulated and (**f**) TRAP-6 stimulated platelets from each experimental condition from figure panels (**a**) through (**d**). Notch in the box plot and the horizontal line depicts median and mean, respectively, and the interquartile ranges. The full distribution of the data for each parameter is depicted by half-violin plots and staggered dots and dotted lines with arrowheads represent the median values of respective parameters from the non-stimulated platelets. Statistical assessment by Kruskal–Wallis test followed by Dunn's multiple comparisons test. $p < 0.05$ was considered significant.

such as ACD-A, Na-Citrate, or r-Hirudin and not to exchange it if possible since comparability of the results cannot be guaranteed. With the RT-FDC, we have a highly promising method to examine the platelet cytoskeleton in PRP, which according to our study, provides very solid and fast results.

Methods

Ethics. The use of platelet-rich plasma (PRP) from healthy adult individuals and *MYH9* patients was approved by the ethics committee of the University Medicine Greifswald, Germany. All participants gave written, informed consent

Platelet preparation. The donors had not taken any medication in the previous ten days before blood collection. Whole blood was collected by venipuncture in BD Vacutainer® Tubes containing acid citrate dextrose solution A (ACD-A), 3.8% buffered trisodium citrate (Na-Citrate), 102 I.U. Lithium-Heparin (Li-Heparin), 1.8 mg/mL dipotassium ethylenediaminetetraacetic acid (K_2 -EDTA), or 171 ATU/mL recombinant hirudin (r-Hirudin) (REVASC, Canyon Pharmaceuticals, USA). Whole blood was stored at room temperature for 15 min (at 45° angle to the horizontal surface) and then centrifuged (120 × *g* for 20 min at room temperature). PRP was transferred to a new polypropylene tube and incubated for 15 min at 37 °C. All experimental measurements were performed within 3 h of drawing the blood.

Real-time fluorescence deformability cytometry (RT-FDC). The RT-FDC setup (AcCellerator, Zellmechanik Dresden, Germany) is built around an inverted microscope (Axio Observer A1, Carl Zeiss AG, Germany) mounted with a Zeiss A-Plan 100× NA 0.8 objective. The RT-FDC fluorescence module (Supplementary Fig. 1a) is equipped with 488 nm, 561 nm, 640 nm excitation lasers, and emission is collected at the following wavelengths: 500–550, 570–616, 663–737 nm on avalanche photodiodes (Supplementary Fig. 1a).

For functional mechanophenotyping of platelets based on molecular specificity in RT-FDC, platelets in PRP were labeled with a mouse anti-human monoclonal antibody CD61-PE (Beckman Coulter). Platelet activation was detected by direct immunofluorescence labeling of alpha granule release marker CD62P (P-selectin) with mouse anti-human monoclonal antibody CD62P-AlexaFluor647 (Clone AK4, Cat. No. 304918, BioLegend, USA)and activation associated conformational change in integrin αIIbβ3 was detected with a mouse anti-human monoclonal antibody PAC-1-FITC (Clone PAC-1, Cat. No. 340507, B.D. Biosciences, USA), respectively. PBS (Cat.No. P04-36500, PAN Biotech GmbH, Germany) and TRAP-6 (20 µM) (Haemochrom Diagnostica GmbH, Germany) were used as vehicle control and platelet agonist, respectively. Incubations were performed at room temperature for 10 min in the dark. Assessment of effects of actin disassembly by LatB and its effects on agonist-induced alterations in deformation in the presence of different ex vivo anticoagulants were performed as follows: for non-stimulated platelets, PRP was incubated (37 °C, in the dark) for 10 min with DMSO (0.99%) (Cat.No. D2650-5x5m, Sigma-Aldrich) or LatB (0.5 µg/ml) (cat.no. Cay10010631; Biomol GmbH). For measurement of TRAP-6 activated platelets, PRP was previously incubated (37 °C, in the dark) with DMSO (0.99 %) or LatB (0.5 µg/ml) for 10 min and then TRAP-6 (20 µM) (Haemochrom Diagnostica GmbH, Germany) was added for 10 min (37 °C, in the dark).

Deformability measurements were performed in a microfluidic chip with a constriction of 15 µm × 15 µm cross-section and a length of 300 µm (Flic15, Zellmechanik Dresden, Germany) (Supplementary Fig. 1b). Platelets in suspension are injected by a syringe pump (NemeSys, Cetoni GmbH, Germany), and cell deformation occurs due to the hydrodynamic pressure gradient created by the surrounding fluid only.[55]

Based on cellular circularity, deformation (Eq. 1) is calculated on the fly using bright-field images captured by a camera:[32]

$$\text{Deformation} = 1 - \frac{2\sqrt{\pi A}}{P} \quad (1)$$

where A is the cross-sectional area of the cell and P its perimeter.

RT-FDC measurements were carried out in buffer CellCarrier B (Zellmechanik Dresden, Germany), which is composed of 0.6% (w/v) methylcellulose in PBS (without Ca^{2+}, Mg^{2+}). Here, 50 µL of immunofluorescently labeled PRP was suspended in 450 µL CellCarrier B. The PRP suspension was then driven through the microfluidic chip at flow rates of 0.006 µl/s, and the measurement was stopped after achieving 5000 single platelet count (hard-gate 150-33000 arbitrary units, A.U. for CD61-PE of fluorescence intensity) or after 10 min RT-FDC data was acquired using the ShapeIn software (Version 2.0, Zellmechanik Dresden, Germany). Using the Shape-Out analysis software (https://github.com/ZELLMECHANIK-DRESDEN/ShapeOut2/releases/tag/2.3.0 Version 2.3, Zellmechanik Dresden, Germany), kernel density estimation (KDE) plots of event density were generated, and statistical analysis was performed to determine the median values for platelet deformation, their size and the geometric mean of fluorescence (gMean) of the relevant functional variables. The range area ratio was limited to 0–1.1 and the cell size to 0–10 µm for the analysis (Supplementary Fig. 2 and 3).

Flow cytometry. Platelets were treated as described above for RT-FDC. We used PerFix-nc Kit (Cat.No. B31167; Beckman Coulter GmbH, Germany) and Phalloidin-Atto-647 (Atto-Tec GmbH, Germany) to measure changes in total F-actin content in the platelets. Flow cytometry data were processed using FlowJo™ software for Windows, Version v10.6.2. (Becton, Dickinson and Company, USA), and the gMean of the relevant variables was determined.

Fluorescence microscopy. Platelets in PRP were incubated with PBS (vehicle control, non-stimulated) or stimulated with TRAP-6 for 10 min followed by fixation in 2% paraformaldehyde (Morphisto, Germany) for 15 min Fixed platelets were transferred into a Shandon™ Single Cytofunnel™ (Thermo Fisher, USA) and were centrifuged on a microscope slide for 5 min at 700 rpm (Cytospin ROTOFIX 32 A, Hettich, Germany), washed thrice with PBS (5 min intervals). Platelet was permeabilized in 0.5 % saponin with 0.2% bovine serum albumin (BSA) (Cat. No. 11924.03, SERVA Electrophoresis GmbH, Germany) for 25 min, and followed by blocking for 30 min in 0.5% saponin supplemented with heat-inactivated 10% normal goat serum. Permeabilized platelets were incubated with 1:500 dilution of mouse monoclonal anti-α-Tubulin IgG (Clone DM1A, Cat. No. T9026, Sigma-Aldrich GmbH, Germany) primary antibody diluted in 0.5% saponin with 0.2% BSA in PBS for 16 h at 4 °C followed by three washing steps in PBS for 5 min each. Afterward, platelets were incubated with 1:750 dilution of goat polyclonal anti-mouse AF488 IgG prepared in 0.5% saponin with 0.2% BSA in PBS for 60 min in the dark at room temperature, followed by three washing steps with PBS for 5 min each. F-actin was labeled with 20 pM Phalloidin-Atto 647N (Cat. No. AD 647N-81, Atto-Tec GmbH, Germany) for 60 min, followed by three washes in PBS for 5 min each. Slides were covered by a permanent mounting medium Roti®-Mount FluorCare (Cat. No. HP19.1, Karl-Roth GmbH, Germany). Fluorescence microscopy was performed on a Leica SP5 confocal laser scanning microscope (Leica Microsystems, Wetzlar, Germany) equipped with HCX PL APO lambda blue 40×/1.25 OIL UV objective. For image acquisition, AF488 and ATTO647 were excited by argon (488 nm) and helium-neon (HeNe) (633 nm) laser lines selected with an acousto-optic tunable filter, and fluorescence emission was collected between 505–515 and 640–655 nm respectively on hybrid detectors. Assessment of F-actin distribution and organization of marginal band α-tubulin staining was performed by measuring cross-sectional line profile (5 µm length and 1 µm width) of non-saturated grayscale fluorescence intensities (pixel values) of immunofluorescent probes across individual platelets in confocal images using Leica Application Suite X (Version 3.7.1, Leica Microsystems, Wetzlar, Germany). For data plotting, GraphPad Prism version 8.0.0 for Windows (GraphPad Software, San Diego, California USA) was used.

Statistical plots and analysis of RT-FDC data. Statistical plots showing parameters of the platelet population were prepared with ShapeOut software (https://github.com/ZELLMECHANIK-DRESDEN/ShapeOut2/releases/tag/2.3.0 Version 2.3, Zellmechanik Dresden), PlotsOfDifferences (https://huygens.science.uva.nl/PlotsOfDifferences/), Raincloud Plots (https://gabrifc.shinyapps.io/raincloudplots/) and BoxPlotR (http://shiny.chemgrid.org/boxplotr/)[56,57].

Statistics and reproducibility. The number of single platelets analyzed, biological replicates, and the number of blood donors involved for each experiment are specified in the corresponding figure legend and figure description. All statistical assessments are performed in GraphPad Prism version 9.0.0 for Windows (GraphPad Software, San Diego, California USA). Details of specific statistical tests performed are described in figure descriptions, and $p < 0.05$ was considered significant.

Reporting summary. Further information on research design is available in the Nature Research Reporting Summary linked to this article.

Data availability

Source data of corresponding figures are available in Supplementary Data 1. In addition, all raw data and accompanying software for analysis of RT-FDC data are available in a citable public repository and can be accessed directly at the following https://doi.org/10.5281/zenodo.4461273 or by requesting the corresponding author(s).

Received: 28 April 2021; Accepted: 17 December 2021;
Published online: 21 January 2022

References

1. Machlus, K. R. & Italiano, J. E. Jr The incredible journey: from megakaryocyte development to platelet formation. *J. Cell Biol.* **201**, 785–796 (2013).
2. Jurk, K. & Kehrel, B. E. Platelets: physiology and biochemistry. *Semin Thromb. Hemost.* **31**, 381–392 (2005).
3. Koupenova, M., Clancy, L., Corkrey, H. A. & Freedman, J. E. Circulating platelets as mediators of immunity, inflammation, and thrombosis. *Circ. Res.* **122**, 337–351 (2018).

4. Gaertner, F. & Massberg, S. Blood coagulation in immunothrombosis-at the frontline of intravascular immunity. *Semin. Immunol.* **28**, 561–569 (2016).
5. Hansen, C. E., Qiu, Y., McCarty, O. J. T. & Lam, W. A. Platelet mechanotransduction. *Annu Rev. Biomed. Eng.* **20**, 253–275 (2018).
6. Zhang, Y. et al. Platelet integrins exhibit anisotropic mechanosensing and harness piconewton forces to mediate platelet aggregation. *Proc. Natl Acad. Sci. USA* **115**, 325–330 (2018).
7. Qiu, Y., Myers, D. R. & Lam, W. A. The biophysics and mechanics of blood from a materials perspective. *Nat. Rev. Mater.* **4**, 294–311 (2019).
8. Qiu, Y., Ciciliano, J., Myers, D. R., Tran, R. & Lam, W. A. Platelets and physics: how platelets "feel" and respond to their mechanical microenvironment. *Blood Rev.* **29**, 377–386 (2015).
9. Kim, O. V., Litvinov, R. I., Alber, M. S. & Weisel, J. W. Quantitative structural mechanobiology of platelet-driven blood clot contraction. *Nat. Commun.* **8**, 1274 (2017).
10. Lam, W. A. et al. Mechanics and contraction dynamics of single platelets and implications for clot stiffening. *Nat. Mater.* **10**, 61–66 (2011).
11. Gaertner, F. et al. Migrating platelets are mechano-scavengers that collect and bundle bacteria. *Cell* **171**, 1368–1382 e1323 (2017).
12. Palankar, R. et al. Platelets kill bacteria by bridging innate and adaptive immunity via platelet factor 4 and FcgammaRIIA. *J. Thromb. Haemost.* **16**, 1187–1197 (2018).
13. Nicolai, L. et al. Vascular surveillance by haptotactic blood platelets in inflammation and infection. *Nat. Commun.* **11**, 5778 (2020).
14. Myers, D. R. et al. Single-platelet nanomechanics measured by high-throughput cytometry. *Nat. Mater.* **16**, 230–235 (2017).
15. White, J. G., Burris, S. M., Tukey, D., Smith, C. 2nd & Clawson, C. C. Micropipette aspiration of human platelets: influence of microtubules and actin filaments on deformability. *Blood* **64**, 210–214 (1984).
16. Burris, S. M., Smith, C. M. 2nd, Tukey, D. T., Clawson, C. C. & White, J. G. Micropipette aspiration of human platelets after exposure to aggregating agents. *Arteriosclerosis* **6**, 321–325 (1986).
17. Haga, J. H., Beaudoin, A. J., White, J. G. & Strony, J. Quantification of the passive mechanical properties of the resting platelet. *Ann. Biomed. Eng.* **26**, 268–277 (1998).
18. Radmacher, M., Fritz, M., Kacher, C. M., Cleveland, J. P. & Hansma, P. K. Measuring the viscoelastic properties of human platelets with the atomic force microscope. *Biophys. J.* **70**, 556–567 (1996).
19. Sorrentino, S., Studt, J. D., Horev, M. B., Medalia, O. & Sapra, K. T. Toward correlating structure and mechanics of platelets. *Cell Adh Migr.* **10**, 568–575 (2016).
20. Nguyen, T. H. et al. Rupture forces among human blood platelets at different degrees of activation. *Sci. Rep.* **6**, 25402 (2016).
21. Rheinlaender, J. et al. Imaging the elastic modulus of human platelets during thrombin-induced activation using scanning ion conductance microscopy. *Thromb. Haemost.* **113**, 305–311 (2015).
22. Seifert, J., Rheinlaender, J., Lang, F., Gawaz, M. & Schaffer, T. E. Thrombin-induced cytoskeleton dynamics in spread human platelets observed with fast scanning ion conductance microscopy. *Sci. Rep.* **7**, 4810 (2017).
23. Schwarz Henriques, S., Sandmann, R., Strate, A. & Koster, S. Force field evolution during human blood platelet activation. *J. Cell Sci.* **125**, 3914–3920 (2012).
24. Hanke, J., Probst, D., Zemel, A., Schwarz, U. S. & Koster, S. Dynamics of force generation by spreading platelets. *Soft Matter* **14**, 6571–6581 (2018).
25. Liang, X. M., Han, S. J., Reems, J. A., Gao, D. & Sniadecki, N. J. Platelet retraction force measurements using flexible post force sensors. *Lab Chip* **10**, 991–998 (2010).
26. Feghhi, S. et al. Glycoprotein Ib-IX-V complex transmits cytoskeletal forces that enhance platelet adhesion. *Biophys. J.* **111**, 601–608 (2016).
27. Lickert, S. et al. Platelets exploit fibrillar adhesions to assemble fibronectin matrix revealing new force-regulated thrombus remodeling mechanisms. *bioRxiv* https://doi.org/10.1101/2020.04.20.050708 (2020).
28. Sachs, L., Denker, C., Greinacher, A. & Palankar, R. Quantifying single-platelet biomechanics: an outsider's guide to biophysical methods and recent advances. *Res Pract. Thromb. Haemost.* **4**, 386–401 (2020).
29. Penington, D. G., Streatfield, K. & Roxburgh, A. E. Megakaryocytes and the heterogeneity of circulating platelets. *Br. J. Haematol.* **34**, 639–653 (1976).
30. Corash, L., Tan, H. & Gralnick, H. R. Heterogeneity of human whole blood platelet subpopulations. I. Relationship between buoyant density, cell volume, and ultrastructure. *Blood* **49**, 71–87 (1977).
31. Radziwon-Balicka, A. et al. Differential eNOS-signalling by platelet subpopulations regulates adhesion and aggregation. *Cardiovasc. Res.* **113**, 1719–1731 (2017).
32. Otto, O. et al. Real-time deformability cytometry: on-the-fly cell mechanical phenotyping. *Nat. Methods* **12**, 199–202 (2015).
33. Rosendahl, P. et al. Real-time fluorescence and deformability cytometry. *Nat. Methods* **15**, 355–358 (2018).
34. Herbig, M. et al. Image-based cell sorting using artificial intelligence. *Proc. SPIE* Vol. 11250, High-Speed Biomedical Imaging and Spectroscopy V, https://doi.org/10.1117/12.2544809 (2020).
35. Nawaz, A. A. et al. Intelligent image-based deformation-assisted cell sorting with molecular specificity. *Nat. Methods* **17**, 595–599 (2020).
36. Jacobi, A. et al. Analysis of biomechanical properties of hematopoietic stem and progenitor cells using real-time fluorescence and deformability cytometry. *Methods Mol. Biol.* **2017**, 135–148 (2019).
37. Luhr, J. J. et al. Maturation of monocyte-derived DCs leads to increased cellular stiffness, higher membrane fluidity, and changed lipid composition. *Front Immunol.* **11**, 590121 (2020).
38. Guck, J. Some thoughts on the future of cell mechanics. *Biophys. Rev.* **11**, 667–670 (2019).
39. Shattil, S. J., Motulsky, H. J., Insel, P. A., Flaherty, L. & Brass, L. F. Expression of fibrinogen receptors during activation and subsequent desensitization of human platelets by epinephrine. *Blood* **68**, 1224–1231 (1986).
40. Canobbio, I. et al. Altered cytoskeleton organization in platelets from patients with MYH9-related disease. *J. Thromb. Haemost.* **3**, 1026–1035 (2005).
41. Toepfner, N. et al. Detection of human disease conditions by single-cell morpho-rheological phenotyping of blood. *Elife* **7** (2018).
42. Xavier, M. et al. Mechanical phenotyping of primary human skeletal stem cells in heterogeneous populations by real-time deformability cytometry. *Integr. Biol.* **8**, 616–623 (2016).
43. Aurich, K. et al. Label-free on chip quality assessment of cellular blood products using real-time deformability cytometry. *Lab Chip* **20**, 2306–2316 (2020).
44. Kubankova, M. et al. Physical phenotype of blood cells is altered in COVID-19. *Biophys. J.* **120**, 2838–2847 (2021).
45. Gao, C. et al. Heparin promotes platelet responsiveness by potentiating alphaIIbbeta3-mediated outside-in signaling. *Blood* **117**, 4946–4952 (2011).
46. Sobel, M. et al. Heparin modulates integrin function in human platelets. *J. Vasc. Surg.* **33**, 587–594 (2001).
47. Gachet, C. et al. Alpha IIb beta 3 integrin dissociation induced by EDTA results in morphological changes of the platelet surface-connected canalicular system with differential location of the two separate subunits. *J. Cell Biol.* **120**, 1021–1030 (1993).
48. Golanski, J., Pietrucha, T., Baj, Z., Greger, J. & Watala, C. Molecular insights into the anticoagulant-induced spontaneous activation of platelets in whole blood-various anticoagulants are not equal. *Thromb. Res.* **83**, 199–216 (1996).
49. White, J. G. EDTA-induced changes in platelet structure and function: clot retraction. *Platelets* **11**, 49–55 (2000).
50. Ma, Y. & Wong, K. Reassociation and translocation of glycoprotein IIB-IIIA in EDTA-treated human platelets. *Platelets* **18**, 451–459 (2007).
51. Woronowicz, K. et al. The platelet actin cytoskeleton associates with SNAREs and participates in alpha-granule secretion. *Biochemistry* **49**, 4533–4542 (2010).
52. Kalb, M. L., Potura, L., Scharbert, G. & Kozek-Langenecker, S. A. The effect of ex vivo anticoagulants on whole blood platelet aggregation. *Platelets* **20**, 7–11 (2009).
53. Kaiser, A. F. et al. Which is the best anticoagulant for whole blood aggregometry platelet function testing? Comparison of six anticoagulants and diverse storage conditions. *Platelets* **23**, 359–367 (2012).
54. Pignatelli, P. et al. Acid citrate dextrose (ACD) formula A as a new anticoagulant in the measurement of in vitro platelet aggregation. *J. Clin. Lab Anal.* **9**, 138–140 (1995).
55. Mietke, A. et al. Extracting cell stiffness from real-time deformability cytometry: theory and experiment. *Biophys. J.* **109**, 2023–2036 (2015).
56. Allen, M., Poggiali, D., Whitaker, K., Marshall, T. & Kievit, R. Raincloud plots: a multi-platform tool for robust data visualization [version 2; peer review: 2 approved]. *Wellcome Open Res.* **4**, 63 https://doi.org/10.12688/wellcomeopenres.15191.2 (2021).
57. Goedhart, J. SuperPlotsOfData-a web app for the transparent display and quantitative comparison of continuous data from different conditions. *Mol. Biol. Cell* **32**, 470–474 (2021).

Acknowledgements

O.O gratefully acknowledges funding from the German Ministry of Education and Research (BMBF) within the project 03Z22CN11 (ZIK grant) and the German Center for Cardiovascular Research within the project 81X3400107 (Postdoc start-up grant). This work was supported by the Deutsche Forschungsgemeinschaft project number 374031971–CRC/TR 240 project A06 to M.B., O.O. and R.P.

Author contributions

L.S., A.G., M.B., O.O., and R.P. designed the study. L.S. performed all RT-FDC experiments. J.W. and L.L. performed flow cytometry. L.S. and R.P. performed CLSM experiments. L.S. and R.P. analyzed the data and prepared figures. L.S. wrote the manuscript. A.G. provided access to *MYH9* patient platelets. A.G., M.B., O.O., and R.P. contributed to writing the manuscript. All authors contributed to the critical revision of the manuscript. M.B., O.O., and R.P. obtained funding.

Funding
Open Access funding enabled and organized by Projekt DEAL.

Competing interests
O.O. is co-founder and shareholder of Zellmechanik Dresden GmbH, distributing real-time deformability cytometry. All other authors declare no competing interests.

Additional information
Supplementary information The online version contains supplementary material available at https://doi.org/10.1038/s42003-021-02982-6.

Correspondence and requests for materials should be addressed to Oliver Otto or Raghavendra Palankar.

Peer review information *Communications Biology* thanks Kandace Gollomp and the other, anonymous, reviewers for their contribution to the peer review of this work. Primary Handling Editors: Alexander Cartagena-Rivera and Anam Akhtar. Peer reviewer reports are available.

9.3. Manuscript 3: Reduced platelet forces underlie impaired hemostasis in mouse models of *MYH9*-related disease.

Baumann, J., **Sachs, L.**, Oliver, O., Schoen, I., Nestler, P., Zaninetti, C., Kenny, M., Kranz, R., von Eysmondt, H., Rodriguez, J., Schäffer, T. E., Nagy, Z., Greinacher, A., Palankar, P., Bender, M. Reduced platelet forces underlie impaired hemostasis in mouse models of *MYH9*-related disease. Accepted at *Science Advances* (2022).

Accepted at *Science Advances* on February 25, 2022
Submission ID: abn2627

Reduced platelet forces underlie impaired hemostasis in mouse models of *MYH9*-related disease

Short title: Reduced forces of *Myh9* mutant platelets

Juliane Baumann[1†], Laura Sachs[2†], Otto Oliver[3], Ingmar Schoen[4], Peter Nestler[3], Carlo Zaninetti[2,5], Martin Kenny[4], Ruth Kranz[1], Hendrik von Eysmondt[6], Johanna Rodriguez[6], Tilman E. Schäffer[6], Zoltan Nagy[1], Andreas Greinacher[2], Raghavendra Palankar[2†*], Markus Bender[1†*]

[1]Institute of Experimental Biomedicine – Chair I, University Hospital and Rudolf Virchow Center, Würzburg, Germany. [2]Institute for Immunology and Transfusion Medicine, University Medicine Greifswald, Greifswald, Germany. [3]Zentrum für Innovationskompetenz – Humorale Immunreaktionen bei Kardiovaskulären Erkrankungen, University Greifswald, Greifswald, Germany. [4]School of Pharmacy and Biomolecular Sciences, Irish Centre for Vascular Biology, Royal College of Surgeons in Ireland, Dublin, Ireland. [5]University of Pavia, Pavia, Italy. [6]Institute of Applied Physics, University of Tübingen, Tübingen, Germany.

[†]These authors contributed equally to this work.

*Correspondence to:
Markus Bender: Bender_M1@ukw.de
Raghavendra Palankar: raghavendra.palankar@med.uni-greifswald.de

Abstract

MYH9-related disease patients with mutations in the contractile protein non-muscle myosin heavy chain IIA display, among others, macrothrombocytopenia and a mild to moderate bleeding tendency. In this study, we used three mouse lines, each with one point mutation in the *Myh9* gene at positions 702, 1424, or 1841, to investigate mechanisms underlying the increased bleeding risk. Agonist-induced activation of *Myh9* mutant platelets was comparable to controls. However, myosin light chain phosphorylation after activation was reduced in mutant platelets, which displayed altered biophysical characteristics and generated lower adhesion, interaction, and traction forces. Treatment with tranexamic acid restored clot retraction in the presence of tPA and reduced bleeding. We verified our findings from the mutant mice with platelets from patients with the respective mutation. These data suggest that reduced platelet forces lead to an increased bleeding tendency in *MYH9*-related disease patients, and treatment with tranexamic acid can improve the hemostatic function.

Teaser

Impaired hemostasis in *Myh9* mutant mice due to reduced platelet forces can be improved by tranexamic acid.

Introduction

The platelet cytoskeleton ensures normal size and the discoid shape under resting conditions and undergoes rapid rearrangement upon activation. Platelets respond to the biophysical properties of the extracellular environment through integrin-based adhesion sites, which results in actomyosin-mediated contractile forces (*1, 2*). Several inherited platelet bleeding disorders are caused by mutations in key cytoskeletal-regulatory proteins (*3*). *MYH9*-related disease (*MYH9*-RD) is a rare inherited platelet disorder (*4*). The *MYH9* gene encodes the heavy chain of non-muscle myosin IIA, an actin-binding protein with contractile properties. Heterozygous mutations in the *MYH9* gene in humans lead to macrothrombocytopenia with a moderate bleeding tendency. Depending on the position of the mutations (>30 mutations identified (*5*)), the risk increases for other syndromic manifestations such as renal failure, hearing loss, and pre-senile cataract (*5-7*). Patients with a mutation at amino acid position 702, located in the motor domain of non-muscle myosin IIA, are reported to be most affected for non-hematologic defects and have a higher risk for increased bleeding. Mutations located in the rod domain (amino acid positions 1424 and 1841) cause a milder phenotype (*5*). Three different mouse lines with the knock-in mutations Arg702Cys (R702C), Asp1424Asn (D1424N), and Glu1841Lys (E1841K) were generated (*8*), which are the most frequent mutations found in human patients (*9*). These heterozygous point-mutated mice recapitulated key features of human patients, such as macrothrombocytopenia, moderately prolonged bleeding times, decreased ability to retract clots, and non-hematologic defects (*8*). These data show that myosin IIA plays a vital role in platelet production and plug stabilization. However, it is insufficiently understood which factors contribute to the hemostatic defect observed in *MYH9*-RD patients and mutant mice. Given the central role of myosin IIA in force generation and the increased bleeding risk in *MYH9*-RD patients, a better understanding of the underlying biophysical mechanisms in clot formation and its stabilization is warranted (*10*).

Recently, it was demonstrated that biophysical signatures are similar between human and murine platelets (*11*). Therefore, we took advantage of the heterozygous R702C, D1424N, and E1841K point-mutated *Myh9* mice and comprehensively investigated whether altered biomechanical properties might be responsible for the increased bleeding phenotype. While the primary function of mutant mouse platelets was comparable to controls, phosphorylation of the myosin light chain after activation was strongly reduced, the extent of clot retraction decreased, and thrombi were more unstable even when platelet count was adjusted. In line with this, biophysical analyses revealed that *Myh9* mutant platelets generate lower adhesion forces to collagen, lower interaction forces between platelets, and reduced traction forces when spread on fibrinogen-coated micropost arrays. We verified our key findings by analyzing the biophysical function of platelets isolated from *MYH9*-RD patients with the respective mutation. Finally, we observed that treatment with the antifibrinolytic agent, tranexamic acid

(TXA), restored clot retraction and reduced bleeding in all three mouse lines. These data suggest that the most common *MYH9*-RD mutations impair the generation of contractile forces by myosin IIA that is necessary to prevent increased bleeding.

Results

Unaltered activation but impaired deformability of *Myh9* mutant platelets

While the role of platelets in hemostatic plug and thrombus formation has been intensively studied from a biological perspective, the mechanobiological aspects are only poorly understood. To investigate the biological and biophysical properties of the contractile protein non-muscle myosin IIA, we capitalized on mice with three different point mutations in the *Myh9* gene. Most results of the D1424N mutation are shown in the main manuscript; results regarding the R702C and E1841K mutations are shown in supplemental results. We confirmed the presence of the protein myosin IIA in platelet lysates from control and heterozygous mutant mice (*Myh9*$^{R702C/+}$, *Myh9*$^{D1424N/+}$, *Myh9*$^{E1841K/+}$) by western blot analysis (Supplemental Fig. 1, A and B). The expression levels of non-muscle myosin IIA were comparable to controls (Supplemental Fig. 1C). *Myh9* mutant mice displayed a significant reduction in platelet count and increased platelet size as determined by a hematology analyzer (Fig. 1, A and B, and Supplemental Fig. 2, A and B; and reference (*8*)). Other blood parameters like red blood cell (RBC) count, hematocrit (HCT), and hemoglobin (HGB) were unaltered in mutant mice (Supplemental Table 1). Due to the increased platelet size in mutant mice, control and mutant platelets were gated for a population of similar size in glycoprotein expression and platelet activation studies (Supplemental Fig. 2C). Analysis of expression of prominent platelet surface proteins by flow cytometry revealed moderate differences of some receptors, most notably the GPIb-V-IX complex, even when comparing platelet populations of similar size (Fig. 1C, and Supplemental Fig. 2, C and D). Next, surface exposure of P-selectin and activation of the platelet integrin αIIbβ3 was analyzed after incubation with different agonists. Overall comparable results were obtained for control, and mutant platelets after stimulation of G-protein coupled receptors with ADP, the thromboxane A2 analog U46619, a combination of both, or thrombin (Fig. 1, D and E, and Supplemental Fig. 3, A and B). Similarly, *Myh9* mutant platelets exhibited a comparable degree of activation upon stimulation of the GPVI-ITAM (immunoreceptor tyrosine-based activation motif) pathway with collagen-related peptide (CRP) or convulxin, and of the hemITAM receptor, CLEC2 (C-type lectin-like receptor 2), with rhodocytin. To clarify the role of mutated myosin IIA for platelet shape change and aggregation, *in vitro* aggregation studies were performed. Both agonists, Horm collagen and thrombin, induced a comparable activation-dependent shape change of control and mutant platelets (Supplemental Fig. 4, A and B). Further, *Myh9* mutant platelets showed a normal onset and degree of aggregation (Supplemental Fig. 4, A and B, and Supplemental Table 2). Next, we

investigated whether the mutation in myosin IIA leads to ultrastructural changes in platelets. Transmission electron microscopic (TEM) analysis of mutant platelets revealed a heterogeneous population of platelet size but an otherwise comparable ultrastructure (Fig. 1F, and Supplemental Fig. 4C). Taken together, *Myh9* point-mutated mice display a macrothrombocytopenia, and their platelets can get activated and form aggregates in response to platelet agonists.

In contrast, real-time fluorescence deformability cytometry (RT-FDC) measurements revealed a significantly decreased deformation and increased size of *Myh9* mutant platelets (Fig. 1G, and Supplemental Fig. 5, A and B), which points to an increased Young's modulus. Since most agonist-induced platelet functions otherwise were normal, we further investigated the structure and function of cytoskeletal components.

Decreased phosphorylation of the myosin light chain in *Myh9* mutant platelets

To test possible differences in F-actin content, we performed flow cytometry with phalloidin-stabilized resting platelets. Mutant platelets exhibited an increased F-actin content, most likely due to the increased platelet size (Fig. 2A, and Supplemental Fig. 6A). To investigate the organization and rearrangement of the cytoskeleton in *Myh9* mutant platelets, we performed spreading experiments on a fibrinogen-coated surface. Differential interference contrast imaging revealed comparable spreading kinetics of $Myh9^{R702C/+}$ mutant platelets and slightly faster spreading of $Myh9^{D1424N/+}$ and $Myh9^{E1841K/+}$ mutant platelets on a fibrinogen-coated surface (Fig. 2B, and Supplemental Fig. 6B). The increased size might explain the faster adhesion kinetics of these platelets. Similar to control platelets, mutant platelets were able to rearrange the cytoskeleton and form filopodia and lamellipodia, as revealed by platinum replica electron and confocal microscopy (Fig. 2C, and Supplemental Fig. 6, C and D). Phosphorylation of the myosin light chain 2 is responsible for the generation of contractile forces in platelets. Therefore, a capillary-based immunoassay approach was used to detect myosin light chain 2 (MLC2) phosphorylation in resting and thrombin-activated platelets. MLC2 and myosin phosphatase 1 (MYPT1) expression were comparable in control and mutant samples (Fig. 2D, and Supplemental Fig. 1B and 7A). However, phosphorylation of MLC2 after activation with thrombin was strongly reduced to 56% in $Myh9^{D1424N/+}$, to 40% in $Myh9^{R702C/+}$, and to 58% $Myh9^{E1841K/+}$ mutant platelets compared to $Myh9^{+/+}$ controls (Fig. 2D and Supplemental Fig. 7, A and B). Although we have not identified the interaction of myosin heavy and light chain of mutant myosin IIA, we can hypothesize no impaired interaction. The instability of the regulatory light chain upon the absence or interrupted interaction of the heavy chain would result in rapid degradation of MLC (*12-14*). In contrast, we observed no alteration in MLC2 total expression. These data suggest that heterozygous mutations in the motor

domain (R702C) and rod domain (D1424N, E1841K) might impair the mutant platelets´ contractile properties.

Low contractile force generation and impaired clot retraction of *Myh9* mutant platelets

To measure contractile forces, platelets were allowed to adhere and spread on fibrinogen-coated micropost arrays and pulled at posts to different extents. The mean traction force per post beneath each cell was significantly reduced by 38% in *Myh9*$^{D1424N/+}$, 29% in *Myh9*$^{R702C/+}$, and 28% in *Myh9*$^{E1841K/+}$ platelets compared to their corresponding controls, as readily perceived from the images of the deformed posts (Fig. 3A, arrows; and Supplemental Fig. 8). However, the total force per cell was not significantly different for *Myh9*$^{D1424N/+}$ platelets due to the larger platelet volume of mutant platelets (Fig. 1B), which compensated for the lower reduced intrinsic contractility (Fig. 3A). The total traction forces per single platelet in *Myh9*$^{R702C/+}$, and *Myh9*$^{E1841K/+}$ compared to control platelets were significantly lower, indicating that their platelet volume, which is not as increased as for *Myh9*$^{D1424N/+}$ platelets (Fig. 1B, and Supplemental Fig. 2B), was not sufficient to compensate for the reduced intrinsic contractility (Supplemental Fig. 8). Platelets spread on a fibrinogen-coated surface were also analyzed for stiffness using scanning ion conductance microscopy (SICM). *Myh9*$^{R702C/+}$ and *Myh9*$^{D1424N/+}$ platelets displayed a softer appearance on fibrinogen compared to *Myh9*$^{+/+}$ platelets, as revealed by a lower Young's modulus (Fig. 3B, and Supplemental Fig. 9). In contrast *Myh9*$^{E1841K/+}$ platelets showed a comparable Young's modulus to *Myh9*$^{+/+}$ platelets (Supplemental Fig. 9). Next, we performed a clot retraction assay since platelet-mediated compaction is an important mechanism to stabilize thrombi (*10*). The extent of clot retraction was significantly different between control and mutant mice. *Myh9* mutant samples showed an impaired clot retraction (*8*), even when the platelet count had been adjusted to 3 x 10^5 platelets/µL (Fig. 3C, and Supplemental Fig. 10, A and C). Quantification of the residual clot revealed a heavier, less retracted clot and a corresponding lower volume of residual fluid in *Myh9* mutant samples (Fig. 3D, and Supplemental Fig. 10, B and D). These findings strongly suggest that impaired clot retraction of *Myh9* mutant platelets is due to a defect in the generation of contractile forces and not because of a reduction in platelet count.

Lower adhesion and interaction forces of mutant platelets

To investigate the mechanisms of platelet biomechanics under shear flow, we analyzed the effect of the heterozygous point mutations in myosin IIA in an *ex vivo* thrombus formation assay. At first, we studied platelet adhesion to collagen fibers in a whole-blood perfusion assay at shear rates of 1,000 s^{-1}. Control and mutant platelets adhered to collagen and formed thrombi both under platelet count adjusted (5 x 10^5 platelets/µL) and unadjusted conditions. However, platelets from *Myh9*$^{D1424N/+}$ and *Myh9*$^{R702C/+}$ mutant mice formed fewer and smaller

thrombi than controls (Fig. 4A, and Supplemental Fig. 11A). Surprisingly, platelets from *Myh9*$^{E1841K/+}$ mutant mice formed only fewer and smaller thrombi under thrombocytopenic conditions (Supplemental Fig. 11A). Next, platelet adhesion forces on collagen were measured using single platelet force spectroscopy (SPFS). Platelets of *Myh9* mutant mice displayed lower adhesion forces to collagen (Fig. 4B, and Supplemental Fig. 11B; reduced by 69% in *Myh9*$^{D1424N/+}$, by 33% in *Myh9*$^{R702C/+}$, and by 42% in *Myh9*$^{E1841K/+}$ platelets). Similarly, interaction forces between two single platelets were reduced for all three mouse lines (Fig. 4C, and Supplemental Fig. 11C; *Myh9*$^{D1424N/+}$ by 39%, *Myh9*$^{R702C/+}$ by 50%, and *Myh9*$^{E1841K/+}$ by 29%). Thrombi formed at a shear rate of 1,000 s^{-1} on collagen were analyzed for their stiffness by colloidal probe spectroscopy. Thrombi formed by platelets of *Myh9* mutant mice were softer compared to thrombi of control mice, as revealed by a decreased Young's modulus (Fig. 4D, and Supplemental Fig. 11D). In summary, these results suggest that reduced platelet-substrate and platelet-platelet forces lead to reduced thrombus formation under shear.

Samples of *MYH9*-RD patients recapitulate the biomechanical phenotype observed in the respective mutant mice

To verify our biophysical results obtained from the analyses of mutant mice, we analyzed deformability and force generation of platelets from two patients with the respective mutations (*MYH9* p.D1424N, *MYH9* p.E1841K). Mechanophenotyping using RT-FDC showed that platelets from patients are less deformable and larger, which is in line with the mouse data (Fig. 5A, and Supplemental Fig. 12A). Other blood parameters like red blood cell (RBC) count, hematocrit (HCT) and hemoglobin (HGB) were unaltered in patient blood (Supplemental Table 3). Next, we assessed platelet adhesion and thrombus formation on collagen under shear. We observed significantly less and smaller thrombi when whole patient blood was perfused over collagen fibers. Moreover, the kinetics of thrombus formation overtime was decreased in the patient sample (Fig. 5B, and Supplemental Fig. 12B). We measured the stiffness of the formed thrombi by colloidal probe spectroscopy. In agreement with the data obtained from *Myh9*$^{D1424N/+}$ mutant mice, thrombi were significantly softer for *MYH9* p.D1424N (Fig. 5C). In contrast, stiffness was moderately but not significantly reduced for *MYH9* p.E1841K (Supplemental Fig. 12C). These results show that the mechanical characteristics of human and mouse platelets with point mutations in non-muscle myosin IIA are overall comparable, except for thrombus stiffness of the *MYH9* p.E1841K sample, which shows only a tendency to softer thrombi.

Treatment with tranexamic acid improves hemostatic function in mutant mice

MYH9-RD patients have an increased bleeding risk. The antifibrinolytic drug, tranexamic acid (TXA), is one option to control bleeding complications in those patients (*5, 6*). We thus hypothesized that gaps of a less compact clot might allow for increased diffusion of

plasminogen into the clot, thereby accelerating clot instability and that TXA may help to prevent clot degradation and stabilize the clot of *Myh9* mutant mice. TXA was beneficial in combination with threshold concentration (0.0138 nM, Supplemental Fig. 13A) of the recombinant tissue plasminogen activator (rtPA) (Fig. 6A). The addition of clinically relevant TXA concentration of 100 µM inhibited the fibrinolytic effect of rtPA and restored clot retraction under platelet count unadjusted conditions (Fig. 6, A and B, and Supplemental Fig. 13B and 14). However, TXA in a concentration of 1 µM was too low to restore clot retraction. No adverse effects could be observed at high concentrations of 10 mM TXA. As expected (*8*), *Myh9* mutant mice displayed prolonged bleeding times (Fig. 6C, and Supplemental Fig. 15). TXA concentration of 10 µg/g was injected to induce a plasma concentration measured in humans of 15 mg/L resulting in substantial inhibition of fibrinolysis (*15*). Strikingly, treatment with tranexamic acid significantly reduced the bleeding time in the three *Myh9* mutant mouse models (Fig. 6C, and Supplemental Fig. 15). In summary, the increased bleeding phenotype due to reduced platelet forces in *Myh9* mutant mice can be compensated by the addition of TXA.

TXA delays clot lysis of samples from *MYH9*-RD patients

The improved clot stability of mutant mouse samples prompted us to test the effect of TXA on clot formation and stability in patient samples. While the onset of lysis (LOT) measured by thromboelastometry occurred earlier for the human patient sample when adding rtPA, the addition of TXA rescued the defect (Fig. 7A, and Supplemental Fig. 16). Similarly, *ex vivo* thrombus stability of *MYH9*-RD patient platelets under shear was improved in the presence of TXA (Fig. 7, B and C, and Supplemental Fig. 17, A and B). We measured the stiffness of the thrombi with colloidal probe spectroscopy and found that TXA significantly increased the stiffness of thrombi from the *MYH9* p.D1424N sample for an extent of 1.589 (Fig. 7D). Improvement of thrombus stiffness with TXA could be achieved, however, to a lower extent by the factor of 1.20 for patient sample with E1841K mutation (Supplemental Fig. 17C). Together, this shows that TXA can also stabilize clots and thrombi of *MYH9*-RD patients.

Discussion

While the role of platelets in preventing blood loss is well characterized from a biological perspective, the mechanobiological aspects are only poorly understood. Therefore, we analyzed point-mutated *Myh9* mouse models, which recapitulate clinical manifestations observed in *MYH9*-RD patients. Our study demonstrates that non-muscle myosin IIA-mediated platelet force generation is crucial for sufficient clot compaction and hemostatic function. Our major conclusions are: (1) heterozygous point mutations in the *Myh9* gene lead to reduced platelet adhesion and platelet-platelet interaction forces in mice and *MYH9*-RD patients; (2) impaired clot retraction and prolonged bleeding time are caused by lower platelet force

generation, whereas the reduced platelet count is less critical; (3) the mutations R702C, D1424N, and E1841K have a similar impact on the biophysical platelet function, even though the mutation E1841K had less impact on thrombus formation and stiffness; and (4) inhibition of fibrinolysis with TXA can improve the hemostatic function in *Myh9* mutant mice.

We analyzed platelet activation of the *Myh9* R702C, D1424N, and E1841K mutant mice, which was overall comparable to controls when platelets of similar size were compared. The kinetics and extent of platelet aggregation did not differ between mutants and controls. Absent platelet shape change has been observed for myosin IIA-deficient mouse platelets (*13*) and patient platelets (*5, 16*). Surprisingly, we observed initial platelet shape change of the mutant platelets after activation with collagen and thrombin. Myosin IIA-deficient mouse platelets have, in general, a more pronounced phenotype and thus might explain the difference (*13, 17*). However, the difference regarding shape change between the point-mutated mouse platelets and platelets from patients remains unclear. We detected platelet shape change in aggregometry for all three mouse lines and two different agonists, suggesting that the localization of mutation or type of agonist does not explain the difference. Thus far, the point-mutated mouse models recapitulated the key features of *MYH9-RD* patients (reference (*8*) and our findings). However, we cannot exclude that platelets of the patients have a more severe defect in cytoskeletal rearrangement than we observed in the mouse models.

The degree of thrombocytopenia and bleeding varies among *MYH9*-RD patients. It was reported that the patients' platelet function is normal and severity of bleeding tendency correlates with platelet count (*7, 18*). Interestingly, it was previously demonstrated that the hemostatic function efficiently occurs at unexpectedly low platelet counts when platelets are fully functional, at least in mice (*19*). Therefore, our study addressed the relevance of how strongly mechanical forces contribute to the *MYH9*-related bleeding diathesis. We show that *in vitro* clot retraction of samples from *Myh9* R702C, D1424N, and E1841K point-mutated mice was impaired in both unadjusted and adjusted platelet count conditions, pointing to a less central role of the platelet count. However, clot retraction was still possible to some extent, in contrast to studies using the knockout mice with abrogated clot retraction (*13*). While so far the myosin activity inhibitor, blebbistatin, has been mainly used to analyze platelet force generation (*10, 20-22*), this approach cannot be used to assess the impact of the clinically relevant heterozygote mutations. Therefore we have taken a comprehensive biophysical approach to study the mechanical properties of heterozygously point-mutated *Myh9* platelets. Using SPFS, we demonstrate that *Myh9* R702C, D1424N, and E1841K mutant mouse platelets generate lower adhesion forces on collagen and reduced platelet-platelet interaction forces. We also measured traction forces of mutant mouse platelets on fibrinogen using a micropost deflection assay, which has already been successfully used to measure platelet contractile forces and evaluate platelet functionality (*21-23*). In line with the SPFS results, the average contractile

force per post of mutant platelets was decreased. While the total contractile force generated per platelet of *Myh9*$^{D1424N/+}$ mice was comparable to their corresponding controls. One possible explanation might be the enlarged size of *Myh9*$^{D1424N/+}$ platelets combined with a higher number of surface receptors. However, for a platelet-rich thrombus, in which contractility per unit volume is the relevant parameter, forces per post must be considered. These findings support the concept (*24*) that the inability of platelets to generate optimal contractile forces is associated with increased bleeding and is the predominant factor over reduced platelet numbers in *MYH9*-RD. Recently, high-throughput hydrogel-based platelet-contraction cytometry, which allows quantifying single-platelet contraction forces, revealed subpopulations of highly contractile human platelets (>30 nN) and that average platelet contractile forces varied considerably amongst healthy donors (*24*). In our study, the average total contractile force generated by wild-type mouse platelets ranged from 15.3 – 26.4 nN. However, a direct comparison of the two approaches cannot be made due to the different experimental conditions.

We further found that point-mutated *Myh9* platelets were less deformable under resting conditions (non-activated, non-spreading platelets) as determined by high-throughput RT-FDC. However, SICM analysis unveiled that spread *Myh9*$^{R702C/+}$ and *Myh9*$^{D1424N/+}$ platelets are more deformable than controls. While the increased F-actin content might explain the first finding in non-activated mutant platelets, the latter could be due to an altered actomyosin network under the platelet plasma membrane. It is tempting to speculate that the increased deformation of spread mutant platelets might contribute to the reduced traction forces. In support of this, it was shown in mouse embryonic fibroblasts that stiffer cells had a higher net contractile moment and were more prestressed than softer cells (*25*). Interestingly, *MYH9*-RD patients have normal red blood cell osmotic deformability as determined by ektacytometry (*26*). This suggests that *MYH9*-RD mutations have a distinct impact on the deformability of the two blood cell types.

We analyzed the spreading behavior of mutant mouse platelets on fibrinogen and found that heterozygous point-mutated *Myh9* mouse platelets form filopodia and lamellipodia to the same extent as controls. This is in contrast to a previous study, which showed reduced lamellipodia formation and observed more unspread D1424N mutant mouse platelets (*27*). We even found slightly increased spreading kinetics of mutant platelets (D1424N, E1841K) at an early time point, which may probably result from the enlarged platelet size and, therefore, earlier adhesion to the activating surface. We recently showed that lamellipodial structures cannot be observed in a blood clot and therefore are dispensable for the hemostatic function and thrombus formation (*28*). Kim *et al.* demonstrated that platelet filopodia extension and retraction are needed to transmit platelet contractile force and rearrange the fibrin matrix (*29*). In a very recent publication, the cytoskeletal structure in platelet protrusions was analyzed by applying

cryo-electron tomography, revealing a nonuniform polarity of actin filaments in protrusions, indicating that this organization may allow the generation of contractile forces (*30*). Our data in this study demonstrate that impaired clot formation is most likely due to reduced mechanical forces and not because of a defect in shape change or cytoskeletal rearrangement. Although we did not directly analyze actin stress fiber formation upon platelet spreading, immunofluorescent and platinum replica electron microscopic images revealed that most mutant platelets were able to form stress fibers on a continuously fibrinogen-coated surface. In contrast, myosin IIA-deficient platelets are unable to form stress fiber-like structures (*13*). This again shows that a complete deficiency of the protein myosin IIA in platelets produces a more severe phenotype than an amino acid change on one position.

In clinics, there are different approaches to treat bleeding complications in *MYH9*-RD patients (*31*). Thrombopoietin receptor agonists are an option for short-term treatment by increasing the platelet count (*32*). Desmopressin can be given to adults before surgery in combination with TXA. In addition, TXA is also used alone to treat excessive bleeding during menses or is locally applied after dental surgery (*6, 33*). Samson and colleagues showed that limited fibrinolysis paradoxically facilitates more efficient clot retraction, and TXA prevents clot shrinkage (*34*). But if TXA prevents clot retraction, why is it beneficial for *MYH9*-RD patients with bleeding complications? We hypothesized that plasminogen could better enter the gaps between platelets and more efficiently lyse the clot due to reduced interaction forces between mutant platelets. TXA, in turn, stabilizes the clot and prevents plasmin-induced clot instability. Indeed, we found that the administration of TXA could reverse the prolonged bleeding phenotype in mutant mice. Moreover, plasmin-induced clot lysis *in vitro* was prevented by TXA at a final concentration of 100 µM, which is expected to inhibit fibrinolysis (*15*). These findings suggest that insufficient hemostatic plug compaction due to reduced forces of *Myh9* mutant platelets can be overcome by TXA-mediated clot stabilization. Concerning the increased bleeding time observed in *Myh9* mutant mice, the impact of respective point mutations on the contribution of cytoskeleton-dependent mechanical properties of the endothelial and vascular smooth muscle cells remains to be investigated. Within this context, previous work by Goeckeler *et al.* in a bovine pulmonary artery endothelial cell line suggests that myosin II regulates endothelial cell tension which is abrogated by blebbistatin, resulting in the disappearance of stress fibers (*35*). Recently, Singh *et al.* demonstrated the association of non-muscle myosin IIA with contractile filaments in mouse aortic smooth muscle cells and how it is regulated through tension-dependent phosphorylation of focal adhesion proteins (*36*).

In summary, we comprehensively analyzed the molecular and mechanical characteristics of human and mouse platelets with heterozygous point mutations in non-muscle myosin IIA. We found that impaired clot retraction and increased bleeding tendency can be linked to reduced force generation and that interfering with the fibrinolytic system improves hemostatic function.

Materials and Methods

Animals

Myh9 mutant mice (*8*) were purchased from Mutant Mouse Resource & Research Centers (MMRRC). Stock numbers are 036196-UNC (R702C), 036210-UNC (D1424N), and 036698-MU (E1841K). Wild-type littermates were used as controls for the heterozygous mice from each mutant strain because of the different backgrounds. Female and male mice were between 6 and 16 weeks of age. Animal studies were approved by the district government of Lower Franconia, Germany (license number 2-523). Mice were kept at a 12-hour light and 12-hour dark cycle with food and water available *ad libitum* in the experimental area of the animal facility. We followed the guidelines of ARRIVE.

Human blood samples

The use of whole blood and PRP from healthy adult individuals and *MYH9*-RD patients was approved by the ethics committee of the University Medicine Greifswald, Germany (license number: BB 014/14). All participants gave written informed consent.

Platelet preparation

Mouse: Mice were anesthetized with isoflurane. Blood was collected in a tube containing heparin (20 U/mL, Ratiopharm) and platelet-rich plasma (PRP) was obtained by centrifugation at 80*g* for 5 min at room temperature (RT). For the preparation of washed platelets, PRP was centrifuged at 640*g* for 5 min at RT. The platelet pellet was resuspended in modified Tyrode's-HEPES buffer (134 mM NaCl, 0.34 mM Na_2HPO_4, 2.9 mM KCl, 12 mM $NaHCO_3$, 5 mM HEPES, 1 mM $MgCl_2$, 5 mM glucose, and 0.35% bovine serum albumin [BSA; pH 7.4]) in the presence of prostacyclin (0.5 µM) and apyrase (0.02 U/mL). Platelets were finally resuspended in the same buffer without prostacyclin (pH 7.4; 0.02 U/mL apyrase) and incubated at 37°C for 30 min before use.

Human: The donors had not taken any medication in the previous ten days before blood collection. Whole blood was collected by venipuncture in BD Vacutainer® Tubes containing acid citrate dextrose solution A (ACD-A) and 3.8% buffered trisodium citrate (Na-Citrate). Whole blood was stored at 37°C for at least 30 min. Centrifugation was not performed due to the large platelets of the *MYH9*-RD patients would sediment with the other blood cells due to their larger size. To maximize the number of platelets available for experiments (due to their reduced number in the patient sample), the ACD-A whole blood tubes were kept at a 45° angle, and PRP was transferred to a new polypropylene tube. All experimental measurements were performed within 3 hours of drawing the blood.

Immunoblotting

Washed platelets were lysed, separated by sodium dodecyl sulfate-polyacrylamide gel electrophoresis and blotted onto polyvinylidene difluoride membranes. Membranes were incubated with the respective antibodies against GAPDH (Sigma; 1:1000) and myosin IIA (Sigma; 1:200). Horseradish peroxidase-conjugated secondary antibodies and enhanced chemiluminescence solution (BioRad Clarity™ Western ECL Substrate) were used for visualization on an Amersham Imager 680 (GE Healthcare).

Immunoblotting with ProteinSimple Jess

Protein levels of MLC2, myosin IIA, MYPT1, and phosphorylation levels of MLC2 were analyzed using an automated capillary-based immunoassay platform (*37*); Jess (ProteinSimple). $5x10^8$ platelets/mL were lysed by addition of equal volume ice-cold 2x lysis buffer (300 mM NaCl, 20 mM TRIS, 2 mM EGTA, 2 mM EDTA, 10 mM NaF, 4 mM Na_3VO_4, 1% IGEPAL-CA630). The lysis buffer contained 2x Halt Protease and Phosphatase Inhibitor Cocktail, EDTA-Free (Thermo Scientific) to prevent protease and phosphatase activity. Lysates were diluted to the required concentration with 0.1x Sample Buffer 2 (diluted from 10x Sample Buffer 2). Lysates were prepared by the addition of 5x master mix containing 200 mM dithiothreitol (DTT), 5x sample buffer and fluorescent standards (Standard Pack 1) and boiled for 5 minutes at 95°C according to the manufacturer's instructions. The optimized antibody dilutions and respective lysate concentrations for each antibody (all from CST) are listed below: anti-MLC2 antibody 1:10, 0.1 mg/mL; anti-myosin IIA antibody 1:10, 0.025 mg/mL; anti-MLC2 p-S19 antibody 1:10, 0.4 mg/mL; anti-MYPT1 antibody 1:10, 0.1 mg/mL. For most antibodies, either anti-rabbit secondary HRP antibody (DM-001) or anti-mouse secondary HRP antibody was utilized and the chemiluminescent signal was recorded by using the High Dynamic Range (HDR) profile. For detection of myosin IIA, and MYPT1 signals in the R702C and E1841K knock-in samples, near-infrared (NIR) anti-rabbit secondary NIR Antibody was used with the corresponding fluorescent detection profile. NIR signal is presented in greyscale. All antibodies were diluted in antibody diluent 2. Samples, antibody diluent 2, primary and secondary antibodies, luminol-S and peroxide mix and wash buffer were displaced into 12-230 kDa prefilled microplates (prefilled with Separation Matrix 2, Stacking Matrix 2, Split Running Buffer 2 and Matrix Removal Buffer). The microplate was centrifuged for 5 minutes at 2500 rpm at room temperature. To start the assays, the capillary cartridge was inserted into the cartridge holder and the microplate placed on the plate holder. To operate Jess and analyze results Compass Software for Simple Western was used (version 4.1.0, ProteinSimple). Separation matrix loading time was set to 200 seconds, stacking matrix loading time to 15 seconds, sample loading time to 9 seconds, separation time to 30 minutes, separation voltage to 375

volts, antibody diluent time to 5 minutes, primary antibody incubation time to 90 minutes and secondary antibody incubation time to 30 minutes.

Transmission electron microscopy

Washed platelets in a concentration of 3 x 10^5 platelets/µL were fixed with 2.5% glutaraldehyde (Electron Microscopy Science) in cacodylate buffer (pH 7.2, AppliChem). Epon 812 (Electron Microscopy Science) was used to embed platelets. After generation of ultra-thin sections, platelets were stained with 2% uranyl acetate (Electron Microscopy Science) and lead citrate (Electron Microscopy Science). Sections were analyzed on a Zeiss EM900 electron microscope. Platinum replica electron microscopy of spread platelets was performed as previously described (*28*).

Flow cytometry

Whole blood was withdrawn from anaesthetized mice into heparin and diluted in Tyrode's-HEPES buffer. To determine glycoprotein expression blood was incubated for 15 minutes with respective fluorophore-conjugated antibodies (anti-GPIb: p0p4; anti-GPV: DOM1; anti-GPIX: p0p6; anti-αIIbβ3: JON1; anti-α2: LEN1; anti-CD9: ULF1; anti-GPVI: JAQ1; anti-CLEC2: INU1) (*38-42*). For activation studies, washed blood was resuspended in calcified Tyrode's-HEPES buffer (2 mM Ca^{2+}) after washing twice with Tyrode's-HEPES buffer. Platelets were incubated with agonists for 15 min and stained with fluorophore-labeled antibodies for 15 min at room temperature. For F-actin content analysis, washed platelets were incubated with an anti-GPIX antibody derivate labeled with Dylight-649 (20 µg/mL, Emfret). Cells were fixed in 10% paraformaldehyde (PFA), centrifuged and resuspended in Tyrode's-HEPES buffer in the presence of Ca^{2+} and 0.1% Triton X-100. Permeabilized cells were stained with 10 µM phalloidin-fluorescein isothiocyanate (FITC) for 30 minutes. Measurements were performed on a FACSCalibur (F-actin content of mouse line D1424N) or FACSCelesta (all others) (BioSciences, Heidelberg, Germany).

Aggregometry

Washed platelets (160 µL with 0.5 x 10^6 platelets/µL) were analyzed in the presence (collagen) or absence (thrombin) of 70 µg/mL human fibrinogen (Sigma). Light transmission was recorded on a four-channel aggregometer (Fibrintimer, APACT, Hamburg, Germany) for 10 min and expressed in arbitrary units, with buffer representing a light transmission of 100%.

Platelet spreading

Coverslips were coated with 100 µg/mL human fibrinogen (Sigma) for 2 hours at 37°C. After blocking with 1% BSA in PBS coverslips were washed thrice with PBS. Platelets (3 x 10^5

platelets/µL) were allowed to spread on the coated surface after the addition of 0.01 U/ml thrombin (Roche) and Ca^{2+}. After 5, 15 or 30 minutes, platelets were fixed with 4% PFA and permeabilized with IGEPAL CA-630. Images were taken with a Zeiss incubation microscope (100x objective, DIC).

Immunostaining of platelets

Fixed and permeabilized platelets were stained for myosin IIA using anti-myosin IIA (M8064 Sigma; 1:200 in PBS) and donkey anti-rabbit IgG-Alexa 546 antibodies (1:350 in PBS). F-actin was stained using phalloidin-Atto647N (A22287 Invitrogen; 1:500 in PBS) and α-tubulin using Alexa488-conjugated anti-α-tubulin antibodies (sc-23948 Santa Cruz; 1:500 in PBS), respectively. Visualization was performed using a Leica TCS SP8 confocal microscope (100x oil objective; NA 1.4). Confocal microscopy was performed with HC PL APO CS2 objectives. Depending on the stainings, a set of monochromatic lasers (488 nm; 561 nm; HeNe 633 nm) tuned to specific wavelengths were used. Detection filters (PMT Trans or ultrasensitive Hybrid detectors) were set to match the spectral properties of fluorochromes.

Clot retraction

PRP was filled up to a volume of 250 µL with Tyrode's-HEPES buffer to reach a platelet concentration of 3 x 10^5 platelets/µL. To investigate clot retraction with unadjusted platelet count 50 µl PRP was filled up to 250 µL with Tyrode's-HEPES buffer and 1 µL of red blood cells. After the addition of 0.2 U/ml thrombin (Roche) and 20 mmol/L $CaCl_2$ clot retraction was observed over a time period of 60 minutes. To investigate treatment with rtPA and TXA, concentrations of 1 µM, 100 µM and 10,000 µM of TXA (Merck) and 0.0138 nM rtPA (Abcam) were used and added together with thrombin and $CaCl_2$.

Bleeding time

Mice were anesthetized with a combination of pain reduction and narcotics (Fentanyl, Midazolam, Medetomidine; according to license 2-944) and a 1 mm segment of the tail tip was removed with a scalpel. Tail bleeding was monitored by gently absorbing blood with filter paper at 20-second intervals without making contact with the wound site. When no blood was observed on the paper, bleeding was determined to have ceased. Otherwise, experiments were stopped after 20 minutes. Bleeding times exceeding 20 minutes were excluded in the statistical analysis. TXA (Merck, 10 µg/g) or sodium chloride, as control, was injected intravenously 5 minutes before cutting the tail for bleeding time experiment.

Platelet adhesion under shear flow

Mouse: Heparinized whole blood was diluted in a ratio of 2:1 in Tyrode's-HEPES buffer containing Ca^{2+} (*43*). Whole blood or mixed platelet count adjusted blood (5 x 10^5 platelets/µL) was incubated with 0.2 µg/mL of an anti-GPIX antibody derivate conjugated with Dylight-488 at 37°C for 5 minutes. Coverslips were coated with 200 µg/mL Horm collagen (Nycomed) at 37°C over night and blocked with 1% BSA in PBS for 30 minutes. Whole blood was perfused over cover slips in the flow chamber (slit depth 50 µm) at shear stress equivalent to a wall shear rate of 1000 s^{-1} (Maastricht chamber (*44*)). Videos and images were taken with a Leica DMI6000 B inverted microscope (63x objective, light source Leica EL 6000, microscope controller Leica CTR6000). Analysis was performed using ImageJ software.

Human: Ex vivo thrombus formation assays was performed at a wall shear rate of 1000 s^{-1} on collagen-passivated surfaces (200 µg/mL HORM collagen type I from horse tendon; Nycomed) in a microfluidic parallel platelet flow chamber (on µ-Slide VI 0.1 with physical dimensions: 1 mm width, 100 µm height, and 17 mm length Ibidi GmbH, Germany). To visualize thrombus formation, prior to perfusion, platelets in ACD-A anticoagulated whole blood were stained with FITC-labelled anti-human CD61 antibody (Clone: RUU-PL7F12, Cat No: 340715 BD Pharmingen, USA, used at final ratio 1:100). Fibrin formation was visualized by spiking whole blood with human fibrinogen conjugated to Alexa Fluor 647 (Cat. No. F35200, Invitrogen, used at final concentration of 7.5 µg/mL). Whole blood was recalcified immediately before perfusion. Time-lapse confocal imaging (intervals of 10 seconds per image) was perfomed on a Leica SP5 confocal laser scanning microscope (Leica, Wetzlar, Germany) equipped with HCX PL APO λ blue 40.0×/1.25 oil objective. For image acquisition, fluorophores FITC and Alexa Fluor 647 were excited with Argon-Krypton (488 nm) and Helium-Neon (HeNe, 633 nm) laser lines, respectively, that were selected with an acousto-optic tunable filter (AOTF). Fluorescence emission was collected between 505-515 nm for FITC (detector HyD), and 640-655 nm for Alexa Fluor 647 (detector HyD). To assess the impact of TXA in some experiments, whole blood was preincubated with TXA (100 µM) for 10 minutes prior to perfusion over collagen. Impact of rtPA (137 ng/mL) on fibrin degradation was assessed under shear flow of 100 s^{-1}, added after 10 minutes of thrombus formation. Quantitative assessment of platelet adhesion and thrombus formation was performed to obtain the percentage area covered by thrombi over time by computational image analysis using the surfaces creation wizard algorithm in Bitplane Imaris version 7.65 (Oxford Instruments, Abingdon, United Kingdom). Experiments were performed according to International Society on Thrombosis and Haemostasis Scientific and Standardization Committee (ISTH SSC) subcommittee on Biorheology recommendations (*45*).

Real-time fluorescence deformability cytometry (RT-FDC)

Mouse: 25 µL of whole blood bled in citrate was suspended in 425 µL CellCarrier B. The measurement was stopped after achieving 10,000 single platelet count (hard gate Area 0 - 40 μm^2). Using the Shape-Out analysis software (https://github.com/ZELLMECHANIK-DRESDEN/ShapeOut2/releases/tag/2.3.0 Version 2.3, Zellmechanik Dresden, Germany), kernel density estimation (KDE) plots of event density were generated, and statistical analysis using Holm-Sidak method was performed to determine the median values for platelet deformation and their size. The range area ratio was limited to 0 - 1.1 and the cell size to 0 - 10 μm^2 for the analysis.

Human: Platelets in PRP were labeled with a mouse anti-human monoclonal antibody CD61-PE (Cat. No. IM3605, Beckman Coulter). Incubation was performed at room temperature for 10 minutes in the dark. Deformation measurements were performed in a microfluidic chip with a constriction of 15 µm x 15 µm cross-section and a length of 300 µm (Flic15, Zellmechanik Dresden, Germany). RT-FDC measurements were carried out in buffer CellCarrier B (Zellmechanik Dresden, Germany), which is composed of 0.6% (w/v) methylcellulose in PBS (without Ca^{2+}, Mg^{2+}). Here, 50 µL of immunofluorescently labeled human PRP was suspended in 450 µL CellCarrier B. The human PRP suspension was then driven through the microfluidic chip at flow rates of 0.006 µL/s, and the measurement was stopped after achieving 5,000 single platelet count (hard-gate 150-33000 arbitrary units, A.U. for CD61-PE of fluorescence intensity) or after 10 min. RT-FDC data was acquired using the ShapeIn software (Version 2.0, Zellmechanik Dresden, Germany). Using the Shape-Out analysis software, kernel density estimation (KDE) plots of event density were generated, and statistical analysis was performed to determine the median values for platelet deformation and their size. The range area ratio was limited to 0 - 1.1 and the cell size to 0 - 25 μm^2 for the analysis.
The RT-FDC setup (AcCellerator, Zellmechanik Dresden, Germany) is built around an inverted microscope (Axio Observer A1, Carl Zeiss AG, Germany) mounted with a Zeiss A-Plan 100x NA 0.8 objective (*46, 47*).

Single platelet force spectroscopy (SPFS)

Silicon CSC12, 0.6 N/m tipless cantilevers (MicroMasch, Tallin, Estonia) and Glass-bottom 35 mm dishes (IBIDI, Martinsried, Germany) were exposed to UV cleaner (Bioforce Labs, Ames, IA, USA) for 30 min. Before coating, the cantilever spring constants were independently measured by a thermal tune procedure (JPK). Cantilevers were incubated with 50 µg/mL collagen G for 3h at 37°C and rinsed three times with Tyrode´s buffer. An aliquot of 15 x 10^3 platelets/µL in Tyrode´s buffer containing 1.0 mM $CaCl_2$ and 0.5 mM $MgCl_2$ was dropped onto the passivated glass right before each measurement (10 min, RT). Unbound platelets were removed by Tyrode´s buffer. To immobilize a single platelet on the cantilever, the collagen

passivated-cantilever was brought into contact (setpoint 200 pN) with a non-activated platelet on BSA passivated glass slide. It was waited until a single platelet firmly adhered to the ventral surface at the tip of the cantilever. The cantilever with the adhered platelet was then moved to HORM collagen passivated surface and single platelets firmly attached to the HORM collagen for platelet-substrate and platelet-platelet interaction SPFS measurements, respectively. All measurements were carried out in Tyrode's with Ca^{2+}, glucose and BSA using a JPK NanoWizard 3 (JPK, Berlin, Germany). Force distance (F-D) curves were recorded with a Z-length of 7 µm and a setpoint value of 200 pN to control the maximal force of the cantilever against the surface. A velocity of 15 µm/s was used for all measurements to avoid merging of two platelets during contact and to rupture completely two platelets from each other. For each passivated-substrate, the last 500 force-distance curves were taken from 7 to 10 single platelets.

Colloidal probe spectroscopy

To determine the Young's modulus of platelet aggregates, indentation experiments were performed by means of colloidal force spectroscopy using an atomic force microscope (Nanowizard 3, JPK Instruments). The atomic force microscope is combined with an optical system comprised of an inverted optical microscope (IX8, Olympus; 20x objective). Gold-coated cantilevers (Cat. No. CP-qp-CONT-AU-A-5, NANOANDMORE GmbH, AFM tip: sphere (1.5 µm – 3 µm)) coated with 8.45 mM poly(ethylene glycol)methyl ether thiol (Mn 800, Cat. No. 729108, Sigma Aldrich) solution for 2 h at room temperature were used. Measurements were carried out in suspension buffer (136 mM NaCl, 0.41 mM Na_2HPO_4, 2.65 mM KCl, 12 mM $NaHCO_3$, 2.13 mM $MgCl_2$, 2.0 mM $CaCl_2$, 5.5 mM D-glucose, and 0.35% BSA, pH 7.4). Before each experiment the sensitivity and spring constant of each cantilever were determined individually in suspension buffer. For sensitivity calibration the cantilever deflection upon contact with a freshly cleaved mica surface was analyzed (ensemble average 23,3 ± 3.1 nm/V) and spring constant was measured by thermal noise technique (ensamble average 98 ± 30 mN/m). 1 ml ACD-A human whole blood was treated with 7.5 µl 1 M $CaCl_2$ x 2 H_2O and 1.88 µl 2 M $MgCl_2$ x 6 H_2O solution. Heparinized whole blood was used for the mouse experiments. Coverslips, which were coated with 80 µg/ml Horm collagen (Nycomed) at 37°C overnight and blocked with 1% BSA in PBS for 10 minutes, were installed into a flow chamber with a slit depth of 55 µm (Cat.No. 20000209, straight channel chip, microfluidic ChipShop). Recalcified whole blood was perfused at shear stress 1000 s^{-1} for 5 minutes. Coverslips were washed three times with suspension solution. The cantilever was brought into contact with platelet aggregates at a speed of 2.7 µm s^{-1} with a force setpoint defined at 2 nN. Measurements were performed at room temperature in suspension buffer. Platelet Young's modulus *E* was calculated from AFM indentation force curves by applying the Hertz model which describes

how the force increases as the AFM probe pushes into the cell. In short, cantilever deflection force *F* was fitted to the equation $F(z) = \frac{4}{3}E \cdot R_{sphere}^{\frac{1}{2}} \cdot z^{\frac{3}{2}}/(1-\nu^2)$. Here, R_{sphere} is the radius of the AFM sphere probing the cells, *z* is the cell indentation and the Poisson's ratio *υ* was set to 0.5 assuming cell volume conservation. Details can be found elsewhere (*48, 49*). Five platelet aggregates with at least 25 force curves per aggregate were recorded per coverslide and each force curve was analyzed individually. Thus, for each experimental condition platelet Young's modulus is given as the mean value of more than 100 individual force curves.
For rtPA measurements, 500 µl of 137 ng/mL rtPA (Cat No. ab92637; Abcam) was added to the coverslide immediately after measurement of the untreated or TXA sample and incubated for 5 minutes. For TXA measurements, 1 ml whole blood was incubated with 100 µM TXA (Merck) for 10 minutes and further treated as described above.

Micropost assay

Micropost arrays were fabricated from hPDMS (#PP2-RG07; Gelest Inc) by replica molding from negative molds. Micropost arrays contained cylindrical posts with 1.05 µm diameter and 2.6 µm height arranged on a hexagonal grid with 2.0 µm center-to-center spacing. The Young's modulus of hPDMS was 4.7 MPa. Flat stamps for microcontact printing were made from Sylgard 184 (Dow Corning Inc). Fluorescently labeled (Alexa Fluor 488 NHS ester; Invitrogen) fibrinogen (Sigma) was physisorbed from solution (0.1 mg/mL in PBS) onto stamps for one hour, quickly washed with distilled water, and blown dry under nitrogen. Coated stamps were brought into conformal contact with micropost arrays, which had been pre-activated for 7 minutes by UV/Ozone treatment, pressed down using a forceps, and removed. The transfer efficiency of fibrinogen was confirmed by fluorescence microscopy of stamps and microposts and typically was >90%. Micropost arrays were passivated using a 1:2 mix (0.5 mg/mL in PBS) of fluorescently labeled (DyLight 405 NHS ester; Fisher Scientific Ireland) endotoxin-free bovine serum albumin (BSA; Sigma) to non-labeled BSA for 30 minutes, followed by Pluronics F127 (0.5% w/v in PBS) for 30 minutes, before washing three times with PBS. Washed platelets were resuspended in Tyrode's buffer and seeded in the presence of thrombin (0.01 U/mL) onto the coverslips at a density of ~ 2 million cm^{-2} for 60 minutes at 37°C, fixed in 3% paraformaldehyde in PBS for 15 minutes, and washed three times in PBS. Samples were permeabilized, blocked and stained for F-actin (phalloidin-Alexa Fluor 647; Invitrogen; 1:100 in 3% BSA in PBS) for 30 minutes, washed, and mounted in a chamber (Chamlide; Live Cell Instruments Co Ltd) containing PBS. Confocal images were obtained on a Leica SP8 from top and bottom slices of the microposts. Image analysis of traction forces was performed by custom MATLAB code. Posts were detected by template matching and their positions refined by a radial symmetry fit. Post deflections were deduced from the positions of the same post in top and bottom slices after removal of systematic offsets between the slices. Traction forces

were calculated from the post deflections by Hooke's law using a spring constant of 34.51 nN/µm (*50*).

Scanning ion conductance microscopy (SICM)

35 mm round polystyrene cell culture dishes (Greiner Bio One, Ref. 627161) were coated with fibrinogen (Sigma-Aldrich, F3879, 0.1 mg/mL) by incubation for 1 h at 37°C. Washed mouse platelets were resuspended in Tyrode's buffer supplemented with 1 mM Ca^{2+} and seeded in the presence of thrombin (Sigma-Aldrich, T6884, 0.01 U/mL) for 15 min at room temperature. Afterwards, the culture dishes were washed three times with Tyrode's buffer to remove non-adherent platelets. The dishes were then installed in custom-built SICM setups (*51*) and imaged within one hour. Platelet morphology and elastic modulus were visualized using borosilicate pipettes with an inner radius of ≈90 nm and an applied pressure of 10 kPa. Imaging was done at a 20 Hz pixel rate, with 32 x 32 or 64 x 64 pixels at scan sizes between 6 x 6 and 12 x 12 μm^2. Data were pooled from two donors. Analysis of elastic modulus *E* was calculated as described before (*52*).

Thromboelastography

Rotational thromboelastometry (ROTEM) was used with a modified version of the commercial tissue factor-activated test (EXTEM) to detect changes in fibrinolytic activity (*53*). In detail, we triggered the lysis *ex vivo* by adding rtPA (Abcam) at a final concentration of 137 ng/mL as reported (*53*). In a parallel application, we tried to contrast the lysis stimulation by contemporarily adding tranexamic acid (Merck) at a final concentration of 100 µM, which is expected to inhibit fibrinolysis (*15*). The ROTEM device was from Pentapharm GmbH, Munich, Germany. The maximum runtime was set to 150 minutes. The following standard parameters were analyzed: lysis onset time (LOT), and lysis time (LT) in minutes.

Data analysis

Results are from at least two independent experiments per group, if not otherwise stated. Correction for multiple comparisons was analyzed using the Holm-Sidak method and differences between control and mutant sample were statistically analyzed using the Mann-Whitney-U test. P-values < 0.05 were considered as statistically significant: *0.05 > p ≥ 0.01; **0.01 > p ≥ 0.001; ***p < 0.001. Results with a P-value ≥ 0.05 were considered as not significant.

References

1. W. A. Lam *et al.*, Mechanics and contraction dynamics of single platelets and implications for clot stiffening. *Nat Mater* **10**, 61-66 (2011).
2. Y. Qiu, J. Ciciliano, D. R. Myers, R. Tran, W. A. Lam, Platelets and physics: How platelets "feel" and respond to their mechanical microenvironment. *Blood Rev* **29**, 377-386 (2015).
3. J. G. Drachman, Inherited thrombocytopenia: when a low platelet count does not mean ITP. *Blood* **103**, 390-398 (2004).
4. M. Seri *et al.*, Mutations in MYH9 result in the May-Hegglin anomaly, and Fechtner and Sebastian syndromes. The May-Heggllin/Fechtner Syndrome Consortium. *Nat Genet* **26**, 103-105 (2000).
5. K. Althaus, A. Greinacher, MYH9-related platelet disorders. *Semin Thromb Hemost* **35**, 189-203 (2009).
6. K. Althaus, J. Najm, A. Greinacher, MYH9 related platelet disorders - often unknown and misdiagnosed. *Klin Padiatr* **223**, 120-125 (2011).
7. A. Pecci *et al.*, MYH9-related disease: a novel prognostic model to predict the clinical evolution of the disease based on genotype-phenotype correlations. *Hum Mutat* **35**, 236-247 (2014).
8. Y. Zhang *et al.*, Mouse models of MYH9-related disease: mutations in nonmuscle myosin II-A. *Blood* **119**, 238-250 (2012).
9. C. L. Balduini, A. Pecci, A. Savoia, Recent advances in the understanding and management of MYH9-related inherited thrombocytopenias. *Br J Haematol* **154**, 161-174 (2011).
10. A. Ono *et al.*, Identification of a fibrin-independent platelet contractile mechanism regulating primary hemostasis and thrombus growth. *Blood* **112**, 90-99 (2008).
11. O. Oshinowo *et al.*, Significant differences in single-platelet biophysics exist across species but attenuate during clot formation. *Blood Adv* **5**, 432-437 (2021).
12. J. D. Franke, A. L. Boury, N. J. Gerald, D. P. Kiehart, Native nonmuscle myosin II stability and light chain binding in Drosophila melanogaster. *Cell Motil Cytoskeleton* **63**, 604-622 (2006).
13. C. Leon *et al.*, Megakaryocyte-restricted MYH9 inactivation dramatically affects hemostasis while preserving platelet aggregation and secretion. *Blood* **110**, 3183-3191 (2007).
14. D. A. Knecht, W. F. Loomis, Developmental consequences of the lack of myosin heavy chain in Dictyostelium discoideum. *Dev Biol* **128**, 178-184 (1988).
15. R. Picetti, H. Shakur-Still, R. L. Medcalf, J. F. Standing, I. Roberts, What concentration of tranexamic acid is needed to inhibit fibrinolysis? A systematic review of pharmacodynamics studies. *Blood Coagul Fibrinolysis* **30**, 1-10 (2019).
16. I. Canobbio *et al.*, Altered cytoskeleton organization in platelets from patients with MYH9-related disease. *J Thromb Haemost* **3**, 1026-1035 (2005).
17. F. Pertuy *et al.*, Myosin IIA is critical for organelle distribution and F-actin organization in megakaryocytes and platelets. *Blood* **123**, 1261-1269 (2014).
18. A. Pecci, X. Ma, A. Savoia, R. S. Adelstein, MYH9: Structure, functions and role of non-muscle myosin IIA in human disease. *Gene* **664**, 152-167 (2018).
19. M. Morowski *et al.*, Only severe thrombocytopenia results in bleeding and defective thrombus formation in mice. *Blood* **121**, 4938-4947 (2013).
20. L. H. Ting *et al.*, Contractile forces in platelet aggregates under microfluidic shear gradients reflect platelet inhibition and bleeding risk. *Nat Commun* **10**, 1204 (2019).
21. S. Feghhi, W. W. Tooley, N. J. Sniadecki, Nonmuscle Myosin IIA Regulates Platelet Contractile Forces Through Rho Kinase and Myosin Light-Chain Kinase. *J Biomech Eng* **138**, (2016).
22. S. Feghhi *et al.*, Glycoprotein Ib-IX-V Complex Transmits Cytoskeletal Forces That Enhance Platelet Adhesion. *Biophys J* **111**, 601-608 (2016).
23. X. M. Liang, S. J. Han, J. A. Reems, D. Gao, N. J. Sniadecki, Platelet retraction force measurements using flexible post force sensors. *Lab Chip* **10**, 991-998 (2010).

24. D. R. Myers *et al.*, Single-platelet nanomechanics measured by high-throughput cytometry. *Nat Mater* **16**, 230-235 (2017).
25. N. Schierbaum, J. Rheinlaender, T. E. Schaffer, Combined atomic force microscopy (AFM) and traction force microscopy (TFM) reveals a correlation between viscoelastic material properties and contractile prestress of living cells. *Soft Matter* **15**, 1721-1729 (2019).
26. A. S. Smith *et al.*, MYH9-related disease mutations cause abnormal red blood cell morphology through increased myosin-actin binding at the membrane. *Am J Hematol* **94**, 667-677 (2019).
27. K. Pal *et al.*, Megakaryocyte migration defects due to nonmuscle myosin IIA mutations underlie thrombocytopenia in MYH9-related disease. *Blood* **135**, 1887-1898 (2020).
28. Y. Schurr *et al.*, Platelet lamellipodium formation is not required for thrombus formation and stability. *Blood* **134**, 2318-2329 (2019).
29. O. V. Kim, R. I. Litvinov, M. S. Alber, J. W. Weisel, Quantitative structural mechanobiology of platelet-driven blood clot contraction. *Nat Commun* **8**, 1274 (2017).
30. S. Sorrentino *et al.*, Structural analysis of receptors and actin polarity in platelet protrusions. *Proc Natl Acad Sci U S A* **118**, (2021).
31. A. Pecci, C. L. Balduini, Inherited thrombocytopenias: an updated guide for clinicians. *Blood Rev* **48**, 100784 (2021).
32. C. Zaninetti *et al.*, Eltrombopag in preparation for surgery in patients with severe MYH9-related thrombocytopenia. *Am J Hematol* **94**, E199-E201 (2019).
33. K. Althaus, A. Greinacher, MYH-9 Related Platelet Disorders: Strategies for Management and Diagnosis. *Transfus Med Hemother* **37**, 260-267 (2010).
34. A. L. Samson *et al.*, Endogenous fibrinolysis facilitates clot retraction in vivo. *Blood* **130**, 2453-2462 (2017).
35. Z. M. Goeckeler, P. C. Bridgman, R. B. Wysolmerski, Nonmuscle myosin II is responsible for maintaining endothelial cell basal tone and stress fiber integrity. *Am J Physiol Cell Physiol* **295**, C994-1006 (2008).
36. K. Singh, A. B. Kim, K. G. Morgan, Non-muscle myosin II regulates aortic stiffness through effects on specific focal adhesion proteins and the non-muscle cortical cytoskeleton. *J Cell Mol Med* **25**, 2471-2483 (2021).
37. T. Heib *et al.*, RhoA/Cdc42 signaling drives cytoplasmic maturation but not endomitosis in megakaryocytes. *Cell Rep* **35**, 109102 (2021).
38. B. Nieswandt, W. Bergmeier, K. Rackebrandt, J. E. Gessner, H. Zirngibl, Identification of critical antigen-specific mechanisms in the development of immune thrombocytopenic purpura in mice. *Blood* **96**, 2520-2527 (2000).
39. B. Nieswandt *et al.*, Expression and function of the mouse collagen receptor glycoprotein VI is strictly dependent on its association with the FcRgamma chain. *J Biol Chem* **275**, 23998-24002 (2000).
40. W. Bergmeier, K. Rackebrandt, W. Schroder, H. Zirngibl, B. Nieswandt, Structural and functional characterization of the mouse von Willebrand factor receptor GPIb-IX with novel monoclonal antibodies. *Blood* **95**, 886-893 (2000).
41. B. Nieswandt *et al.*, Glycoprotein VI but not alpha2beta1 integrin is essential for platelet interaction with collagen. *EMBO J* **20**, 2120-2130 (2001).
42. F. May *et al.*, CLEC-2 is an essential platelet-activating receptor in hemostasis and thrombosis. *Blood* **114**, 3464-3472 (2009).
43. Y. Schurr, M. Spindler, H. Kurz, M. Bender, The cytoskeletal crosslinking protein MACF1 is dispensable for thrombus formation and hemostasis. *Sci Rep* **9**, 7726 (2019).
44. L. Herfs *et al.*, Multiparameter microfluidics assay of thrombus formation reveals increased sensitivity to contraction and antiplatelet agents at physiological temperature. *Thromb Res* **203**, 46-56 (2021).
45. P. H. Mangin *et al.*, In vitro flow based systems to study platelet function and thrombus formation: Recommendations for standardization: Communication from the SSC on Biorheology of the ISTH. *J Thromb Haemost* **18**, 748-752 (2020).
46. O. Otto *et al.*, Real-time deformability cytometry: on-the-fly cell mechanical phenotyping. *Nat Methods* **12**, 199-202, 194 p following 202 (2015).

47. P. Rosendahl *et al.*, Real-time fluorescence and deformability cytometry. *Nat Methods* **15**, 355-358 (2018).
48. A. Weber, J. Iturri, R. Benitez, J. L. Toca-Herrera, Measuring biomaterials mechanics with atomic force microscopy. 1. Influence of the loading rate and applied force (pyramidal tips). *Microsc Res Tech* **82**, 1392-1400 (2019).
49. M. Glaubitz *et al.*, A novel contact model for AFM indentation experiments on soft spherical cell-like particles. *Soft Matter* **10**, 6732-6741 (2014).
50. I. Schoen, W. Hu, E. Klotzsch, V. Vogel, Probing cellular traction forces by micropillar arrays: contribution of substrate warping to pillar deflection. *Nano Lett* **10**, 1823-1830 (2010).
51. J. Seifert, J. Rheinlaender, F. Lang, M. Gawaz, T. E. Schaffer, Thrombin-induced cytoskeleton dynamics in spread human platelets observed with fast scanning ion conductance microscopy. *Sci Rep* **7**, 4810 (2017).
52. J. Rheinlaender *et al.*, Imaging the elastic modulus of human platelets during thrombin-induced activation using scanning ion conductance microscopy. *Thromb Haemost* **113**, 305-311 (2015).
53. G. J. Kuiper *et al.*, Validation of a modified thromboelastometry approach to detect changes in fibrinolytic activity. *Thromb J* **14**, 1 (2016).

Acknowledgments

The authors thank Daniela Naumann, Kim Ulbrich, Tamara Nahm, Doreen Biedenweg, Manu Emanuel, Nguyen Thi-Huong, Julia Klauke, Ricarda Raschke and Jan Wesche for excellent technical assistance.

Funding: This work was supported by TR240 grant with project number 374031971 of the Deutsche Forschungsgemeinschaft (DFG; German Research Foundation), by the Deutsches Zentrum für Herz-Kreislauf-Forschung (Postdoc start-up grant under grant agreement 81X3400107), by the Bundesministerium für Bildung und Forschung (ZIK grant under grant agreement 03Z22CN11) and by the DFG - project number 335549539/GRK2381. I.S. acknowledges funding from RCSI.

Author contributions:

Performed experiments: JB, LS, OO, IS, CZ, RK, HE, JR, ZN, RP, MB
Data analysis: all authors
Writing – original draft: JB, LS, RP, MB
Supervised research: OO, AG, TES, RP, MB
Funding acquisition: OO, IS, TES, RP, MB
All authors have critically revised and approved the final version of the manuscript.

Competing interests: O.O. is co-founder and shareholder of Zellmechanik Dresden distributing the AcCellerator for real-time fluorescence and deformability cytometry measurements. All other authors declare no competing financial interests.

Data and materials availability: All data needed to evaluate the conclusions in the paper are present in the paper and/or the Supplementary Materials.

Figures

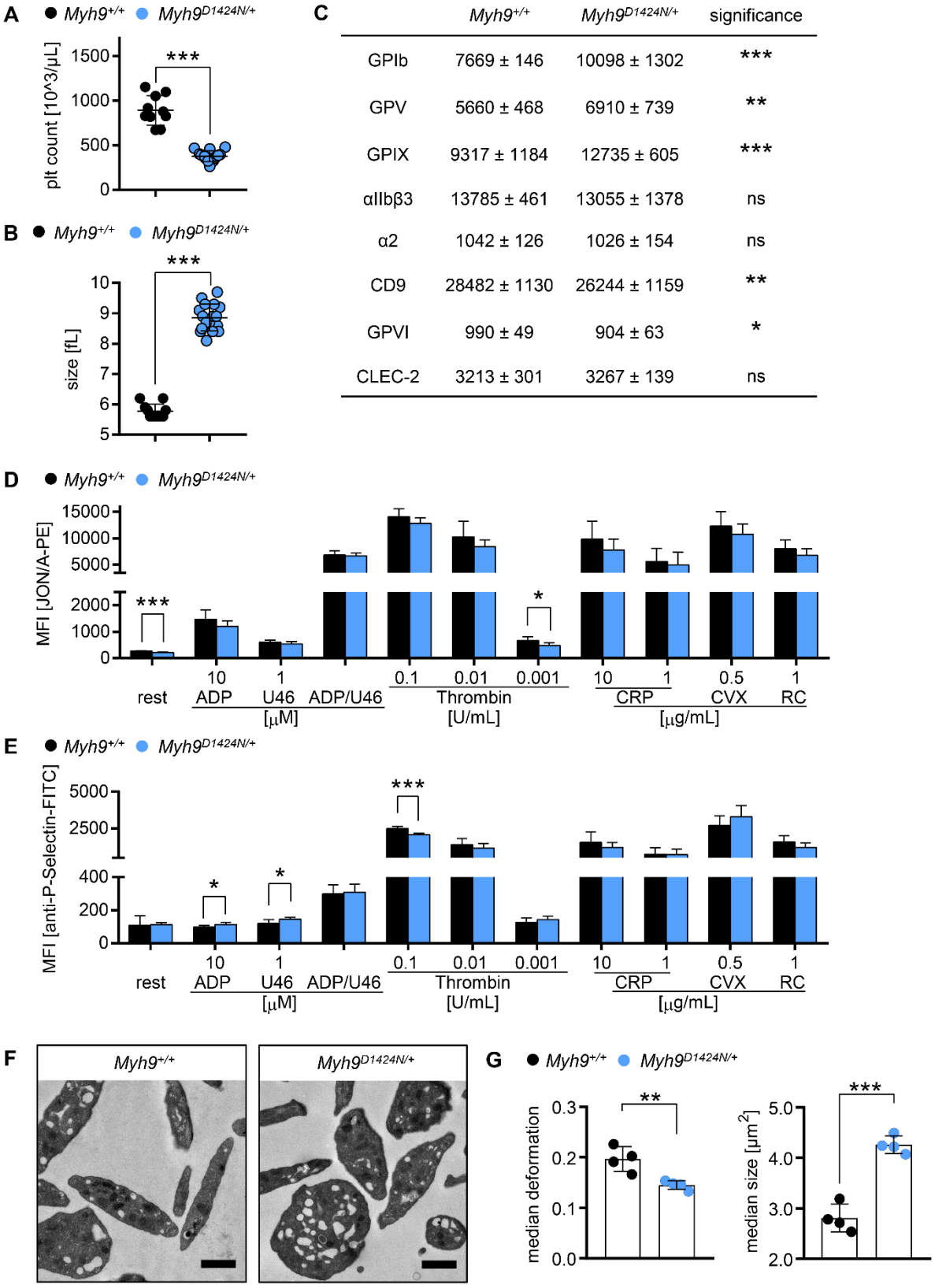

Fig. 1. Mutation in *Myh9* gene impairs platelet size and stiffness. (**A**) Platelet count per microliter and (**B**) platelet size of *Myh9*$^{+/+}$ and *Myh9*$^{D1424N/+}$ mice were determined by a

hematology analyzer. (**A** and **B**) Each symbol represents one individual mouse (mean ± S.D.; Mann-Whitney U-test ***p < 0.001). (**C**) Expression of glycoproteins on the platelet surface was determined by flow cytometry (n=6). (**D**) Activation of platelet αIIbβ3-integrin (JON/A-phycoerythrin [PE]) and (**E**) α-granule release (anti-P-Selectin-fluorescein isothiocyanate [FITC]) were assessed under resting (rest) conditions and upon stimulation with different agonists by flow cytometry (n=6). ADP: adenosine diphosphate; U46: thromboxane A2 analog U46619; CRP: collagen-related peptide; CVX: Convulxin; RC: Rhodocytin. (**C** to **E**) Data are expressed as mean fluorescence intensity [MFI]. (**F**) Transmission electron micrographs from *Myh9*$^{+/+}$ and *Myh9*$^{D1424N/+}$ platelets; scale bars represent 1 µm. (**G**) Each data point of RT-FDC measurement shows the median deformation or median area of at least 2000 platelets from one subject and bar plots show mean ± S.D. of platelet deformation or platelet area (n=4). Statistics: Multiple comparison using Holm-Sidak (ns $p \geq 0.05$; *$0.05 > p \geq 0.01$; **$0.01 > p \geq 0.001$; ***$p < 0.001$).

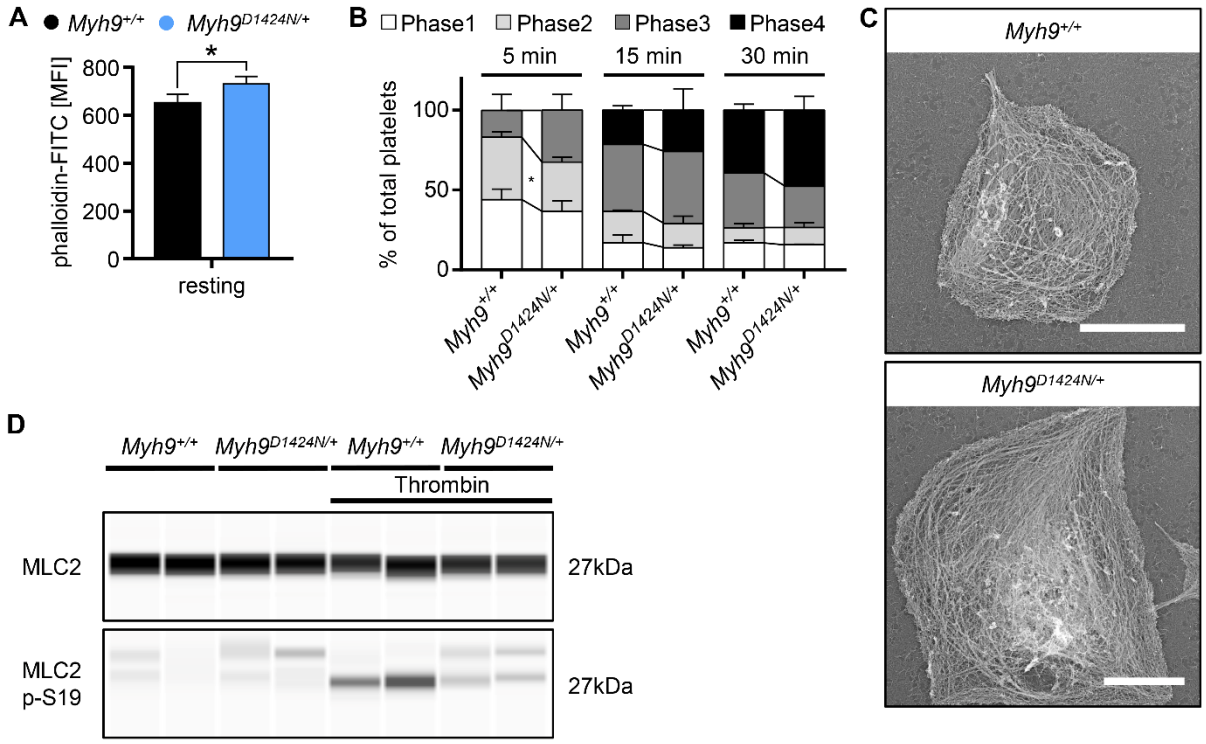

Fig. 2. Phosphorylation of MLC2 is decreased in *Myh9*$^{D1424N/+}$ platelets. (**A**) F-actin content of resting platelets was measured by flow cytometry after incubation with phalloidin-FITC (n=3-7). The mean fluorescence intensity is shown. (**B**) Statistical analysis of the different spreading phases (phase 1: resting platelets; phase 2: platelets forming filopodia; phase 3: platelets forming lamellipodia and filopodia; phase 4: fully spread platelets) of fixed *Myh9*$^{+/+}$ and *Myh9*$^{D1424N/+}$ platelets on fibrinogen at different time points expressed as mean ± S.D. (n=2). (**C**) Representative PREM images of the cytoskeleton ultrastructure of platelets spread on fibrinogen in the presence of thrombin (scale bars 2 µm). (**D**) Expression of MLC2 and phosphorylated MLC2p-S19 in resting and thrombin-activated (0.05 U/mL, 1 min) platelets was determined by using an automated quantitative capillary-based immunoassay platform, Jess (ProteinSimple). Representative immunoblot of three independent experiments is shown (n=2). Statistics: Multiple comparison using Holm-Sidak (*0.05 > p ≥ 0.01).

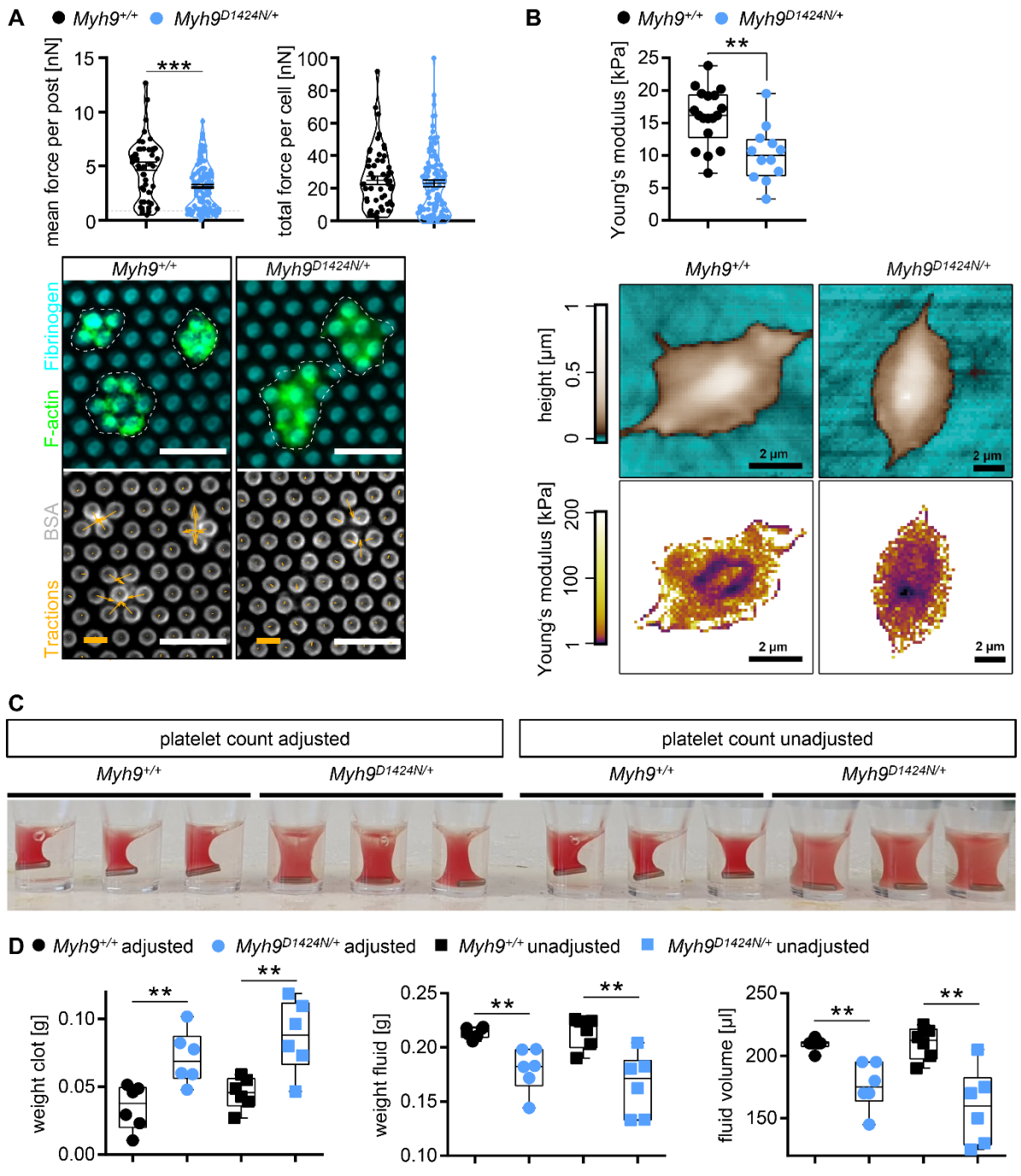

Fig. 3. Less contractile forces and reduced clot retraction of *Myh9* mutant platelets. (**A**) Platelet contractile forces were measured per post and the sum of posts per cell (mean ± S.D.; *Myh9*$^{+/+}$: n=51 platelets; *Myh9*$^{D1424N/+}$: n=124 platelets). Representative images of individual platelets (dashed white), stained for F-actin, and its traction on micropost stained for fibrinogen, and BSA (scale bars 5 µm, force bar 10 nN). Statistics: Mann-Whitney U-test (ns $p \geq 0.05$; ***$p < 0.001$). (**B**) Washed *Myh9*$^{+/+}$ and *Myh9*$^{D1424N/+}$ platelets spread on fibrinogen in the presence of thrombin were analyzed of their Young's modulus using scanning ion conductance microscopy. Each symbol represents one platelet (*Myh9*$^{+/+}$: n=20 platelets; *Myh9*$^{D1424N/+}$: n=12 platelets) and box plots represents median ± S.D (Statistics: Mann-Whitney U-test **$0.01 > p$

≥ 0.001). Representative images showing the height (upper row) or Young's modulus (lower row) of *Myh9*$^{+/+}$ and *Myh9*$^{D1424N/+}$ platelets. (**C**) Representative image of clot formation at time point 60 minutes (n=3). (**D**) Statistical analysis of weight from residual clot and fluid, and of volume from residual fluid depict median ± S.D. Each symbol represents one individual mouse (Multiple comparison using Holm-Sidak **0.01 > p ≥ 0.001).

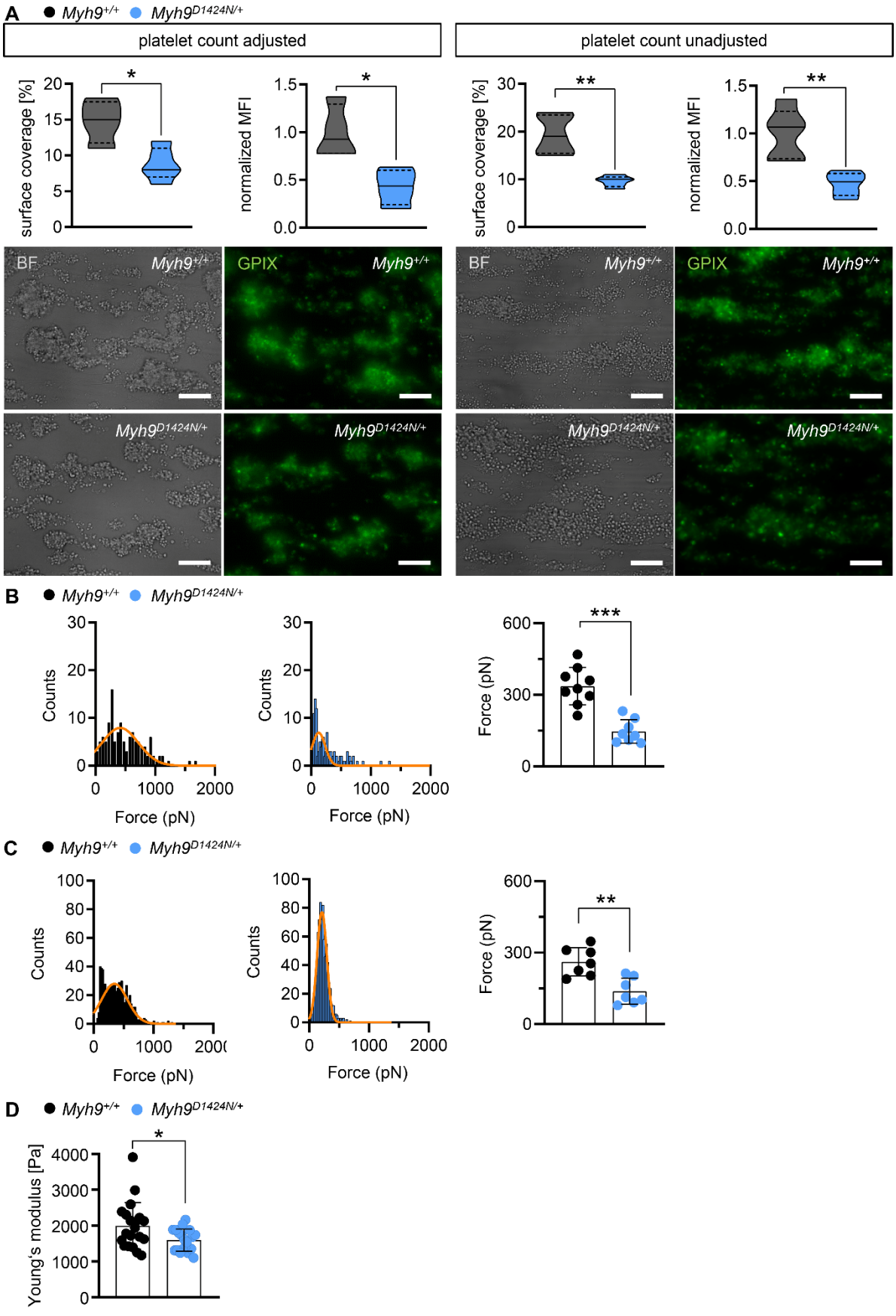

Fig. 4. Lower adhesion and interaction forces of *Myh9*$^{D1424N/+}$ platelets lead to smaller, and softer thrombi. (**A**) Assessment of platelet adhesion and aggregate formation under flow

(1000/s) on collagen of *Myh9*$^{+/+}$ and *Myh9*$^{D1424N/+}$ samples. Analysis of the surface area covered by platelets (%) and the relative normalized thrombus MFI of anti-GPIX (Alexa 488) are shown of platelet count adjusted conditions on the left side (mean ± S.D.; n=4) and unadjusted conditions on the right side (mean ± S.D.; n=5). Respective representative images taken at the end of the perfusion time are shown in brightfield and fluorescent images with platelets labeled with the anti-GPIX-antibody (scale bars 30 µm). Single platelet force spectroscopy was performed to determine (**B**) adhesion forces (platelet to collagen) and (**C**) platelet to platelet interaction forces. (**B** and **C**) Representative SPFS curves from one platelet adhering to collagen or interacting with another platelet of *Myh9*$^{+/+}$ or *Myh9*$^{D1424N/+}$ sample is shown. Each data point of summary graphs (mean ± S.D.) shows one platelet to collagen (n=9) or platelet to platelet (n=7) interaction. (**D**) Each data point of colloidal probe spectroscopy shows the median Young's modulus of one *Myh9*$^{+/+}$ or *Myh9*$^{D1424N/+}$ aggregate and bar plots show mean ± S.D. of Young's modulus (n=4). Statistics: Mann-Whitney U-test (*0.05 > p ≥ 0.01; **0.01 > p ≥ 0.001; ***p < 0.001).

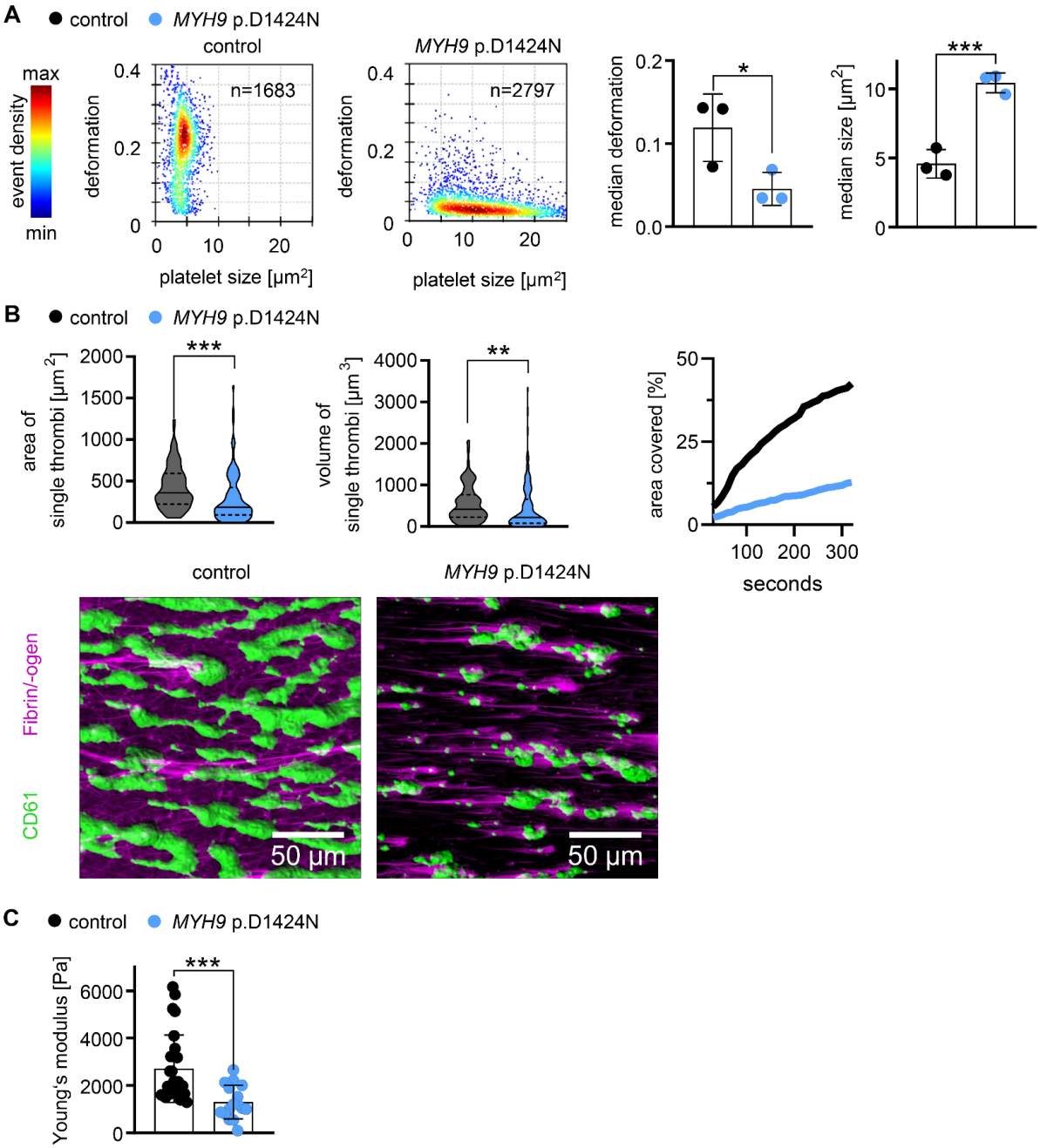

Fig. 5. Platelets of patient with the *MYH9* p.D1424N point mutation resemble the biomechanical phenotype of mouse platelets. (**A**) Representative KDE scatter plots from RT-FDC measurements displaying the distribution of single platelet deformation and their corresponding size between single platelets from a healthy individual (control) and from a *MYH9* p.D1424N patient (n= number of single platelets). Summary data points show the median deformation or median platelet size of individual donors and one *MYH9* p.D1424N patient on three different days and bar plots show mean ± S.D. of deformation and size from non-stimulated platelets (Multiple comparison using Holm-Sidak *0.05 > p ≥ 0.01; ***p < 0.001). (**B**) Platelet adhesion and aggregate formation under flow (1000/s) on collagen of human

patient samples were assessed using a flow chamber. Area of single thrombi and the volume of single thrombi are shown as median ± quartiles of platelet count unadjusted conditions (n=100 single thrombi). Area covered over time shows the mean of thrombi from control and patient blood. Representative images taken at the end of the perfusion time (20 minutes) are shown in fluorescent images with platelets labeled with the anti-CD61-antibody and labeled fibrin/-ogen (scale bars 50 µm). (**C**) Whole blood from healthy individuals and *MYH9* p.D1424N patient was examined by colloidal probe spectroscopy. Each data point shows the median Young's modulus of one healthy individual or *MYH9* p.D1424N aggregate and bar plots show mean ± S.D. of Young's modulus. Statistics: Mann-Whitney U-test (**0.01 > p ≥ 0.001; ***p < 0.001).

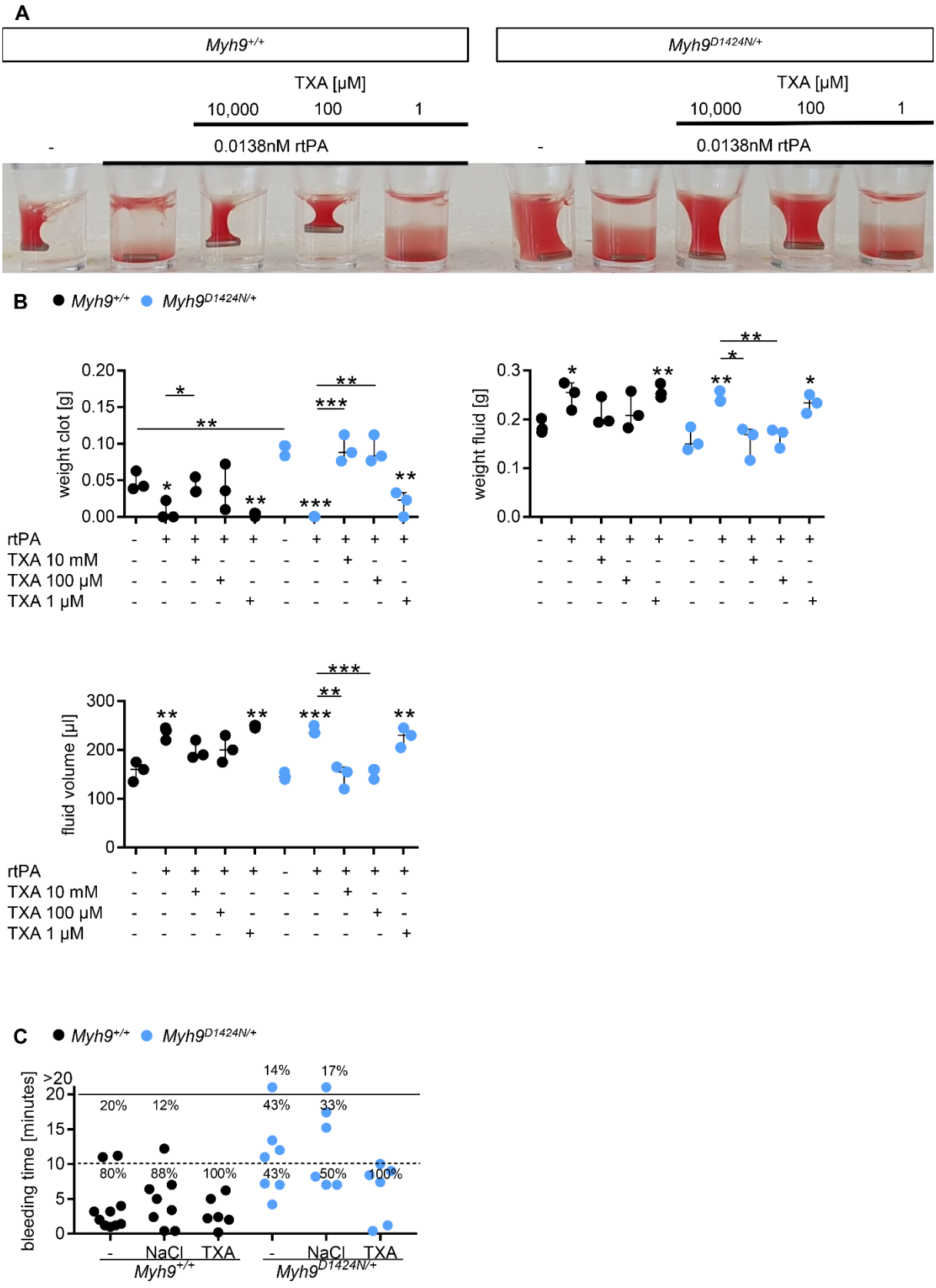

Fig. 6. Treatment with tranexamic acid improves hemostatic function in mutant mice. (**A**) Representative image of clot retraction from *Myh9*$^{+/+}$ and *Myh9*$^{D1424N/+}$ samples treated with rtPA in a threshold concentration where lysis occurs. Platelet count was not adjusted to reflect

the *in vivo* situation. Addition of TXA in different concentrations 10,000 µM, 100 µM and 1 µM; representative for three independent experiments. (**B**) Quantification of weight clot, weight fluid and fluid volume from clot retraction with rtPA and TXA treatment. Results are mean ± S.D. Each symbol represents one individual mouse. Statistics: Mann-Whitney U-test (ns $p \geq 0.05$; *$0.05 > p \geq 0.01$; **$0.01 > p \geq 0.001$; ***$p < 0.001$). Stars above symbol indicate comparison to control or untreated mutant sample. (**C**)Tail bleeding times on filter paper of *Myh9*$^{+/+}$ and *Myh9*$^{D1424N/+}$ mice. Injection of sodium chloride served as injection control. Each symbol represents one individual mouse (mean ± S.D.). Statistics: Mann-Whitney U-test (ns $p \geq 0.05$; *$0.05 > p \geq 0.01$; **$0.01 > p \geq 0.001$; ***$p < 0.001$).

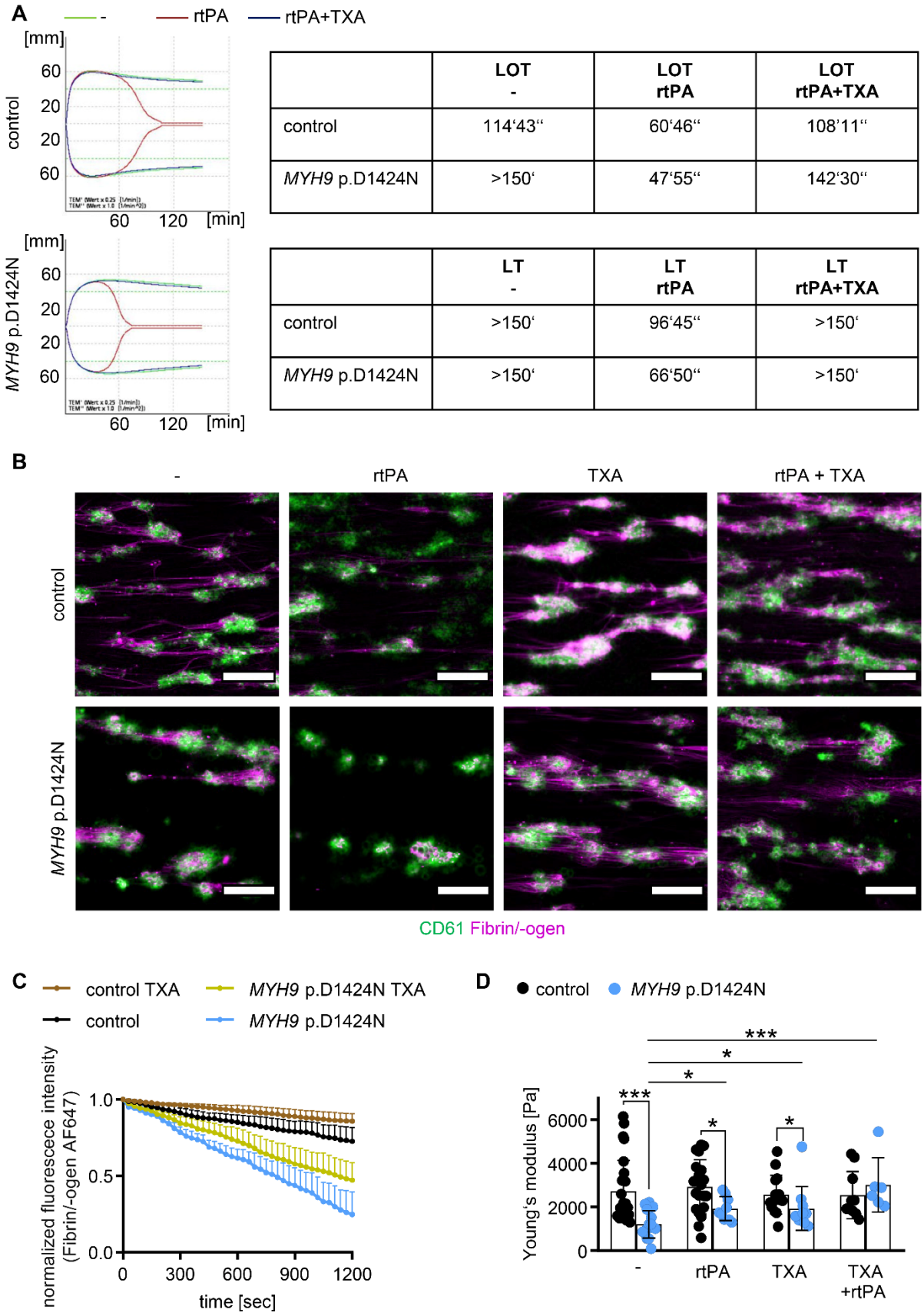

	LOT -	LOT rtPA	LOT rtPA+TXA
control	114‘43“	60‘46“	108’11“
MYH9 p.D1424N	>150‘	47‘55“	142‘30“

	LT -	LT rtPA	LT rtPA+TXA
control	>150‘	96‘45“	>150‘
MYH9 p.D1424N	>150‘	66‘50“	>150‘

Fig. 7. TXA improves clot and thrombus stability of patient sample. (**A**) Lysis onset time (LOT) and lysis time (LT) assessed with ROTEM without treatment (-), stimulation with rtPA,

and after addition of TXA to contrast rtPA-induced lysis stimulation. Overlapping of the modified ROTEM analysis curves (green: no treatment; red: rtPA stimulation; blue: rtPA and TXA stimulation). (**B**) Representative fluorescence images of human platelet thrombi (CD61; green) and fibrin (magenta) at 20 minutes after treatment in microfluidic flow chamber at a shear of 100 s^{-1} (scale bars 50 µm). (**C**) Time course of changes in stability of fibrin/-ogen (normalized fluorescence of fibrin/-ogen AF647, mean ± S.D.) on sites of platelet thrombi after addition of TXA (100 µM) compared to non-treated control. (**D**) Whole blood from healthy individuals and *MYH9* p.D1424N patient was examined (untreated, with rtPA, with TXA and with TXA + rtPA) using colloidal probe spectroscopy. Each data point shows the median Young's modulus of one healthy individual or *MYH9* p.D1424N aggregate and bar plots show mean ± S.D. of Young's modulus. Statistics: Mann-Whitney U-test (ns $p \geq 0.05$; *$0.05 > p \geq 0.01$; ***$p < 0.001$).

SUPPLEMENTAL INFORMATION

Reduced platelet forces underlie impaired hemostasis in mouse models of *MYH9*-related disease

Juliane Baumann[1†], Laura Sachs[2†], Otto Oliver[3], Ingmar Schoen[4], Peter Nestler[3], Carlo Zaninetti[2,5], Martin Kenny[4], Ruth Kranz[1], Hendrik von Eysmondt[6], Johanna Rodriguez[6], Tilman E. Schäffer[6], Zoltan Nagy[1], Andreas Greinacher[2], Raghavendra Palankar[2*], Markus Bender[1*]

[1]Institute of Experimental Biomedicine – Chair I, University Hospital and Rudolf Virchow Center, Würzburg, Germany. [2]Institute for Immunology and Transfusion Medicine, University Medicine Greifswald, Greifswald, Germany. [3]Zentrum für Innovationskompetenz – Humorale Immunreaktionen bei Kardiovaskulären Erkrankungen, University Greifswald, Greifswald, Germany. [4]School of Pharmacy and Biomolecular Sciences, Irish Centre for Vascular Biology, Royal College of Surgeons in Ireland, Dublin, Ireland. [5]University of Pavia, Pavia, Italy. [6]Institute of Applied Physics, University of Tübingen, Tübingen, Germany.

†These authors contributed equally to this work.

*Correspondence to:
Markus Bender: Bender_M1@ukw.de
Raghavendra Palankar: raghavendra.palankar@med.uni-greifswald.de

	Myh9$^{+/+}$	*Myh9*$^{R702C/+}$	*Myh9*$^{+/+}$	*Myh9*$^{D1424N/+}$	*Myh9*$^{+/+}$	*Myh9*$^{E1841K/+}$
WBC [10^3/µl]	5.4 ± 1.6	6.3 ± 1.2	7.2 ± 1.2	6.6 ±0.7	9.2 ± 2.1	10.5 ± 1.3
LYM [10^3/µl]	3.5 ± 1.2	4.5 ± 0.9	5.9 ± 1.1	5.3 ± 0.5	7.4 ± 1.7	8.5 ± 1.0
MON [10^3/µl]	0.2 ± 0.1	0.2 ± 0.1	0.2 ± 0.1	0.2 ± 0.1	0.3 ± 0.1	0.3 ± 0.1
GRA [10^3/µl]	1.7 ± 0.9	1.6 ± 0.3	1.1 ± 0.3	1.1 ± 0.3	1.5 ± 0.4	1.7 ± 0.3
EOS [10^3/µl]	0.04 ± 0.01	0.05 ± 0.01	0.04 ± 0.01	0.04 ± 0.01	0.06 ± 0.01	0.06 ± 0.01
RBC [10^6/µl]	8.7 ± 0.6	9.2 ± 0.6	8.2 ± 0.3	8.0 ± 0.3	8.6 ± 0.3	8.9 ± 0.3
HGB [g/dl]	16.1 ± 1.0	16.7 ± 0.6	15.4 ± 0.6	15.1 ± 0.3	14.2 ± 0.3	14.4 ± 0.4
HCT [%]	47.7 ± 1.9	50.0 ± 2.2	46.7 ± 1.3	45.8 ± 2.6	42.4 ± 1.1	43.6 ± 1.6

Supplemental Table 1. Blood parameters of *Myh9* mutant mice are comparable to control. Blood count parameters were measured with Scil Vet abc Plus hematology analyzer (n=7). WBC white blood cells; LYM lymphocytes; MON monocytes; GRA granulocytes; EOS eosinophils; RBC red blood cells; HGB hemoglobin; HCT hematocrit. Values are given in mean ± S.D. and show no significance (Mann-Whitney; $p \geq 0.05$).

Thrombin 0.05 U/ml	*Myh9*$^{+/+}$	*Myh9*$^{R702C/+}$	sig.	*Myh9*$^{+/+}$	*Myh9*$^{D1424N/+}$	sig.	*Myh9*$^{+/+}$	*Myh9*$^{E1841K/+}$	sig.
Max. Agg. [%]	70.5 ± 4.8	71.2 ± 2.0	ns	81.7 ± 10.1	74.2 ± 14.4	ns	77.1 ± 8.5	69.7 ± 5.1	ns
Max. Grad. [%/min]	40.4 ± 18.3	33.0 ± 1.9	ns	44.9 ± 6.6	48.5 ± 4.6	ns	50.8 ± 8.5	64.6 ± 19.8	ns
lag time [sec]	25.2 ± 2.0	25.3 ± 1.7	ns	32.0 ± 6.7	32.7 ± 5.9	ns	25.2 ± 2.3	25.0 ± 1.4	ns

Thrombin 0.01 U/ml	*Myh9*$^{+/+}$	*Myh9*$^{R702C/+}$	sig.	*Myh9*$^{+/+}$	*Myh9*$^{D1424N/+}$	sig.	*Myh9*$^{+/+}$	*Myh9*$^{E1841K/+}$	sig.
Max. Agg. [%]	71.7 ± 3.5	68.8 ± 4.3	ns	64.2 ± 16.5	56.2 ± 3.0	ns	65.2 ± 21.5	70.5 ± 6.2	ns
Max. Grad. [%/min]	34.2 ± 3.1	41.3 ± 8.7	ns	49.6 ± 10.7	59.9 ± 14.2	ns	52.6 ± 8.1	77.2 ± 7.3	**
lag time [sec]	26.0 ± 0.8	26.7 ± 0.6	ns	26.3 ± 1.0	23.8 ± 3.2	ns	28.0 ± 1.4	27.0 ± 2.9	ns

Collagen 10 µg/ml	*Myh9*$^{+/+}$	*Myh9*$^{R702C/+}$	sig.	*Myh9*$^{+/+}$	*Myh9*$^{D1424N/+}$	sig.	*Myh9*$^{+/+}$	*Myh9*$^{E1841K/+}$	sig.
Max. Agg. [%]	82.9 ± 8.3	80.5 ± 17.8	ns	88.0 ± 10.2	85.0 ± 8.4	ns	83.8 ± 15.8	79.4 ± 9.9	ns
Max. Grad. [%/min]	49.5 ± 15.4	69.1 ± 27.5	ns	84.0 ± 12.0	92.2 ± 19.1	ns	58.0 ± 18.7	69.0 ± 17.2	ns
lag time [sec]	81.7 ± 21.2	61.5 ± 6.9	*	55.8 ± 15.5	63.0 ± 8.7	ns	64.5 ± 4.2	62.5 ± 21.4	ns

Collagen 2 µg/ml	*Myh9*$^{+/+}$	*Myh9*$^{R702C/+}$	sig.	*Myh9*$^{+/+}$	*Myh9*$^{D1424N/+}$	sig.	*Myh9*$^{+/+}$	*Myh9*$^{E1841K/+}$	sig.
Max. Agg. [%]	70.0 ± 15.1	85.4 ± 8.5	ns	80.4 ± 4.2	82.1 ± 8.3	ns	83.8 ± 3.7	73.7 ± 6.5	ns
Max. Grad. [%/min]	41.8 ± 14.7	48.6 ± 12.4	ns	57.0 ± 10.1	66.0 ± 25.6	ns	54.4 ± 3.3	55.6 ± 10.1	ns
lag time [sec]	155.0 ± 32.6	129.6 ± 33.5	ns	101.7 ± 17.0	102.3 ± 19.0	ns	126.5 ± 8.3	109.2 ± 25.3	ns

Supplemental Table 2. Shape change and aggregation of *Myh9* mutant platelets are unaltered. Washed platelets were activated with thrombin (upper two) and collagen (lower two) and light transmission was recorded to determine maximum aggregation (Max. Agg.), maximum gradient (Max. Grad.), and time until shape change starts (lag time). Values are given in mean ± S.D. (n=4) and statistical significance was calculated with Mann-Whitney U-test (ns $p \geq 0.05$; *$0.05 > p \geq 0.01$; **$0.01 > p \geq 0.001$; ***$p < 0.001$).

	control	*MYH9* p.D1424N	control	*MYH9* p.E1841K
WBC [10^3/µl]	4.7	4.3	5.1	4.0
LYM [10^3/µl]	1.9	1.6	2.2	1.6
MON [10^3/µl]	0.5	0.6	0.4	0.2
NEUT [10^3/µl]	2.3	2.1	2.5	2.2
PLT [10^3/µl]	188	15	197	51
RBC [10^6/µl]	3.67	4.64	3.88	4.25
HGB [mmol/l]	7.0	8.4	7.5	7.7
HCT [l/l]	0.323	0.394	0.343	0.372

Supplemental Table 3. Blood parameters of *MYH9*-RD patients. Blood count parameters measured with Sysmex Hemato Analyzer pocH-100i (n=1). WBC white blood cells; LYM lymphocytes; MON monocytes; NEUT neutrophiles; PLT platelets; RBC red blood cells; HGB hemoglobin; HCT hematocrit.

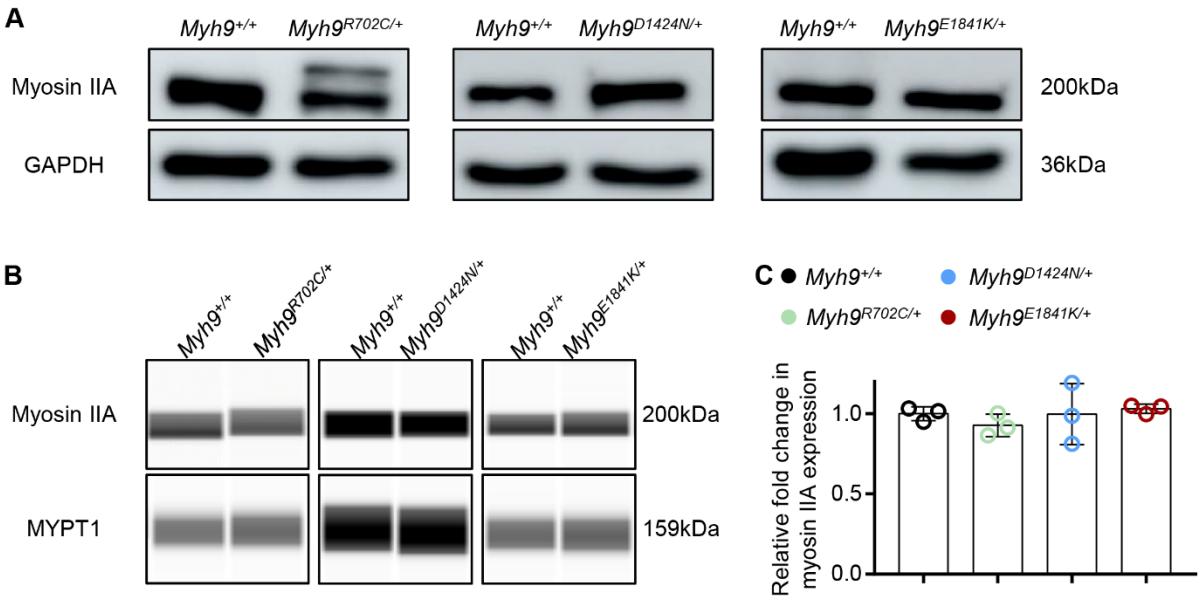

Supplemental Fig. 1. Myosin IIA is expressed in platelets of *Myh9* mutant mice. (**A**) Expression of myosin IIA in *Myh9*$^{D1424N/+}$, *Myh9*$^{E1841K/+}$ and corresponding control (*Myh9*$^{+/+}$) platelet lysates. Immunoblotting was performed on a 10% SDS-PAGE. Immunoblotting of *Myh9*$^{R702C/+}$ and control lysates was performed on a 7.5% SDS-PAGE. R702C mutant non-muscle myosin IIA-GFP and endogenous non-muscle myosin IIA could be detected. GAPDH served as loading control (n=3). (**B**) Myosin IIA and myosin phosphatase 1 (MYPT1) expression was confirmed using a capillary-based immunoassay approach. Fold change in myosin IIA expression relative to corresponding wildtype myosin IIA expression are shown in (**C**) for all mouse lines. Control shown corresponds to mouse line *Myh9*$^{D1424N/+}$. Each symbol represents one individual mouse.

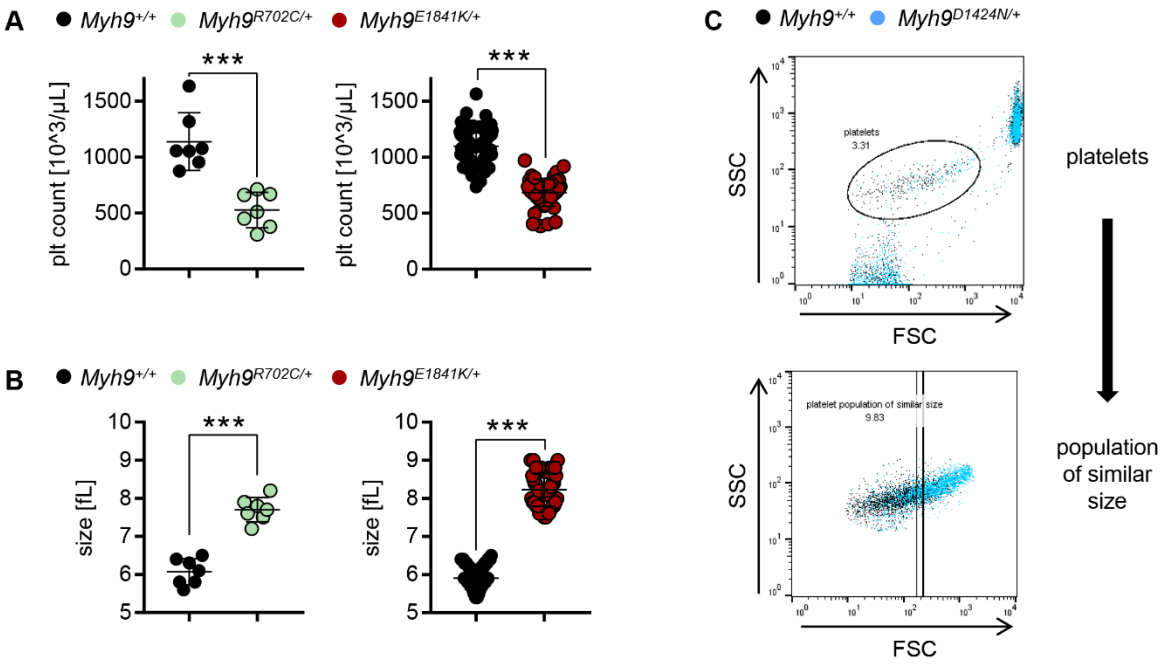

D

	Myh9$^{+/+}$	*Myh9*$^{R702C/+}$	significance	*Myh9*$^{+/+}$	*Myh9*$^{E1841K/+}$	significance
GPIb	10930 ± 461	12225 ± 737	*	8370 ± 296	9694 ± 746	**
GPV	9337 ± 414	10129 ± 922	ns	5244 ± 1520	7442 ± 178	**
GPIX	15084 ± 1491	15826 ± 1028	ns	7640 ± 4253	12564 ± 270	*
αIIbβ3	10573 ± 500	10669 ± 320	ns	9882 ± 5074	13384 ± 759	ns
α2	463 ± 24	483 ± 12	ns	1437 ± 93	1551 ± 76	ns
CD9	27814 ± 775	29337 ± 1791	ns	32612 ± 2048	34219 ± 2280	ns
GPVI	1591 ± 213	1795 ± 174	ns	843 ± 479	1202 ± 74	ns
CLEC-2	3158 ± 80	3498 ± 115	***	1694 ± 1414	3583 ± 230	*

Supplemental Fig. 2. Macrothrombocytopenia in R702C and E1841K mutant mice. Determination of (**A**) platelet count and (**B**) platelet size. Each symbol represents one individual mouse (mean ± S.D.; Mann-Whitney U-test ***p < 0.001). (**C**) Gating strategy to determine platelet population of similar size for analysis of glycoprotein expression and platelet activation. (**D**) Glycoprotein expression on the platelet surface was determined by flow cytometry (n=4-7). Data are expressed as mean fluorescence intensity (Multiple comparison using Holm-Sidak; ns $p \geq 0.05$; *$0.05 > p \geq 0.01$; **$0.01 > p \geq 0.001$; ***$p < 0.001$).

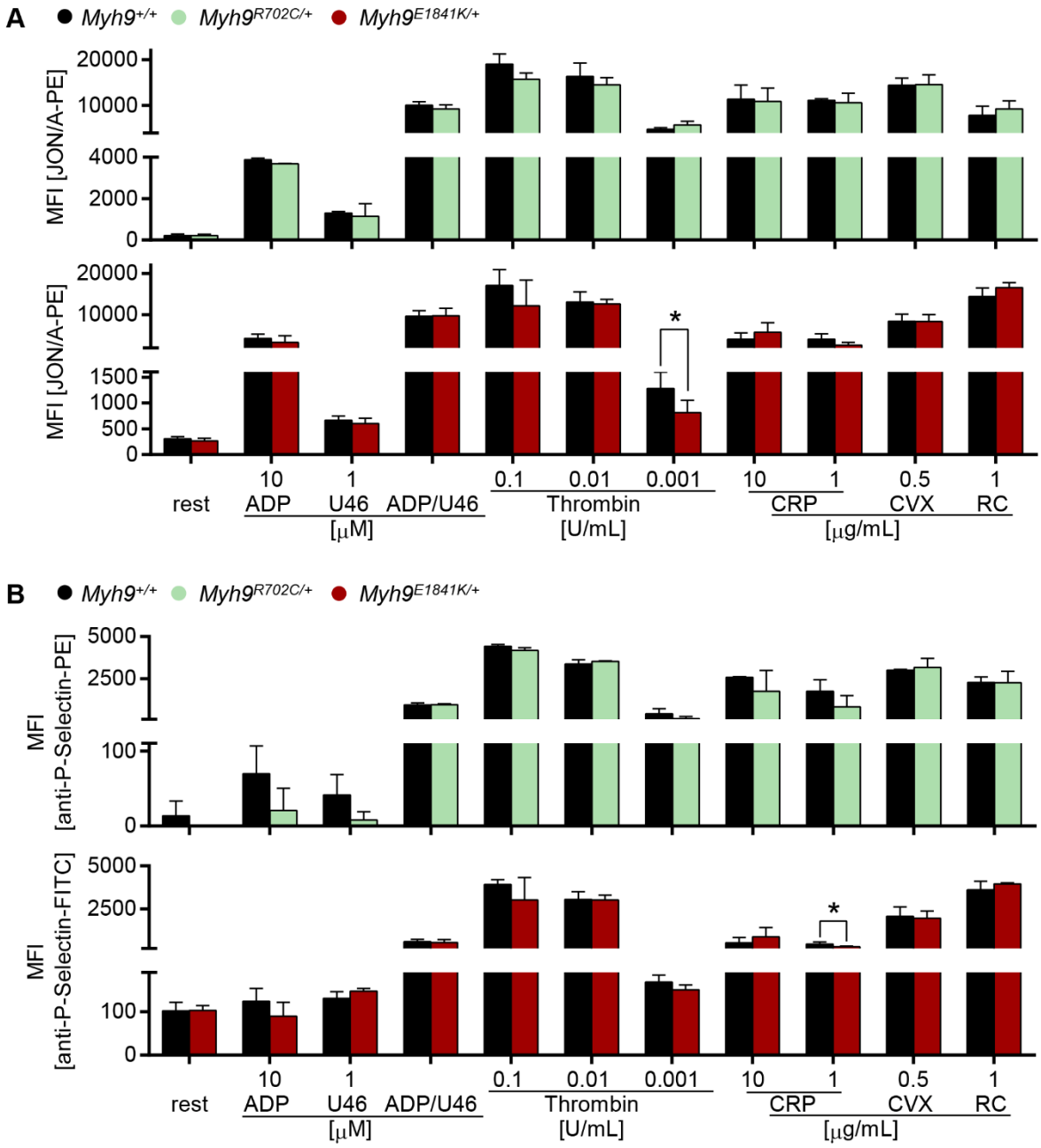

Supplemental Fig. 3. Inside-out activation is unaltered in mutant platelets. (**A**) Activation of platelet αIIbβ3-integrin (JON/A-phycoerythrin [PE]) and (**B**) α-granule release (anti-P-Selectin-fluorescein isothiocyanate [FITC]) under resting (rest) conditions and upon stimulation with different agonists (n=5, MFI). ADP: adenosine diphosphate; U46: thromboxane A2 analog U46619; CRP: collagen-related peptide; CVX: Convulxin; RC: Rhodocytin. Statistics: Multiple comparison using Holm-Sidak (ns $p \geq 0.05$; *$0.05 > p \geq 0.01$).

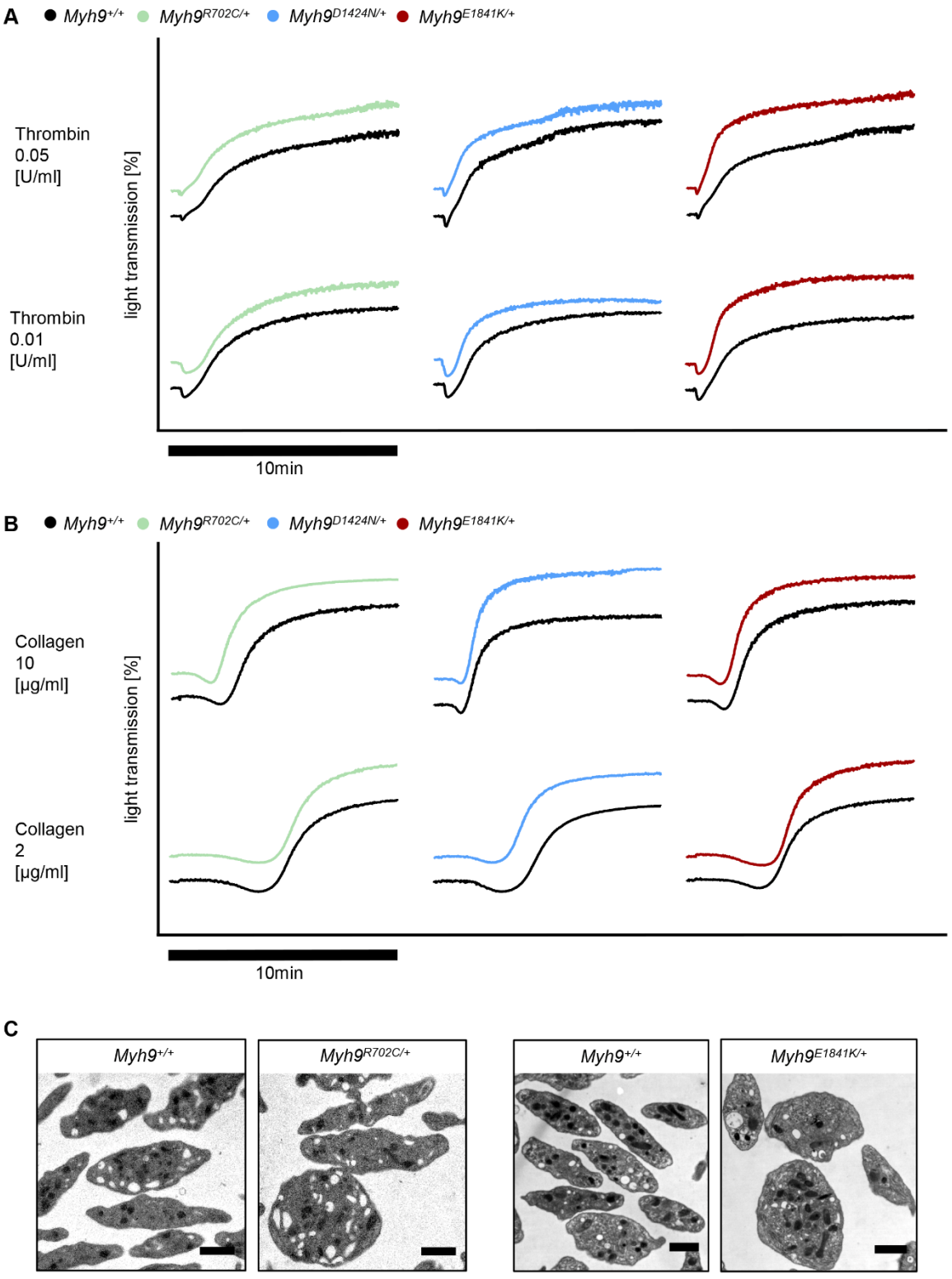

Supplemental Fig. 4. Normal shape change and aggregation of *Myh9* mutant platelets. Washed platelets were stimulated with (**A**) thrombin or (**B**) collagen and light transmission was recorded using a 4-channel aggregometer. Representative curves of two independent experiments are shown (n=2). (**C**) Representative transmission electron micrographs of mutant and control platelets. Scale bar: 1 µm.

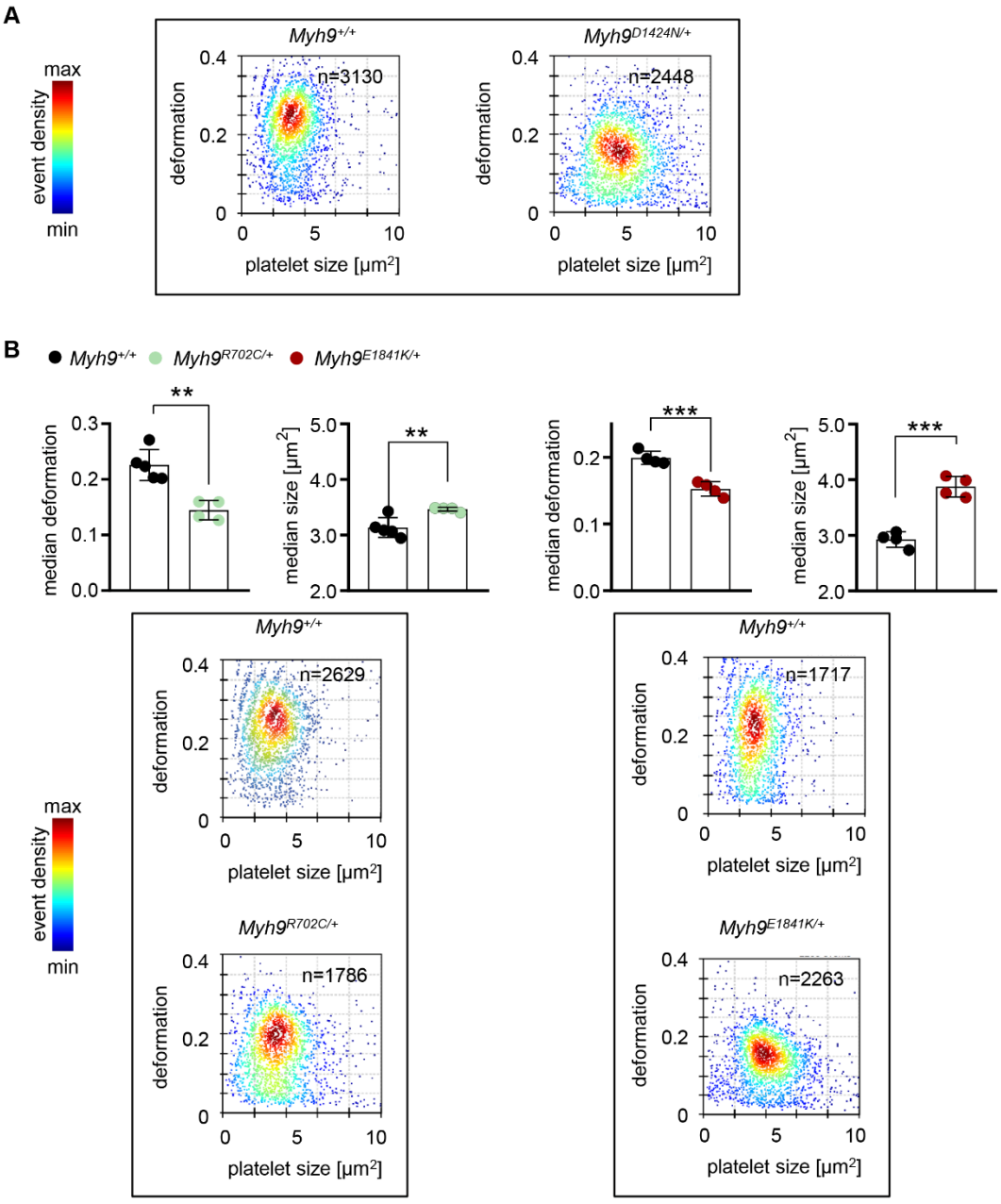

Supplemental Fig. 5. Deformability measurements by RT-FDC. (**A**) Representative KDE scatter plots from RT-FDC measurements displaying the distribution of single platelet deformability and their corresponding size between single platelets from *Myh9*$^{+/+}$ or *Myh9*$^{D1424N/+}$ mice (n= number of single platelets). (**B**) Each data point of RT-FDC measurement shows the median deformation and area of *Myh9*$^{+/+}$, *Myh9*$^{R702C/+}$ or *Myh9*$^{E1841K/+}$ platelets with ~ 2000 platelets of one individual mouse. Bar plots show mean ± S.D. of platelet deformation or platelet area (n=4-5). Representative KDE scatter plots from RT-FDC measurements displaying the distribution of single platelet deformability and their corresponding size between single platelets from *Myh9*$^{+/+}$, *Myh9*$^{R702C/+}$, or *Myh9*$^{E1841K/+}$ mice (n= number of single platelets). Statistics: Multiple comparison using Holm-Sidak (**0.01 > p ≥ 0.001; ***p < 0.001).

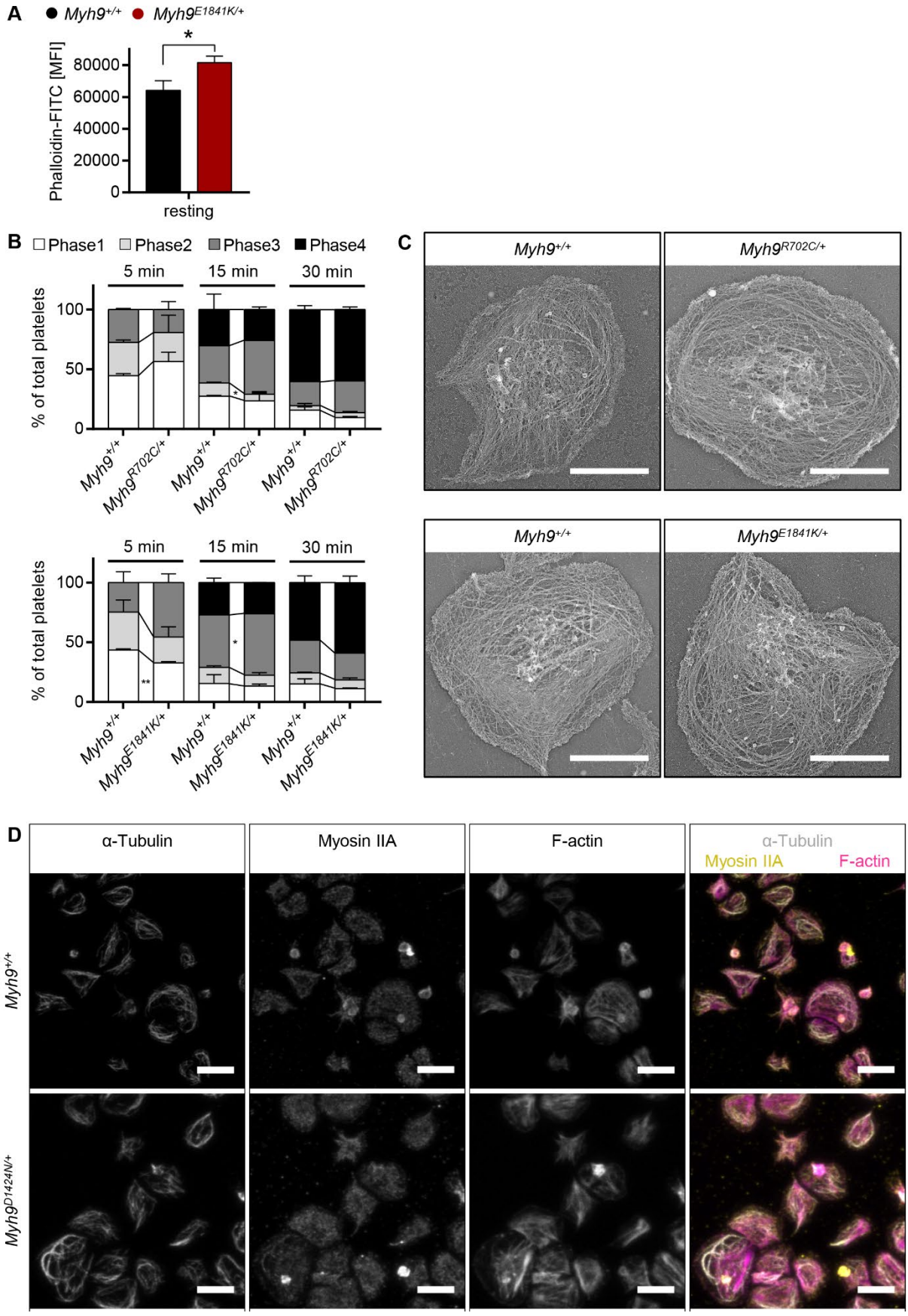

Supplemental Fig. 6. Outside-in signaling of *Myh9* mutant platelets. (**A**) F-actin content of resting platelets from mouse line E1841K was measured by flow cytometry after

incubation with phalloidin-FITC (n=4). The mean fluorescence intensity is shown. (**B**) Platelets were spread on fibrinogen in the presence of thrombin and statistical analysis was performed of the different spreading phases of fixed platelets at different time points (n=2). Platelets of phase 1 were resting discoid shaped, phase 2 platelets formed filopodia, phase 3 platelets displayed lamellipodia and filopodia and phase 4 platelets were fully spread with only lamellipodia (mean ± S.D.). (**C**) Platinum replica electron microscopy of the cytoskeleton ultrastructure of spread platelets on fibrinogen was performed (scale bars: 2 µm). (**D**) Representative single stained and merged confocal images of *Myh9*$^{+/+}$ and *Myh9*$^{D1424N/+}$ platelets spread on fibrinogen in the presence of thrombin, stained for α-tubulin (grey), myosin IIA (yellow), and F-actin (magenta) (scale bars: 5 µm). Statistics: Multiple comparison using Holm-Sidak (*0.05 > p ≥ 0.01; **0.01 > p ≥ 0.001).

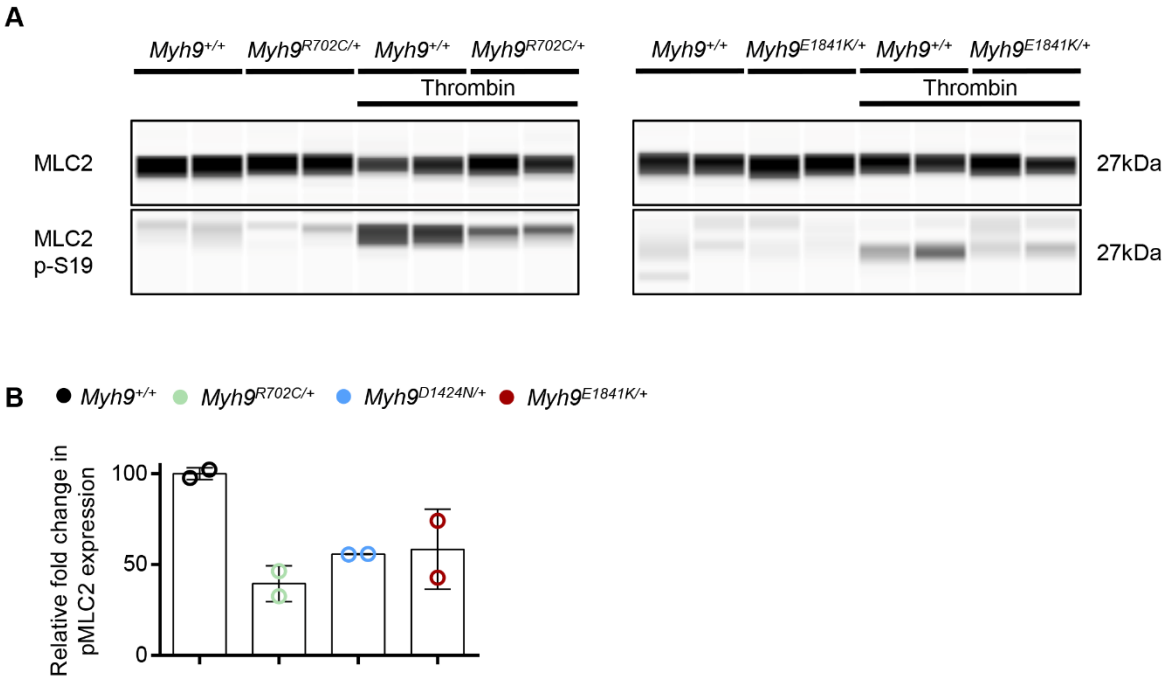

Supplemental Fig. 7. Reduced myosin light chain 2 phosphorylation in *Myh9* mutant platelets. (**A**) Expression of myosin light chain 2 (MLC2) and phosphorylated myosin light chain 2 (MLC2p-S19) of resting and thrombin-activated (0.05 U/mL, 1 min) platelets was determined. Representative immunoblot of two independent experiments are shown (n=2). (**B**) Quantification of pMLC2 expression upon activation with thrombin relative to control, representative from mouse line D1424N (mean ± S.D.).

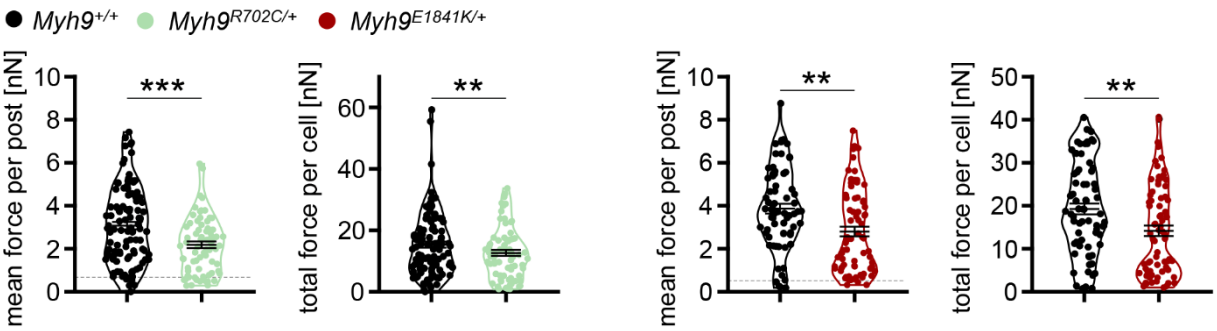

Supplemental Fig. 8. *Myh9* mutant platelets show less contractile forces on micropost arrays. Platelet contractile forces were measured per post and the sum of posts per cell (mean ± S.D.; *Myh9*$^{+/+}$: n=106; *Myh9*$^{R702C/+}$: n=73; *Myh9*$^{+/+}$: n=69; *Myh9*$^{E1841K/+}$: n=74). Statistics: Mann-Whitney U-test (**0.01 > p ≥ 0.001; ***p < 0.001).

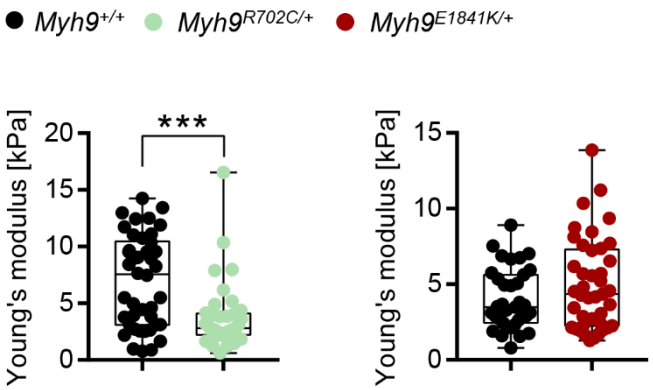

Supplemental Fig. 9. Spread platelets of *Myh9*$^{R702C/+}$ but not *Myh9*$^{E1841K/+}$ mice are softer. Washed *Myh9*$^{+/+}$, *Myh9*$^{R702C/+}$ and *Myh9*$^{E1841K/+}$ platelets spread on fibrinogen in the presence of thrombin were analyzed of their Young's modulus using scanning ion conductance microscopy. Each symbol represents one platelet (*Myh9*$^{+/+}$: n=42 platelets; *Myh9*$^{R702C/+}$: n=36 platelets; *Myh9*$^{+/+}$: n=36 platelets; *Myh9*$^{E1841K/+}$: n=41 platelets) and box plots represents median ± S.D. Statistics: Mann-Whitney U-test (ns p ≥ 0.05; ***p < 0.001).

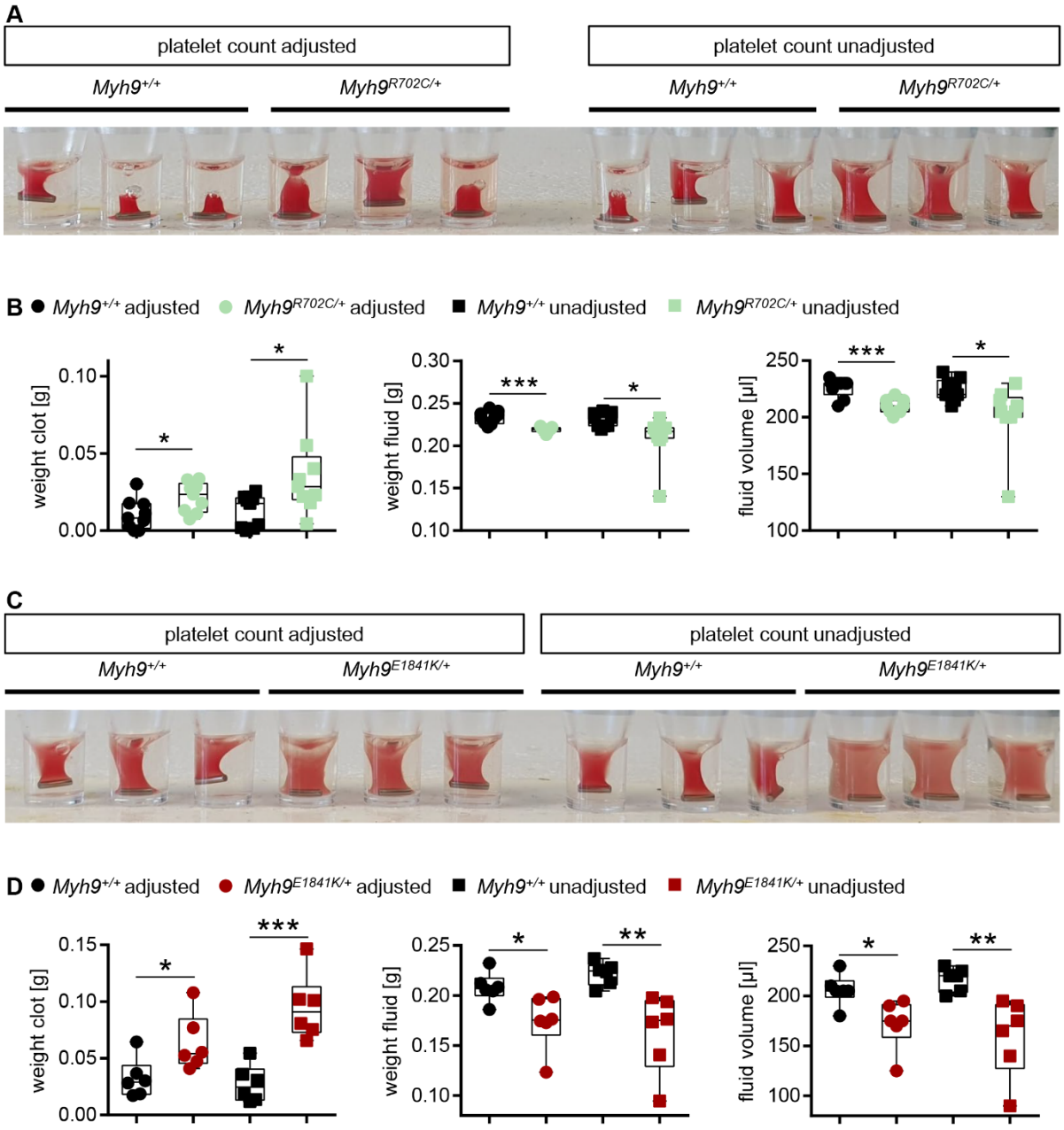

Supplemental Fig. 10. Reduced extent of clot retraction in *Myh9* mutant samples. (**A**) Representative image of clot formation of *Myh9*$^{+/+}$ and *Myh9*$^{R702C/+}$ samples at time point 60 minutes (n=3). (**B**) Results are median ± S.D. Each symbol represents one individual mouse. (**C**) Representative image of clot formation of *Myh9*$^{+/+}$ and *Myh9*$^{E1841K/+}$ samples at time point 60 minutes (n=3). (**D**) Results are median ± S.D. Each symbol represents one individual mouse. Statistics: Multiple comparison using Holm-Sidak (*0.05 > p ≥ 0.01; **0.01 > p ≥ 0.001; ***p < 0.001).

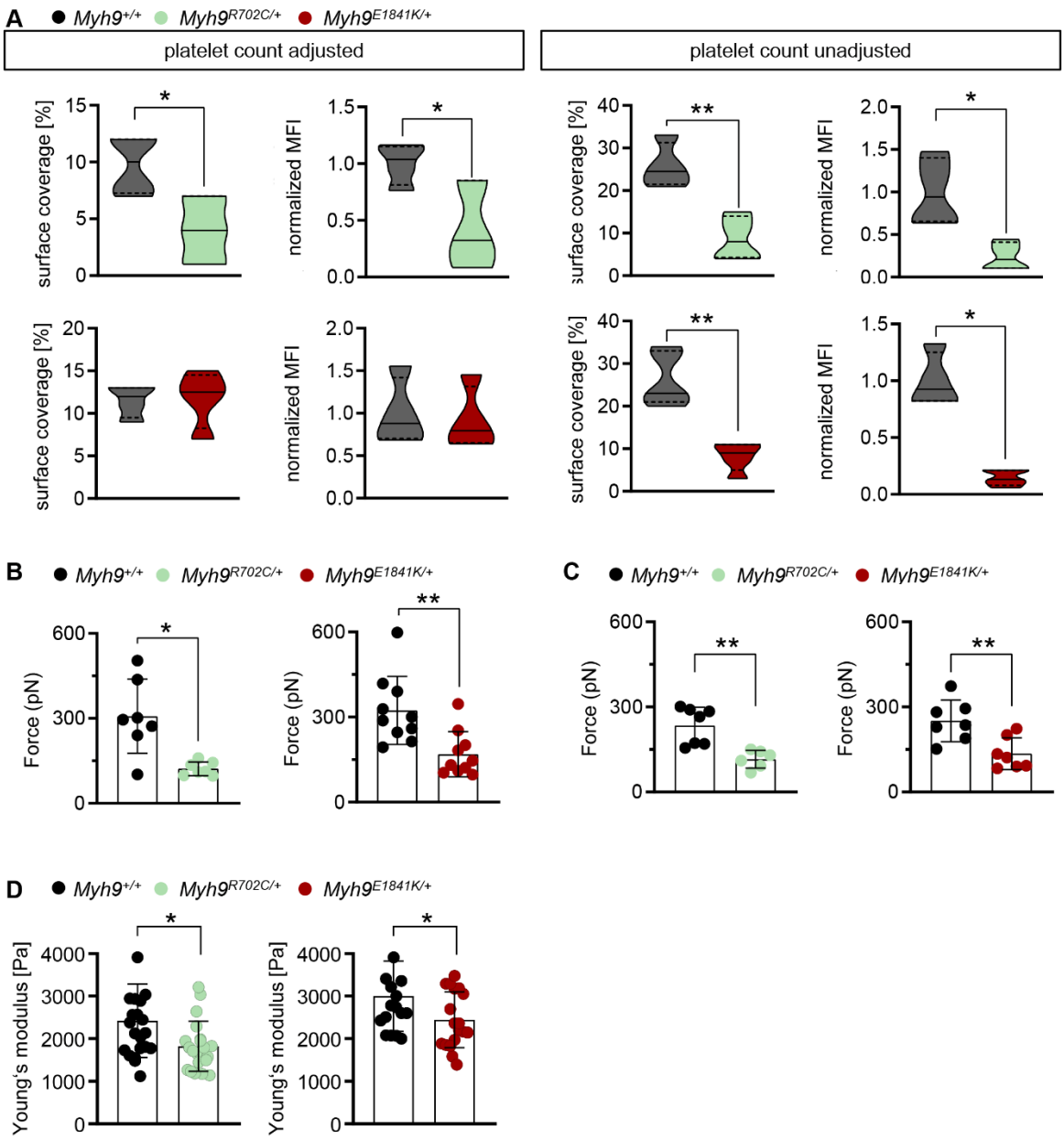

Supplemental Fig. 11. Reduced thrombus formation under flow of *Myh9* mutant platelets. (**A**) Assessment of platelet adhesion and aggregate formation under flow (1000/s) on collagen of *Myh9*$^{+/+}$ and *Myh9*$^{R702C/+}$ samples (upper row), and of *Myh9*$^{+/+}$ and *Myh9*$^{E1841K/+}$ samples (lower row). Analysis of the surface area covered by platelets (%) and the relative normalized MFI of anti-GPIX (Alexa 488) are shown for platelet count adjusted conditions on the left side (n=4, mean ± S.D.) and unadjusted conditions on the right side (n=4-5, mean ± S.D.). Single platelet force spectroscopy of (**B**) platelet adhesion to collagen and (**C**) platelet-platelet interaction forces. (**B** to **C**) Each data point of summary graphs (mean ± S.D.) shows one platelet to collagen (n=7-10) or platelet to platelet (n=7) interaction. (**D**) Each data point of colloidal probe spectroscopy shows the median Young's modulus of one *Myh9*$^{+/+}$, *Myh9*$^{R702C/+}$ or *Myh9*$^{E1841K/+}$ aggregate and bar plots show mean ± S.D. of Young's modulus (n=4-5). Statistics: Mann-Whitney U-test (ns $p \geq 0.05$; *$0.05 > p \geq 0.01$; **$0.01 > p \geq 0.001$).

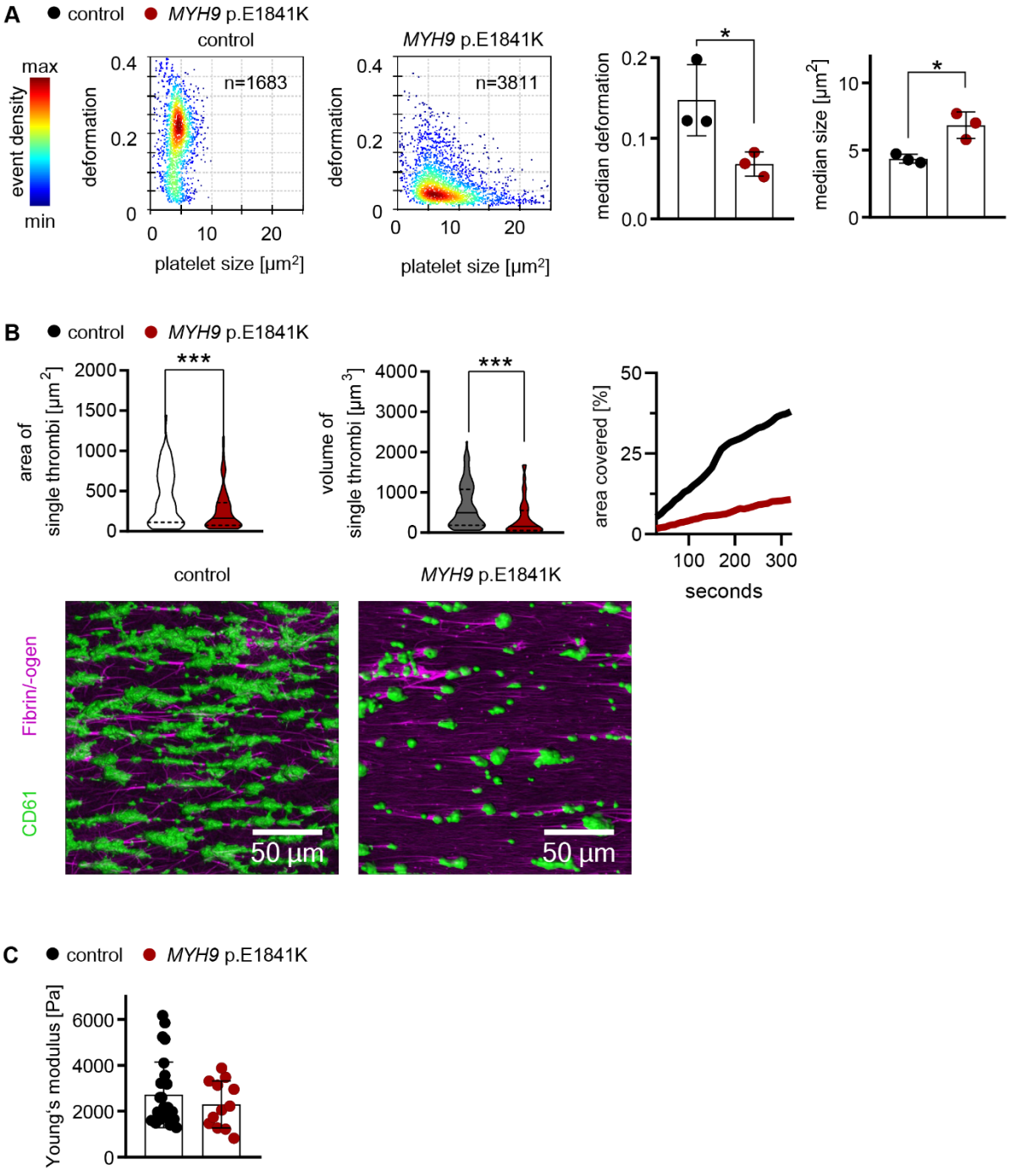

Supplemental Fig. 12. *MYH9* p.E1841K patient platelets form smaller thrombi under flow. (**A**) Representative KDE scatter plots from RT-FDC measurements displaying the distribution of single platelet deformability and their corresponding size between single platelets from a healthy individual (control) and from a *MYH9* p.E1841K patient (n= number of single platelets). Summary data points show the median values of individual donors and one *MYH9* p.E1841K patient on three different days and bar plots show mean ± S.D. of platelet deformation and size from non-stimulated platelets (Multiple comparison using Holm-

Sidak *0.05 > p ≥ 0.01). (**B**) Platelet adhesion and aggregate formation under flow (1000/s) on collagen of human patient samples were assessed by a flow chamber assay. Area and volume of single thrombi are shown as median ± quartiles of platelet count unadjusted conditions (n=67 single thrombi). Area covered over time shows the mean of thrombi from control and patient blood. Representative images taken at the end of the perfusion time (20 minutes) are shown in fluorescent images with platelets labeled with the anti-CD61-antibody and labeled fibrin/-ogen (scale bars 50 µm). (**C**) Whole blood from healthy individuals and *MYH9* p.E1841K patient was examined by colloidal probe spectroscopy. Each data point shows the median Young's modulus of one aggregate and bar plots show mean ± S.D. of Young's modulus. Statistics: Mann-Whitney U-test (ns p ≥ 0.05; ***p < 0.001).

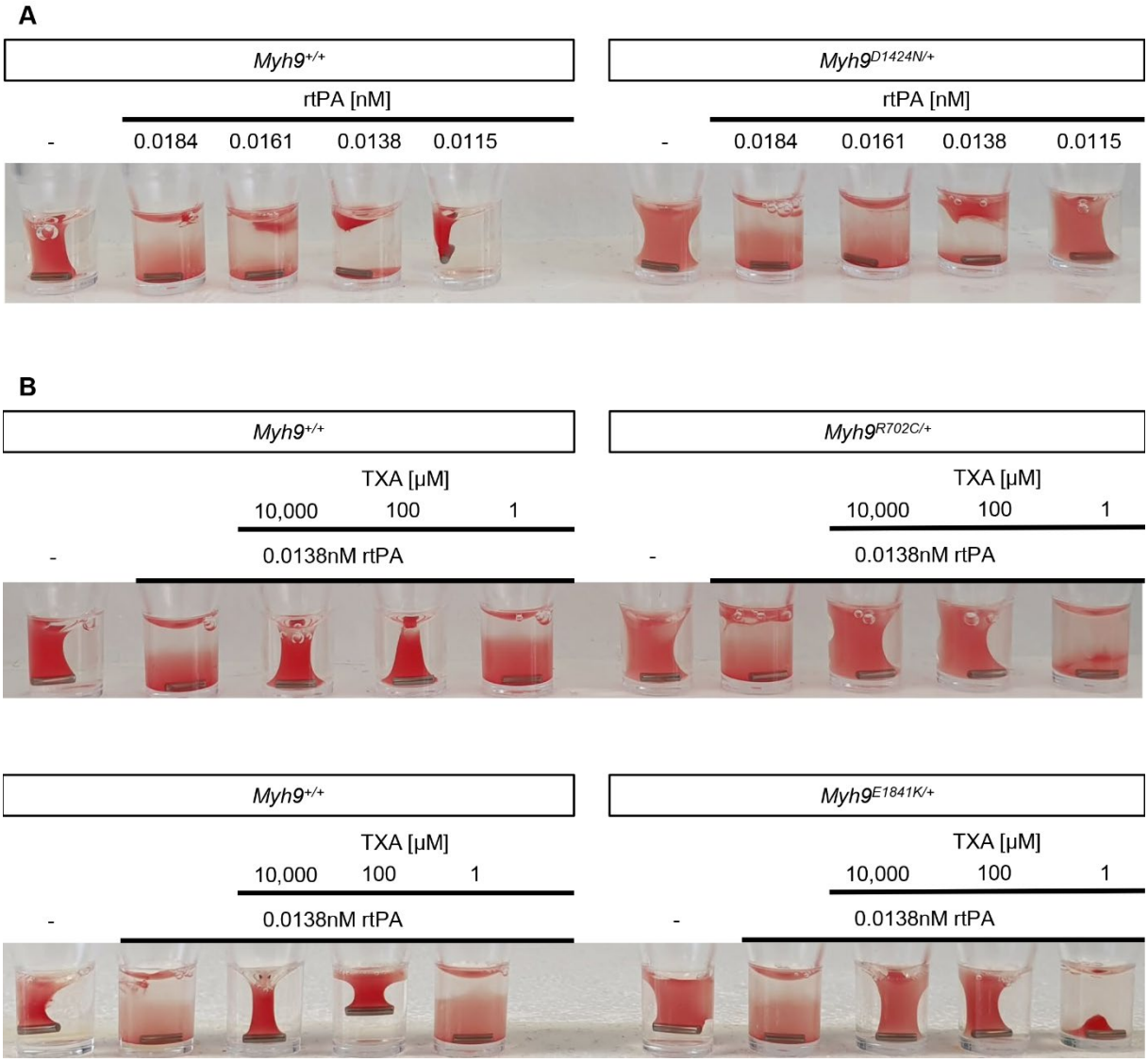

Supplemental Fig. 13. Clot lysis induced by rtPA can be reversed by high concentrations of TXA. (**A**) Concentration-dependent effect of rtPA on *Myh9*$^{+/+}$ and *Myh9*$^{D1424N/+}$ samples. Representative image of three independent experiments. (**B**) Representative image (three independent experiments) of clot retraction of *Myh9*$^{+/+}$, *Myh9*$^{R702C/+}$, and *Myh9*$^{E1841K/+}$ samples treated with rtPA in a threshold concentration where lysis occurs. Addition of TXA at different concentrations.

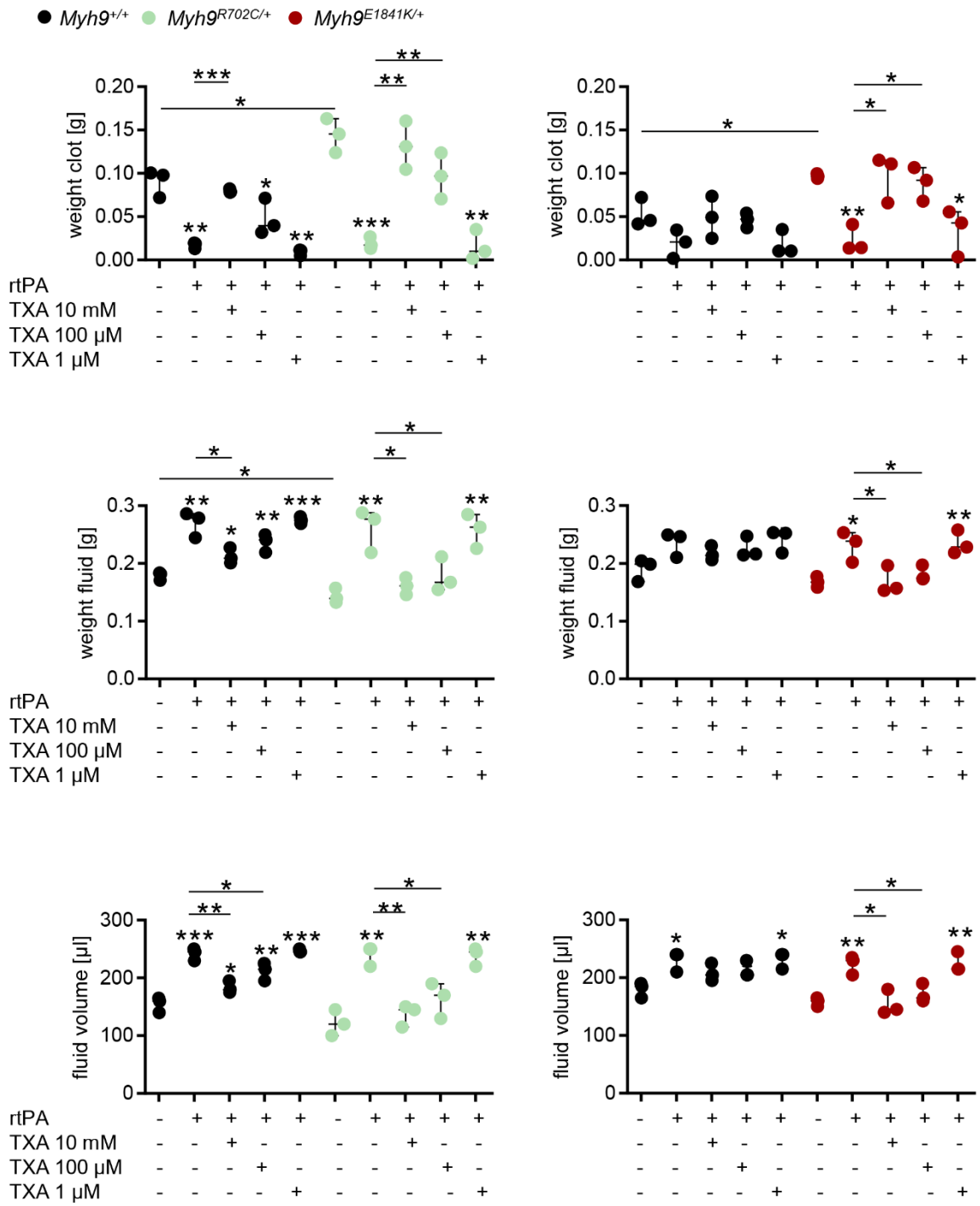

Supplemental Fig. 14. TXA in concentrations of 100 µM and 10 mM improves clot retraction. Quantification of weight clot, weight fluid and fluid volume of clot retraction with rtPA and TXA treatment. Results are mean ± S.D. Each symbol represents one individual mouse. Statistics: Mann-Whitney U-test (ns $p \geq 0.05$; *$0.05 > p \geq 0.01$; **$0.01 > p \geq 0.001$; ***$p < 0.001$). Stars above symbol indicate comparison to control or mutant sample untreated.

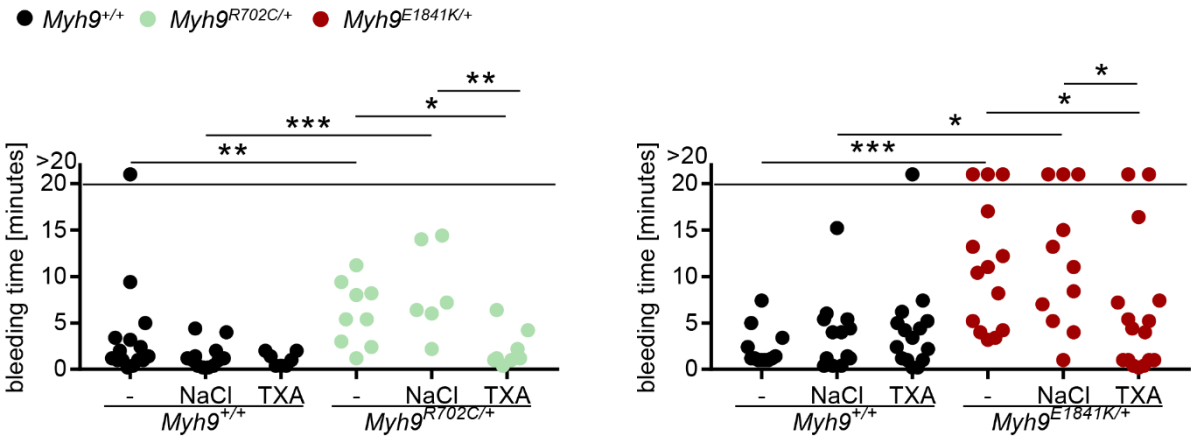

Supplemental Fig. 15. Tranexamic acid improves hemostasis. Tail bleeding times on filter paper of *Myh9* mutant mouse lines R702C and E1841K. Injection of sodium chloride served as control. Each symbol represents one individual mouse (mean ± S.D.). Mann-Whitney-U test was used to analyze data excluding data points exceeding 20 minutes (ns $p \geq 0.05$; *$0.05 > p \geq 0.01$; **$0.01 > p \geq 0.001$; ***$p < 0.001$).

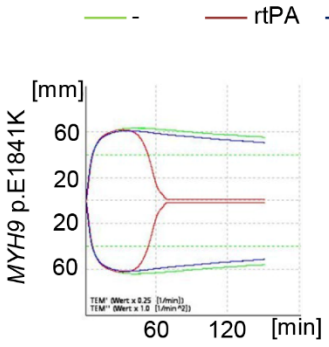

	LOT -	LOT rtPA	LOT rtPA+TXA
MYH9 p.E1841K	>150‘	46‘13“	136‘27“

	LT -	LT rtPA	LT rtPA+TXA
MYH9 p.E1841K	>150‘	63‘	>150‘

Supplemental Fig. 16. Shortened LOT and LT of *MYH9* p.E1841K sample can be reverted by TXA. Lysis onset time (LOT) and lysis time (LT) of human sample assessed with ROTEM. Overlapping of the modified ROTEM analysis curves (green: no treatment; red: rtPA stimulation; blue: rtPA and TXA stimulation).

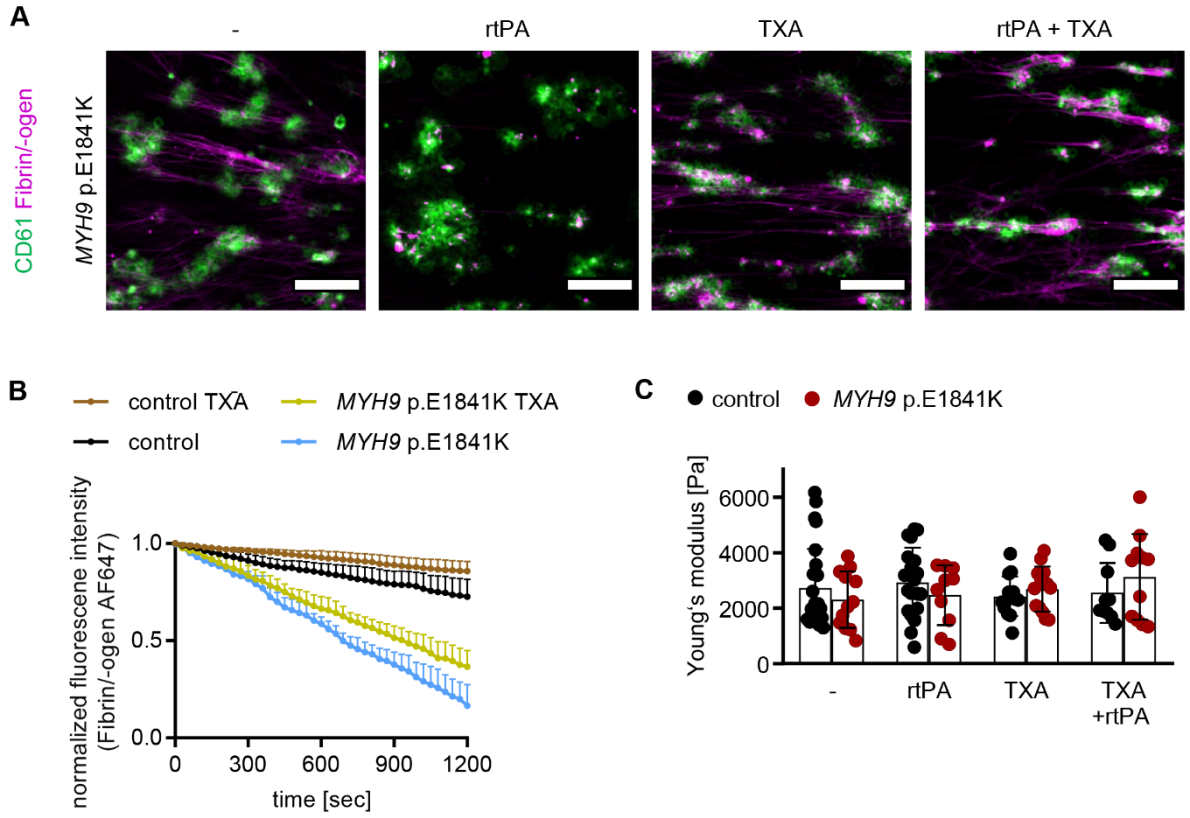

Supplemental Fig. 17. Fibrinolysis in a microfluidic flow chamber is decreased by TXA. (**A**) Representative fluorescence images of human platelet thrombi (CD61; green) and fibrin (magenta) at 20 minutes after treatment in microfluidic flow chamber at a shear of 100 s^{-1} (scale bars 50µm) and (**B**) Time course of changes in stability of fibrin/-ogen (normalized fluorescence of fibrin/-ogen AF647, mean ± S.D.) on sites of platelet thrombi after addition of TXA (100 µM) compared to non-treated control. (**C**) Thrombus stiffness in whole blood from healthy individual and *MYH9* p.E1841K patient was examined (untreated, with rtPA, with TXA and with TXA + rtPA) using colloidal probe spectroscopy. Each data point shows the median Young's modulus of one healthy individual or *MYH9* p.E1841K aggregate and bar plots show mean ± S.D. of Young's modulus. Statistics: Mann-Whitney U-test (ns $p \geq 0.05$).

10. Eigenständigkeitserklärung

11. Curriculum vitae

12. Publications

12.1. Peer-reviewed articles

Sachs, L.; Denker, C.; Greinacher, A.; Palankar, R. Quantifying single-platelet biomechanics: An outsider's guide to biophysical methods and recent advances. *Research and practice in thrombosis and haemostasis* 2020, 4 (3), 386–401. DOI: 10.1002/rth2.12313.

Sachs, L.; Wesche, J.; Lenkeit, L.; Greinacher, A.; Bender, M.; Otto, O.; Palankar, R. *Ex vivo* anticoagulants affect human blood platelet biomechanics with implications for high-throughput functional mechanophenotyping. *Communications biology* 2022, 5 (1), 86. DOI: 10.1038/s42003-021-02982-6.

12.2. Accepted manuscript

Baumann, J., **Sachs, L.**, Oliver, O., Schoen, I., Nestler, P., Zaninetti, C., Kenny, M., Kranz, R., von Eysmondt, H., Rodriguez, J., Schäffer, T. E., Nagy, Z., Greinacher, A., Palankar, P., Bender, M. Reduced platelet forces underlie impaired hemostasis in mouse models of *MYH9*-related disease. Accepted at *Science Advances* (2022).

Accepted at *Science Advances* on February 25, 2022
Submission ID: abn2627

12.3. Further article

Zaninetti, C.; **Sachs, L.**; Palankar, R. Role of Platelet Cytoskeleton in Platelet Biomechanics: Current and Emerging Methodologies and Their Potential Relevance for the Investigation of Inherited Platelet Disorders. *Hamostaseologie* 2020, 40 (3), 337–347. DOI: 10.1055/a-1175-6783.

13. Conference Contributions

L. Sachs, J. Wesche, A. Greinacher, O. Otto, R. Palankar.
Influence of anticoagulants on biomechanical phenotype of platelets.
3rd Symposium Platelets.
24 – 26 October 2019. Tübingen, Germany.
poster presentation

L. Sachs, J. Wesche, A. Greinacher, O. Otto, R. Palankar.
Influence of anticoagulants on biomechanical phenotype of platelets.
64th Annual Meeting of the Society of Thrombosis and Hämostasis Research e.v.
18 – 21 February 2020. Bremen, Germany.
poster presentation

L. Sachs, J. Baumann, J. Wesche, P. Nestler, C. Zaninetti, L. Lenkeit, A. Greinacher, M. Bender, O. Otto, R. Palankar.
Platelets from patients with *MYH9*-related disorders are mechanically stiffer.
65th Annual Meeting of the Society of Thrombosis and Hämostasis Research e.v.
22 – 26 February 2021. Online.
oral presentation

L. Sachs, J. Baumann, J. Wesche, P. Nestler, C. Zaninetti, A. Greinacher, M. Bender, O. Otto, R. Palankar.
Platelets from patients with *MYH9*-related disorders are mechanically stiffer.
XXIX Congress of the International Society on Thrombosis and Haemostasis.
17 – 21 July 2021. Online.
oral presentation.

14. Acknowledgements

Science is teamwork. The studies in this thesis could not have been done and this thesis would never have been written if many people had not contributed in numerous ways.

First of all, I would like to thank my supervisor **Dr. Raghavendra Palankar** for giving me the chance to perform my thesis in the exciting field of biomechanics. Thank you for your trust, support and patience. I could not have had a better supervisor during my thesis.

Prof. Dr. Otto I would like to thank you for being a member of my thesis committee. Oli, I want to thank you for believing in me and always supporting me. I thank you for always having an open ear, sharing your expertise with me, and teaching me about biophysics with your calm and relaxed nature.

Further, I would like to thank **Prof. Dr. Greinacher** for being a member of my thesis committee. I am grateful for the time you spend in our regular meetings to exchange ideas, discuss problems and giving helpful advice.

I would like to thank **Prof. Dr. Hammerschmidt** for being a member of my thesis committee and for the good cooperation and support.

I want to thank the whole transfusion medicine research group, I am happy to work with all of you. I love our valuable centrifugation breaks and group activities. Thank you for the great working atmosphere. **Jan**, thank you for your support with the experiments, help with the evaluations and your always open ear. **Julia**, thank you for the support during the many experiments, without you many things would not have been possible. Thank you for being a friend. **Jessi** supported me with the orders and was always there for me in case of emergency. **Stefan** I would like to thank for answering numerous annoying questions and for the support.

From the ZIK HIKE I would like to thank **Doreen** and **Peter**, for the training on the RT-FDC and AFM and the lovely help with problems.

I would like to thank **Dr. Bender** and **Juliane Baumann** from Würzburg, who made a significant contribution to the third research article.

And last but not least, I would like to thank my **parents**, my **grandparents**, my **sister**, **Niklas** and **Lisa** who have rejoiced with me, suffered with me and breathed a sigh of relief. Thank you for your patience and always listening.
And a very special thank you to you, my wonderful future husband **Marcel**, for your endless love, your everlasting understanding, your unlimited support and your almost endless patience with me. All your faith in me has motivated me to achieve my goals.